

NASA/TP-1999-209344



# Crossflow Stability and Transition Experiments in Swept-Wing Flow

*J. Ray Dagenhart*  
*Langley Research Center, Hampton, Virginia*

*William S. Saric*  
*Arizona State University, Tempe, Arizona*

National Aeronautics and  
Space Administration

Langley Research Center  
Hampton, Virginia 23681-2199

---

July 1999

## Acknowledgments

The authors are grateful to Helen L. Reed of Arizona State University who provided theoretical data for comparison with the experimental results and W. Pfenninger of the NASA Langley Research Center who continually provided technical insight and discussion throughout the project. Jon Hoos, Marc Mousseux, Ronald Radeztsky, and Dan Clevenger of Arizona State University provided important assistance and valuable discussion of the research at the Unsteady Wind Tunnel. Thanks are extended to Harry L. Morgan and J. P. Stack of the NASA Langley Research Center for assistance in computational and measurement aspects of the research. Finally, technical discussions with many members of the Experimental Flow Physics Branch contributed significantly to the work.

This report was completed by Ronald D. Joslin of the NASA Langley Research Center and William S. Saric of Arizona State University, due to the untimely death of J. Ray Dagenhart. Ray will be missed by his many friends and colleagues. This work took place during 1988 and 1989. It was, in fact, the foundation experiment that spawned 5 doctor's and 1 master's degrees in the subsequent 7 years. We now know a great deal more about crossflow instabilities because of the vision and hard work of the late Ray Dagenhart.

---

### Available from:

NASA Center for Aerospace Information (CASI)  
7121 Standard Drive  
Hanover, MD 21076-1320  
(301) 621-0390

National Technical Information Service (NTIS)  
5285 Port Royal Road  
Springfield, VA 22161-2171  
(703) 605-6000

## Contents

List of Tables .....	v
List of Figures.....	vii
Symbols .....	xv
1. Summary.....	1
2. Introduction .....	1
2.1. Background .....	1
2.2. Instability Modes .....	3
2.3. Transition Experiments .....	4
2.4. Detailed Theory and Simulation .....	5
2.5. Stability Experiments.....	5
2.6. State of Present Knowledge .....	7
2.7. Present Experiment .....	7
2.8. Organization of Publication .....	8
3. Experimental Facility .....	8
3.1. Arizona State University Unsteady Wind Tunnel .....	8
3.2. New Test Section .....	9
4. Model and Liner Design.....	10
4.1. Airfoil Selection .....	10
4.1.1. Pressure Gradient Effects.....	10
4.1.2. Wind Tunnel Wall Interference Effects.....	11
4.2. Stability Calculations .....	11
4.2.1. Stationary Crossflow Vortices.....	12
4.2.2. Tollmien-Schlichting Waves .....	13
4.2.3. Travelling Crossflow Vortices.....	14
4.2.4. Crossflow-Tollmien-Schlichting Interaction.....	14
4.3. Selection of Experimental Test Condition .....	15
4.4. Reynolds Number Variation.....	15
4.5. Test Section Liner Shape .....	15
5. Experimental Results and Discussion .....	17
5.1. Free-Stream Flow Quality .....	17
5.2. Pressure Distributions .....	17
5.3. Flow Visualizations .....	18
5.4. Transition Locations.....	18
5.5. Boundary-Layer Spectra .....	19
5.6. Boundary-Layer Hot-Wire Surveys.....	19
5.6.1. Streamwise Velocity Measurements .....	19
5.6.2. Spanwise Variation of Streamwise Velocity .....	20
5.6.3. Disturbance Profiles.....	21
5.6.4. Streamwise Velocity Contour Plots.....	23

5.7. Experimental and Theoretical Comparisons .....	25
5.7.1. Theoretical Disturbance Profiles .....	25
5.7.2. Disturbance Profile Comparisons .....	26
5.7.3. Velocity Contour Plots and Vector Plots .....	27
5.7.4. Wavelength Comparison .....	28
5.7.5. Growth-Rate Comparison .....	28
6. Conclusions .....	29
Appendix A—Relationships Between Coordinate Systems. ....	32
Appendix B—Hot-Wire Signal Interpretation Procedure .....	34
Appendix C—Error Analysis .....	36
References .....	39
Tables .....	45
Figures .....	47

## List of Tables

Table 1. Crossflow Stability Analysis With SALLY Code for $\alpha = -4^\circ$ and $R_c = 3.81 \times 10^6$ . . . . .	45
Table 2. Transition Locations and Wavelengths From Naphthalene Flow Visualization . . . . .	45
Table 3. $N$ -Factors at Transition Computed With SALLY Code for $\alpha = -4^\circ$ , $R_c = 2.37 \times 10^6$ , and $(x/c)_{tr} = 0.58$ . . . . .	45
Table 4. $N$ -Factors at Transition Computed With SALLY Code for $\alpha = -4^\circ$ , $R_c = 2.37 \times 10^6$ , and $(x/c)_{tr} = 0.45$ . . . . .	46
Table 5. $N$ -Factors at Transition Computed With SALLY Code for $\alpha = -4^\circ$ , $R_c = 3.73 \times 10^6$ , and $(x/c)_{tr} = 0.30$ . . . . .	46



## List of Figures

Figure 1. Curved streamlines over swept wing .....	47
Figure 2. Boundary-layer velocity profiles on swept wing .....	47
Figure 3. Plan view of Arizona State University Unsteady Wind Tunnel .....	48
Figure 4. New UWT test section with liner under construction .....	48
Figure 5. NASA NLF(2)-0415 airfoil .....	49
Figure 6. NASA NLF(2)-0415 design point pressure distribution at $\alpha = 0^\circ$ and $\delta_f = 0^\circ$ in free air .....	49
Figure 7. NASA NLF(2)-0415 pressure distribution for $\alpha = -4^\circ$ and $\delta_f = 0^\circ$ in free air .....	50
Figure 8. NASA NLF(2)-0415 pressure distribution for $\alpha = -2^\circ$ and $\delta_f = 0^\circ$ in free air .....	50
Figure 9. NASA NLF(2)-0415 pressure distribution for $\alpha = 2^\circ$ and $\delta_f = 0^\circ$ in free air .....	51
Figure 10. NASA NLF(2)-0415 pressure distribution for $\alpha = 4^\circ$ and $\delta_f = 0^\circ$ in free air .....	51
Figure 11. NASA NLF(2)-0415 pressure distribution for $\alpha = 0^\circ$ and $\delta_f = -20^\circ$ in free air .....	52
Figure 12. NASA NLF(2)-0415 pressure distribution for $\alpha = 0^\circ$ and $\delta_f = -10^\circ$ in free air .....	52
Figure 13. NASA NLF(2)-0415 pressure distribution for $\alpha = 0^\circ$ and $\delta_f = 10^\circ$ in free air .....	53
Figure 14. NASA NLF(2)-0415 pressure distribution for $\alpha = 0^\circ$ and $\delta_f = 20^\circ$ in free air .....	53
Figure 15. NASA NLF(2)-0415 pressure distribution for $\alpha = -4^\circ$ and $\delta_f = 0^\circ$ in UWT .....	54
Figure 16. NASA NLF(2)-0415 pressure distribution for $\alpha = -2^\circ$ and $\delta_f = 0^\circ$ in UWT .....	54
Figure 17. NASA NLF(2)-0415 pressure distribution for $\alpha = 0^\circ$ and $\delta_f = 0^\circ$ in UWT .....	55
Figure 18. NASA NLF(2)-0415 pressure distribution for $\alpha = 2^\circ$ and $\delta_f = 0^\circ$ in UWT .....	55
Figure 19. NASA NLF(2)-0415 pressure distribution for $\alpha = 4^\circ$ and $\delta_f = 0^\circ$ in UWT .....	56
Figure 20. Local spatial growth rates for stationary crossflow vortices at $\alpha = -4^\circ$ and $\delta_f = 0^\circ$ in UWT at $R_c = 3.81 \times 10^6$ .....	56
Figure 21. Local spatial growth rates for stationary crossflow vortices at $\alpha = -2^\circ$ and $\delta_f = 0^\circ$ in UWT at $R_c = 3.81 \times 10^6$ .....	57
Figure 22. Local spatial growth rates for stationary crossflow vortices at $\alpha = 0^\circ$ and $\delta_f = 0^\circ$ in UWT at $R_c = 3.81 \times 10^6$ .....	57
Figure 23. Local spatial growth rates for stationary crossflow vortices at $\alpha = 2^\circ$ and $\delta_f = 0^\circ$ in UWT at $R_c = 3.81 \times 10^6$ .....	58
Figure 24. Local spatial growth rates for stationary crossflow vortices at $\alpha = 4^\circ$ and $\delta_f = 0^\circ$ in UWT at $R_c = 3.81 \times 10^6$ .....	58
Figure 25. $N$ -factors for stationary crossflow vortices at $\alpha = -4^\circ$ and $\delta_f = 0^\circ$ in UWT at $R_c = 3.81 \times 10^6$ .....	59
Figure 26. $N$ -factors for stationary crossflow vortices at $\alpha = -2^\circ$ and $\delta_f = 0^\circ$ in UWT at $R_c = 3.81 \times 10^6$ .....	59
Figure 27. $N$ -factors for stationary crossflow vortices at $\alpha = 0^\circ$ and $\delta_f = 0^\circ$ in UWT at $R_c = 3.81 \times 10^6$ .....	60

Figure 28. $N$ -factors for stationary crossflow vortices at $\alpha = 2^\circ$ and $\delta_f = 0^\circ$ in UWT at $R_c = 3.81 \times 10^6$ .....	60
Figure 29. $N$ -factors for stationary crossflow vortices at $\alpha = 4^\circ$ and $\delta_f = 0^\circ$ in UWT at $R_c = 3.81 \times 10^6$ .....	61
Figure 30. Maximum $N$ -factors for stationary crossflow vortices at $\alpha = -4^\circ$ and $\delta_f = 0^\circ$ in UWT at $R_c = 3.81 \times 10^6$ .....	61
Figure 31. Maximum $N$ -factors for stationary crossflow vortices at $\alpha = -2^\circ$ and $\delta_f = 0^\circ$ in UWT at $R_c = 3.81 \times 10^6$ .....	62
Figure 32. Maximum $N$ -factors for stationary crossflow vortices at $\alpha = 0^\circ$ and $\delta_f = 0^\circ$ in UWT at $R_c = 3.81 \times 10^6$ .....	62
Figure 33. Maximum $N$ -factors for stationary crossflow vortices at $\alpha = 2^\circ$ and $\delta_f = 0^\circ$ in UWT at $R_c = 3.81 \times 10^6$ .....	63
Figure 34. Maximum $N$ -factors for stationary crossflow vortices at $\alpha = 4^\circ$ and $\delta_f = 0^\circ$ in UWT at $R_c = 3.81 \times 10^6$ .....	63
Figure 35. Maximum $N$ -factors for Tollmien-Schlichting waves for $\alpha = 0^\circ, 2^\circ$ , and $4^\circ$ and $\delta_f = 0^\circ$ in UWT at $R_c = 3.81 \times 10^6$ .....	64
Figure 36. Maximum $N$ -factors for stationary crossflow vortices at $\alpha = -4^\circ$ and $\delta_f = 0^\circ$ in UWT for a range of Reynolds number .....	64
Figure 37. Streamline traces of wind tunnel end liner on $X_L$ - $Z_L$ plane for $\alpha = -4^\circ$ .....	65
Figure 38. Lateral deflections of end-liner surface at various distances from wing chord plane for $\alpha = -4^\circ$ .....	65
Figure 39. End-liner contours in $Y_L$ - $Z_L$ plane at various longitudinal positions for $\alpha = -4^\circ$ .....	66
Figure 40. Wind tunnel test section with swept-wing model and end liners installed .....	67
Figure 41. Free-stream velocity spectrum for $R_c = 3.27 \times 10^6$ .....	68
Figure 42. Measured and predicted model pressure coefficients at upper end of model for $\alpha = -4^\circ$ .....	68
Figure 43. Measured and predicted model pressure coefficients at lower end of model for $\alpha = -4^\circ$ .....	69
Figure 44. Naphthalene flow visualization at $\alpha = -4^\circ$ and $R_c = 1.93 \times 10^6$ .....	70
Figure 45. Naphthalene flow visualization at $\alpha = -4^\circ$ and $R_c = 2.19 \times 10^6$ .....	71
Figure 46. Naphthalene flow visualization at $\alpha = -4^\circ$ and $R_c = 2.40 \times 10^6$ .....	72
Figure 47. Naphthalene flow visualization at $\alpha = -4^\circ$ and $R_c = 2.73 \times 10^6$ .....	73
Figure 48. Naphthalene flow visualization at $\alpha = -4^\circ$ and $R_c = 3.27 \times 10^6$ .....	74
Figure 49. Naphthalene flow visualization with vortex tracks in turbulent regions shown .....	75
Figure 50. Liquid-crystal flow visualization .....	76
Figure 51. Transition location versus Reynolds number at $\alpha = -4^\circ$ .....	76
Figure 52. Boundary-layer velocity spectrum at $\alpha = -4^\circ$ and $R_c = 2.62 \times 10^6$ at $x/c = 0.40$ .....	77
Figure 53. Boundary-layer velocity spectrum at $\alpha = -4^\circ$ and $R_c = 2.82 \times 10^6$ at $x/c = 0.40$ .....	77



Figure 54. Boundary-layer velocity spectrum at $\alpha = -4^\circ$ and $R_c = 2.92 \times 10^6$ at $x/c = 0.40$ . . . . .	78
Figure 55. Boundary-layer velocity spectrum at $\alpha = -4^\circ$ and $R_c = 3.28 \times 10^6$ at $x/c = 0.40$ . . . . .	78
Figure 56. Measured and predicted boundary-layer velocity spectra at $\alpha = -4^\circ$ and $R_c = 2.92 \times 10^6$ . . . . .	79
Figure 57. Streamwise velocity profiles at $x/c = 0.20$ , $\alpha = -4^\circ$ , and $R_c = 2.62 \times 10^6$ . . . . .	79
Figure 58. Streamwise velocity profiles at $x/c = 0.25$ , $\alpha = -4^\circ$ , and $R_c = 2.37 \times 10^6$ . . . . .	80
Figure 59. Streamwise velocity profiles at $x/c = 0.30$ , $\alpha = -4^\circ$ , and $R_c = 2.37 \times 10^6$ . . . . .	80
Figure 60. Streamwise velocity profiles at $x/c = 0.35$ , $\alpha = -4^\circ$ , and $R_c = 2.37 \times 10^6$ . . . . .	81
Figure 61. Streamwise velocity profiles at $x/c = 0.40$ , $\alpha = -4^\circ$ , and $R_c = 2.37 \times 10^6$ . . . . .	81
Figure 62. Streamwise velocity profiles at $x/c = 0.45$ , $\alpha = -4^\circ$ , and $R_c = 2.37 \times 10^6$ . . . . .	82
Figure 63. Streamwise velocity profiles at $x/c = 0.50$ , $\alpha = -4^\circ$ , and $R_c = 2.37 \times 10^6$ . . . . .	82
Figure 64. Streamwise velocity profiles at $x/c = 0.55$ , $\alpha = -4^\circ$ , and $R_c = 2.37 \times 10^6$ . . . . .	83
Figure 65. Stationary crossflow disturbance velocity profiles for $f = 0$ Hz at $x/c = 0.20$ , $\alpha = -4^\circ$ , and $R_c = 2.37 \times 10^6$ obtained from $\bar{u}_s - \bar{u}_{s,avg}$ . . . . .	83
Figure 66. Stationary crossflow disturbance velocity profiles for $f = 0$ Hz at $x/c = 0.25$ , $\alpha = -4^\circ$ , and $R_c = 2.37 \times 10^6$ obtained from $\bar{u}_s - \bar{u}_{s,avg}$ . . . . .	84
Figure 67. Stationary crossflow disturbance velocity profiles for $f = 0$ Hz at $x/c = 0.30$ , $\alpha = -4^\circ$ , and $R_c = 2.37 \times 10^6$ obtained from $\bar{u}_s - \bar{u}_{s,avg}$ . . . . .	84
Figure 68. Stationary crossflow disturbance velocity profiles for $f = 0$ Hz at $x/c = 0.35$ , $\alpha = -4^\circ$ , and $R_c = 2.37 \times 10^6$ obtained from $\bar{u}_s - \bar{u}_{s,avg}$ . . . . .	85
Figure 69. Stationary crossflow disturbance velocity profiles for $f = 0$ Hz at $x/c = 0.40$ , $\alpha = -4^\circ$ , and $R_c = 2.37 \times 10^6$ obtained from $\bar{u}_s - \bar{u}_{s,avg}$ . . . . .	85
Figure 70. Stationary crossflow disturbance velocity profiles for $f = 0$ Hz at $x/c = 0.45$ , $\alpha = -4^\circ$ , and $R_c = 2.37 \times 10^6$ obtained from $\bar{u}_s - \bar{u}_{s,avg}$ . . . . .	86
Figure 71. Stationary crossflow disturbance velocity profiles for $f = 0$ Hz at $x/c = 0.50$ , $\alpha = -4^\circ$ , and $R_c = 2.37 \times 10^6$ obtained from $\bar{u}_s - \bar{u}_{s,avg}$ . . . . .	86
Figure 72. Stationary crossflow disturbance velocity profiles for $f = 0$ Hz at $x/c = 0.55$ , $\alpha = -4^\circ$ , and $R_c = 2.37 \times 10^6$ obtained from $\bar{u}_s - \bar{u}_{s,avg}$ . . . . .	87
Figure 73. Stationary crossflow disturbance velocity profiles for $f = 0$ Hz at $x/c = 0.20$ , $\alpha = -4^\circ$ , and $R_c = 2.37 \times 10^6$ obtained from $\bar{u}_s - \bar{u}_{s,ref}$ . . . . .	87
Figure 74. Stationary crossflow disturbance velocity profiles for $f = 0$ Hz at $x/c = 0.25$ , $\alpha = -4^\circ$ , and $R_c = 2.37 \times 10^6$ obtained from $\bar{u}_s - \bar{u}_{s,ref}$ . . . . .	88
Figure 75. Stationary crossflow disturbance velocity profiles for $f = 0$ Hz at $x/c = 0.30$ , $\alpha = -4^\circ$ , and $R_c = 2.37 \times 10^6$ obtained from $\bar{u}_s - \bar{u}_{s,ref}$ . . . . .	88
Figure 76. Stationary crossflow disturbance velocity profiles for $f = 0$ Hz at $x/c = 0.35$ , $\alpha = -4^\circ$ , and $R_c = 2.37 \times 10^6$ obtained from $\bar{u}_s - \bar{u}_{s,ref}$ . . . . .	89
Figure 77. Stationary crossflow disturbance velocity profiles for $f = 0$ Hz at $x/c = 0.40$ , $\alpha = -4^\circ$ , and $R_c = 2.37 \times 10^6$ obtained from $\bar{u}_s - \bar{u}_{s,ref}$ . . . . .	89

Figure 78. Stationary crossflow disturbance velocity profiles for $f = 0$ Hz at $x/c = 0.45$ , $\alpha = -4^\circ$ , and $R_c = 2.37 \times 10^6$ obtained from $\bar{u}_s - \bar{u}_{s,\text{ref}}$ .....	90
Figure 79. Stationary crossflow disturbance velocity profiles for $f = 0$ Hz at $x/c = 0.50$ , $\alpha = -4^\circ$ , and $R_c = 2.37 \times 10^6$ obtained from $\bar{u}_s - \bar{u}_{s,\text{ref}}$ .....	90
Figure 80. Stationary crossflow disturbance velocity profiles for $f = 0$ Hz at $x/c = 0.55$ , $\alpha = -4^\circ$ , and $R_c = 2.37 \times 10^6$ obtained from $\bar{u}_s - \bar{u}_{s,\text{ref}}$ .....	91
Figure 81. Travelling wave disturbance velocity profiles for $f = 100$ Hz at $x/c = 0.20$ , $\alpha = -4^\circ$ , and $R_c = 2.37 \times 10^6$ .....	91
Figure 82. Travelling wave disturbance velocity profiles for $f = 100$ Hz at $x/c = 0.25$ , $\alpha = -4^\circ$ , and $R_c = 2.37 \times 10^6$ .....	92
Figure 83. Travelling wave disturbance velocity profiles for $f = 100$ Hz at $x/c = 0.30$ , $\alpha = -4^\circ$ , and $R_c = 2.37 \times 10^6$ .....	92u
Figure 84. Travelling wave disturbance velocity profiles for $f = 100$ Hz at $x/c = 0.35$ , $\alpha = -4^\circ$ , and $R_c = 2.37 \times 10^6$ .....	93
Figure 85. Travelling wave disturbance velocity profiles for $f = 100$ Hz at $x/c = 0.40$ , $\alpha = -4^\circ$ , and $R_c = 2.37 \times 10^6$ .....	93
Figure 86. Travelling wave disturbance velocity profiles for $f = 100$ Hz at $x/c = 0.45$ , $\alpha = -4^\circ$ , and $R_c = 2.37 \times 10^6$ .....	94
Figure 87. Travelling wave disturbance velocity profiles for $f = 100$ Hz at $x/c = 0.50$ , $\alpha = -4^\circ$ , and $R_c = 2.37 \times 10^6$ .....	94
Figure 88. Travelling wave disturbance velocity profiles for $f = 100$ Hz at $x/c = 0.55$ , $\alpha = -4^\circ$ , and $R_c = 2.37 \times 10^6$ .....	95
Figure 89. Mean streamwise velocity contours at $x/c = 0.20$ , $\alpha = -4^\circ$ , and $R_c = 2.37 \times 10^6$ .....	95
Figure 90. Mean streamwise velocity contours at $x/c = 0.25$ , $\alpha = -4^\circ$ , and $R_c = 2.37 \times 10^6$ .....	96
Figure 91. Mean streamwise velocity contours at $x/c = 0.30$ , $\alpha = -4^\circ$ , and $R_c = 2.37 \times 10^6$ .....	96
Figure 92. Mean streamwise velocity contours at $x/c = 0.35$ , $\alpha = -4^\circ$ , and $R_c = 2.37 \times 10^6$ .....	97
Figure 93. Mean streamwise velocity contours at $x/c = 0.40$ , $\alpha = -4^\circ$ , and $R_c = 2.37 \times 10^6$ .....	97
Figure 94. Mean streamwise velocity contours at $x/c = 0.45$ , $\alpha = -4^\circ$ , and $R_c = 2.37 \times 10^6$ .....	98
Figure 95. Mean streamwise velocity contours at $x/c = 0.50$ , $\alpha = -4^\circ$ , and $R_c = 2.37 \times 10^6$ .....	98
Figure 96. Mean streamwise velocity contours at $x/c = 0.55$ , $\alpha = -4^\circ$ , and $R_c = 2.37 \times 10^6$ .....	99
Figure 97. Stationary crossflow vortex velocity contours obtained from $\bar{u}_s - \bar{u}_{s,\text{avg}}$ at $x/c = 0.20$ , $\alpha = -4^\circ$ , and $R_c = 2.37 \times 10^6$ .....	99
Figure 98. Stationary crossflow vortex velocity contours obtained from $\bar{u}_s - \bar{u}_{s,\text{avg}}$ at $x/c = 0.25$ , $\alpha = -4^\circ$ , and $R_c = 2.37 \times 10^6$ .....	100
Figure 99. Stationary crossflow vortex velocity contours obtained from $\bar{u}_s - \bar{u}_{s,\text{avg}}$ at $x/c = 0.30$ , $\alpha = -4^\circ$ , and $R_c = 2.37 \times 10^6$ .....	100
Figure 100. Stationary crossflow vortex velocity contours obtained from $\bar{u}_s - \bar{u}_{s,\text{avg}}$ at $x/c = 0.35$ , $\alpha = -4^\circ$ , and $R_c = 2.37 \times 10^6$ .....	101
Figure 101. Stationary crossflow vortex velocity contours obtained from $\bar{u}_s - \bar{u}_{s,\text{avg}}$ at $x/c = 0.40$ , $\alpha = -4^\circ$ , and $R_c = 2.37 \times 10^6$ .....	101

Figure 102. Stationary crossflow vortex velocity contours obtained from $\bar{u}_s - \bar{u}_{s,avg}$ at $x/c = 0.45$ , $\alpha = -4^\circ$ , and $R_c = 2.37 \times 10^6$ .....	102
Figure 103. Stationary crossflow vortex velocity contours obtained from $\bar{u}_s - \bar{u}_{s,avg}$ at $x/c = 0.50$ , $\alpha = -4^\circ$ , and $R_c = 2.37 \times 10^6$ .....	102
Figure 104. Stationary crossflow vortex velocity contours obtained from $\bar{u}_s - \bar{u}_{s,avg}$ at $x/c = 0.55$ , $\alpha = -4^\circ$ , and $R_c = 2.37 \times 10^6$ .....	103
Figure 105. Stationary crossflow vortex velocity contours obtained from $\bar{u}_s - \bar{u}_{s,ref}$ at $x/c = 0.20$ , $\alpha = -4^\circ$ , and $R_c = 2.37 \times 10^6$ .....	103
Figure 106. Stationary crossflow vortex velocity contours obtained from $\bar{u}_s - \bar{u}_{s,ref}$ at $x/c = 0.25$ , $\alpha = -4^\circ$ , and $R_c = 2.37 \times 10^6$ .....	104
Figure 107. Stationary crossflow vortex velocity contours obtained from $\bar{u}_s - \bar{u}_{s,ref}$ at $x/c = 0.30$ , $\alpha = -4^\circ$ , and $R_c = 2.37 \times 10^6$ .....	104
Figure 108. Stationary crossflow vortex velocity contours obtained from $\bar{u}_s - \bar{u}_{s,ref}$ at $x/c = 0.35$ , $\alpha = -4^\circ$ , and $R_c = 2.37 \times 10^6$ .....	105
Figure 109. Stationary crossflow vortex velocity contours obtained from $\bar{u}_s - \bar{u}_{s,ref}$ at $x/c = 0.40$ , $\alpha = -4^\circ$ , and $R_c = 2.37 \times 10^6$ .....	105
Figure 110. Stationary crossflow vortex velocity contours obtained from $\bar{u}_s - \bar{u}_{s,ref}$ at $x/c = 0.45$ , $\alpha = -4^\circ$ , and $R_c = 2.37 \times 10^6$ .....	106
Figure 111. Stationary crossflow vortex velocity contours obtained from $\bar{u}_s - \bar{u}_{s,ref}$ at $x/c = 0.50$ , $\alpha = -4^\circ$ , and $R_c = 2.37 \times 10^6$ .....	106
Figure 112. Stationary crossflow vortex velocity contours obtained from $\bar{u}_s - \bar{u}_{s,ref}$ at $x/c = 0.55$ , $\alpha = -4^\circ$ , and $R_c = 2.37 \times 10^6$ .....	107
Figure 113. Travelling wave rms velocity contours for $f = 100$ Hz at $x/c = 0.20$ , $\alpha = -4^\circ$ , and $R_c = 2.37 \times 10^6$ .....	107
Figure 114. Travelling wave rms velocity contours for $f = 100$ Hz at $x/c = 0.25$ , $\alpha = -4^\circ$ , and $R_c = 2.37 \times 10^6$ .....	108
Figure 115. Travelling wave rms velocity contours for $f = 100$ Hz at $x/c = 0.30$ , $\alpha = -4^\circ$ , and $R_c = 2.37 \times 10^6$ .....	108
Figure 116. Travelling wave rms velocity contours for $f = 100$ Hz at $x/c = 0.35$ , $\alpha = -4^\circ$ , and $R_c = 2.37 \times 10^6$ .....	109
Figure 117. Travelling wave rms velocity contours for $f = 100$ Hz at $x/c = 0.40$ , $\alpha = -4^\circ$ , and $R_c = 2.37 \times 10^6$ .....	109
Figure 118. Travelling wave rms velocity contours for $f = 100$ Hz at $x/c = 0.45$ , $\alpha = -4^\circ$ , and $R_c = 2.37 \times 10^6$ .....	110
Figure 119. Travelling wave rms velocity contours for $f = 100$ Hz at $x/c = 0.50$ , $\alpha = -4^\circ$ , and $R_c = 2.37 \times 10^6$ .....	110
Figure 120. Travelling wave rms velocity contours for $f = 100$ Hz at $x/c = 0.55$ , $\alpha = -4^\circ$ , and $R_c = 2.37 \times 10^6$ .....	111
Figure 121. Theoretical mean chordwise velocity profiles for $\alpha_{ref} = -5^\circ$ and $R_c = 2.37 \times 10^6$ .....	111

Figure 122. Theoretical mean spanwise velocity profiles for $\alpha_{\text{ref}} = -5^\circ$ and $R_c = 2.37 \times 10^6$ .....	112
Figure 123. Theoretical stationary crossflow disturbance velocity profiles (chordwise component) for $\alpha_{\text{ref}} = -5^\circ$ and $R_c = 2.37 \times 10^6$ .....	112
Figure 124. Theoretical stationary crossflow disturbance velocity profiles (surface normal component) for $\alpha_{\text{ref}} = -5^\circ$ and $R_c = 2.37 \times 10^6$ .....	113
Figure 125. Theoretical stationary crossflow disturbance velocity profiles (spanwise component) for $\alpha_{\text{ref}} = -5^\circ$ and $R_c = 2.37 \times 10^6$ .....	114
Figure 126. Theoretical mean streamwise velocity profiles for $\alpha_{\text{ref}} = -5^\circ$ and $R_c = 2.37 \times 10^6$ .....	114
Figure 127. Theoretical mean cross-stream velocity profiles for $\alpha_{\text{ref}} = -5^\circ$ and $R_c = 2.37 \times 10^6$ .....	115
Figure 128. Theoretical stationary crossflow disturbance velocity profiles (streamwise component) for $\alpha_{\text{ref}} = -5^\circ$ and $R_c = 2.37 \times 10^6$ .....	115
Figure 129. Theoretical stationary crossflow disturbance velocity profiles (cross-stream component) for $\alpha_{\text{ref}} = -5^\circ$ and $R_c = 2.37 \times 10^6$ .....	116
Figure 130. Theoretical mean velocity profiles along vortex axis for $\alpha_{\text{ref}} = -5^\circ$ and $R_c = 2.37 \times 10^6$ .....	116
Figure 131. Theoretical mean velocity profiles perpendicular to vortex axis for $\alpha_{\text{ref}} = -5^\circ$ and $R_c = 2.37 \times 10^6$ .....	117
Figure 132. Theoretical stationary crossflow disturbance velocity profiles along vortex axis for $\alpha_{\text{ref}} = -5^\circ$ and $R_c = 2.37 \times 10^6$ .....	117
Figure 133. Theoretical stationary crossflow disturbance velocity profiles perpendicular to vortex axis for $\alpha_{\text{ref}} = -5^\circ$ and $R_c = 2.37 \times 10^6$ .....	118
Figure 134. Theoretical stationary crossflow disturbance velocity vectors across single vortex wavelength for $\alpha_{\text{ref}} = -5^\circ$ and $R_c = 2.37 \times 10^6$ .....	118
Figure 135. Theoretical total velocity vectors (disturbance plus mean flow) across single vortex wavelength for $\alpha_{\text{ref}} = -5^\circ$ and $R_c = 2.37 \times 10^6$ .....	119
Figure 136. Theoretical total velocity vectors (disturbance plus mean flow) across single vortex wavelength with normal velocity components scaled 100 for $\alpha_{\text{ref}} = -5^\circ$ and $R_c = 2.37 \times 10^6$ .....	119
Figure 137. Experimental streamwise disturbance velocity profile determined from $\bar{u}_s - \bar{u}_{s,\text{avg}}$ and theoretical eigenfunction for $x/c = 0.20$ , $\alpha = -4^\circ$ , and $R_c = 2.37 \times 10^6$ .....	120
Figure 138. Experimental streamwise disturbance velocity profile determined from $\bar{u}_s - \bar{u}_{s,\text{avg}}$ and theoretical eigenfunction for $x/c = 0.25$ , $\alpha = -4^\circ$ , and $R_c = 2.37 \times 10^6$ .....	120
Figure 139. Experimental streamwise disturbance velocity profile determined from $\bar{u}_s - \bar{u}_{s,\text{avg}}$ and theoretical eigenfunction for $x/c = 0.30$ , $\alpha = -4^\circ$ , and $R_c = 2.37 \times 10^6$ .....	121
Figure 140. Experimental streamwise disturbance velocity profile determined from $\bar{u}_s - \bar{u}_{s,\text{avg}}$ and theoretical eigenfunction for $x/c = 0.30$ , $\alpha = -4^\circ$ , and $R_c = 2.37 \times 10^6$ .....	121
Figure 141. Experimental streamwise disturbance velocity profile determined from $\bar{u}_s - \bar{u}_{s,\text{avg}}$ and theoretical eigenfunction for $x/c = 0.40$ , $\alpha = -4^\circ$ , and $R_c = 2.37 \times 10^6$ .....	122

Figure 142. Experimental streamwise disturbance velocity profile determined from $\bar{u}_s - \bar{u}_{s,avg}$ and theoretical eigenfunction for $x/c = 0.45$ , $\alpha = -4^\circ$ , and $R_c = 2.37 \times 10^6$ . . . . .	122
Figure 143. Experimental streamwise disturbance velocity profile determined from $\bar{u}_s - \bar{u}_{s,avg}$ and theoretical eigenfunction for $x/c = 0.50$ , $\alpha = -4^\circ$ , and $R_c = 2.37 \times 10^6$ . . . . .	123
Figure 144. Experimental streamwise disturbance velocity profile determined from $\bar{u}_s - \bar{u}_{s,avg}$ and theoretical eigenfunction for $x/c = 0.55$ , $\alpha = -4^\circ$ , and $R_c = 2.37 \times 10^6$ . . . . .	123
Figure 145. Experimental mean streamwise velocity contours and theoretical vortex velocity vector field for $x/c = 0.20$ , $\alpha = -4^\circ$ , and $R_c = 2.37 \times 10^6$ . . . . .	124
Figure 146. Experimental mean streamwise velocity contours and theoretical vortex velocity vector field for $x/c = 0.25$ , $\alpha = -4^\circ$ , and $R_c = 2.37 \times 10^6$ . . . . .	124
Figure 147. Experimental mean streamwise velocity contours and theoretical vortex velocity vector field for $x/c = 0.30$ , $\alpha = -4^\circ$ , and $R_c = 2.37 \times 10^6$ . . . . .	125
Figure 148. Experimental mean streamwise velocity contours and theoretical vortex velocity vector field for $x/c = 0.35$ , $\alpha = -4^\circ$ , and $R_c = 2.37 \times 10^6$ . . . . .	125
Figure 149. Experimental mean streamwise velocity contours and theoretical vortex velocity vector field for $x/c = 0.40$ , $\alpha = -4^\circ$ , and $R_c = 2.37 \times 10^6$ . . . . .	126
Figure 150. Experimental mean streamwise velocity contours and theoretical vortex velocity vector field for $x/c = 0.45$ , $\alpha = -4^\circ$ , and $R_c = 2.37 \times 10^6$ . . . . .	126
Figure 151. Experimental mean streamwise velocity contours and theoretical vortex velocity vector field for $x/c = 0.50$ , $\alpha = -4^\circ$ , and $R_c = 2.37 \times 10^6$ . . . . .	127
Figure 152. Experimental mean streamwise velocity contours and theoretical vortex velocity vector field for $x/c = 0.55$ , $\alpha = -4^\circ$ , and $R_c = 2.37 \times 10^6$ . . . . .	127
Figure 153. Experimental stationary crossflow disturbance velocity contours and theoretical vortex velocity vector field for $x/c = 0.20$ , $\alpha = -4^\circ$ , and $R_c = 2.37 \times 10^6$ . . . . .	128
Figure 154. Experimental stationary crossflow disturbance velocity contours and theoretical vortex velocity vector field for $x/c = 0.25$ , $\alpha = -4^\circ$ , and $R_c = 2.37 \times 10^6$ . . . . .	128
Figure 155. Experimental stationary crossflow disturbance velocity contours and theoretical vortex velocity vector field for $x/c = 0.30$ , $\alpha = -4^\circ$ , and $R_c = 2.37 \times 10^6$ . . . . .	129
Figure 156. Experimental stationary crossflow disturbance velocity contours and theoretical vortex velocity vector field for $x/c = 0.35$ , $\alpha = -4^\circ$ , and $R_c = 2.37 \times 10^6$ . . . . .	129
Figure 157. Experimental stationary crossflow disturbance velocity contours and theoretical vortex velocity vector field for $x/c = 0.40$ , $\alpha = -4^\circ$ , and $R_c = 2.37 \times 10^6$ . . . . .	130
Figure 158. Experimental stationary crossflow disturbance velocity contours and theoretical vortex velocity vector field for $x/c = 0.45$ , $\alpha = -4^\circ$ , and $R_c = 2.37 \times 10^6$ . . . . .	130
Figure 159. Experimental stationary crossflow disturbance velocity contours and theoretical vortex velocity vector field for $x/c = 0.50$ , $\alpha = -4^\circ$ , and $R_c = 2.37 \times 10^6$ . . . . .	131
Figure 160. Experimental stationary crossflow disturbance velocity contours and theoretical vortex velocity vector field for $x/c = 0.55$ , $\alpha = -4^\circ$ , and $R_c = 2.37 \times 10^6$ . . . . .	131
Figure 161. Theoretical and experimental stationary crossflow vortex wavelengths for $\alpha = -4^\circ$ and $R_c = 2.37 \times 10^6$ . . . . .	132
Figure 162. Theoretical and experimental stationary crossflow vortex growth rates for $\alpha = -4^\circ$ and $R_c = 2.37 \times 10^6$ . . . . .	132



## Symbols

$A$	amplitude
$A, B$	coefficients in King's law for hot-wire anemometer (see appendix C)
$A_0$	amplitude at initial station
$A_1, A_2, A_3$	experimental disturbance amplitude functions (see eqs. (7), (8), and (9), respectively)
$C_p$	pressure coefficient
$C_{p,3}$	swept-wing pressure coefficient (see eq. (6))
$c$	chord, m
$E$	hot-wire steady state voltage (see appendix B), V
$e$	hot-wire voltage (see appendix B), V
$F, g$	hot-wire voltage functions (see appendix B)
$f$	frequency, 1/sec
$L/D$	ratio of length to diameter of wind tunnel contraction
$l$	length, m
$N$	$N$ -factor, $\ln (A/A_0)$
$p$	static pressure, mm Hg
$q$	dynamic pressure, $\frac{\rho U^2}{2}$
$R$	Reynolds number, $\frac{\rho U l}{\mu}$
$R$	gas constant
$U$	velocity
$u, v, w$	disturbance velocity component in $x$ , $y$ , and $z$ direction, respectively
$\bar{u}, \bar{v}, \bar{w}$	mean velocity component in $x$ , $y$ , and $z$ direction, respectively
$X, Y, Z$	axes
$x, y, z$	Cartesian coordinates
$\alpha$	angle of attack, deg
$\Delta$	measurement uncertainty (see appendix C)
$\delta$	boundary-layer thickness

$\delta_f$	flap deflection angle, deg
$\epsilon$	local boundary-layer edge flow angle measured with respect to $Z_m$ -axis (see appendix A), deg
$\theta$	disturbance wave orientation angle measured with respect to $Z_m$ -axis (see appendix A), deg
$\Lambda$	wing sweep angle, deg
$\lambda$	disturbance function wavelength, mm
$\mu$	dynamic viscosity, kg-sec/m <sup>2</sup>
$\rho$	mass density, kg/m <sup>3</sup>
$\sigma$	disturbance growth rate measured with respect to local boundary-layer edge velocity vector
$\psi$	wave orientation angle

Subscripts:

avg	average
bp	blade passing
bps	blade passing plus stators
$c$	chord
cf	crossflow
cf,max	maximum crossflow amplitude
crit	critical
$e$	edge
$L$	liner
$L0$	liner origin
$M$	measured
$m$	model
$m_0$	model reference point
max	maximum
$r$	real
ref	reference



$s$	streamwise (i.e., parallel to free-stream velocity vector)
$s, e$	streamwise at boundary-layer edge
$T$	total or stagnation condition
$t$	tangential (i.e., parallel to local boundary-layer edge velocity vector)
$t, e$	tangential at boundary-layer edge
tr	transition
$v$	vortex track
$w$	wave
$\lambda$	disturbance wavelength
0	origin or beginning value
45	at 45° angle
$\infty$	free stream

Superscripts:

'	fluctuating quantity
---	----------------------

Abbreviations:

AC	alternating current
A/D	analog to digital
D/A	digital to analog
DC	direct current
DLR	nationale Forschungszentrum für Luft- und Raumfahrt und zugleich die nationale Raumfahrtagentur (Germany's National Aerospace Research Center as well as the National Space Agency)
LFC	laminar flow control
NBS	National Bureau of Standards
NLF	natural laminar flow
RAM	random access memory
rms	root mean square
TS	Tollmien-Schlichting
UWT	Arizona State University Unsteady Wind Tunnel



# 1. Summary

This report covers an experimental examination of crossflow instability and transition on a 45° swept wing that was conducted in the Arizona State University Unsteady Wind Tunnel during the period 1988–1989. The stationary vortex pattern and transition location are visualized by using both sublimating chemical and liquid-crystal coatings. Extensive hot-wire measurements were obtained at several measurement stations across a single vortex track. The mean and travelling wave disturbances were measured simultaneously. Stationary crossflow disturbance profiles were determined by subtracting either a reference or a span-averaged velocity profile from the mean velocity profiles. Mean, stationary crossflow, and travelling wave velocity data were presented as local boundary-layer profiles and contour plots across a single stationary crossflow vortex track. Disturbance-mode profiles and growth rates were determined. The experimental data are compared with predictions from linear stability theory.

Comparisons of measured and predicted pressure distributions showed that a good approximation of infinite swept-wing flow was achieved. A fixed wavelength vortex pattern was observed throughout the flow-visualization range with the observed wavelength 20 percent shorter than that predicted by the linear stability theory. Linear stability computations for the dominant stationary crossflow vortices showed that the  $N$ -factors at transition ranged from 6.4 to 6.8.

The mean velocity profiles varied slightly across the stationary crossflow vortex at the first measurement station. The variation across the vortex increased with downstream distance until nearly all profiles became highly distorted S-shaped curves. Local stationary crossflow disturbance profiles had either purely excess or deficit values develop at the upstream measurement stations. Farther downstream, the profiles took on crossover shapes not predicted by the linear theory. The maximum streamwise stationary crossflow velocity disturbances reached 20 percent of the edge velocity just prior to transition. The travelling wave disturbances had single lobes at the upstream measurement stations as expected, but farther downstream double-lobed travelling wave profiles developed. The maximum disturbance intensity remained quite low until just ahead of the transition location,

where it suddenly peaked at 0.7 percent of the edge velocity and then dropped sharply. The travelling wave intensity was always more than an order of magnitude lower than the stationary crossflow vortex strength.

The mean streamwise velocity contours were nearly flat and parallel to the model surface at the first measurement station. Farther downstream, the contours rose up and began to roll over like a wave breaking on the beach. The stationary crossflow contours showed that a plume of low-velocity fluid rose near the center of the wavelength while high-velocity regions developed near the surface at each end of the wavelength. No distinct pattern to the low-intensity travelling wave contours appeared until a short distance upstream of the transition location where the travelling wave intensity suddenly peaked near the center of the vortex and then fell abruptly.

The experimental disturbance-mode profiles agreed quite well with the predicted eigenfunctions for the forward measurement stations. At the later stations, the experimental mode profiles took on double-lobed shapes with maxima above and below the single maximum predicted by the linear theory. The experimental growth rates were found to be less than or equal to the predicted growth rates from the linear theory. Also, the experimental growth-rate curve oscillated over the measurement range, whereas the theoretically predicted growth rates decreased monotonically.

## 2. Introduction

### 2.1. Background

The flow over aircraft surfaces can be either laminar or turbulent. Laminar flow smoothly follows the aircraft contours and produces much lower local skin friction drag than the more chaotic turbulent flow. Often both laminar and turbulent flow regions are found on a given aircraft. The amount of laminar and turbulent flow areas is highly dependent on the size, shape, surface finish, speed, and flight environment of the aircraft. The process of minimizing aircraft drag by maintaining laminar flow by using active means such as suction, heating, or cooling is referred to as "laminar flow control (LFC)." LFC technology is being considered for applications on new large

transonic and supersonic transport aircraft. The goal of this effort is to reduce direct operating costs of new aircraft by reducing the drag and, therefore, the fuel consumption. Adequate understanding of the boundary-layer transition process from laminar to turbulent flow lies at the heart of LFC technology. The present research effort is aimed at investigating an important component of the transition process on swept wings, namely the development and growth of crossflow vortices.

The boundary-layer transition problem usually consists of three important phases: receptivity, linear disturbance amplification, and nonlinear interaction and breakdown (ref. 1). The Navier-Stokes equations model the appropriate physics for all these phases. However, techniques to solve these equations for the entire range of the transition problem are only now being developed. Until recently most experimental and theoretical examinations have focused on the second phase, namely, linear disturbance growth in a laminar boundary layer. For two-dimensional flows the experimental and theoretical investigations in this linear regime are in general agreement and are considered to be conceptually well understood (ref. 2). However, for three-dimensional flows, several important phenomena remain unresolved even for the linear stability phase (ref. 1). These phenomena include (1) determination of the dominance of stationary or travelling crossflow waves, (2) whether the crossflow vortex wavelength remains fixed over the region of instability or increases as the boundary layer thickens, and (3) determination of the influence of surface roughness and sound on crossflow vortex growth. The resolution of these uncertainties has broad implications not only for linear stability analyses but also for the entire transition problem for three-dimensional flows.

Receptivity is the process by which disturbances in the external environment enter the boundary layer to begin the transition process (ref. 3). Examples of external disturbance mechanisms include free-stream turbulence (with both vortical and acoustic components), wing surface irregularities and roughness, and surface vibrations. These small disturbances provide the initial amplitude conditions for unstable waves.

The sensitivity of the laminar boundary layer to small amplitude disturbances can be estimated by

solving a set of linear disturbance equations obtained from the governing nonlinear Navier-Stokes equations (ref. 4). The best known example of this is the Orr-Sommerfeld equation for two-dimensional, incompressible Tollmien-Schlichting waves (ref. 4), but similar equations can be derived for more general three-dimensional, compressible, or incompressible flows. These linear equations are obtained by assuming that the complete flow field can be divided into a steady base flow and a disturbance or perturbation flow that varies both spatially and temporally. The base flow is assumed to be a known solution of the Navier-Stokes equations. By eliminating the known base flow solution from the complete problem, nonlinear disturbance equations result. The disturbance equations can be linearized by assuming that the input disturbances are small so that products of disturbance components are neglected. Although the equations are linear, the disturbances actually grow exponentially in either time or space, but the linearity of the equations allows a Fourier decomposition of the problem into modes where each mode has its own characteristic frequency, wavelength, and wave orientation angle. The linear equations can be solved locally when the base flow solution is known by selecting two of the three characteristic variables—frequency, wavelength, or orientation. Upon specifying two variables, the local growth rate and the third characteristic variable are obtained from the linear equation solution. To estimate a transition location by using the so-called  $e^N$  method of Smith and Gamberoni (ref. 5) and Van Ingen (ref. 6), the local solutions to the linear equations are integrated over the wing surface subject to some parametric constraint. The definition of the proper constraint for the three-dimensional swept-wing flow problem is unknown. Examples of the parameter-constraint relation which have been suggested (often very arbitrarily) by various researchers include maximum local amplification rate, fixed wavelength, and fixed spanwise wave number. Widely different values for the integrated  $e^N$  solutions (and thus estimated transition locations) are obtained with the various constraint relations.

The nonlinear interaction and breakdown phase of the transition problem begins when the individual modes attain sufficient magnitude that products of the disturbance components can no longer be neglected as being small when compared with the base flow. From that point, the linear stability method ( $e^N$  method) is no longer valid. At this stage, the disturbances may

have become so large that they begin to severely distort the base flow either spatially or temporally. Reed's computations (ref. 7) indicate that the initial departure from linearity is characterized by double exponential growth of the interacting modes; however, a complete nonlinear analysis is necessary to demonstrate that this is a physically realistic result. Fortunately, this phase of the transition process usually occurs over a fairly short distance when compared with the total laminar flow extent so that almost all the prebreakdown flow region can be approximated by the linear equations only.

## 2.2. Instability Modes

The laminar boundary layer on a swept wing has four fundamental instability modes: attachment line, streamwise, crossflow, and centrifugal. These modes may exist independently or in combinations. The curved streamlines of a typical three-dimensional flow are illustrated in figure 1, and the tangential and crossflow velocity profiles are shown in figure 2. (Appendix A outlines relationships between the coordinate systems used in the present experiment.) The streamwise instability in a three-dimensional boundary layer is similar to the Tollmien-Schlichting waves in two-dimensional flows. Crossflow vortices arise as a result of a dynamic (or inviscid) instability of the inflectional crossflow velocity profile produced by the three-dimensionality of the mean flow field. Both these instabilities are governed to first order by the Orr-Sommerfeld eigenvalue problem or its three-dimensional analog. This equation is obtained by assuming a separation of variables solution to the linearized Navier-Stokes disturbance equations. The results obtained are predictions of the local disturbance amplification rates subject to the constraints required by the separation of variables assumption. Görtler vortices may develop because of a centrifugal instability in the concave regions of a wing. Appropriate curvature terms must be included in the governing equations to account for this instability. The attachment-line instability problem may be significant on wings with large leading-edge radii. For the present experiment on a model with a small leading-edge radius and no upper surface concave regions neither Görtler vortices nor attachment-line contamination are expected to be present, and the most important effects are caused by crossflow and Tollmien-Schlichting instabilities.

The principal motivation for the study of three-dimensional boundary layers is to understand the transition mechanisms on swept wings. The crossflow instability was first identified by Gray (ref. 8) when he found that high-speed swept wings had only minimal laminar flow even though unswept versions of the same wings had laminar flow to approximately 60 percent chord. He used sublimating chemical coatings to visualize the stationary crossflow vortex pattern in the short laminar flow region near the wing leading edge. These findings were subsequently verified by Owen and Randall (ref. 9) and Stuart (ref. 10). Owen and Randall introduced a crossflow Reynolds number (based on the maximum crossflow velocity and the boundary-layer height where the crossflow velocity was 10 percent of the maximum) and determined that the minimum critical crossflow Reynolds number near the leading edge of a swept wing was very low ( $R_{cf,crit} = 96$ ). This work was put on a firm footing both experimentally and theoretically in the classic paper of Gregory, Stuart, and Walker (ref. 11), who established the generality of the results for three-dimensional boundary layers and presented the complete disturbance-state equations.

Brown (refs. 12-14), working under Pfenninger's direction, was the first to integrate the three-dimensional disturbance equations. Brown obtained results in agreement with Gray (ref. 8) and Owen and Randall (ref. 9), but, in addition, showed the potential of suction in controlling the crossflow instability on swept wings. Pfenninger and his coworkers examined suction LFC in a series of experiments—Pfenninger, Gross, and Bacon (ref. 15); Bacon, Tucker, and Pfenninger (ref. 16); Pfenninger and Bacon (ref. 17); Gault (ref. 18); and Boltz, Kenyon, and Allen (ref. 19). They verified the achievement of full-chord laminar flow to a maximum chord Reynolds number of  $29 \times 10^6$ . With this first successful swept-wing LFC program, Pfenninger and his group thus established the foundation of future efforts in this area. See Pfenninger (ref. 20) for a collection of references on LFC efforts.

Smith and Gamberoni (ref. 5) and Van Ingen (ref. 6) introduced the so-called  $e^N$  linear stability method by integrating the local growth rates to determine an overall amplification factor at transition for two-dimensional and axisymmetric flows. They found that transition occurred whenever the  $N$ -factor reached

about 10 (or a disturbance amplification of  $e^{10}$ ). Many investigators including Jaffe, Okamura, and Smith (ref. 21); Mack (refs. 22 to 24); Hefner and Bushnell (ref. 25); Bushnell and Malik (ref. 26); and Berry et al. (ref. 27) verified that similar results applied for the crossflow instability on swept wings. Recent wind tunnel transition studies that added to the  $N$ -factor transition database include Arnal, Casalis, and Juillen (ref. 28); Creel, Malik, and Beckwith (ref. 29); and Bieler and Redeker (ref. 30). Flight tests involving natural laminar flow (NLF) transition studies include Collier et al. (ref. 31); Parikh et al. (ref. 32); Collier et al. (ref. 33); Obara et al. (ref. 34); Lee, Wusk, and Obara (ref. 35); Horstmann et al. (ref. 36); Waggoner et al. (ref. 37); and Obara, Lee, and Vijgen (ref. 38). Suction LFC wind tunnel transition experiments include Berry et al. (ref. 39); Harvey, Harris, and Brooks (ref. 40); Arnal, Juillen, and Casalis (ref. 41); flight tests with suction LFC include Maddalon et al. (ref. 42); and Runyan et al. (ref. 43). These  $N$ -factor transition studies were facilitated by the use of linear stability codes such as SALLY (ref. 44), MARIA (ref. 45), COSAL (refs. 46 and 47), and Linear-X (ref. 48). Arnal (ref. 49), Saric (refs. 50 and 2), Stetson (ref. 51), Malik (ref. 52), Poll (ref. 53), and Arnal and Aupoix (ref. 54) gave general discussions of the applicability of the  $e^N$ -transition methods in three-dimensional flows.

The basic equations for the linear stability analysis of compressible parallel flows were derived by Lees and Lin (ref. 55), Lin (ref. 56), Dunn and Lin (ref. 57), and Lees and Reshotko (ref. 58) by using small disturbance theory. Mack's numerical results (refs. 59 to 61 and 22) have long been heralded as the state of the art in both compressible and incompressible parallel stability analysis. Other investigations of the crossflow instability in compressible flows include Lekoudis (ref. 62); Mack (refs. 63 and 64); El-Hady (ref. 65); Reed, Stuckert, and Balakumar (ref. 66); and Balakumar and Reed (ref. 67). These investigations showed that compressibility reduced the local amplification rates and changed the most unstable wave orientation angles. The largest impact of this stabilizing influence, however, is on the streamwise instability, whereas little effect is noted for the crossflow instability.

Nonparallel flow effects on the crossflow instability were considered by Padhye and Nayfeh (ref. 68),

Nayfeh (refs. 69 and 70), El-Hady (ref. 65), and Reed and Nayfeh (ref. 71). Malik and Poll (ref. 72) and Reed (ref. 7) found that the most highly amplified crossflow disturbances were travelling waves rather than stationary waves. Viken et al. (ref. 73); Mueller, Bippes, and Collier (ref. 74); Collier and Malik (ref. 75); and Lin and Reed (ref. 76) investigated the influence of streamline and surface curvature on crossflow vortices. The interaction of various primary disturbance modes was considered by Lekoudis (ref. 77); Fischer and Dallmann (ref. 78); El-Hady (ref. 79); and Bassom and Hall (refs. 80 to 83). Transition criteria other than the  $e^N$  method were considered by Arnal, Coustols, and Juillen (ref. 84); Arnal, Habiballah, and Coustols (ref. 85); Arnal and Coustols (ref. 86); Michel, Arnal, and Coustols (ref. 87); Arnal, Coustols, and Jelliti (ref. 88); Michel, Coustols, and Arnal (ref. 90); Arnal and Juillen (ref. 90); and King (ref. 91).

### 2.3. Transition Experiments

Many transition experiments involving both NLF and LFC in wind tunnels and flight are discussed in section 2.2 in relation to  $N$ -factor correlation studies. Several transition experiments such as Poll (ref. 92); Michel et al. (ref. 93); and Kohama, Ukaku, and Ohta (ref. 94) deserve further discussion.

Poll (ref. 92) studied the crossflow instability on a long cylinder at various sweep angles. He found that increasing the yaw angle strongly destabilized the flow producing both stationary and travelling wave disturbances. The fixed disturbance pattern was visualized with either surface-evaporation or oil flow techniques. These disturbances appeared as regularly spaced streaks nearly parallel to the inviscid flow direction and ended at a sawtooth transition line. The unsteady or travelling disturbances appear as high-frequency ( $f = 1$  kHz) harmonic waves that reached amplitudes in excess of 20 percent of the local mean velocity before the laminar flow broke down.

Michel et al. (ref. 93) investigated the crossflow instability on a swept airfoil model. Surface visualization studies show the regularly spaced streamwise streaks and a sawtooth transition pattern found by Poll (ref. 92). Hot-wire probes were used to examine both the stationary vortex structure and the unsteady wave motion. Based on their hot-wire studies Michel et al.

concluded that the ratio of the spanwise wavelength to boundary-layer thickness was nearly constant at  $\lambda/\delta = 4$ . They also found a small spectral peak near 1 kHz, which was attributed to the streamwise instability. Theoretical work included in the paper showed that the disturbance flow pattern consisted of a layer of counterrotating vortices with axes aligned approximately parallel to the local mean flow. But, when the mean flow was added to the disturbance pattern the vortices were no longer clearly visible.

Kohama, Ukaku, and Ohta (ref. 94) used hot-wire probes and smoke to examine the three-dimensional transition mechanism on a swept cylinder. A travelling wave disturbance appeared in the final stages of transition that was attributed to an inflectional secondary instability of the primary stationary crossflow vortices. The secondary instability consisted of ringlike vortices surrounding the primary vortex. They concluded that the high-frequency waves detected by Poll (ref. 92) were actually produced by the secondary instability mechanism.

## 2.4. Detailed Theory and Simulation

Several papers that investigated the development and growth of crossflow vortices on swept wings by using detailed theoretical and simulation techniques have recently appeared. Choudhari and Streett (ref. 95) investigated the receptivity of three-dimensional and high-speed boundary layers to several instability mechanisms. They used both numerical and asymptotic procedures to develop quantitative predictions of the localized generation of boundary-layer disturbance waves. Both primary and secondary instability theories were applied by Fischer and Dallmann (refs. 78, 96, and 97) to generate theoretical results for comparison with the DLR swept flat-plate experiments (refs. 98 to 101). They used the Falkner-Skan-Cooke similarity profiles as a model of the undisturbed flow to find that the secondary instability model yielded good agreement with the experimental results, especially the spatial distribution of the root-mean-square velocity fluctuations. Meyer and Kleiser (refs. 102 and 103); Singer, Meyer, and Kleiser (ref. 104); Meyer (ref. 105); and Fischer (ref. 106) used temporal simulations to investigate the nonlinear stages of crossflow vortex growth and the interaction between stationary and travelling crossflow vortices. They found generally good agreement between their

numerical solutions and the DLR swept flat-plate experimental results. A primary stability analysis of the nonlinearly distorted, horizontally averaged velocity profiles showed stability characteristics similar to the undistorted basic flow.

Probably the most relevant computations are those which allow spatial evolution of the flow field especially for the nonlinear interaction problems where large distortions of the mean flow occur. However, these methods require a fixed spanwise periodicity and allow the streamwise pattern to evolve naturally. This method seems to inappropriately eliminate constant wavelength crossflow vortices from computational consideration. Spalart (ref. 107) solved the spatial Navier-Stokes equations for the case of swept Hiemenz flow to show the development of both stationary and travelling crossflow vortices with initial inputs consisting of either random noise, single disturbance waves, or wave packets. He found disturbance amplification beginning at crossflow Reynolds numbers of 100 and a smooth nonlinear saturation when the vortex strength reached a few percent of the edge velocity. Also, preliminary evidence of a secondary instability was obtained. Reed and Lin (ref. 108) and Lin (ref. 109) conducted a direct numerical simulation of the flow over an infinite swept wing similar to that of the present experiment. Malik and Li (ref. 110) used both linear and nonlinear parabolized stability equations (Herbert (ref. 111)) to analyze the swept Hiemenz flow that approximates the flow near the attachment line of a swept wing. Their linear computations agreed with the direct numerical simulations of Spalart (ref. 107). Malik and Li (ref. 110) showed a wall vorticity pattern that they concluded is remarkably similar to the experimental flow visualization patterns seen near a swept-wing leading edge. The nonlinear growth rate initially agreed with the linear result, but farther downstream it dropped below the linear growth rate and oscillated with increasing downstream distance. When both stationary and travelling waves were used as initial conditions, the travelling waves were shown to dominate even when the travelling wave was initially an order of magnitude smaller than the stationary vortex.

## 2.5. Stability Experiments

Detailed experimental investigations of the cross-flow instability in three-dimensional boundary layers

similar to those on swept wings have been conducted in two ways—with swept flat plates having a chordwise pressure gradient imposed by an associated wind tunnel wall bump or with actual swept wings (or swept cylinders). Experiments using the flat-plate technique include Saric and Yeates (ref. 112); the DLR experiments of Bippes and coworkers (refs. 98 to 100 and 113 to 115) and Kachanov and Tararykin (ref. 116). The swept flat-plate crossflow experiments offered the advantage of allowing easy hot-wire probe investigation over the flat model surface but suffered from the lack of a properly curved leading edge where the boundary-layer crossflow began its development. Arnal and coworkers at ONERA (refs. 84 and 90) and Saric and coworkers (refs. 117 to 120) have conducted experiments on swept-wing or swept-cylinder models.

Arnal, Coustols, and Juillen (ref. 84) found the mean velocity exhibited a wavy pattern along the span due to the presence of stationary crossflow vortices. The spanwise wavelength of this wavy pattern corresponded to the streamwise streaks observed in flow visualization studies. The crossflow-vortex wavelength increased with downstream distance as some streaks observed in the flow visualizations coalesce while others vanish. The ratio of spanwise wavelength to local boundary-layer thickness remained approximately constant at  $\lambda/\delta \approx 4$ . Low-frequency travelling waves were observed that reached large amplitudes ( $\pm 20$  percent of the local edge velocity) before transition to turbulence took place. They concluded that both stationary and travelling crossflow waves constituted the primary instability of the flow on a swept wing. Arnal and Juillen (ref. 90) investigated a swept-wing configuration with both negative and positive chordwise pressure gradients. They found that when transition occurred in the accelerated flow region, their crossflow transition criterion gave good results. In the mildly positive pressure gradient regions they found that interactions between crossflow vortices and Tollmien-Schlichting waves produced a complicated breakdown pattern that was not properly characterized by their crossflow transition criterion.

Saric and Yeates (ref. 112) originated the technique of using contoured wall bumps to force a chordwise pressure gradient on a separate swept flat plate. This technique sets the foundation for detailed crossflow instability research that has been repeated by other investigators. They used the naphthalene flow

visualization technique to show a steady crossflow vortex pattern with nearly equally spaced streaks aligned approximately with the inviscid flow direction. The wavelength of these streaks agreed quite well with the predictions from linear stability theory. Saric and Yeates used straight and slanted hot-wire probes to measure both streamwise and crossflow velocity profiles. The probes are moved along the model span ( $z$  direction) at a fixed height  $y$  above the model surface for a range of locations using two different free-stream velocities. Typical results showed a steady vortex structure with vortex spacing half that predicted by the linear stability theory and shown by the surface flow visualization studies. Reed (ref. 7) used her wave-interaction theory to show that the observed period doubling was apparently due to a resonance between the dominant vortices predicted by the linear theory and other vortices of half that wavelength, which were slightly amplified in the far upstream boundary layer. This period doubled pattern persisted for a long distance down the flat plate without the subsequent appearance of subharmonics. Unsteady disturbances were observed by Saric and Yeates but only in the transition region.

Nitschke-Kowsky (ref. 113) and Nitschke-Kowsky and Bippes (ref. 98) used oil coatings and naphthalene for flow visualization studies on the swept flat plate. Flow velocities and surface shear disturbances were measured with hot-wire and hot-film probes. They found a stationary crossflow vortex pattern with  $\lambda/\delta \approx 4$  and travelling waves in a broad frequency band. The rms values for the travelling waves were modulated by the stationary vortex pattern; this modification indicated disturbance interaction. The wavelength of the stationary vortices and the frequencies of the travelling waves were found to be well predicted by the generalized Orr-Sommerfeld equation. Bippes (ref. 99); Mueller (refs. 100 and 114); Bippes and Mueller (ref. 115); and Bippes, Mueller, and Wagner (ref. 115) found that stationary crossflow vortices dominated the instability pattern when the free-stream disturbance level was low and that travelling waves tended to dominate in a high-disturbance environment. They found that when the swept plate was moved laterally in the open-jet wind tunnel flow the stationary vortex pattern remained fixed and moved with the plate. The most amplified travelling wave frequency was observed to differ between wind tunnels. Nonlinear effects were found to dominate although the



linear theory adequately predicted the stationary vortex wavelengths and the travelling wave frequency band.

Saric, Dagenhart, and Mousseux (ref. 117) and Dagenhart et al. (refs. 118 and 119) used contoured end liners on a  $45^\circ$  swept wing in a closed-return wind tunnel to simulate infinite swept-wing flow. Measured pressure distributions indicated that a good approximation of infinite swept-wing flow was achieved. The transition process was believed to be dominated by the crossflow instability because a favorable (i.e., negative) pressure gradient existed on the model to  $x/c = 0.71$ . Stationary fixed wavelength crossflow vortices were observed by flow visualization techniques at several chord Reynolds numbers. The vortex wavelength, which remained fixed over the entire crossflow instability region for a given Reynolds number, varied with Reynolds number approximately as predicted by linear stability theory but with the predicted wavelengths about 25 percent larger than those observed. Hot-wire and hot-film measurements indicated travelling waves in the frequency range predicted by linear theory. In addition, higher frequency travelling waves that may be harmonics of the primary travelling waves were observed. Near the transition location a complicated flow situation developed with highly distorted mean flow and disturbance velocity profiles. Radeztsky et al. (ref. 120) showed that micron-sized roughness can strongly influence crossflow-dominated transition. This effect was confined to roughness near the attachment line and was not influenced by sound. They quantify the effects of roughness height and diameter on transition location.

Kachanov and Tararykin (ref. 116) duplicated the experiments of Saric and Yeates (ref. 112) with identical swept flat-plate and wall-bump geometries. They demonstrated that streamwise slots with alternate suction and blowing could be used to artificially generate stationary crossflow vortices.

## 2.6. State of Present Knowledge

Few detailed crossflow instability experiments have been made, yet some significant observations were made. Both stationary and travelling crossflow waves were observed. The balance between stationary and travelling waves was shown to vary with external environmental conditions. Some evidence of nonlinear

developments including disturbance interactions and disturbance-mode saturation was detected.

Theoretical and computational methods are currently being developed at a rapid pace. Benchmark experimental data sets are urgently needed for comparison with results from these new codes. Many uncertainties about three-dimensional boundary-layer stability and transition remain to be explained. Stationary crossflow vortices seem to dominate in low disturbance environments even though the existing theories indicate that the travelling waves are more highly amplified. The stationary vortex flow patterns observed in different environments are observed to vary. That is, some studies show a fixed stationary vortex pattern throughout the flow and others show an evolving vortex pattern with vortices occasionally merging or vanishing. One must determine how to accurately compute disturbance growth rates and transition locations for engineering applications. The effects of compressibility, curvature, nonparallelism, and nonlinearity on disturbance evolution must be properly accounted for. Three-dimensional flow transition must be compared and contrasted with the situation in two-dimensional mean flow. Information about the transition process is extremely important for the design of aircraft ranging from subsonic transports to hypersonic space vehicles. Understanding the instability mechanisms to be controlled by LFC systems is central to their design and optimization.

## 2.7. Present Experiment

The intent of the present investigation was to isolate the crossflow instability of the three-dimensional flow over a  $45^\circ$  swept wing in such a way that it is independent of the other instabilities. The  $45^\circ$  sweep angle was chosen because the crossflow instability had maximum strength at this angle. The wing consisted of a NASA NLF(2)-0415 airfoil that had its minimum pressure point for its design condition at  $x/c = 0.71$ . (See refs. 121 and 122.) The model was tested at angles of attack from  $-4^\circ$  to  $+4^\circ$ , adjustable in steps of  $1^\circ$ . Contoured end liners are used in a closed-return 1.37- by 1.37-m wind tunnel test section to simulate infinite swept-wing flow. When operated at  $\alpha = -4^\circ$ , the wing produces a long extent of favorable streamwise pressure gradient that stabilizes the Tollmien-Schlichting waves while strongly amplifying crossflow vortices. The streamwise chord of 1.83 m allows

the development of a relatively thick boundary layer ( $\approx 2$  to 4 mm in the measurement region) so that detailed velocity profile measurements are possible in the region of crossflow vortex development. Because the wing had a small leading-edge radius and the upper surface had no concave regions, attachment-line instability and Görtler vortices were not expected. Thus, this test condition allows the examination of the crossflow instability in isolation from the other three instability modes.

Naphthalene sublimation and liquid-crystal flow visualization studies were performed at several test conditions to determine both the extent of laminar flow and the stationary vortex wavelengths. Detailed streamwise velocity profiles were measured with hot-wire anemometers at several spanwise stations across a selected vortex track. The evolution of the vortex is analyzed over this single wavelength and compared with theoretical computations. Velocity profiles at the various spanwise locations and velocity contours across the vortex wavelength for both the mean and disturbance velocities are presented. Vector plots of the theoretical disturbance vortices are shown overlaid on the experimental velocity contour plots. Experimental and theoretical growth rates and wavelengths are compared.

## 2.8. Organization of Publication

The research philosophy employed for this investigation consists of three steps:

1. Use available computational methods to design the experiment
2. Conduct the experiment
3. Compare the experimental results with computational predictions

With the exception of the theoretical disturbance profiles introduced in section 5.7.1, all computations presented were performed by the authors.

The experimental facility is described in section 3. Wind tunnel dimensions and features that produce low disturbance flow are discussed along with descriptions of the instrumentation, hot-wire traverse, and data-acquisition systems. Section 4 gives details of the model and liner design. Extensive computations

including linear stability analyses are performed for the highest possible test Reynolds number to ensure, to the extent possible, that the proper parameter range is selected for the experiment. The relevant coordinate systems are introduced in appendix A. The hot-wire data-acquisition and analysis procedures are outlined in appendix B. The experimental results are presented and discussed in section 5. These data include model pressure distributions, flow visualization photographs, boundary-layer spectra, and detailed hot-wire velocity profiles and contour plots. Comparisons of the experimental results with those from linear stability analyses for the exact test conditions are also shown. These comparisons require the introduction of computational results provided by other researchers. An analysis of the experimental measurement errors is discussed in appendix C.

## 3. Experimental Facility

### 3.1. Arizona State University Unsteady Wind Tunnel

The experiments are conducted in the Arizona State University Unsteady Wind Tunnel (UWT). The wind tunnel was originally located at the National Bureau of Standards and was reconstructed at Arizona State during 1984 to 1988 (ref. 123).

The tunnel is a low-turbulence, closed-return facility that is equipped with a 1.4- by 1.4- by 5-m test section, in which oscillatory flows of air can be generated for the study of unsteady problems in low-speed aerodynamics. It can also be operated as a conventional low-turbulence wind tunnel with a steady speed range of 1 to 36 m/s that is controlled to within 0.1 percent. A schematic plan view of the tunnel is shown in figure 3. The facility is powered by a 150-hp variable-speed DC motor and a single-stage axial blower.

The UWT is actually a major modification of the original NBS facility. A new motor drive with the capability of continuous speed variation over a 1:20 range was purchased. In order to improve the flow quality, the entire length of the facility was extended by 5 m. On the return leg of the tunnel, the diffuser was extended to obtain better pressure recovery and to minimize large-scale fluctuations. The leg just upstream of the fan was internally contoured with

rigid foam. The contour was shaped to provide a smooth contraction and a smooth square-to-circular transition at the fan entrance. A large screen was added to the old diffuser to prevent flow separation and a nacelle was added to the fan motor. Another screen was added downstream of the diffuser splitter plates. Steel turning vanes with a 50-mm chord, spaced every 40 mm, are placed in each corner of the tunnel.

On the test section leg of the tunnel, the contraction cone was redesigned by using a fifth-degree polynomial with  $L/D = 1.25$  and a contraction ratio of 5.33. It was fabricated from 3.2-mm-thick steel sheet. The primary duct had seven screens that were uniformly spaced at 230 mm. The first five screens had an open area ratio of 0.70 and the last two had an open area ratio of 0.65. This last set of screens was seamless and had dimensions of 2.74 by 3.66 m with 0.165-mm-diameter stainless steel wire on a 30 wire/inch mesh. Aluminum honeycomb, with a 6.35-mm cell size and  $L/D$  of 12, was located upstream of the screens. This location helped to lower the turbulence levels to less than 0.02 percent (high pass at 2 Hz) over the entire velocity range.

Both the test section and the fan housing are completely vibration isolated from the rest of the tunnel by means of isolated concrete foundations and flexible couplings. The test section is easily removable and each major project has its own test section.

Static and dynamic pressure measurements are made with a 1000-torr and a 10-torr temperature-compensated transducers. These are interfaced with 14-bit signal conditioners. Real-time data-processing capabilities are provided by 32-bit wind tunnel computers with output via floppy disk, printer, CRT display, and digital plotting. The computers control both the experiment and the data acquisition. They are built around a real-time UNIX operating system. All static and instantaneous hot-wire calibrations, mean-flow measurements, proximeter calibration, three-dimensional traverse control, conditional sampling, free-stream turbulence, and boundary-layer disturbance measurements are interfaced into the data-acquisition system. The facility has a two-dimensional laser Doppler anemometer system and a low-noise hot-wire anemometer system to measure simultaneously two velocity components in the neighborhood

of model surfaces. Signal analysis devices include two computer-controlled differential filter amplifiers, three differential amplifiers, a dual phase-lock amplifier, a function generator, an eight-channel oscilloscope, a single-channel spectrum analyzer, fourth-order band-pass filters, and two tracking filters. A three-dimensional traverse system is included in the facility. The  $x$  traverse guide rods are mounted exterior to the test section parallel to the tunnel side walls. A slotted, moveable plastic panel permits the insertion of the hot-wire strut through the tunnel side wall. The traverse system has total travel limits of 3700 mm, 100 mm, and 300 mm in the  $x$ ,  $y$ , and  $z$  directions, respectively, where  $x$  is in the free-stream flow direction,  $y$  is normal to the wing chord plane, and  $z$  spans the tunnel. The data-acquisition system automatically moves the probe within the boundary layer for each set of measurements after an initial manual alignment. The  $x$  traverse is driven by stepping motors through a lead screw with a minimum step size of 286  $\mu\text{m}$ . The  $y$  and  $z$  traverses are operated by precision lead screws (2.54 mm lead, 1.8 percent per step) which give minimum steps of 13  $\mu\text{m}$ .

Further details of the wind tunnel, data-acquisition system, and operating conditions of the UWT are discussed by Saric (ref. 123) and Saric, Takagi, and Mousseux (ref. 124).

### 3.2. New Test Section

A new test section was designed and fabricated for these experiments in the UWT. Figure 4 shows a photograph of the new test section with the liner under construction. It is fully interchangeable with the existing test section. The 45° swept-wing model, which weighs approximately 500 kg, is supported by a thrust bearing mounted to the floor of the new test section. With the model weight supported on the thrust bearing, the two-dimensional model angle of attack can be easily changed from  $-4^\circ$  to  $+4^\circ$  in steps of  $1^\circ$ . Contoured end liners must be fabricated and installed inside the test section for each angle of attack. Once the system of model and end liners are installed in the new test section, the entire unit replaces the existing test section. This unit allows alternate tests of the crossflow experiment and other experiments in the UWT without disrupting the attachment and alignment of the model in the test section.

## 4. Model and Liner Design

Section 4 gives the design procedure for the experiment. The expected pressure distributions on the selected airfoil in free air and on the swept wing in the UWT including wind tunnel wall-interference effects are shown. Linear stability analyses for stationary and travelling crossflow waves and Tollmien-Schlichting waves at the maximum chord Reynolds number are performed. The experimental test condition and a test-section liner shape to simulate infinite swept-wing flow are selected.

### 4.1. Airfoil Selection

In order to investigate crossflow vortex development and growth in isolation from other boundary-layer instabilities, it is necessary to design or select an experimental configuration that strongly amplifies the crossflow vortices while keeping the other instabilities subcritical. The NASA NLF(2)-0415 airfoil (refs. 121 and 122) is designed as a low-drag wing for commuter aircraft with unswept wings. It has a relatively small leading-edge radius and no concave regions on its upper surface. The NLF(2)-0415 airfoil shape and theoretical pressure distribution for the design angle of attack of  $0^\circ$  are shown in figures 5 and 6. The minimum pressure point on the upper surface at this condition is at 0.71 chord. The decreasing pressure from the stagnation point to the minimum pressure point is intended to maintain laminar flow on the unswept wing by eliminating the Tollmien-Schlichting instability.

#### 4.1.1. Pressure Gradient Effects

As discussed earlier in section 2, positive or negative pressure gradients act to generate boundary-layer crossflow on a swept wing. For the present application on a  $45^\circ$  swept wing, the NASA NLF(2)-0415 airfoil functions as a nearly ideal crossflow generator when operated at a small negative angle of attack. Its relatively small leading-edge radius eliminates the attachment-line instability mechanism for the range of Reynolds numbers achievable in the UWT. The Görtler instability is not present because no concave regions are on the upper surface. The negative pressure gradient on the upper surface keeps the Tollmien-Schlichting instability subcritical to  $x/c = 0.71$  for

angles of attack at or below the design angle of attack of  $0^\circ$ .

Figures 7, 8, 9, and 10 show the NASA NLF(2)-0415 airfoil pressure distributions predicted with the Eppler airfoil code (ref. 125) for angles of attack of  $-4^\circ$ ,  $-2^\circ$ ,  $2^\circ$ , and  $4^\circ$ , respectively. These computations neglect viscous effects and assume that the airfoil is operating in free air; that is, no wind tunnel wall interference is present. Note that for  $\alpha = -4^\circ$ ,  $-2^\circ$ , and  $0^\circ$ , the minimum pressure point on the upper surface is located at about  $x/c = 0.71$ . Beyond  $x/c = 0.71$  the pressure recovers gradually at first and then more strongly to a value somewhat greater than the free-stream static pressure ( $C_p > 0$ ) for all angles of attack shown in figures 6 to 10. For positive angles of attack, the minimum pressure point shifts far forward to  $x/c < 0.02$ . For  $\alpha = 2^\circ$ , the pressure recovery is very gradual to  $x/c = 0.30$  followed by a slight acceleration to a second pressure minimum at  $x/c = 0.71$ . For  $\alpha = 4^\circ$ , a relatively strong pressure recovery follows the pressure minimum and a nearly flat pressure region is observed over the middle portion of the airfoil.

This shift in the pressure distribution with angle of attack has important implications for the strength of the boundary-layer crossflow generated in the leading-edge region. The strength of the crossflow varies with the magnitude of the pressure gradient, the extent of the pressure gradient region, and the local boundary-layer thickness. The leading-edge crossflow is driven most strongly by the strong negative pressure gradients for the positive angles of attack, but because the extent of the negative pressure gradient region is quite small and the boundary layer is very thin near the leading edge, very little boundary-layer crossflow is actually generated. Furthermore, for the positive angles of attack, the positive pressure gradient that follows the pressure minimum overcomes the initial leading-edge crossflow to drive the crossflow in the opposite direction. This positive pressure gradient also accelerates the development of Tollmien-Schlichting waves. For negative angles of attack, the negative pressure gradient in the leading-edge region is a somewhat weaker crossflow driver, but the negative pressure gradient region ( $0 \leq x/c \leq 0.71$ ) is much larger. Thus, as the angle of attack decreases from  $4^\circ$  to  $-4^\circ$ , the leading-edge crossflow increases in strength. This indicates that the desired crossflow-dominated test condition

should be achieved at  $\alpha = -4^\circ$ . Interaction between Tollmien-Schlichting waves and crossflow vortices generated in the pressure recovery region is possible for  $\alpha = 4^\circ$ . Quantitative computational results to support these statements are presented in section 4.2.

Figures 6 to 10 show that a considerable range of pressure distributions is achievable by varying the model angle of attack. To ensure even more flexibility in the pressure distributions, the model is also equipped with a 20-percent-chord trailing-edge flap. Figures 11 to 14 show typical effects of the 20-percent-chord flap for the nominal design angle of attack of  $0^\circ$  and a range of flap-deflection angles from  $-20^\circ$  to  $20^\circ$ . Using this flap-deflection range, the airfoil lift is changed from a negative value for  $\delta_f = -20^\circ$  to a large positive value at  $\delta_f = 20^\circ$  with corresponding upper surface pressure gradients that vary from mildly negative to strongly positive. However, these calculations neglect viscous effects, which yield some very strong positive pressure gradients that are probably not physically achievable in the wind tunnel. But they indicate that changes in the angle of attack and flap deflection angles can be used together to achieve a large range of pressure gradient conditions on the upper surface.

#### 4.1.2. Wind Tunnel Wall Interference Effects

The large model chord of 1.83 m was selected to permit the examination of the crossflow vortex development in a relatively thick (2 to 4 mm) boundary layer. However, wind tunnel wall interference effects are expected when a 1.83-m chord model is installed in a 1.37-m square test section. To eliminate the influence of the walls on the model pressure distribution, the model could be surrounded by a four-wall test section liner that follows streamline paths in free air flow. At each end of the swept wing, the liner would have to follow the curved streamlines as shown in figure 1. The liner would have to bulge on the walls opposite the airfoil surfaces to accommodate the flow over the wing shape. However, contoured top and bottom wall shapes make visual observation of the model very difficult during testing.

For the present experiment, a two-wall liner design was selected. In this approach, the wind tunnel walls opposite the upper and lower wing surfaces were not contoured to match the free-air streamlines but

were simply left flat. However, the presence of the flat walls must be accounted for in the design of the end-liner shapes and in the data interpretation. To accomplish this, a two-dimensional airfoil code (MCARF) that includes wind tunnel wall effects (ref. 126) was modified for  $45^\circ$  swept-wing flow. The influence of the flat tunnel walls on the pressure distribution is shown in figures 15, 16, 17, 18, and 19 for angles of attack of  $-4^\circ$ ,  $-2^\circ$ ,  $0^\circ$ ,  $2^\circ$ , and  $4^\circ$ , respectively. The influence of the flat walls on the airfoil pressure distributions is not negligible, but the qualitative features of the pressure distributions remain the same when the wall interference is included. Negative angles of attack still produce gradual accelerations of the flow to the minimum pressure point at  $x/c = 0.71$ , whereas positive angles of attack give a rapid drop to minimum pressure near the leading edge followed by pressure recovery to a nearly constant level in the midchord region. The required end-liner shapes to achieve quasi-infinite swept-wing flow are discussed in section 4.5.

## 4.2. Stability Calculations

Extensive stability calculations were conducted prior to any experiments in order to determine the appropriate parameter range for this study. Two boundary-layer stability codes—MARIA (ref. 45) and SALLY (ref. 44) are used to predict the performance of the experimental configuration to assure (to the extent possible) that the experimental parameter range covers the physical phenomena of interest. Both codes use mean laminar boundary-layer profiles computed with the Cebeci swept and tapered wing boundary-layer code (ref. 126) with pressure boundary conditions such as those shown in figures 15 to 19. The MARIA code analyzes the stationary crossflow instability subject to the constraint of constant crossflow vortex wavelength. It does not actually solve the crossflow eigenvalue problem discussed earlier in section 2.4, but estimates the local spatial growth rates from a range of known solutions to the Orr-Sommerfeld equation for crossflow velocity profiles. On the other hand, the SALLY code can analyze either the crossflow or Tollmien-Schlichting instabilities with a variety of constraint conditions. In the SALLY code, the crossflow instability is not limited to stationary vortices; travelling crossflow modes are also permissible.

The boundary-layer stability analysis methods are strictly eigenvalue solvers that give local disturbance growth rates. The  $e^N$  method of transition prediction employs the integrated amplification factors ( $N$ -factors) as functions of location on the wing as given by

$$N(x/c) = \int_{(x/c)_0}^{x/c} -\alpha_i d\frac{x}{c} \quad (1)$$

where the local spatial amplification rate  $\alpha_i$  indicates amplification whenever  $\alpha_i < 0$ . The values of  $\alpha_i$  are determined by applying the eigenvalue solver at numerous locations along a streamline for various instability Fourier components. Each Fourier component is specified by its frequency and the eigenvalue solution must be constrained by some parameters to make the integral of equation (1) physically meaningful. As mentioned in section 2.4, this constraint parameter is often selected in an apparently arbitrary fashion. In this paper, the fixed wavelength constraint is used for crossflow vortices, whereas the maximum amplification constraint is employed for Tollmien-Schlichting wave calculations. At this point, the constant wavelength constraint for crossflow is simply an assumption; however, a full justification for this selection based on the experimental observations are presented later in section 5. Because this investigation is aimed at the examination of crossflow vortices in the absence of primary Tollmien-Schlichting waves, it is critical that the strength of the Tollmien-Schlichting instability not be underestimated. Hence, we make the selection of the maximum amplification constraint for Tollmien-Schlichting waves.

The factor  $A/A_0$  represents the amplification from the neutral point  $(x/c)_0$  to an arbitrary location  $(x/c)$  and is obtained as

$$\frac{A}{A_0} = e^{N(x/c)} \quad (2)$$

for each disturbance component. The maximum  $N$ -factor ( $N_{\max}$ ) for each wavelength is obtained by continuing the integration in equation (1) to the end of the amplification range as

$$N(x/c) = \int_{(x/c)_0}^{(x/c)_e} -\alpha_i d\frac{x}{c} \quad (3)$$

where  $(x/c)_e$  indicates the end of the amplification region. The amplification region may end because of the occurrence of a second neutral point. The maximum amplification over the entire crossflow zone ( $0 \leq x/c \leq 0.71$ ) is given by

$$\left(\frac{A}{A_0}\right)_{\max} = e^{N_{\max}} \quad (4)$$

or, equivalently, the natural logarithm of the amplification ratio is given by

$$\ln\left(\frac{A}{A_0}\right)_{\max} = N_{\max} \quad (5)$$

which is, of course, still a function of the disturbance component wavelength.

#### 4.2.1. Stationary Crossflow Vortices

Figures 20 to 34 show predicted stationary crossflow vortex growth rates, local amplification factors ( $N$ -factors), and maximum amplification factors ( $N_{\max}$ ) computed with the MARIA code (ref. 45) for the  $45^\circ$  swept wing installed in UWT at angles of attack ranging from  $-4^\circ$  to  $+4^\circ$ . The growth rates are normalized with respect to the chord. Travelling crossflow vortices, which are more highly amplified than stationary vortices, are considered in section 4.2.3. Emphasis is placed on the stationary vortices because they arise because of surface roughness effects that seem likely to dominate on practical wing surfaces operated in low-disturbance wind tunnel or flight environments. (See Bippes and Mueller, ref. 101.) These computations set an upper bound on the stationary crossflow vortex amplification ratios by assuming that laminar flow is maintained to the beginning of the strong pressure recovery region at  $x/c = 0.71$  for the highest achievable chord Reynolds number of  $3.81 \times 10^6$ . Of course, the amplification of crossflow vortices may cause boundary-layer transition before  $x/c = 0.71$  for this or even lower Reynolds numbers.

The local spatial growth rate is shown for each angle of attack in figures 20 to 24. The data are plotted for a range of wavelength for each angle of attack. Note that the distribution of local amplification is considerably different for the five cases. Short wavelength disturbances are amplified over a fairly narrow range

near the leading edge, whereas the amplification region for the longer wavelengths begins farther downstream and continues to the beginning of the strong pressure recovery at  $x/c = 0.71$ . In all cases, the maximum local amplification occurs in the leading-edge region ( $x/c < 0.10$ ) and is of similar magnitude. Downstream of the leading-edge region ( $x/c > 0.10$ ) the amplification rates vary considerably from case to case. For  $\alpha = -4^\circ$ , the growth rates for intermediate wavelengths level off at a plateau slightly greater than half the initial short wavelength amplification peak. As  $\alpha$  increases from  $-4^\circ$ , this plateau level decreases until it disappears completely at  $\alpha = 2^\circ$ . For  $\alpha = 2^\circ$  and  $4^\circ$ , the amplification region divides into two crossflow regions. At  $\alpha = 2^\circ$ , both these crossflow regions are associated with mean flow accelerations, the first in the leading-edge region and the second in the slight acceleration region from  $x/c = 0.20$  to  $0.71$ . (See fig. 18.) For  $\alpha = 4^\circ$ , the two crossflow regions are associated with pressure gradients of opposite sign (fig. 19) with the mean boundary-layer crossflow going in opposite directions. The first region corresponds to the leading-edge negative pressure gradient (and inboard crossflow), whereas the other is associated with the relatively strong positive pressure gradient following the early pressure minimum at  $x/c = 0.02$  (outboard crossflow). Thus, the crossflow instability pattern changes progressively as the angle of attack is increased from  $\alpha = -4^\circ$ , where fairly strong crossflow amplification continues following the initial crossflow surge, to a complete reversal of the crossflow direction when  $\alpha = 4^\circ$ .

Figures 25 to 29 show  $N$ -factors obtained by applying equation (1) for the five angles of attack. The values of  $N(x/c)$  are shown as functions of location on the wing for various ratios of wavelength to chord. Short wavelength disturbances are shown to begin amplification in the thin boundary layer near the leading edge, reach maximum amplification in the range  $0.10 < x/c < 0.30$ , then decay back to initial intensity levels. Mid and long wavelength vortices begin amplification farther downstream from the leading edge and continue to grow to the beginning of the strong pressure recovery at  $x/c = 0.71$ . Values of  $N_{\max}$  obtained by continuing the integration of equation (3) over the entire crossflow region ( $0 \leq x/c \leq 0.71$ ) are displayed in figures 30 to 34 as functions of the wavelength for each angle of attack. The maximum stationary crossflow amplification decreases progressively as the

angle of attack is increased from  $\alpha = -4^\circ$  to  $2^\circ$ . The  $N_{\max}$  curves peak at 15, 9.5, 4.4, and 0.5 for  $\alpha = -4^\circ$ ,  $-2^\circ$ ,  $0^\circ$ , and  $2^\circ$ , respectively. For  $\alpha = 4^\circ$ , the leading-edge crossflow is negligible and the pressure recovery crossflow is fairly weak ( $N_{\max} = 2.3$ ). These results indicate that significant stationary crossflow amplification should occur for  $\alpha = -4^\circ$  and  $-2^\circ$ , moderate crossflow at  $\alpha = 0^\circ$ , and only minimal amplification for  $\alpha \geq 2^\circ$ .

Previous correlations between computed stationary crossflow amplification factors and experimental transition locations in low disturbance wind tunnels indicate that  $N_{\max}$  at transition is about 7 (ref. 45). Thus, selecting either  $\alpha = -4^\circ$  or  $-2^\circ$  should ensure sufficient crossflow amplification to cause transition on the wing at the highest Reynolds number,  $R_c = 3.81 \times 10^6$ . In fact, crossflow-generated transition should occur well ahead of the pressure minimum at  $x/c = 0.71$  in the more extreme case ( $\alpha = -4^\circ$ ) and move progressively back toward the pressure minimum as Reynolds number is decreased.

#### 4.2.2. Tollmien-Schlichting Waves

Significant stationary crossflow vortex amplification is predicted in section 4.2.1 for the selected configuration when  $\alpha = -4^\circ$  or  $-2^\circ$ . The experimental goal is to examine crossflow vortex amplification and breakdown in the absence of Tollmien-Schlichting waves. Figure 35 shows the maximum  $N$ -factors for TS amplification predicted by the SALLY code as functions of frequency for  $\alpha = 0^\circ$ ,  $2^\circ$ , and  $4^\circ$ . The maximum amplification rate constraint (envelope method) is employed for these computations. In this method, the wave orientation angle is allowed to vary while the code searches for the maximum amplification rate at the selected frequency. Examination of the computational results indicates that at least two peaks are possible in the local amplification rate solutions, one near  $\psi = 0^\circ$  and the other near  $\psi = 40^\circ$ . The irregularity of the  $N$ -factor curves in figure 35 is probably caused by the code switching back and forth between these two possible solutions.

Figure 35 shows large TS amplification for  $\alpha = 4^\circ$ , much weaker disturbance growth for  $\alpha = 2^\circ$ , minimal amplification at  $\alpha = 0^\circ$ , and no amplification for negative angles of attack. The large TS amplification for

$\alpha = 4^\circ$  is easily anticipated from the pressure distribution shown in figure 19. The relatively strong positive pressure gradient in the region  $0.02 < x/c < 0.18$  strongly excites TS waves. For  $\alpha = 2^\circ$ , much less TS amplification results from the weaker positive pressure gradient in the region  $0.02 < x/c < 0.10$ . (See fig. 18). For  $\alpha = 0^\circ$ , the flow accelerates (negative pressure gradient) to  $x/c = 0.71$ ; as a result, figure 35 shows minimal TS amplification. For  $\alpha = -4^\circ$  and  $-2^\circ$ , figures 15 and 16 show that fairly strong flow accelerations continuing to  $x/c = 0.71$  prevent any TS amplification. Thus,  $\alpha = -4^\circ$  and  $-2^\circ$  produce the desired flow conditions—strong crossflow amplification with no Tollmien-Schlichting wave growth.

#### 4.2.3. Travelling Crossflow Vortices

Travelling crossflow vortices are examined theoretically for  $\alpha = 4^\circ$  at the maximum Reynolds number,  $R_c = 3.81 \times 10^6$ , with the SALLY stability code subject to the constraint of fixed vortex wavelength. Table 1 summarizes the predicted  $N_{\max}$  values for a range of frequencies and wavelengths where the local amplification rates are integrated using equation (3) over the entire crossflow region  $(x/c)_0 \leq x/c \leq 0.71$ . The local amplification rates, integrated  $N$ -factors, and total amplification values for these cases vary in a manner similar to the MARIA code results shown in figures 20, 25, and 30. The frequencies  $f$  investigated range from  $-50$  to  $500$  Hz and include stationary vortices ( $f = 0$ ) as a subset. The negative frequency waves may be physically possible and simply correspond to waves that travel in the direction opposite to the direction of the wave-number vector. The orientation of the wave-number vector is shown in appendix C.

Table 1 shows that the most amplified wavelength varies slightly with frequency but in all cases lies in the range  $0.004 \leq x/c \leq 0.006$ . This slight adjustment of the maximum-amplification wavelength is probably caused by local pressure gradient effects and is not considered to be particularly significant. The stationary vortex results are very similar to those obtained with the MARIA code. The wavelength having maximum total amplification for both codes is  $\lambda/c = 0.004$ , but the maximum  $N$ -factor from the SALLY code is lower— $N_{\max} = 13.1$  compared with  $15.0$  from the MARIA code. This difference is not surprising since the MARIA code does not actually solve the boundary-layer stability eigenvalue problem but only

estimates the amplification rates from known solutions. On the other hand, the maximum predicted  $N$ -factor for all cases investigated is  $N = 17.3$  for travelling crossflow waves with  $f = 200$  Hz and  $\lambda/c = 0.005$ . Thus, the travelling crossflow vortices are predicted to be considerably more amplified (by the factor  $e^{4.2} = e^{17.3}/e^{13.1} = 66.7$ ) than the stationary waves. Of course, the actual vortex strength depends not only on the amplification factor but, also, on the external disturbance input. That is, the receptivity portion of the transition process is equally important in the vortex development, growth, and eventual breakdown. The moving vortices are driven by time-varying sound and vorticity fluctuations in the free stream, whereas local surface roughness and discontinuities are most important for stationary vortices. The balance between these two types of disturbance input is critical to developments in the transition process.

#### 4.2.4. Crossflow–Tollmien-Schlichting Interaction

The goal of the present experiment is to examine crossflow vortex development and growth in the absence of Tollmien-Schlichting waves. However, the results of sections 4.2.1 and 4.2.2 indicate two test conditions where the potential interaction between crossflow vortices and TS waves may be fruitfully pursued. The most promising of these conditions is at  $\alpha = 0^\circ$  where moderate crossflow amplification and weak TS waves are predicted. The other possible interaction condition exists at  $\alpha = 4^\circ$  where very strong TS waves and weak pressure-recovery crossflow should coexist. These instability estimates are independent of any such interaction effects themselves because they are computed with linear stability methods.

Figure 32 shows that for  $\alpha = 0^\circ$  the maximum amplified stationary crossflow is  $N_{\max} = 4.6$ , whereas figure 35 shows that the TS amplification peaks at  $N_{\max} = 3$ . The presence of the moderate strength crossflow vortices may sufficiently distort the mean flow velocity profiles so as to produce enhanced TS wave amplification and early breakdown to turbulence. If, however, these disturbance intensities are insufficient to generate mode interaction, the disturbance intensities can be increased by one of two methods. The simplest way to increase the interaction is to increase the Reynolds number, which will increase the strength of both fundamental instabilities. However,



this way is probably not possible in the UWT because the calculations presented are for  $U_\infty = 35$  m/s, which is near the tunnel speed limit. The other alternative is to boost the disturbance intensities by the selective use of two-dimensional or three-dimensional roughness elements and sound. This alternative is similar to the use of vibrating ribbons to introduce disturbances into flat-plate TS instability experiments.

### 4.3. Selection of Experimental Test Condition

In sections 4.1 and 4.2, we have discussed the airfoil selection process, wind tunnel wall interference effects, and boundary-layer stability analysis. The NASA NLF(2)-0415 airfoil is selected as a strong crossflow generator with minimal TS wave amplification. The interference effects of installing a large wing model in the UWT are found nonnegligible. These effects do not change the basic character of the pressure distributions and, therefore, do not change the expected instability characteristics. The stationary crossflow instability is found to be strong for  $\alpha = -4^\circ$  and  $-2^\circ$  but to get progressively weaker as the angle of attack is increased. For  $\alpha = 2^\circ$ , the crossflow instability essentially disappears and only a fairly weak pressure recovery crossflow region is found for  $\alpha = 4^\circ$ . The Tollmien-Schlichting instability is determined to be very strong at  $\alpha = 4^\circ$  and to get progressively weaker as the angle of attack is reduced. This instability is predicted to be totally absent for angles of attack less than zero. Travelling crossflow vortices are examined for  $\alpha = -4^\circ$ , where it was shown that the travelling waves are more amplified than stationary vortices by a factor of 66.7. Selecting the test point for the crossflow-dominated transition experiment is now appropriate.

The selected test point is at  $\alpha = -4^\circ$ . This condition has the strongest crossflow instability and no Tollmien-Schlichting wave amplification. This selection allows the isolated examination of crossflow vortex development and growth. In addition, with the predicted crossflow being very strong at this angle of attack, the Reynolds number can be reduced from the maximum to achieve a range of test conditions where crossflow-induced transition is likely. The effect of Reynolds number variation on the crossflow instability is examined in section 4.4; section 4.5 illustrates the wind tunnel liner shape required to achieve quasi-infinite swept-wing flow.

### 4.4. Reynolds Number Variation

Figure 36 shows the effect of decreasing Reynolds number on the strength of the stationary crossflow instability computed with the MARIA code. The peak of the maximum  $N$ -factor curve is seen to decrease from  $N_{\max} = 15$  to 8.5 as the Reynolds number is reduced from  $R_c = 3.81 \times 10^6$  to  $2.0 \times 10^6$ . The peak  $N$ -factor is reduced approximately in proportion to the Reynolds number reduction; however, this corresponds to a nearly 700 fold reduction in the total amplification. Thus, a very large range for the crossflow vortex strength can be achieved simply by varying the test Reynolds number for the selected test condition of  $\alpha = -4^\circ$ .

### 4.5. Test Section Liner Shape

The pressure distributions and boundary-layer stability predictions in sections 4.1, 4.2, and 4.3 are computed with the assumption that the flow could be approximated as that on an infinite swept wing (i.e., no spanwise pressure gradients). The infinite swept wing produces a three-dimensional boundary layer caused by the combined effects of wing sweep and chordwise pressure gradient, but the boundary-layer profiles and stability parameters are invariant along lines of constant chord. This ideal situation is not possible if a swept wing is installed in a wind tunnel with flat sides on all four walls. With a large chord model installed in a flat-walled wind tunnel, pressure-interference effects will produce a highly three-dimensional pressure pattern and, potentially, a highly three-dimensional boundary-layer instability and transition pattern. To obtain a flow field that is invariant along lines of constant chord, one must employ contoured wind tunnel liners. In the most idealized condition, all four walls of the wind tunnel would be contoured to follow stream surface shapes for an infinite swept wing in free air. For the present application of a large chord model installed in the UWT, the less restrictive approach of contouring only the end liners is adopted. For this approach to be successful, the interference due to the flat side walls adjacent to the upper and lower wing surfaces must be properly taken into account. These effects are considered by employing a modified version of the MCARF two-dimensional airfoil code (ref. 127) that includes the effects of wind tunnel side walls by modeling both the wing and tunnel walls by singularity distributions.

Figures 37 to 39 show various contour lines on the end liners designed for the NASA NLF(2)-0415 airfoil when operated at an angle of attack of  $-4^\circ$  in the UWT. The liner coordinates ( $x_L, y_L, z_L$ ) are parallel to the streamwise coordinates ( $x_s, y_s, z_s$ ) defined in appendix A with the origin taken at the liner entrance. Figure 40 shows a schematic diagram of the model and liners installed in the UWT. These lines are computed with a modified version of a code called TRACES that was written by H. Morgan of Langley Research Center to use output from the MCARF code. The TRACES code is modified to include a constant velocity component along the span of the  $45^\circ$  swept wing (i.e., the infinite swept-wing approximation). Twenty-five streamline tracks are computed for the end liners, but for clarity of presentation, only six are shown in figure 37. The lines are projected in figure 37 onto the  $X_L$ - $Z_L$  tunnel-liner coordinate plane. The model leading edge is located at  $x_L/c = 1.00$ , which is 1 chord downstream of the liner origin. The trailing edge of the model is located at  $x_L/c = 2.00$ . The streamlines shown include lines near each flat side wall ( $z_{LO}/c = 0.306$  and  $-0.417$ ), lines just above and below the wing surface ( $z_{LO}/c = 0$  and  $0.028$ ), and lines intermediate between the model and the tunnel walls ( $z_{LO} = 0.139$ ). Note that the streamlines near the walls are nearly flat as required by the presence of the flat tunnel wall. The other streamlines curve and bulge as they pass the model location. The approximate model shape is discernible from the separation of the streamlines around the model. The negative model angle of attack is indicated by the downward curve of the streamlines just ahead of the model leading edge.

Figure 38 shows the lateral deflections of the end liner required to follow the curved streamlines over the swept wing. Again 25 streamline paths are computed, but only 6 are shown for clarity. The lines all begin with an initial deflection of zero at the liner origin and gradually curve as the model leading edge is approached. In the neighborhood of the model, the streamlines curve more sharply as they pass through regions of strong pressure gradient. Note that the streamlines nearest to the wing surface ( $z_{LO}/c = 0$  and  $0.028$ ) had zero lateral deflection at the liner origin and are separated at the trailing edge by about  $0.02c$  (38 mm). This offset of the streamlines is due to the lift of the wing that causes the upper and lower surface streamlines to deflect different amounts as they pass over the model. The total thickness of liner material

can be seen from figure 38 to be just under  $0.11c$  (0.2 m). The liner contours on the two ends of the swept-wing model must be complementary so that a positive deflection on one wall corresponds to a negative deflection on the other wall. To accommodate these contours in the end liners, the initial liner thickness is taken to be 0.127 m on each end. This leaves about 38 mm of excess material on one end of the model with slightly less than 25 mm minimum thickness on the other end.

Figure 39 shows another view of the liner surface shape. Here surface lines in the  $Y_L$ - $Z_L$  plane are shown for various longitudinal positions along the liner. At the liner origin ( $x_L/c = 0$ ), the contour is flat and the deflection is taken to be zero. At the model leading edge ( $x_L/c = 1.00$ ), the liner is deflected to negative  $y_L$  values over the upper surface side of the model ( $z_L > 0$ ) and a portion of the lower surface side. The liner lateral deflection is purely negative for the upper surface and purely positive for the lower surface of the model at the midchord position ( $x_L/c = 1.50$ ). Note that there is an abrupt jump in the liner contour from the upper to lower surfaces of the model at this location. The jump occurs through the model location itself. This jump or discontinuity continues into the wake region ( $x_L > 2.00$ ) due to the lift on the model.

A schematic view of the model and end liners installed in the UWT is shown in figure 40. The model is mounted with the wing chord plane vertical and the contoured liners located on the floor and ceiling of the test section. The contraction section of the tunnel is equipped with fairings that go from the existing contraction contours to an initial liner depth of 0.127 m at the entrance of the test section. The contraction fairings are each cut from a single large slab of polystyrene material. The end liners are manufactured by laminating 51 mm by 152 mm by 1.22 m (2 in. by 6 in. by 4 ft) pieces of polystyrene material into blocks to form the required liner thickness. The surface contour is then cut into each laminate block with a heated-wire apparatus. This process results in a faceted shape to the liners when all the laminate blocks are assembled into the complete liner. Figure 4 is a photograph of the composite liner during installation in the new UWT test section. To complete the liner construction the polystyrene block surface is sanded lightly to remove the facets and the surface is covered with a thin layer of heat shrink plastic film.

## 5. Experimental Results and Discussion

The experimental results are presented, analyzed, and compared with predictions from the linear stability theory in section 5. Appendix B outlines the hot-wire signal interpretation procedure. Measured wing pressure distributions are given. The stationary cross-flow vortex pattern and the transition line are visualized with sublimating chemical and shear sensitive liquid crystal surface coatings. Free-stream and boundary-layer velocity spectra are shown. Velocity profiles and contour plots are given for the extensive hot-wire measurements taken across a single stationary crossflow vortex track from  $x/c = 0.20$  to  $0.55$  at  $R_c = 2.37 \times 10^6$  and  $\alpha = -4^\circ$ . These data include the mean velocity, stationary crossflow disturbance velocity, and narrow-band-pass travelling wave velocity components in the streamwise direction. Theoretical stationary crossflow disturbance velocity data supplied by Fuciarelli and Reed (ref. 128) are presented and transformed to various coordinate systems for comparison with the experimental results. Theoretical velocity-vector plots are shown overlaid on the experimental velocity contours plots. Observed stationary crossflow vortex wavelengths and growth rates are compared with theoretical predictions.

### 5.1. Free-Stream Flow Quality

The UWT is designed to operate as either an unsteady wind tunnel or as a conventional low-turbulence tunnel. The tunnel is equipped with an aluminum-honeycomb mesh and seven turbulence damping screens which limit the free-stream turbulence level to less than 0.04 percent  $U_\infty$  in the low turbulence mode. For the present experiment the large chord model and associated end liners add disturbances that increase the background turbulence level somewhat, but it generally remains less than 0.09 percent  $U_\infty$ , which is still excellent flow quality for the crossflow experiments. A typical free-stream velocity spectrum measured with a hot wire for  $R_c = 2.66 \times 10^6$  is shown in figure 41. Most of the free-stream disturbance energy is concentrated at low frequencies. Above 10 Hz the energy rolls off with increasing frequency to about 100 Hz, where the spectrum drops below the electronic noise.

### 5.2. Pressure Distributions

Figures 42 and 43 show the measured wing-pressure distributions on the upper surface. These data are measured for three different free-stream velocities, and the three sets of data are almost indistinguishable. The pressure taps are located in streamwise rows with one row near the top end of the model and the other row near the bottom end. The data presented in these two figures are the swept-wing pressure coefficients ( $C_{p,3}$ ) that differ from the airfoil pressure coefficients ( $C_p$ ) given in section 4 by the square of the cosine of the sweep angle as

$$C_{p,3} = \frac{p - p_\infty}{0.5\rho_\infty U_\infty^2} = C_p \cos^2 \Lambda \quad (6)$$

where  $p$  is the local surface pressure and  $p_\infty$ ,  $\rho_\infty$ , and  $U_\infty$  are the free-stream pressure, density, and velocity, respectively. For the top end of the model, the measured pressure distribution is in general agreement with the predicted curve, but the theoretical pressure distribution slightly underestimates the measurements over the whole model (fig. 42). The underestimate is largest in the region  $0.05 < x/c < 0.40$ . Examination of the top end liner contour indicates that the liner is slightly thinner near the model leading edge than designed, which probably accounts for the underprediction of the pressure in this region. At the lower end of the model, the experimental pressure distribution is well predicted to about  $x/c = 0.25$ , but the pressure minimum near  $x/c = 0.70$  is underpredicted (fig. 43). This underprediction may occur because the test section floor is inclined to offset normal tunnel wall boundary-layer growth on all four tunnel walls. Both the top and bottom rows of pressure taps are located within 5 to 15 cm of the liner surfaces; this tunnel wall boundary-layer interference probably exaggerates the influence of liner-contour errors as compared with the impact felt in most of the flow field. Because the measured pressure distributions differ only slightly from the predicted distributions, a reasonable approximation of infinite swept-wing flow appears to have been established in the central portion of the test region. The free-stream and boundary-layer hot-wire measurements confirm this.

### 5.3. Flow Visualizations

A naphthalene-trichlorotrifluoroethane spray is used to place a white sublimating coating over the black model surface. The naphthalene sublimates faster in regions of high shear; this allows the visualization of the stationary crossflow vortices and clearly indicates the transition location. Figures 44 to 48 show naphthalene visualization photographs for  $\alpha = -4^\circ$  and chord Reynolds numbers ranging from  $1.93 \times 10^6$  to  $3.27 \times 10^6$ . The flow is from left to right in the figures with fractions of chord indicated by the markings at 10-percent-chord intervals. In each figure, the naphthalene coating is absent over approximately the first 15 percent of chord because of the high laminar shear stress in this region. From approximately  $x/c = 0.15$  to the jagged transition line, the stationary crossflow vortex pattern is clearly evident. The vortex spacing is determined by counting the number of light and dark streak pairs over a length of 10 cm. The wavelength is observed to remain constant over the model at each test condition. This observation is in agreement with the findings of Saric and Yeates (ref. 112). In contrast with the results obtained by Arnal and Juillen (ref. 90), no vortex dropouts or other adjustments to the vortex spacing are observed. The laminar region is terminated in each case at a jagged transition line produced by overlapping turbulent wedges. Table 2 shows the average transition location and measured vortex spacing as a function of the chord Reynolds number. The transition location is estimated from the photographs as the average of the beginning and ending locations of the turbulent wedges. Figure 49 shows a closeup photograph of a heavy coating of naphthalene for  $R_c = 2.65 \times 10^6$  where the stationary crossflow vortex traces can be seen to continue into the turbulent wedge regions.

In addition to naphthalene, liquid crystal coatings are also used to visualize the crossflow vortex streaks and transition pattern. Figure 50 shows an example of a green liquid crystal flow visualization photograph. The black and white view shown does not adequately demonstrate the patterns that are visible in a color image. The stationary crossflow vortices are visible as alternating green and black streaks and the transition location is indicated by an abrupt shift to a deep blue. However, this technique proved less satisfactory than the naphthalene visualization. The crossflow streaks and the transition location are less obvious in the

liquid crystal photographs than in the naphthalene visualizations. Perhaps the relatively low shear stress in the present application limits the utility of the liquid crystal technique. Similar results were obtained when these studies were repeated in a cooperative program with Reda using his technique (ref. 129).

The repeatability of the transition pattern is investigated by marking the jagged transition line on the model with a felt-tipped pen following a naphthalene flow visualization run. The naphthalene visualizations are repeated at the same Reynolds number after several days, during successive tunnel entries, and even after the screens are removed, cleaned, and reinstalled with virtually the same transition patterns observed. The visualization is also repeated with liquid crystals, and again, essentially the same transition patterns are observed. This agreement indicates that the stationary vortex traces and the transition pattern are dominated by small-scale surface roughness effects that are not significantly influenced by the two different flow visualization techniques or the facility condition. Indeed, Bippes and Mueller (ref. 101) find that when they move their flat-plate model laterally in the open-jet test section the vortex streak and transition patterns remain fixed and move with the plate.

### 5.4. Transition Locations

Boundary-layer transition locations are determined by several methods including interpretations of hot-film and hot-wire voltage signals and sublimating chemical flow visualizations. The transition locations are determined from the flow visualization photographs by the abrupt shift in sublimation rate of the naphthalene coating due to turbulence-induced shear stress increases. The sharp change from the streaked naphthalene pattern to black background thus marks the transition location. The rms voltage responses of the hot-film gauges are plotted as functions of the Reynolds number. The point on the curve where the slope increases abruptly with increasing Reynolds number is taken as the transition point. For the boundary-layer hot-wire probes, the onset of abrupt voltage spikes in the time-dependent voltage signal is taken as the transition indicator. Thus, all these methods indicate the beginning of the transition process with the hot wires and hot-film gauges providing local transition measurements and the flow visualization giving a global view of the transition pattern.

Figure 51 is a summary plot of transition measurements on the swept wing versus chord Reynolds number for  $\alpha = -4^\circ$ . A transition band is indicated for the naphthalene flow visualization results. The beginning of the band indicates the origin of the most forward turbulent wedge and the end of the band is the location where the wedges merge. Points are shown for hot-wire transition measurements at  $x/c = 0.40$  and for hot-film transition measurements at several locations. Thus, the naphthalene flow visualization technique is calibrated. For chord Reynolds numbers greater than  $2.3 \times 10^6$ , the transition location is observed to be ahead of the pressure minimum at  $x/c = 0.71$ . For these Reynolds numbers the transition process is presumed to be completely crossflow dominated.

## 5.5. Boundary-Layer Spectra

Figures 52 to 55 show the rms velocity spectra for a hot wire located within the boundary layer at  $x/c = 0.40$ , as the chord Reynolds number is increased from  $2.62 \times 10^6$  to  $3.28 \times 10^6$ . This Reynolds number range is selected because transition is expected to occur in the neighborhood of  $x/c = 0.4$  as seen from figure 51. In figure 52, an amplified-response band is noted near the blade-passing frequency  $f_{bp}$ . As the Reynolds number increases in figures 53 and 54, the response band near  $f_{bp}$  broadens and a second, higher frequency amplified band emerges. For this test condition,  $f_{bp}$  is approximately equal to the maximum amplified crossflow frequency  $f_{cf,max}$ . These frequencies fall within the lower frequency amplified band. The higher frequency band corresponds to approximately  $2f_{cf,max}$ . In addition, the blade passing plus stators frequency,  $f_{bps}$  and  $2f_{bp}$ , are in the higher frequency band. Figure 55 shows the spectrum for  $R_c = 3.28 \times 10^6$ , which is in the turbulent flow region. Here the spectrum is flattened with similar energy levels at all frequencies to 500 Hz. A comparison between the predicted crossflow frequency response and the measured spectrum is shown in figure 56. The lower frequency response band corresponds to a portion of the predicted moving crossflow vortex amplification range near  $f_{bp}$ . The higher frequency response band is located at the extreme upper end of the predicted amplified frequency range where the predicted amplitude rapidly decreases with increasing frequency. Bippes and Mueller (ref. 101) observe travelling crossflow waves that tend to dominate the flows in relatively high disturbance tunnel environments.

They find that stationary crossflow vortices dominate in low disturbance tunnels. Saric and Yeates (ref. 112) do not observe travelling crossflow vortices. However, they do observe a stationary wavelength spectrum with a broad peak near the theoretically predicted maximum amplified wavelength and an additional sharp peak at half the predicted wavelength. Reed (ref. 7) is able to explain this development as a parametric resonance between the primary crossflow vortices that develop relatively far downstream and vortices of half this wavelength, which are slightly amplified in the thin upstream boundary layer.

## 5.6. Boundary-Layer Hot-Wire Surveys

### 5.6.1. Streamwise Velocity Measurements

Constant-temperature hot-wire anemometers are used to make detailed mean streamwise velocity profile measurements across a single stationary crossflow vortex for  $\alpha = -4^\circ$  and  $R_c = 2.37 \times 10^6$ . The measurements are made at intervals of  $x/c$  of 0.05 from  $x/c = 0.20$  to 0.55 with two hot-wire elements. A single hot-wire probe is located inside the boundary layer, and a second single wire probe is located in the free stream. Both wires are oriented parallel to the model surface and perpendicular to the free-stream velocity vector. The ratio of the velocity indications from the two anemometers yields the streamwise boundary-layer velocity ratio. The hot-wire calibration and data reduction procedure is given in appendix B. The experimental error analysis is given in appendix C. Figure 20 shows that the stationary crossflow vortices become unstable at  $x/c = 0.05$ , whereas figure 51 shows that the average transition line lies at approximately  $x/c = 0.58$ . Thus, the measurement locations cover a large portion of the unstable crossflow region from slightly downstream of the first neutral point to just ahead of the transition location.

A high-shear vortex track (i.e., dark streak) on the model is marked with a soft felt-tipped pen following a sublimating chemical flow visualization study. The beginning point of the track is arbitrarily chosen as the midspan location for  $x/c = 0.20$ . For most locations, the measurements are made at seven spanwise locations across the vortex along lines parallel to the leading edge of the  $45^\circ$  swept wing. These seven profiles represent six steps across the vortex with the first and seventh profiles expected to be essentially the same.

The spanwise measurement locations are separated by intervals of  $\Delta s = 1.6$  mm. The spanwise step size is dictated by the step size in the downstream and lateral directions and the desire to make an integral number of steps across the vortex; this can be demonstrated as follows. Figure 47 shows that the stationary vortex tracks lie at an angle of approximately  $\theta_v = 5^\circ$  with respect to the free-stream direction. Then, lines parallel to the leading edge cut across the vortex tracks at  $\theta_M = \Lambda - \theta_v \approx 40^\circ$ , where  $\Lambda$  is the wing sweep angle. Now, the wavelength measured parallel to the leading edge can be obtained as  $\lambda_{45} = \lambda / \cos \theta_M$ . Table 2 indicates that for  $R_c = 2.37 \times 10^6$  the ratio of wavelength to chord  $\lambda/c$  is approximately 0.004 or  $\lambda = 7.32$  mm. Thus,  $\lambda_{45} = 9.5$  mm.

Both the mean and fluctuating velocity components are measured simultaneously by separating the anemometer output signals into DC and AC components. The AC component is quite small and can not be measured accurately in its raw state. It is measured by blocking the DC component of the signal, amplifying the remaining fluctuating signal, narrow-band-pass filtering at  $f = 100$  Hz, and amplifying again before the computer analog to digital (A/D) converter measures the signal. The amplifier gains are then divided out to obtain the final fluctuating signal values. The selected central frequency of  $f = 100$  Hz is chosen because it is near the maximum amplified frequency for travelling crossflow vortices as indicated both by computations and experimental hot-wire spectra.

The motion of the hot-wire probe inside the boundary layer is controlled by the data-acquisition computer after the initial position is set by hand. This initial alignment is accomplished by locating the hot-wire probe above the intersection of the marked vortex track and the local fractional chord line. The starting point for each boundary-layer survey station is set in this fashion. During the data-acquisition procedure, the experimenter has to actively observe the hot-wire AC signals on an oscilloscope, adjust the amplifier gain settings to assure maximum signal strength with overranging the instruments, and stop the traverse mechanism before the probe collides with the model surface. The data-acquisition computer measures the anemometer voltages and moves to the next point only after acceptance of the data by the experimenter.

The velocity data are presented in figures 57 to 120 in two forms—velocity profiles at several span-

wise stations across the crossflow vortex and velocity contours over the  $45^\circ$  spanwise measurement cuts. Figures 57 to 64 show the actual velocity ratios obtained from the hot-wire data reduction procedure outlined in appendix B. The height above the wing surface is determined by extrapolating the velocity data to a zero value at the surface for each profile. The presence of the stationary crossflow vortex is indicated in figures 65 to 72 by subtracting the average value of the streamwise velocity from the local profile values. The resultant disturbance velocity profiles show the excess or deficit of velocity produced by the stationary vortex. An alternate representation of the stationary crossflow vortex disturbance intensity is given in figures 73 to 80 where reference-computed velocity profiles are subtracted from the local velocity measurements. In both representations, the velocity difference is made nondimensional by dividing by the local boundary-layer edge velocity magnitude. Thus, the plots represent local disturbance intensity values, but because the boundary-layer edge velocity increases slightly from  $x/c = 0.20$  to  $0.55$ , the velocity ratios are scaled down by a small amount as  $x/c$  increases. The root-mean-square velocity profiles for travelling waves of  $f = 100$  Hz are given in figures 81 to 88. The velocity values are again nondimensionalized by the local boundary-layer edge velocity. Contour plots of the mean streamwise velocity across the vortex are shown in figures 89 to 96. Stationary vortex velocity contours are plotted in figures 97 to 104 for  $U_{s,avg}$  removed and in figures 105 to 112 for  $U_{s,ref}$  removed. Figures 113 to 120 show rms intensity contours for  $f = 100$  Hz.

### 5.6.2. Spanwise Variation of Streamwise Velocity

Figure 57 shows that the mean velocity profiles across the vortex are very similar in shape at  $x/c = 0.20$ , but there is already some variation in fullness of the profiles due the presence of the stationary crossflow vortex. As the stationary vortex grows in strength in the downstream direction, the variation in the velocity profiles across the vortex increases. At  $x/c = 0.35$  (fig. 60), some profiles have developed distinct inflectional shapes, whereas other profiles remain rather full. Figure 64 shows that at  $x/c = 0.55$  (only a short distance ahead of the breakdown region) all six velocity profiles have taken on a distorted inflectional shape and several profiles are severely distorted into S-shaped profiles. These highly distorted streamwise

velocity profiles are expected to respond very differently to streamwise or secondary instabilities than the undisturbed profiles.

As noted earlier, for each fractional chord location, the first velocity profile measurement is centered on the dark (high-shear) vortex track marked with the felt-tipped pen. In examining figures 57 to 64, it is evident that for the minimum measurement height the initial profile is very near the smallest velocity ratio and thus the highest surface shear at each station except at  $x/c = 0.20, 0.50$ , and  $0.55$ . At these stations, the maximum shear location appears to be approximately 2 or 3 mm away from the initial profile location. Earlier the flow visualization patterns were noted to be repeatable for matching Reynolds numbers. However, lateral shifts of the whole vortex pattern by a small fraction of a wavelength are not unexpected. The deviation of the initial profile from the maximum shear location at  $x/c = 0.20, 0.50$ , and  $0.55$  could be due to a small shift in the vortex pattern or to a small lateral misalignment ( $\approx 2$  to 3 mm) of the traverse rig at the beginning of the measurements. The influence of this misalignment at the beginning of the measurement region is evident in the results that follow.

### 5.6.3. Disturbance Profiles

Figures 65 to 72 show the stationary crossflow disturbance velocity profiles determined by subtracting the average streamwise velocity ratio at a given height from the measured velocity ratio at each location. The abscissa scale is chosen to keep the local velocity scales essentially the same for each chordwise station. As noted previously, the local boundary-layer edge velocity, which is used as a reference value, increases slightly from  $x/c = 0.20$  to  $0.55$  so that the disturbance velocity ratios are scaled down slightly with this nondimensionalization as  $x/c$  is increased. For the crossflow instability, the disturbance vortex axes are nearly streamwise and the primary disturbance vortex components in a streamwise coordinate system are the velocity components  $v$  and  $w$ . The perturbation in the streamwise direction (velocity component  $u$ ) is a secondary effect due to the convection arising from the velocity components  $v$  and  $w$ . However, the streamwise component (component  $\bar{u}$ ) of the boundary-layer velocity has a large gradient in the direction perpendicular to the wing surface ( $d\bar{u}/dy$ ) so that when combined with small convective velocity

components  $v$  and  $w$ , it produces a large secondary streamwise velocity perturbation. This streamwise velocity perturbation is the one shown in figures 65 to 72 and later in figures 73 to 80. Over a single vortex wavelength, these perturbation velocity profiles are expected to exhibit either excesses or deficits from the mean, depending on the lateral location in the streamwise vortex. Over that portion of the vortex where the velocity components  $y$  and  $w$  convect the high momentum flow from the outer portion of the boundary layer toward the surface, the local profile should have an excess (or bulging) shape. On the other hand, when the vortex velocity components convect low momentum flow away from the surface, the local profile is expected to have a deficit shape.

Note that in figures 65 and 67 only five velocity profiles are measured. Nonetheless, it is apparent in figure 65 that some of the local disturbance profiles show excess velocities, whereas others show deficit velocities as expected. However, the profiles in figure 65 have two unexpected features. First, the disturbance profiles do not approach 0 for large values of the height  $y$  above the wing surface; this is due to temperature drift effects in the UWT. The UWT has no temperature control; the test temperature is governed by the ambient temperature in the wind tunnel building (which is cooled by an electrical air-conditioning unit) and, more importantly, by the power input to the wind-tunnel fan. To eliminate this effect for the other measurement stations, the tunnel was run in a preheat mode for 30 to 45 min before acquiring boundary-layer disturbance data. This preheat time is used each day to verify instrumentation connections, filter settings, and so forth. The second anomalous aspect of the profiles in figure 65 is the bulge in excess and deficit velocities below  $y \approx 0.5$  mm. These bulges are unexpected and are almost as large as the maximum disturbance intensities found for  $y \approx 1.2$  mm. The presence of these velocity perturbations is traced to residue left behind by cleaning the model with alcohol and supposedly lint-free cloths. This contamination had not been noted earlier during the preliminary velocity profile measurements probably because single velocity profile measurements were generally made following a flow visualization study in which the model surface was effectively cleaned by the trichlorotrifluoroethane solvent used with the naphthalene. The model cleaning procedure was modified to a two-step procedure—cleaning first with alcohol and

then with distilled water. A single velocity profile measurement at  $x/c = 0.20$  confirmed that the residue problem was solved, but the complete set of velocity profiles at  $x/c = 0.20$  were not measured again due to lack of sufficient time. The data at all subsequent measurement stations are taken following the two-step model cleaning process and no further contamination problems are encountered.

Examination of figures 65 to 72 shows that the maximum disturbance intensity of the stationary crossflow vortex grows progressively from  $x/c = 0.20$  to 0.55. At  $x/c = 0.20$ , the profiles show either excess or deficit velocities only. But by  $x/c = 0.35$ , some of the disturbance profiles have taken on definite crossover shapes. These crossover profiles have both excess and deficit velocity regions. At the last measurement station ( $x/c = 0.55$ ) the maximum disturbance intensity exceeds 20 percent of the edge velocity and all the profiles have taken on highly distorted shapes. The nature and significance of these crossover profiles are discussed further in section 5.7.3 where the disturbance velocities are displayed as contour plots.

Figures 73 to 80 show stationary crossflow disturbance profiles obtained by a different procedure. Here local theoretical velocities are subtracted from the measured profiles to yield the local disturbance vortex intensities. Note that the angle of attack for the reference case is taken as  $\alpha = -5^\circ$  rather than the actual angle of attack,  $\alpha = -4^\circ$ . This adjustment in the theoretical angle of attack is required because the theoretical profiles for  $\alpha = -4^\circ$  are obviously fuller than the experimentally measured profiles. The reason for this discrepancy is uncertain, but it may arise from a slight flow angularity in the UWT test section or a minor misalignment of the model mounting bearing.

The stationary crossflow profiles in figures 73 to 80 agree in general trends with those shown in figures 65 to 72. For both sets of figures, the maximum disturbance intensity grows progressively with increasing  $x/c$ , definite crossover profiles develop by  $x/c = 0.35$ , and all profiles are highly distorted at  $x/c = 0.55$ . However, there are some slight differences between removing the average velocity profile and the theoretical velocity profile from the measured data. These differences arise because the averaged profiles from the experiment include flow history effects

produced by the presence of the stationary crossflow vortices within the boundary layer, whereas the theoretical profiles completely neglect this effect. The most notable of the differences in the two sets of profiles is observed by comparing figures 65 and 73 for  $x/c = 0.20$ . In figure 73, the influence of the surface contamination discussed earlier produces velocity deficits in all profiles for  $y < 0.5$  mm. In figure 65, this deficit effect is included in the averaged profile, and as a result, the disturbance profiles are not biased toward a deficit condition. Of course, this deficit effect is an experimental error which would have been removed completely by retaking the data at  $x/c = 0.20$  if time had allowed. Other notable, and experimentally more significant, differences are observed for  $x/c > 0.45$  where flow history effects become more pronounced. This effect is shown more clearly in the disturbance-velocity contour plots.

Root-mean-square velocity profiles for travelling waves are shown in figures 81 to 88. As mentioned previously, these data are measured simultaneously with the mean velocity by splitting the hot-wire anemometer signal into mean and fluctuating components. The fluctuating component is amplified, narrow-band-pass filtered, and amplified again before recording with the UWT A/D converter system. The selected central frequency for the narrow-band-pass filter is  $f = 100$  Hz, which is near the frequency of maximum amplification according to both experimental and theoretical considerations. Again, these data are plotted with an abscissa scale that is essentially unchanged over the range of measurement locations; this allows for easy visual examination of the disturbance amplification with increasing  $x/c$ . For travelling crossflow waves, rms-averaged profiles of the streamwise velocity are expected to yield profiles with a single maximum and, of course, only positive values. Furthermore, in the absence of nonlinear distortions caused by the stationary crossflow vortices or the presence of some other travelling waves in the same frequency range, the rms velocity profiles are expected to be identical at each spanwise location.

For the first two measurement stations ( $x/c = 0.20$  and 0.25, figs. 81 and 82), the disturbance intensities are quite small and the velocity profiles have essentially the same shape at all spanwise locations across the stationary crossflow vortex. Here the rms streamwise velocity profiles have a single lobe (or maximum) as expected for travelling crossflow vortices.



By  $x/c = 0.30$ , the shapes of the travelling wave velocity profiles have begun to distort, but the profiles continue to have single-lobed shapes. This distortion of the profile shape may arise from the development of other travelling wave disturbance modes of the same frequency but different direction of travel or the non-linear distortion of travelling crossflow waves by the strong stationary crossflow vortex layer. For  $x/c > 0.40$  (figs. 85 to 88), definite double-lobed travelling wave disturbance velocity profiles are apparent at some spanwise locations across the stationary crossflow vortex. Between  $x/c = 0.40$  and  $0.50$ , the travelling waves grow considerably in strength. However, from  $x/c = 0.50$  to  $0.55$ , the largest amplitudes decrease by greater than a factor of 2. Note that even at their maximum intensity, the travelling waves are quite small as compared with the strength of the stationary crossflow vortex (e.g., only 3.5 percent as large). Thus, it appears that the travelling waves which initially have very low amplitude, grow and distort considerably for  $0.40 < x/c < 0.50$ , and then decay for  $x/c > 0.50$ . The nature of the distortion of the travelling waves due to the stationary crossflow vortices is more apparent when viewed as contour plots in section 5.6.4.

#### 5.6.4. Streamwise Velocity Contour Plots

Contour plots of the mean velocity, stationary crossflow disturbance intensities, and the travelling wave disturbances are given in figures 89 to 120. These plots show the various experimentally determined quantities plotted on a grid which is 4 mm deep in the  $y$  (surface normal) direction and extends 9.5 mm along a  $45^\circ$  swept line parallel to the wing leading edge. As mentioned previously, the spanwise coordinate cuts across the stationary crossflow vortex tracks at approximately a  $40^\circ$  angle and the stationary vortex wavelength along a line parallel to the leading edge is  $\lambda_{45} = 9.5$  mm. The abscissa is taken as  $z_\lambda = -(z_m - z_{m,0})/\lambda_{45}$  and is a local coordinate with  $z_\lambda = 0$  on the marked stationary vortex track and  $z_\lambda > 0$  in the direction of spanwise motion of the hot-wire probe. With this coordinate selection, the abscissa actually runs in the direction opposite to the model spanwise coordinate  $z_m$ . The plots show the situation an observer would see when looking upstream from the hot-wire probe location. These data are plotted for  $0.20 \leq x/c \leq 0.55$ . For  $x/c = 0.20$  and  $0.30$ , the data are not measured across the full crossflow vortex wavelength; but, for the other stations, these data

are shown for a full stationary crossflow vortex wavelength. For each boundary-layer station, all velocities are made nondimensional by dividing by the local streamwise boundary-layer edge velocity. Because the edge velocity increases by about 10 percent from  $x/c = 0.20$  to  $0.55$ , the actual velocities are scaled down by this factor.

Figures 89 to 96 show the mean streamwise boundary-layer velocity ratio  $\bar{u}_s/\bar{u}_{s,e}$  in the tunnel coordinate frame. In the absence of stationary crossflow disturbance vortices, the velocity contours are expected to be flat and parallel to the wing surface. Figure 89 shows that the mean velocity contours at  $x/c = 0.20$  are nearly flat and parallel to the wing surface. But some influence of the stationary crossflow vortex is already present at this forward location with the contour levels somewhat wavy and inclined slightly toward the surface for increasing values of  $z_\lambda$ . The waviness of the contours increases with  $x/c$  until the contours obviously bulge upward at approximately the middle of the wavelength for  $x/c = 0.35$  (fig. 92). This upward bulge of the contours corresponds to low-momentum fluid being swept upward from the wing surface by the stationary crossflow vortex. The bulge continues to grow as  $x/c$  increases until the contours actually begin to roll over like a breaking wave for  $x/c = 0.50$  (figs. 95 and 96).

This mean velocity contour pattern is consistent with expectations for boundary-layer flow with embedded stationary crossflow vortices. The flow visualization photographs (figs. 44 to 48) show that the crossflow vortex axes are aligned almost parallel to the free-stream velocity vector. The instability produces a layer of counterrotating disturbance vortices that combine with the mean boundary-layer crossflow to yield a layer of crossflow vortices all with the same rotational direction (corotating pattern). This pattern develops because the flow is most unstable to the crossflow instability at some small angle to the pure crossflow direction (ref. 45). The mean-velocity profile in the most unstable crossflow direction has a crossover shape with flow streaming in the crossflow direction near the wing surface but in the opposite direction farther out from the surface (ref. 8). When this crossover velocity profile is combined with the counterrotating disturbance vortices, it reinforces the strength of one pair of vortices while cancelling the other. This produces the observed velocity field with

flow streaming in the crossflow direction near the wing ( $z_\lambda$  direction) while the flow in the outer part of the boundary layer flows in the opposite direction. Hence, the breaking-wave pattern seen in figures 95 and 96 is caused.

As previously noted, the initial velocity profile at each measurement station is intended to be on the line of maximum shear as determined by the flow visualization study. But because the measurements are made over many days of wind tunnel testing, it is not unexpected that small shifts ( $\approx 2$  to 3 mm) in the location of the stationary vortex pattern occur. Such shifts in the vortex pattern can be deduced from the mean streamwise velocity contour plots (figs. 89 to 96). The location of maximum surface shear stress is determined qualitatively by observing the grouping of streamwise velocity contours near the wing surface. Figures 95 and 96 show that the maximum shear stress point appears to have shifted by 1.5 to 3 mm in the  $z_\lambda$  direction. This shift is even more obvious in the stationary vortex velocity field.

Stationary crossflow vortex velocity contours are plotted in figures 97 to 104 and 105 to 112. The first set of contours corresponds to disturbance velocities determined by removing the averaged mean velocity profile from the local measured velocities. The second set of disturbance velocity contours are computed by subtracting the theoretical mean velocity values from the measured velocities. For each set, the disturbance velocity values are nondimensionalized by the local boundary-layer edge velocity that increases slightly from  $x/c = 0.20$  to 0.55. The range of contour levels up to  $\pm 0.20 \bar{u}_{s,e}$  are used for all measurement locations for easy data comparisons. The two sets of contours agree in general shape and levels of the velocity contours. Some relatively small differences can be noted for  $x/c = 0.50$  and 0.55, where the averaged mean velocity profile is distorted by the presence of the stationary crossflow vortex, but the theoretical profiles ignore this effect. Thus, the following discussion of the evolution of the stationary crossflow disturbance velocity contours applies equally well to either set of figures.

The expected stationary crossflow disturbance velocity pattern has excess velocities at the extremes of the plotting field ( $z_\lambda = 0$  and 1) and deficit velocities near the middle of the field ( $z_\lambda = 0.5$ ). This is because

the initial velocity profile ( $z_\lambda = 0$ ) is measured at the supposed maximum shear point, which should correspond to high momentum fluid being swept toward the wing surface. This situation should, of course, recur 1 full wavelength away ( $z_\lambda = 1$ ). Velocity deficits should occur where the stationary crossflow vortex sweeps flow away from the surface ( $z_\lambda = 0.5$ ). Figures 97 and 105 show that at  $x/c = 0.20$  the presence of the stationary crossflow vortices is already detectable with velocity variations exceeding  $\pm 0.20 \bar{u}_{s,e}$ . The expected velocity pattern is not evident for  $x/c = 0.20$  or 0.25 (figs. 97 and 98 and 105 and 106), but it emerges for  $x/c = 0.30$  (figs. 99 and 107). The periodicity of the velocity perturbations is clearly evident for  $0.35 \leq x/c \leq 0.55$  (figs. 100 to 104 and 108 to 112). For  $x/c = 0.35$ , 0.40, and 0.45 the excess velocities occur at the ends of the measurement zone and the deficits in the middle as expected. For  $x/c = 0.50$  and 0.55, the peak excess velocities are shifted in the  $+z_\lambda$  direction by approximately 2 mm. This shift seems to correspond to and is consistent with the observed shift in the maximum shear stress location as discussed previously.

The stationary crossflow disturbance velocities are quite small at the beginning of the measurement region ( $x/c = 0.20$ ). The disturbances grow progressively larger with increasing  $x/c$  to  $x/c = 0.50$  until they exceed  $\pm 0.20 \bar{u}_{s,e}$ . From  $x/c = 0.50$  to 0.55, the deficit velocities continue to increase in intensity, but the velocity excesses drop sharply. This decrease in excess velocity intensity seems surprising because the linear stability analysis presented earlier (fig. 20) shows that the stationary crossflow disturbance vortices should be amplified all the way to the pressure minimum at  $x/c = 0.71$ . For the present case ( $R_c = 2.37 \times 10^6$ ), the average transition line is determined by the flow visualization studies to be at approximately  $x/c = 0.58$ . (See fig. 51 and table 2.) It may be that between  $x/c = 0.50$  and 0.55 energy is being extracted from the stationary crossflow vortices and pumped into some other disturbance mode such as the secondary instability mode.

Figures 113 to 120 show contour plots of the temporal rms velocities of travelling waves with  $f = 100$  Hz for  $x/c = 0.20$  to 0.55. These velocities are again made nondimensional by dividing by the local boundary-layer edge velocity. It was indicated earlier that  $f = 100$  Hz corresponds to a peak in both the

measured and theoretical boundary-layer velocity spectra. The rms values measured are quite small with the maximum values being approximately 0.7 percent  $\bar{u}_{s,e}$ . The same contour levels are used for all the plots so that the disturbance levels can be readily compared. In the absence of complicating factors such as nonlinear interaction with stationary crossflow vortices or the presence of other travelling waves in the same frequency range, the rms velocity contours are expected to be flat and parallel to the wing surface.

The travelling wave intensities are essentially 0 for  $0.20 < x/c < 0.30$  (figs. 113 to 115). For  $x/c = 0.35$  and  $0.40$ , the peak disturbance amplitudes range from about 0.07 to 0.1 percent  $\bar{u}_{s,e}$  (figs. 116 and 117) and the contour lines are very roughly parallel to the wing surface, as anticipated for undistorted travelling crossflow waves. The disturbance velocity profiles shown earlier in figures 83 and 84 for these locations also have the expected single-lobed shapes. By  $x/c = 0.40$  (fig. 118) definite closed-contour shapes have developed. This corresponds to the development of double-lobed disturbance profiles (fig. 86). Between  $x/c = 0.45$  and  $0.50$  the travelling wave disturbance strength grows dramatically with the maximum rms intensity reaching 0.7 percent  $\bar{u}_{s,e}$ . The disturbance intensity also departs strongly from the ideal of equal distribution along the span to peak sharply near the center of the vortex wavelength. Perhaps significantly, figure 63 shows that near the middle of the measurement zone the streamwise velocity profile takes on a distinctly distorted S-shape. From  $x/c = 0.50$  to  $0.55$ , the strength of the travelling waves drops precipitously (fig. 120) and the maximum contour levels shift location. The sharp drop in travelling wave intensity occurs even though the streamwise mean velocity profiles continue to develop ever more distorted S-shaped profiles (fig. 64). This development is in the same region where the stationary crossflow vortices are observed to decrease in strength although the decrease is not as pronounced in the stationary vortex case. As mentioned previously, in the region from  $x/c = 0.50$  to  $0.55$  energy may be transferred to other high-frequency modes, which lead to laminar flow breakdown in the neighborhood of  $x/c = 0.58$ . The nonuniform nature of the rms disturbances along the span seems to indicate that the travelling waves detected may not be travelling crossflow vortices but some other travelling waves in the same frequency range (possibly Tollmien-Schlichting waves generated at the locations of the S-shaped mean velocity profiles).

## 5.7. Experimental and Theoretical Comparisons

In section 5.6, experimental velocity profiles and contours are shown along a single vortex track on the  $45^\circ$  swept wing for  $\alpha = -4^\circ$  at  $R_c = 2.37 \times 10^6$ . Both mean and disturbance velocities extracted from the mean data are given. In this section, those experimental data and other results obtained from them are compared with linear stability theory predictions supplied by Reed using her theoretical code (ref. 128). This theoretical code is used because it gives both growth rates and disturbance eigenfunction profiles, whereas the MARIA (ref. 45) and SALLY (ref. 44) codes employed earlier give only growth rates. The mean velocity profiles supplied to Reed and shown in section 5.7.1 were computed with the method of Kaups and Cebeci (ref. 126). As mentioned previously, theoretical data for  $\alpha = -5^\circ$  are used for this comparison because these data seem to yield a better match to the experimental data which are measured at a nominal angle of attack of  $-4^\circ$ . A small flow angularity in the UWT test section or a slight misalignment of the model could account for this difference.

### 5.7.1. Theoretical Disturbance Profiles

Figures 121 and 122 show the mean velocity profiles at the experimental measurement stations computed with the method of Kaups and Cebeci (ref. 126). The velocity components are given in a model-oriented coordinate system  $(x_m, y_m, z_m)$  with  $x_m$  perpendicular to the wing leading edge,  $y_m$  normal to the wing chord plane, and  $z_m$  parallel to the wing leading edge. (See appendix A.) Note that the spanwise velocities  $\bar{w}_m/\bar{u}_{t,e}$  are taken to be negative because a left-handed coordinate system was used so that the crossflow wave numbers are both positive. The experimental data presented in section 5.6 are shown from the perspective of the hot-wire measurement probe looking upstream. This constitutes essentially a conversion of the experimental coordinate frame into a left-handed system. Thus, the experimental and theoretical data can be compared directly. Stationary crossflow instability eigenfunctions are shown in figures 123 to 125 for each of the coordinate directions. The computations are for a fixed wavelength of  $\lambda = 7$  mm, which essentially matches the experimentally observed wavelength of  $\lambda/c = 0.004$  or  $\lambda = 7.3$  mm. The profiles are scaled to match the

experimentally determined maximum streamwise disturbance amplitudes at each measurement station. This scaling is permissible, of course, since linear stability theory predicts the actual disturbance intensity only to within a multiplicative constant. The phase relationships between the velocity components are not shown in the figures, although they are critically important to the determination of the spatial velocity field of the instability waves. Note also that in the model-oriented coordinate frame, the disturbance velocities in the chordwise direction  $u_m$  and the spanwise direction  $w_m$  are of the same order, whereas the normal velocity component  $v_m$  is an order of magnitude smaller.

For comparison with the experimental data, the velocity profiles given in figures 121 to 125 must be rotated about the  $Y$ -axis to two other coordinate reference frames. One of these frames, the streamwise frame  $(x_s, y_s, z_s)$  is oriented with  $x_s$  parallel to the free-stream velocity vector and  $y_s$  perpendicular to the wing chord plane, whereas in the other frame, the wave-oriented frame  $(x_w, y_w, z_w)$ ,  $x_w$  is along the vortex axis and  $z_w$  is parallel to the wave-number vector. Of course,  $y_m$ ,  $y_s$ , and  $y_w$  are all parallel. The experimental measurements are made in the streamwise coordinate frame  $(u_s, y_s, z_s)$ . The theoretical vortex flow pattern in the wave-oriented frame  $(x_w, y_w, z_w)$  is superposed onto the experimental data plots. The relationships between these coordinate frames are given in appendix A.

The mean flow velocity components in the  $(x_s, y_s, z_s)$  frame are shown in figures 126 and 127. In this coordinate frame (appendix A), the cross-stream mean velocities  $\bar{w}_s$  are considerably smaller than the streamwise velocities  $\bar{u}_s$ . Likewise the cross-stream disturbance velocities  $w_s$  are much smaller than the streamwise-disturbance velocities  $u_s$ . (See figs. 128 and 129.) Figures 130 to 133 show the mean and disturbance velocity components in the wave-oriented coordinate frame. Here both the mean and disturbance velocity components in the  $z_w$  direction are an order of magnitude smaller than the respective velocities components along the vortex axis. In this frame,  $w_w$  is the same order of magnitude as  $v_w = v_m$ . Thus, in both the wave-oriented and streamwise-oriented coordinate frames the velocities along the  $X$ -axes are much larger than the velocity components in the other two directions.

The nature of the disturbance vortex flow is illustrated in figures 134 to 136. A vector plot of  $(v_w, w_w)$ , across a single vortex wavelength is shown in figure 134 in the wave-oriented coordinate frame. The vectors are the projections of the disturbance velocity vectors onto the  $y_w$ - $z_w$  plane. The disturbance is seen to consist of a pair of counterrotating vortices within a single wavelength. The vortex cells are skewed so that a central counterclockwise rotating vortex is bordered on each side by a portion of the alternate clockwise rotating vortices. In figure 135 the mean plus disturbance velocity vectors,  $(v_w, w_w + \bar{w}_w)$  are plotted over a single wavelength. Here the mean normal velocity  $\bar{v}_w$  which is quite small has been neglected. Note that the mean velocity  $\bar{w}_w$  (fig. 131) completely dominates the vector field masking the presence of any disturbance vorticity. The presence of the disturbance vorticity can be illustrated by arbitrarily scaling the  $v_w$  velocities by a factor of 100. This is shown in figure 136 where it is apparent that the mean plus disturbance flows combine to produce a single counterclockwise rotating vortex per wavelength. That is, the total flow consisting of disturbances superposed on a base flow contains a layer of corotating vortices.

### 5.7.2. Disturbance Profile Comparisons

Experimental stationary crossflow disturbance profiles (from  $\bar{u}_s - \bar{u}_{s,avg}$ ) are presented with the linear-theory eigenfunction magnitudes in figures 137 to 144. In each case the streamwise disturbance velocity profiles are shown. Similar results are found by using the experimental profiles determined from  $\bar{u}_s - \bar{u}_{s,avg}$  (figs. 73 to 80) but these are not shown. The experimental profiles are determined by taking the spatial rms of the individual profiles (figs. 65 to 72) across the stationary vortex. This procedure is the spatial analog for a stationary wave of taking the temporal rms of a travelling wave. All profiles are plotted on the same abscissa scale (made nondimensional by reference to the local boundary-layer edge velocity) for easy visual comparison of the disturbance growth with distance along the wing. Because the linear stability theory gives the disturbance velocities only to within a multiplicative constant, the theoretical eigenfunctions are scaled to match the maximum experimental disturbance intensities. Note that the theoretical eigenfunctions have only a single lobe. (See, for example, fig. 128.)

At  $x/c = 0.20$  (fig. 137), the theoretical and experimental profiles are of similar shape in the region of the maximum amplitude near  $y = 1$  mm, but the two curves diverge in the near-surface region and in the outer flow. As mentioned previously, the measured profiles at this location are thought to contain experimental errors that are rectified for the remaining measurements. The near-surface results are affected by a lint-contaminated surface and the outer flow measurements are affected by tunnel-temperature drift. For  $x/c = 0.25, 0.30, 0.35$ , and  $0.40$  (figs. 138 to 141), the experimental and theoretical profiles are of similar single-lobed shapes. However, the point of maximum disturbance intensity is slightly higher in the boundary layer for the theoretical eigenfunctions than for the experimental profiles.

For  $x/c = 0.45$  and beyond (figs. 142 to 144), the experimental profiles take on double-lobed shapes that contrast with the single-lobed theoretical eigenfunctions. The point of maximum disturbance strength for the theoretical profiles lies between the two maxima of the experimental profiles. Recall from the earlier discussion that for  $x/c = 0.45$  and beyond, the local experimental disturbance profiles take on crossover shapes that are not anticipated from the linear theory. This is evident in the local profile plots of figures 70 to 72 and 78 to 80 as well as the disturbance velocity contour plots of figures 102 to 104 and 110 to 112. Figures 94 to 96 show that the mean streamwise-velocity contours for  $0.60 < \bar{u}_s/\bar{u}_{s,e} < 0.90$  rise sharply from the model surface and begin to roll over. This rollover is due to the presence of the stationary crossflow vortex and becomes evident in section 5.7.3.

Thus, there is general agreement between the shapes of the experimental disturbance velocity profiles and the theoretical eigenfunctions up to about  $x/c = 0.40$  where the rms intensity of the stationary vortices is about 7 percent of  $\bar{u}_s$ . But for  $x/c > 0.45$ , the presence of the stationary crossflow vortices distorts the experimental disturbance profiles into double-lobed shapes not predicted by the linear theory. This does not necessarily mean that nonlinear effects are present, even though the stationary disturbance intensities ( $\pm 20$  percent  $\bar{u}_s$  at  $x/c = 0.50$ ) are well beyond the small perturbation limits assumed in the linear theory. In fact, the observed effects may simply be because of flow history. That is, the strong stationary crossflow vortices continually lift low-speed fluid up from the surface and push high-speed

fluid downward so that the flow wraps around the vortex axis. More is shown on this point in section 5.7.3.

### 5.7.3. Velocity Contour Plots and Vector Plots

Figures 145 to 152 show theoretical velocity vectors superposed on the experimental streamwise velocity-contour plots. Theoretical velocity vectors are superposed on the stationary crossflow disturbance velocity contour plots in figures 153 to 160. The velocity vectors in these figures have  $v_w$  scaled up by a factor of 100 (as in fig. 136) so as to illustrate the presence of the stationary crossflow vortex.

Recall that the experimental procedure outlined in section 5.6 called for the experimental profile measurements to be made at various spanwise locations across a single stationary crossflow vortex. To accomplish this a single dark vortex track is traced on the model with a felt-tipped pen following a flow visualization run. For each fractional chord location, the hot-wire probe is manually centered above this trace. After the initial manual setup, the traverse motion is computer controlled in both normal and spanwise steps. The dark vortex track in the flow visualization study corresponds to high-shear path under the stationary crossflow vortex pattern. Thus, this procedure should assure that the measurement locations move in steps from a high-shear region through minimum shear and back to high shear again. However, the experimental situation is not quite this simple. The entire flow visualization pattern is found to be highly repeatable even months apart. The pattern repeats in detail down to the jagged transition line and the individual vortex tracks. But, the vortex wavelength is only  $\lambda = 7.3$  mm so that small errors in the manual alignment of the traverse system or even very small shifts in the location of the vortex track can impact the relative location of the maximum shear. Examination of the streamwise-velocity plots in figures 89 to 96 shows that the maximum shear point (judged by how closely the velocity contours are bunched) is not always located at  $z_\lambda = 0$ . To account for this effect, the maximum shear point in both the experimental and theoretical flow patterns is determined. The phase of the theoretical flow pattern is then shifted to align the maximum shear points in the theoretical and experimental flows.

Examination of figures 145 to 152 shows that the variations of the mean streamwise-velocity contours

over the vortex wavelength can be anticipated from the vector plots. The streamwise-velocity contours spread out when the velocity vectors are directed away from the surface and they crowd together whenever the velocity vectors point toward the surface. In particular, near the surface, the streamwise-velocity contours approach each other to produce the high surface shear (i.e., large  $dU/dy$ ) when the velocity vectors are directed downward. Low surface shear (i.e., small  $dU/dy$ ) results when the velocity vectors are directed upward and the contour lines spread out.

Figures 153 to 160 show that the qualitative features of the streamwise-disturbance velocity contour plots can also be anticipated from the velocity vector field. A plume of low-speed fluid is observed in regions where the velocity vectors are directed sharply outward from the model surface. Concentrations of high-speed fluid near the model surface are found in regions where the velocity vectors are directed sharply toward the surface. Furthermore, both the low- and high-speed regions are skewed in a counterclockwise pattern consistent with the theoretical velocity vector pattern. Note that flow history effects are not expected to produce qualitative differences between the contour and vector plots as found in the disturbance profile and eigenfunction comparisons.

Thus, when the maximum shear points of the experimental and theoretical data are matched, the qualitative features of the flow variables are consistent with expectations gleaned from the velocity vector field. In particular, both the streamwise-velocity contours and the stationary crossflow disturbance velocity contours distort in patterns consistent with the presence of a single counterclockwise rotating vortex. This pattern of qualitative agreement between the theoretical and experimental flow fields persists throughout the measurement region from  $x/c = 0.20$  to  $0.55$  in contrast to the disturbance profile and eigenfunction comparisons that diverge for  $x/c > 0.45$ .

#### 5.7.4. Wavelength Comparison

Tables 3 to 5 show the results of crossflow stability calculations performed by using the SALLY code (ref. 44) subject to the constraint of constant vortex wavelength. As mentioned previously, the naphthalene flow visualization photographs show constant crossflow vortex wavelengths over the entire region for a given Reynolds number. The calculations are

begun at the neutral point and continued to the average transition location as indicated in table 2. Tables 3 to 5 correspond to chord Reynolds numbers of  $2.37 \times 10^6$ ,  $2.73 \times 10^6$ , and  $3.73 \times 10^6$ , respectively. For all three test conditions the most amplified frequency is non-zero. The maximum amplified frequency increases with Reynolds number from  $f_{cf,max} = 100$  Hz at  $R_c = 2.37 \times 10^6$  to  $f_{cf,max} = 300$  Hz at the maximum chord Reynolds number. The maximum  $N$ -factor at transition is found to be about 9.1 at the lower Reynolds number and about 8.5 for the higher Reynolds numbers. These results agree with earlier calibrations of the crossflow stability problem as indicated by Dagenhart (ref. 45). Surface and streamline curvature effects have not been considered in this analysis, but this may not be significant since both the surface and streamline curvatures are small over most of the unstable flow region. The wavelength of maximum stationary crossflow vortex amplification is plotted in figure 161 where it is compared with the experimental observations given in table 2. The experimental and theoretical curves have similar trends with wavelength decreasing as chord Reynolds number increases, but the theoretically predicted wavelengths are approximately 25 percent larger than those observed experimentally. This discrepancy may arise because the crossflow vortex pattern (having a constant wavelength over the entire wing) is established well forward on the wing where the boundary layer is relatively thin. Swept flat-plate experiments generally have shown closer agreement between the theoretically predicted wavelength and the observed wavelength than the predicted disturbance as opposed to swept-wing studies. Perhaps the blunter nose of the swept wing is an important factor in establishing the smaller wavelength.

#### 5.7.5. Growth-Rate Comparison

The stationary crossflow vortex growth rate is estimated by numerically differentiating the amplitude data shown in section 5.7.2. There are several possible choices for the disturbance amplitude function such as

$$A_1(x) = u_{s,max}(x) \quad (7)$$

$$A_2(x) = \frac{1}{y_{max}} \int_0^{y_{max}} u_s(x,y) dy \quad (8)$$

or

$$A_3(x) = \sqrt{\frac{1}{y_{\max}} \int_0^{y_{\max}} [u_s(x, y)]^2 dy} \quad (9)$$

The simplest choice is given in equation (7) where the amplitude function is taken as the maximum of the streamwise velocity disturbance profiles as shown in figures 137 to 144. The second choice given in equation (8) is to use the average of the streamwise disturbance velocity over the thickness of the boundary layer to represent the disturbance amplitude. A third possibility is to use the rms value of the disturbance profile as in equation (9). Then the growth rate (made dimensionless by referring to the chord length) is computed as

$$\sigma_i = \frac{1}{A_i} \frac{dA_i}{d(x/c)} \quad (10)$$

where  $i$  is 1, 2, or 3. If values from the smooth theoretical eigenfunctions shown in figures 137 to 144 are substituted in equations (7) to (9) the resulting growth rates are essentially the same irrespective of the choice of the amplitude function.

Figure 162 shows the various growth-rate estimates obtained from the experimental disturbance profiles and theoretical predictions from the MARIA code (ref. 45) and from Reed's computations (ref. 128). The experimental growth rates are computed from both the profiles shown in figures 137 to 144 and from similar data determined from  $\bar{u}_s - \bar{u}_{s, \text{ref}}$ . The theoretical growth rates peak ahead of the first measurement station at  $x/c = 0.20$  and decrease approximately linearly over the measurement zone from  $0.20 \leq x/c \leq 0.55$ , with the two codes predicting slightly different values. In contrast, the several experimental growth-rate curves have a distinct up and down pattern over the measurement range and the experimental growth rates are all at or below the level of the theoretical estimates. This may be because of nonlinear saturation of the stationary crossflow vortices. The several experimental growth-rate curves differ considerably at each measurement station. The variations in growth rate estimated with the various amplitude functions appear to be a measure of the roughness of the experimental profiles since the smooth theoretical profiles yield

essentially the same growth-rate estimate, no matter which amplitude function is employed.

## 6. Conclusions

An experimental configuration is designed and constructed to permit the examination of a whole range of problems associated with the development, growth, and breakdown of crossflow vortices in a swept-wing flow. Careful control of the model and wind tunnel geometries creates a benchmark experimental setup for the study of swept-wing flows. The range of problems that can be addressed with this experimental configuration include the investigation of crossflow vortex growth and development in a crossflow-dominated flow, the interaction of crossflow vortices with Tollmien-Schlichting waves, surface-roughness effects on crossflow disturbance receptivity, and crossflow vortex breakdown mechanisms.

In the present investigation, we focus largely on the first of these possible research problems. In particular, a small negative angle of attack is selected so that the resulting favorable (i.e., negative) pressure gradient eliminates primary Tollmien-Schlichting waves while strongly amplifying the crossflow vortices. The bulk of the measurements taken at a chord Reynolds number  $R_c$  of  $2.37 \times 10^6$  consists of extensive hot-wire probe surveys across a single stationary vortex track. Both steady and narrow-band-pass travelling wave disturbance velocities are determined in steps across the vortex track at fractional chord locations  $x/c$  ranging from just downstream of the neutral stability point to just ahead of the transition location. The data are presented as local velocity profile plots and as isoline contour plots across the stationary vortex. The experimental results are compared with theoretical eigenfunction shapes, growth rates, and vector velocity plots.

The following conclusions are drawn:

1. Transition locations are determined by using surface-mounted hot-film gauges, boundary-layer hot-wire probes, and flow visualization in the range from  $x/c = 0.80$  at the minimum test chord Reynolds number  $R_c = 1.932 \times 10^6$  to  $x/c = 0.30$  at the maximum chord Reynolds number  $R_c = 3.271 \times 10^6$ . The local Reynolds number at transition varies across the range

from  $1.14 \times 10^6$  to  $1.54 \times 10^6$ , which indicates that some roughness effects may be important.

2. The maximum theoretical crossflow  $N$ -factors for travelling crossflow vortices at transition range from 8.5 to 9.1 in agreement with previous calibrations of the linear stability method. However, the corresponding  $N$ -factors for the dominant stationary crossflow vortices are in the range from 6.4 to 6.8.

3. The boundary-layer hot-wire spectra are observed to contain mostly low-frequency oscillations at the lower test Reynolds numbers. With increasing Reynolds number, two bands of amplified frequencies are observed. The first of these bands is near the blade-pass frequency and within the range of amplified travelling crossflow waves predicted by the linear theory. The second amplified-frequency band falls at approximately twice the blade-pass frequency and at the upper frequency limit of the band of amplified travelling crossflow waves. The travelling waves in the first frequency band are thought not to be travelling crossflow waves, but perhaps Tollmien-Schlichting waves generated locally in the highly distorted mean flow.

4. The measured mean velocity profiles show slight variations across the stationary vortex track even at the first measurement station at  $x/c = 0.20$ . The variations across the vortex grow with downstream distance until distinct S-shaped profiles are observed near the middle of the measurement span at  $x/c = 0.45$ . By  $x/c = 0.55$ , the measured profiles all the way across the stationary vortex have taken on highly distorted S-shapes. The mean streamwise-velocity contours are shown to be approximately flat and parallel to the model surface at  $x/c = 0.20$ , but by  $x/c = 0.50$  to  $0.55$  the velocity contours in the outer portion of the boundary layer actually begin to roll over under the continuing action of the stationary crossflow vortex.

5. The local stationary vortex disturbance profiles have single-lobed shapes with either purely excess or deficit velocities at the forward measurement stations as expected from theoretical considerations. But, for  $x/c \geq 0.45$ , the local stationary disturbance profiles take on distinct crossover shapes not predicted by linear theory. The maximum stationary vortex disturbance intensities reach levels of 20 percent of the local boundary-layer edge velocity just before transition.

The stationary crossflow vortex disturbances have little influence on the velocity contour pattern at the forward measurement stations, but by  $x/c = 0.30$  a distinct pattern forms with a plume of low-velocity fluid rising from the model surface near the middle of the measurement span and concentrations of high-velocity fluid near the wing surface at the ends of the measurement span. For  $x/c = 0.50$  and  $0.55$ , the excess and deficit velocities reach maximum intensities of 20 percent of the local boundary-layer edge velocity, but the established flow pattern is shifted approximately one fourth of the wavelength toward the wing root. This shift is thought to be caused by either a slight misalignment of the traverse mechanism or a small shift in whole stationary crossflow vortex pattern.

6. The travelling wave rms profiles at the forward locations have single-lobed shapes as expected from linear theory, but develop double-lobed shapes for  $x/c \geq 0.45$ , which are not predicted by the linear theory. The travelling wave rms disturbance intensity peaks at 0.7 percent of the local boundary-layer edge velocity which is more than an order of magnitude smaller than the strength of the stationary crossflow vortex. The travelling wave disturbances are found to be very weak with no significant pattern evident until  $x/c = 0.45$  where closed-contour isolines appear. These closed-contour isolines differ from the flat contours expected from linear stability theory. The travelling wave disturbance intensity peaks strongly near the middle of the measurement span at  $x/c = 0.50$  and then abruptly decreases. The travelling wave disturbance energy may be transferred to some other instability mechanism as the transition location at  $x/c = 0.58$  is approached.

7. The experimental streamwise disturbance velocity functions are found to have single-lobed shapes very similar to those predicted by linear stability theory for  $0.20 \leq x/c \leq 0.40$ . The maxima of the theoretical eigenfunctions are located slightly higher in the boundary layer than are the experimental maxima. For  $x/c \geq 0.45$  the experimental disturbance functions take on double-lobed shapes. The theoretical eigenfunction maximum is located at a height between the two experimental maxima. The root-mean-square disturbance strength at the breakpoint between the single- and double-lobed experimental profiles is about 7 percent of the local boundary-layer edge velocity.



8. Qualitative agreement with the experimentally observed flow features is obtained throughout the measurement range when theoretical velocity vector plots (from linear stability theory) are superposed onto the experimental contour plots.

9. A fixed wavelength stationary crossflow vortex pattern is observed for all flow visualization conditions. No vortex dropouts or other adjustments to the vortex spacing are observed in the flow visualization region which extends from approximately  $x/c = 0.15$  to 0.80.

10. The wavelengths observed in the flow visualization studies are found to be approximately 20 percent smaller than the wavelengths predicted by linear theory. This is probably because of the fact that the fixed stationary vortex wavelength is established well forward on the model where the boundary layer is still relatively thin. Perhaps the swept-wing nose radius is an important factor in establishing the smaller vortex wavelengths since swept flat-plate experiments generally have closer agreement between theoretical and observed wavelengths.

11. Three different measures of the experimental growth rate are found to yield similar trends which dif-

fer from the theoretically predicted growth rate. Non-linear saturation of the vortex strength appears to have occurred. The measured growth rates are found to be at or below the values predicted by linear theory. Also, the experimental growth rate alternately increases and decreases over the measurement range, whereas the linear theory predicts an approximately linear decrease with downstream distance over the measurement space.

The present investigation contributes to an improved understanding of the physics of the crossflow instability in a swept-wing flow. The stationary crossflow vortices which are highly sensitive to small-scale surface roughness effects dominate the disturbance flow field and the transition process even though travelling waves are more amplified according to the linear stability theory. The features of the observed flow field evolve from qualitative agreement with expectations from the linear stability theory for the forward measurement stations to highly distorted profiles with marked differences between the observations and the theoretical predictions. A benchmark experimental data set for the crossflow instability is generated for comparison with results from advanced computational codes currently under development.

## Appendix A

### Relationships Between Coordinate Systems

Figure A1 shows a swept wing in a right-handed Cartesian coordinate system  $(x_m, y_m, z_m)$ , where  $x_m$  is taken perpendicular to the wing leading edge,  $y_m$  is perpendicular to the wing chord plane, and  $z_m$  is parallel to the wing leading edge. A positive wing sweep angle  $\Lambda$  is shown and the flow is from left to right. The boundary-layer edge velocity is given by

$$U_{t,e} = \sqrt{u_{m,e}^2 + w_{m,e}^2} \quad (A1)$$

where  $u_m(y) \geq 0$  and  $w_m(y) \geq 0$  for attached flow. The angle of the boundary-layer edge velocity with respect to the  $Z_m$ -axis is obtained as

$$\epsilon = \tan^{-1} \left( \frac{u_{m,e}}{w_{m,e}} \right) \quad (A2)$$

and  $0 \leq \epsilon \leq \pi/2$ . The total wave number is given by

$$\alpha_T = \sqrt{\alpha_r^2 + \beta_r^2} \quad (A3)$$

where  $\alpha_r$  is the wave number in the  $x_m$  direction and  $\beta_r$  is the wave number in the  $z_m$  direction. The wave angle of the disturbance is then

$$\theta = \tan^{-1} \left( \frac{\alpha_r}{\beta_r} \right) \quad (A4)$$

where  $\theta > \pi/2$  for crossflow disturbances. And finally, the wave orientation angle with respect to the local boundary-layer edge velocity is obtained as

$$\psi = \theta - \epsilon \quad (A5)$$

The model-oriented coordinates just described are obtained by rotation about the  $Y_s$ -axis in the stream-wise coordinate system  $(x_s, y_s, z_s)$  by the wing sweep angle  $\Lambda$ . Here  $x_s$  is parallel to the free-stream velocity vector. The relationship between these two coordinate frames is given as

$$\begin{pmatrix} z_m \\ x_m \end{pmatrix} = \begin{bmatrix} \cos \Lambda & \sin \Lambda \\ -\sin \Lambda & \cos \Lambda \end{bmatrix} \begin{pmatrix} z_s \\ x_s \end{pmatrix} \quad (A6)$$

or, inverting, as

$$\begin{pmatrix} z_s \\ x_s \end{pmatrix} = \begin{bmatrix} \cos \Lambda & -\sin \Lambda \\ \sin \Lambda & \cos \Lambda \end{bmatrix} \begin{pmatrix} z_m \\ x_m \end{pmatrix} \quad (A7)$$

And, the relationship between the wave-oriented coordinate system  $(x_w, y_w, z_w)$  and the model coordinates is obtained as a rotation by the angle  $\theta$  about the  $Y_m$ -axis as

$$\begin{pmatrix} z_w \\ x_w \end{pmatrix} = \begin{bmatrix} \cos \Lambda & \sin \Lambda \\ -\sin \Lambda & \cos \Lambda \end{bmatrix} \begin{pmatrix} z_m \\ x_m \end{pmatrix} \quad (A8)$$

Reed's left-handed coordinate system is shown in figure A2 where the  $Z$ -axes are all directed in the opposite directions from those in the right-handed systems used in figure A1. Equations (A1) to (A8) still apply, but all the rotations are taken in the opposite direction. In particular, the wing sweep angle  $\Lambda$  is now negative. Also, as a consequence of this shift  $w_m(y) \leq 0$  and  $u_m(y) \geq 0$  for attached flow. The angle of the boundary-layer edge velocity vector with respect to the  $Z_m$ -axis  $\epsilon$  is now greater than  $\pi/2$  and the crossflow wave orientation angle  $\theta$  is less than  $\pi/2$ .

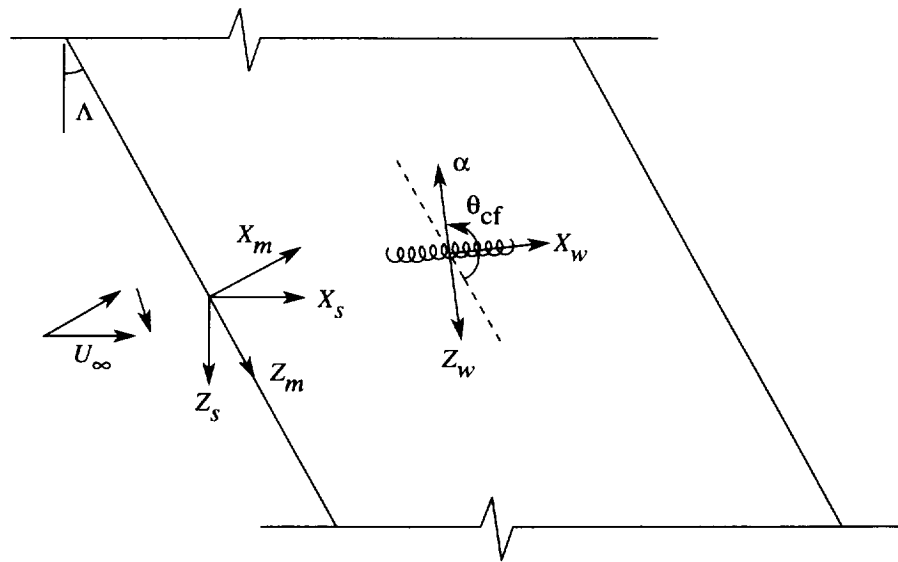


Figure A1. Coordinate system relationships for swept wing.

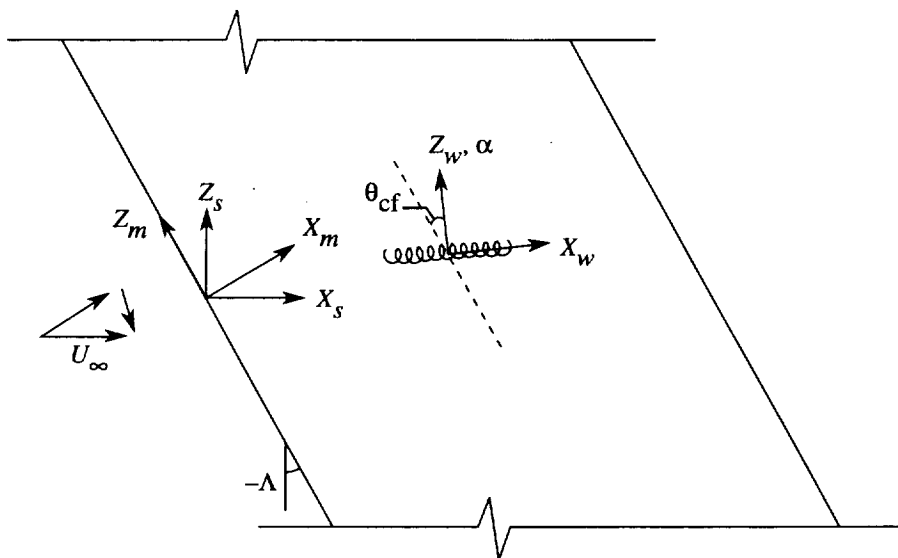


Figure A2. Left-handed coordinate systems for swept wing.

## Appendix B

### Hot-Wire Signal Interpretation Procedure

The free-stream and boundary-layer velocity measurements are performed by using Dantec 55M01 constant-temperature anemometers equipped with 55M10 CTA standard bridges with bridge resistance ratios of 1:20. The hot wires are Dantec type 55P15 miniature boundary-layer probes having 5-m platinum-plated tungsten wires which are 1.25 mm in length. The probe tines are 8 mm long and are offset 3 mm from the probe axis. Standard 4-mm-diameter probe supports are used. The three-dimensional traverse system (described in section 3) is used to support and move the probes through the flow field. The traverse system is mounted external to the test section with only the probe-support sting extending through a sliding opening in the test section wall. The sting consists of a composite element and an aluminum strut. The composite element is 5 mm thick, 0.425 m long, and its chord tapers from 64 mm at the base to 50 mm at the tip. The aluminum strut dimensions are 13 mm by 76 mm by 0.324 m. Both the steady state and fluctuating hot-wire signals are sampled simultaneously with the 16-channel MASSCOMP 12-bit A/D converter which can sample at an aggregate rate of up to 1 MHz. The fluctuating voltage signal is narrow-band-pass filtered using a Spectral Dynamics SD122 equipped with a 4-pole Butterworth tracking filter with 10-Hz passband.

The voltage response of a constant-temperature hot-wire anemometer can be assumed to have the form

$$E = F(\rho, U, T_0) \quad (B1)$$

where  $\rho$  is the ambient air density,  $U$  is the velocity,  $T_0$  is the total temperature, and  $E$  is the anemometer voltage response. Differentiating equation (B1) gives

$$dE = \frac{dF}{d\rho} d\rho + \frac{dF}{dU} dU + \frac{dF}{dT_0} dT_0 \quad (B2)$$

Thus, a small voltage change is dependent on small changes in the density, velocity, and total temperature.

To reduce the complexity of the functional relationship given in equation (B1) can be accomplished by eliminating or at least minimizing the variations in  $\rho$  and  $T_0$  so that the anemometer response depends solely on the velocity. The UWT has no heat exchanger system to maintain a desired tunnel temperature. The tunnel total temperature increases with test time until an equilibrium condition is achieved. For the present experiment, the tunnel flow is preheated by operating the tunnel at the expected test condition for 45 to 60 min before hot-wire probe calibration. This provides sufficient time for the flow temperature to reach its equilibrium value. The air density depends on two factors—atmospheric pressure and flow temperature. To minimize atmospheric pressure effects, the hot-wire calibrations are conducted before each data-acquisition run. These steps ensure that  $dp$  and  $dT_0$  are nearly zero and can be neglected in equation (B2). Then, equation (B1) can be simplified to

$$E = f(U) \quad (B3)$$

The hot-wire probes are calibrated in the UWT flow by varying the free-stream velocity in steps across the range of velocities expected during the experiment. Typically 12 velocities are used for each calibration. Equation (B3) is not actually used for probe calibration; instead,

$$U = g(E) \quad (B4)$$

is used where  $g(E)$  is a fourth-order least-squares curve fit to the calibration data. Then,  $f(U)$  is determined as

$$E = f(U) = g^{-1}(E) \quad (B5)$$

Differentiating equation (B3) gives

$$dE = \frac{df}{dU} dU = f' dU \quad (B6)$$

Now we assume that

$$e = E + e' \quad (B7)$$

and

$$u = U + u' \quad (B8)$$

where  $e$  is made up of a steady (or DC) voltage  $E$  and a small fluctuating voltage  $e'$ , and  $u$  consists of a steady velocity  $U$  and a small fluctuating velocity  $u'$ . Substituting equations (B7) and (B8) into equation (B3) and expanding in a Taylor series while neglecting higher order terms (since they are assumed to be small) give

$$E + e' = f(U + u') = (U) + f'(U)u' \quad (\text{B9})$$

Subtracting equation (B3) from equation (B9) yields

$$e = f'(U)u' \quad (\text{B10})$$

or solving for  $u'$  gives

$$u' = \frac{e'}{f'(U)} \quad (\text{B11})$$

Since  $u'$  and  $e'$  are small deviations from the steady values of  $U$  and  $E$ , we can apply equation (B11) not just at a single point in time but for  $u'(t)$  and  $e'(t)$  as functions of time while holding  $f'(U)$  constant and then take the root-mean-square of these functions to get

$$u'_{\text{rms}} = \frac{e'_{\text{rms}}}{f'(U)} \quad (\text{B12})$$

which gives the rms velocity fluctuations as a function of the measured rms voltage output from the hot-wire anemometer circuit.

For boundary-layer velocity profile measurements, we desire the ratio of local velocity to the boundary-layer edge velocity. Two hot-wire probes are used for this measurement—one probe located in the boundary layer and the other in the external flow. Both probes are mounted on the traverse strut and moved together as the boundary-layer velocity profile is measured. The probe in the external flow is not located at the edge of the boundary layer but is, in fact, located approximately 15 cm from the boundary-layer probe. During the traverse, the two hot-wire probes move only about 4 mm. Over this distance the external flow probe detects only negligible variations in the velocity, but the boundary-layer probe sees the velocity decrease from the edge value to near zero as the surface is approached. The boundary-layer velocity ratio cannot be obtained directly as the ratio  $U_2/U_1$  because  $U_1$  is not at the boundary-layer edge. However, the desired velocity ratio is given by

$$\frac{U_2}{U_{s,e}} = \frac{U_2/U_1}{(U_2/U_1)_{y,\text{max}}} \quad (\text{B13})$$

where  $U/U_{s,e}$  is the boundary-layer velocity ratio,  $U_1$  is the external flow velocity, and  $U_2$  is the boundary-layer velocity. By scaling the measured velocity ratio  $U_2/U_1$  in equation (B13) by the velocity ratio observed at the maximum distance from the surface we normalize the profile to unity at the boundary-layer edge. This accounts for the fact that the external-flow hot-wire probe is not at the boundary-layer edge.

## Appendix C

### Error Analysis

Kline and McClintock (ref. 130) discuss the effects of experimental measurement errors on computed data in various experimental situations. They discuss both single- and multiple-sample experiments, but their primary emphasis is on describing uncertainties in single-sample experiments. For multiple-sample experiments, statistical methods can be used to establish both the mean values and variations from the mean. However, in single-sample experiments, errors in the results computed from experimentally measured quantities can only be estimated. Kline and McClintock showed that the uncertainty  $\Delta R$  for the computed result

$$R = R(v_1, v_2, v_3, \dots, v_n) \quad (C1)$$

can be obtained as

$$\Delta R = \sqrt{\sum_{i=1}^n \left( \frac{\partial R}{\partial v_i} w_i \right)^2} \quad (C2)$$

where  $v_i$  represents the measured quantities used in the computation of  $R$  and  $w_i$  represents the expected error ranges for the measured quantities.

In the present experiment, the range of measured quantities is limited to static and dynamic pressures, pressure differentials, flow temperature, and hot-wire anemometer voltages. From these measured quantities the free-stream velocity, the surface pressure coefficients, boundary-layer and edge velocities, and, most importantly, the boundary-layer velocity ratios are determined. The free-stream velocity can be obtained from the incompressible Bernoulli equation and the perfect-gas equation of state as

$$U_\infty = \frac{2q_\infty RT_\infty}{p_\infty} \quad (C3)$$

where  $U_\infty$  is the free-stream velocity and the measured quantities are the dynamic pressure  $q_\infty$ , the static pressure  $p_\infty$ , and the static temperature  $T_\infty$ , and

$R$  is the gas constant from the equation of state. The surface pressure coefficient is given by

$$C_p = \frac{p - p_\infty}{q_\infty} = \frac{p_D}{q_\infty} \quad (C4)$$

where  $C_p$  is the pressure coefficient and  $p$  is the local surface pressure. The boundary-layer and edge velocities are obtained from the hot-wire calibration functions

$$U = g(E) \quad (C5)$$

whereas

$$f(U) = g^{-1}(E)$$

is the inverse of the hot-wire calibration function.

Equation (C2) can be applied to equations (C3) to (C5) to obtain uncertainty estimates for  $U_\infty$ ,  $C_p$ , and  $U$  as

$$\frac{\Delta U_\infty}{U_\infty} = \sqrt{\left( \frac{w_{q_\infty}}{2q_\infty} \right)^2 + \left( \frac{w_{T_\infty}}{2T_\infty} \right)^2 + \left( \frac{w_{p_\infty}}{2p_\infty} \right)^2} \quad (C6)$$

$$\frac{\Delta C_p}{C_p} = \sqrt{\left( \frac{w_{p_D}}{2p_D} \right)^2 + \left( \frac{w_{q_\infty}}{2q_\infty} \right)^2} \quad (C7)$$

$$\frac{\Delta U}{U} = \sqrt{\left( \frac{w_E}{U(df/dU)} \right)^2} \quad (C8)$$

Equations (C6) and (C7) can be straightforwardly applied because estimates of the uncertainties involved are easily obtained. However, equation (C8) is much more difficult to apply since an estimate of the uncertainty in the hot-wire anemometer voltage is much more difficult to ascertain. This difficulty can be overcome by recognizing that in the present experiment some of the hot-wire measurements can be considered as multiple-sample measurements, whereas other measurements must be regarded as single-sample measurements.

The most important hot-wire measurements involve determining the boundary-layer velocity ratio as

$$U_R = \frac{U}{U_{s,e}} = \frac{U_2/U_1}{(U_2/U_1)_{y,\max}} \quad (C9)$$

where  $U_2$  is the velocity indicated by the hot-wire probe inside the boundary layer and  $U_1$  is the velocity indicated in the outer flow. The quantities  $U_2$  and  $U_2/U_1$  must be regarded as single-sample measurements even though  $U_1$  and  $U_2$  are evaluated as time averages of repeated measurements taken at a frequency  $f_s$  of 1 kHz over a 30-sec interval. On the other hand,  $U_1$  and  $(U_2/U_1)_{y,\max}$  can be regarded as multiple-sample measurements and analyzed statistically since these two variables are measured repeatedly during a hot-wire survey of the boundary layer.

According to the instrument handbook the uncertainty in the measurement of  $q_\infty$  and  $p_\infty$  in equation (C6) is 0.08 percent of reading, but  $q_\infty$  is observed to oscillate due to a very low-frequency modulation of the fan controller at about 1 percent of reading. Thus, the expected uncertainties for  $q_\infty$  and  $p_\infty$  are taken as

$$\Delta q_\infty = 0.02 \text{ torr} \quad (q_\infty = 2.0 \text{ torr})$$

and

$$\Delta p_\infty = 0.6 \text{ torr} \quad (p_\infty = 720.0 \text{ torr})$$

Also, the thermocouple is found to be in error by

$$\Delta T_\infty = -1.5 \text{ K} \quad (T_\infty = 309.0 \text{ K})$$

Substituting these uncertainties into equation (C6) gives

$$\frac{\Delta U_\infty}{U_\infty} = 0.006$$

If the uncertainty in  $C_p$  is evaluated at the maximum pressure point, then substituting

$$w_{p_D} = 0.02 \text{ torr} \quad (p_D = q_\infty = 2.0 \text{ torr})$$

into equation (C7) yields

$$\frac{\Delta C_p}{C_p} = 0.014$$

The uncertainties in  $U_1$  and  $(U_2/U_1)_{y,\max}$  are evaluated statistically at each fractional chord measurement station. The standard deviation for  $U_1$  is found to be between 1 and 3 percent of  $U_{s,e}$  for all measurement locations except  $x/c = 0.55$ , where it reached 5.56 percent. More importantly, the standard deviation in the velocity ratio is much smaller ranging from 0.15 to 1.38 percent.

An alternate method to estimate the error in the boundary-layer velocity ratio can be derived by using King's law as the calibration function for a constant-temperature hot wire

$$E^2 = A + BU^n \quad (C10)$$

where we take  $n = 1/2$ . Or, solving for  $U$  gives

$$U = \left( \frac{E^2 - A}{B} \right)^2 \quad (C11)$$

Strictly speaking, the calibration coefficients depend on the temperatures of the hot wire  $T_w$  and the flow  $T_f$  as

$$A = A_1(T_w - T_f) \quad (C12)$$

and

$$B = B_1(T_w - T_f) \quad (C13)$$

Now, suppose that the flow temperature changes from the calibration temperature giving

$$A = \frac{A_{\text{cab}}(T_w - T_f)}{T_w - T_{\text{cab}}} \quad (C14)$$

and

$$B = \frac{B_{\text{cab}}(T_w - T_f)}{T_w - T_{\text{cab}}} \quad (C15)$$

where  $A_{\text{cab}}$  and  $B_{\text{cab}}$  are the values of and determined at the calibration temperature ( $T_{\text{cab}}$ ). Substituting equations (C14) and (C15) into equation (C11) for hot wires 1 and 2 and taking the ratio  $U_2/U_1$  gives

$$\sqrt{\frac{U_2}{U_1}} = \frac{B_{C1}}{B_{C2}} \frac{E_2^2 - A_{C2}\bar{T}}{E_1^2 - A_{C1}\bar{T}} \quad (\text{C16})$$

where

$$\bar{T} = \frac{T_w - T_f}{T_w - T_{\text{cab}}}$$

But, if equation (C16) reduces to

$$\sqrt{\frac{U_2}{U_1}} = \frac{B_{C1}}{B_{C2}} \frac{E_2^2 - A_{C2}}{E_1^2 - A_{C1}}$$

an estimate of the error in  $U_2/U_1$  is obtained by taking the ratio of equations (C16) and (C17) and squaring the result. Doing so for a typical set of hot-wire calibration data with the maximum temperature shift taken to be  $T_f - T_{\text{cab}} = 4^\circ\text{C}$ , the effect of temperature drift is found to be negligible at the boundary-layer edge, but it increases as  $U_2$  is decreased. For most of the boundary layer,  $0.25 \leq U_2/U_1 \leq 1.0$ , the error does not exceed 2.7 percent. The maximum error is 5.8 percent at the minimum velocity ratio of  $U_2/U_1 = 0.1$ .



## References

1. Reed, Helen L.; and Saric, William S.: Stability of Three-Dimensional Boundary Layers. *Annual Review of Fluid Mechanics*, Volume 21, Ann. Rev., Inc., 1989, pp. 235–284.
2. Saric, William S.: Laminar-Turbulent Transition: Fundamentals. *Special Course on Skin Friction Drag Reduction*, AGARD-R-786, 1992.
3. Morkovin, M. V.: On the Many Faces of Transition. *Viscous Drag Reduction*, C. Sinclair Wells, ed., Plenum Press, 1969, pp. 1–31.
4. Schlichting, Hermann (J. Kestin, transl.): *Boundary-Layer Theory*. McGraw-Hill Book Co., Inc., 1968.
5. Smith, A. M. O.; and Gamberoni, Nathalie: *Transition, Pressure Gradient, and Stability Theory*. Rep. No. ES 26388, Douglas Aircraft Co., Inc., 1956.
6. Van Ingen, J. L.: *A Suggested Semi-Empirical Method for the Calculation of the Boundary Layer Transition Region*. Rep. V.T.H.-74, Tech. Hogeschool Vliegtuigbouwkunde, 1956.
7. Reed, Helen L.: Wave Interactions in Swept-Wing Flows. *Phys. Fluids*, vol. 30, no. 11, Nov. 1987, pp. 3419–3426.
8. Gray, W. E.: *The Effect of Wing Sweep on Laminar Flow*. Tech. Memo. Aero 255, British R.A.E., Feb. 1952.
9. Owen, P. R.; and Randall, D. G.: *Boundary-Layer Transition on a Sweptback Wing*. Tech. Memo. Aero 277, British R.A.E., May 1952.
10. Stuart, J. T.: *The Basic Theory of the Stability of Three-Dimensional Boundary-Layers*. Rep. No. F.M. 1899, British Natl. Phys. Lab. (Rep. No. 15,904, A.R.C.), May 1953.
11. Gregory, N.; Stuart, J. T.; and Walker, W. S.: On the Stability of Three-Dimensional Boundary Layers With Application to the Flow Due to a Rotating Disk. *Philos. Trans. R. Soc. London*, ser. A, vol. 248, no. 943, 1955, pp. 155–199.
12. Brown, W. B.: *Exact Solution of the Orr-Sommerfeld Stability Equation for Low Reynolds Numbers*. Rep. No. BLC-43, Northrop Aircraft, Inc., 1954.
13. Brown, W. B.: *Extension of Exact Solution of the Orr-Sommerfeld Stability Equation to Reynolds Numbers of 4000*. Rep. No. NAI-55-548 (BLC-78), Northrop Aircraft, Inc., 1955.
14. Brown, W. B.: *Numerical Calculation of the Stability of Cross-Flow Profiles in Laminar Boundary Layers on a Rotating Disc and on a Swept-Back Wing and an Exact Calculation of the Stability of the Blasius Velocity Profile*. Rep. No. NAI-59-5 (BLC-117), Northrop Aircraft, Inc., 1959.
15. Pfenninger, W.; Gross, Lloyd; and Bacon, John W., Jr. (appendix I by G. S. Raetz): *Experiments on a 30° Swept 12%-Thick Symmetrical Laminar Suction Wing in the 5-Ft by 7-Ft Michigan Tunnel*. Rep. No. NAI-57-317 (BLC-93), Northrop Aircraft, Inc., 1957.
16. Bacon, J. W., Jr.; Tucker, V. L.; and Pfenninger, W.: *Experiments on a 30° Swept, 12% Thick Symmetrical Laminar Suction Wing in the 5- by 7-Foot University of Michigan Tunnel*. Rep. No. NOR-59-328 (BLC-119), Northrop Aircraft, Inc., Aug. 1959.
17. Pfenninger, W.; and Bacon, J. W., Jr.: About the Development of Swept Laminar Suction Wings With Full Chord Laminar Flow. *Boundary Layer and Flow Control*, Volume 2, G. V. Lachmann, ed., Pergamon Press, 1961, pp. 1007–1032.
18. Gault, Donald E.: *An Experimental Investigation of Boundary-Layer Control for Drag Reduction of a Swept-Wing Section at Low Speed and High Reynolds Numbers*. NASA TN D-320, 1960.
19. Boltz, Frederick W.; Kenyon, George C.; and Allen, Clyde Q.: *Effects of Sweep Angle on the Boundary-Layer Stability Characteristics of an Untapered Wing at Low Speeds*. NASA TN D-338, 1960.
20. Pfenninger, W.: *Laminar Flow Control Laminarization. Special Course on Concepts for Drag Reduction*. AGARD-R-654, 1977.
21. Jaffe, N. A.; Okamura, T. T.; and Smith A. M. O.: Determination of Spatial Amplification Factors and Their Application to Predicting Transition. *AIAA J.*, vol. 8, no. 2, 1970, pp. 301–308.
22. Mack, Leslie M.: Linear Stability Theory and the Problem of Supersonic Boundary-Layer Transition. *AIAA J.*, vol. 13, no. 3, Mar. 1975, pp. 278–289.
23. Mack, Leslie M.: Transition Prediction and Linear Stability Theory. *Laminar-Turbulent Transition*, AGARD-CP-224, Oct. 1977, pp. 1-1–1-22.
24. Mack, Leslie M.: Boundary-Layer Linear Stability Theory. *Special Course on Stability and Transition of Laminar Flow*, AGARD-R-709, June 1984, pp. 3-1–3-81.
25. Hefner, Jerry N.; and Bushnell, Dennis M.: Application of Stability Theory to Laminar Flow Control. *AIAA-79-1493*, July 1979.
26. Bushnell, D. M.; and Malik, M. R.: Application of Stability Theory to Laminar Flow Control—Progress and

- Requirements. *Stability of Time Dependent and Spatially Varying Flows*, Springer-Verlag, 1987, pp. 1–17.
27. Berry, Scott A.; Dagenhart, J. Ray; Yeaton, Robert B.; and Viken, Jeffrey K.: Boundary-Layer Stability Analysis of NLF and LFC Experimental Data at Subsonic and Transonic Speeds. SAE Paper 871859, Oct. 1987.
  28. Arnal, D.; Casalis, G.; and Juillen, J. C.: Experimental and Theoretical Analysis of Natural Transition on 'Infinite' Swept Wing. *Laminar-Turbulent Transition*, R. Michel and D. Arnal, eds., Springer-Verlag, 1990, pp. 311–325.
  29. Creel, T. R., Jr.; Malik, M. R.; and Beckwith, I. E.: Experimental and Theoretical Investigation of Boundary-Layer Instability Mechanisms on a Swept Leading Edge at Mach 3.5. *Research in Natural Laminar Flow and Laminar-Flow Control*, Jerry N. Hefner and Frances E. Sabo, compilers, NASA CP-2487, Part 3, 1987, pp. 981–995.
  30. Bieler, H.; and Redeker, G.: Development of Transition Criteria on the Basis of  $e^N$  for Three Dimensional Wing Boundary Layers. *Flows With Separation*, DGLR, 1988, pp. 103–116.
  31. Collier, F. S., Jr.; Bartlett, D. W.; Wagner, R. D.; Tat, V. V.; and Anderson, B. T.: Correlation of Boundary Layer Stability Analysis With Flight Transition Data. *Laminar-Turbulent Transition*, R. Michel and D. Arnal, eds., Springer-Verlag, 1990, pp. 337–346.
  32. Parikh, P. G.; Sullivan, P. P.; Birmingham, E.; and Nagel, A. L.: Stability of 3D Wing Boundary Layer on a SST Configuration. AIAA-89-0036, Jan. 1989.
  33. Collier, Fayette S., Jr.; Johnson, Joseph B.; Rose, Ollie J.; and Miller, D. S.: Supersonic Boundary-Layer Transition on the LaRC F-106 and the DFRF F-15 Aircraft. Part 1: Transition Measurements and Stability Analysis. *Research in Natural Laminar Flow and Laminar-Flow Control*, Jerry N. Hefner and Frances E. Sabo, compilers, NASA CP-2487, Part 3, 1987, pp. 997–1014.
  34. Obara, Clifford J.; Vijgen, Paul M. H. W.; Lee, Cynthia C.; and Wusk, Michael S.: *Boundary-Layer Stability Analysis of Flight-Measured Transition Data*. SAE Paper 901809, 1990.
  35. Lee, Cynthia C.; Wusk, Michael S.; and Obara, Clifford J.: *Flight Experiments Studying the Growth of the Disturbances in the Laminar Boundary Layer*. SAE Paper 901979, 1990.
  36. Horstmann, K. H.; Redeker, G.; Quast, A.; Dressler, U.; and Bieler, H.: Flight Tests With a Natural Laminar Flow Glove on a Transport Aircraft. AIAA-90-3044, 1990.
  37. Waggoner, Ed G.; Campbell, Richard L.; Phillips, Pam S.; and Hallissy, James B.: Design and Test of an NLF Wing Glove for the Variable-Sweep Transition Flight Experiment. *Research in Natural Laminar Flow and Laminar-Flow Control*, Jerry N. Hefner and Frances E. Sabo, compilers, NASA CP-2487, Part 3, 1987, pp. 753–776.
  38. Obara, Clifford J.; Lee, Cynthia C.; and Vijgen, Paul M. H. W.: Analysis of Flight-Measured Boundary-Layer Stability and Transition Data. AIAA-91-3282, Sept. 1991.
  39. Berry, Scott; Dagenhart, J. R.; Brooks, C.W.; and Harris, C. D.: Boundary-Layer Stability Analysis of LaRC 8-Foot LFC Experimental Data. *Research in Natural Laminar Flow and Laminar-Flow Control*, Jerry N. Hefner and Frances E. Sabo, compilers, NASA CP-2487, Part 2, 1987, pp. 471–489.
  40. Harvey, William D.; Harris, Charles D.; and Brooks, Cuyler, W., Jr.: Experimental Transition and Boundary-Layer Stability Analysis for a Slotted Swept Laminar Flow Control Airfoil. *4th Symposium on Numerical and Physical Aspects of Aerodynamic Flows*, California State Univ., 1989.
  41. Arnal, D.; Juillen, J. C.; and Casalis, G.: The Effects of Wall Suction on Laminar-Turbulent Transition in Three-Dimensional Flow. *Boundary Layer Stability and Transition to Turbulence*, FED-vol. 114, ASME, 1991, pp. 155–162.
  42. Maddalon, D. V.; Collier, F. S., Jr.; Montoya, L. C.; and Putnam, R. J.: Transition Flight Experiments on a Swept Wing With Suction. *Laminar-Turbulent Transition*, R. Michel and D. Arnal, eds., Springer-Verlag, 1990, pp. 53–64.
  43. Runyan, L. J.; Bielak, G. W.; Behbehani, R.; Chen, A. W.; and Rozendaal, R. A.: 757 NLF Glove Flight Test Results. *Research in Natural Laminar Flow and Laminar-Flow Control*, Jerry N. Hefner and Frances E. Sabo, compilers, NASA CP-2487, Part 3, 1987, pp. 795–818.
  44. Srokowski, Andrew J.; and Orszag, Steven A.: Mass Flow Requirements for LFC Wing Design—Laminar Flow Control. AIAA-77-1222, 1977.
  45. Dagenhart, J. Ray: *Amplified Crossflow Disturbances in the Laminar Boundary Layer on Swept Wings With Suction*. NASA TP-1902, 1981.
  46. Malik, M. R.; and Orszag, S. A.: Efficient Computation of the Stability of Three-Dimensional Compressible Boundary Layers. AIAA-81-1277, June 1981.
  47. Malik, Mujeeb R.: *COSAL—A Black-Box Compressible Stability Analysis Code for Transition Prediction*

- in *Three-Dimensional Boundary Layers*. NASA CR-165925, 1982.
48. Herbert, Thorwald: A Code for Linear Stability Analysis. *Instability and Transition*, Volume II, M. Y. Hussaini and R. G. Voigt, eds., Springer-Verlag, 1990, pp. 121–144.
  49. Arnal, D.: Some Transition Problems in Three-Dimensional Flows. *Instability and Transition*, Volume I, M. Y. Hussaini and R. G. Voigt, eds., Springer-Verlag, 1990, pp. 130–135.
  50. Saric, William S.: Low-Speed Experiments: Requirements for Stability Measurements. *Instability and Transition*, Volume I, M. Y. Hussaini and R. G. Voigt, eds., Springer-Verlag, 1990, pp. 162–176.
  51. Stetson, K. F.: Hypersonic Boundary-Layer Transition. *Second Joint Europe/U.S. Short Course in Hypersonics*. U.S. Air Force Academy, 1989.
  52. Malik, Mujeeb R.: Group Summary: Compressible Stability and Transition. *Instability and Transition*, Volume II, M. Y. Hussaini and R. G. Voigt, eds., Springer-Verlag, 1990, pp. 233–234.
  53. Poll, D. I. A.: The Effect of Isolated Roughness Elements on Transition in Attachment-Line Flows. *Laminar-Turbulent Transition*, R. Michel and D. Arnal, eds., Springer-Verlag, 1990, pp. 657–667.
  54. Arnal, D.; and Aupoix, B.: Hypersonic Boundary Layers; Transition and Turbulence Effects. *Aerothermodynamics for Space Vehicles*, B. Battrick, ed., ESA-SP-318, 1991, pp. 25–38.
  55. Lees, Lester; and Lin, Chia Chiao: *Investigation of the Stability of the Laminar Boundary Layer in a Compressible Fluid*. NACA TN 1115, 1946.
  56. Lin, C. C.: *The Theory of Hydrodynamic Stability*. Cambridge Univ. Press, 1955, pp. 75–82.
  57. Dunn, D. W.; and Lin, C. C.: On the Stability of the Laminar Boundary Layer in a Compressible Fluid. *J. Aeronaut. Sci.*, vol. 22, no. 7, 1955, pp. 455–477.
  58. Lees, Lester; and Reshotko, Eli: Stability of a Compressible Laminar Boundary Layer. *J. Fluid Mech.*, vol. 12, pt. 4, 1962, pp. 555–590.
  59. Mack, Leslie M.: Computation of the Stability of the Laminar Compressible Boundary Layer. *Methods in Computational Physics*, Volume 4, Berni Alder, Sidney Fernbach, and Manuel Rotenberg, eds., Academic Press, Inc., 1965, pp. 247–299.
  60. Mack, L. M.: The Stability of the Compressible Laminar Boundary Layer According to a Direct Numerical Solution. *Recent Developments in Boundary Layer Research*, Part I, AGARDograph 97, 1965, pp. 329–362.
  61. Mack, L. M.: *Boundary Layer Stability Theory*. NASA CR-131501, 1969.
  62. Lekoudis, Spyridon G.: Stability of Three-Dimensional Compressible Boundary Layers Over Wings With Suction. AIAA-79-0265, 1979.
  63. Mack, Leslie M.: On the Stability of the Boundary Layer on a Transonic Swept Wing. AIAA-79-0264, 1979.
  64. Mack, Leslie M.: Compressible Boundary-Layer Stability Calculations for Sweptback Wings With Suction. *AIAA J.*, vol. 20, no. 3, Mar. 1982, pp. 363–369.
  65. El-Hady, Nabil M.: On the Stability of Three-Dimensional Compressible Nonparallel Boundary Layers. AIAA-80-1374, 1980.
  66. Reed, H. L.; Stuckert, G.; and Balakumar, P.: Stability of High-Speed Chemically Reacting and Three-Dimensional Boundary Layers. *Laminar-Turbulent Transition*, D. Arnal and R. Michel, eds., Springer-Verlag, 1990, pp. 347–358.
  67. Balakumar, Ponnampalam; and Reed, Helen L.: Stability of Three-Dimensional Supersonic Boundary Layers. *Phys. Fluids A*, vol. 3, no. 4, Apr. 1991, pp. 617–632.
  68. Padhye, A. R.; and Nayfeh, A. H.: Nonparallel Stability of Three-Dimensional Flows. AIAA-81-1281, 1981.
  69. Nayfeh, A.: Stability of Three-Dimensional Boundary Layers. *AIAA J.*, vol. 18, 1980, pp. 406–416.
  70. Nayfeh, A. H.: Three-Dimensional Stability of Growing Boundary Layers. *Laminar-Turbulent Transition*, R. Eppler and H. Fasel, eds., Springer-Verlag, 1980, pp. 201–217.
  71. Reed, H. L.; and Nayfeh, A. H.: Stability of Compressible Three-Dimensional Boundary-Layer Flows. AIAA-82-1009, 1982.
  72. Malik, M. R.; and Poll, D. I. A.: Effect of Curvature on Three-Dimensional Boundary Layer Stability. AIAA-84-1672, 1984.
  73. Viken, J.; Collier, F. S., Jr.; Wagner, R. D.; and Bartlett, D. W.: On the Stability of Swept Wing Laminar Boundary Layers Including Curvature Effects. *Laminar-Turbulent Transition*, R. Michel and D. Arnal, eds., Springer-Verlag, 1990, pp. 381–388.
  74. Mueller, B.; Bippes, H.; and Collier, F. S., Jr.: The Stability of a Three Dimensional Laminar Boundary Layer Over a Swept Flat Plate. *Instability and Transition*, Volume II, M. Y. Hussaini and R. G. Voigt, eds., Springer-Verlag, 1990, pp. 268–277.

75. Collier, F. S., Jr.; and Malik, Mujeeb R.: Curvature Effects on the Stability of Three-Dimensional Boundary Layers. *Fluid Dynamics of Three-Dimensional Turbulent Shear Flows and Transition*, AGARD CP-438, 1990. (Available from DTIC as AD A211 101.)
76. Lin, Ray-Sing; and Reed, Helen L.: Effect of Curvature on Stationary Crossflow Instability of a Three-Dimensional Boundary Layer. *AIAA J.*, vol. 31, no. 9, 1993, pp. 1611–1617.
77. Lekoudis, S. G.: Resonant Wave Interactions on a Swept Wing. *AIAA J.*, vol. 18, no. 1, 1980, pp. 122–124.
78. Fischer, T. M.; and Dallmann, U.: Theoretical Investigation of Secondary Instability of Three-Dimensional Boundary-Layer Flows. AIAA-87-1338, 1987.
79. El-Hady, N. M.: Evolution of Resonant Wave Triads in Three-Dimensional Boundary Layers. AIAA-88-0405, 1988.
80. Bassom, Andrew P.; and Hall, Philip: *On the Interaction of Stationary Crossflow Vortices and Tollmien-Schlichting Waves in the Boundary Layer on a Rotating Disc*. NASA CR-181859, 1989.
81. Bassom, Andrew P.; and Hall, Philip: *Concerning the Interaction of Non-Stationary Cross-Flow Vortices in a Three-Dimensional Boundary Layer*. NASA CR-182037, 1990.
82. Bassom, Andrew; and Hall, Philip: *Vortex Instabilities in 3D Boundary Layers. The Relationship Between Goertler and Crossflow Vortices*. NASA CR-187456, 1990.
83. Bassom, Andrew P.; and Hall, Philip: Vortex Instabilities in Three-Dimensional Boundary Layers: The Relationship Between Görtler and Crossflow Vortices. *J. Fluid Mech.*, vol. 232, Nov. 1991, pp. 647–680.
84. Arnal, D.; Coustols, E.; and Juillen, J.C.: Experimental and Theoretical Study of Transition Phenomena on an Infinite Swept Wing. *La Recherche Aerosp.*, no. 4, 1984, pp. 39–54.
85. Arnal, D.; Habiballah, M.; and Coustols, E.: Laminar Instability Theory and Transition Criteria in Two- and Three-Dimensional Flow. *La Recherche Aerosp.*, no. 2, 1984, pp. 45–63.
86. Arnal, D.; and Coustols, E.: Application of Two and Three-Dimensional Criteria for Calculating Transitions and Boundary Layers Over Swept Wings. *Improvement of Aerodynamic Performance Through Boundary Layer Control and High Lift Systems*. AGARD CP-365, 1984. (Available from DTIC as AD A147 396.)
87. Michel, R.; Arnal, D.; and Coustols, E.: Stability Calculations and Transition Criteria in Two- or Three-Dimensional Flows. *Laminar-Turbulent Transition*, V. V. Koslov, ed., Springer-Verlag, 1985, pp. 455–462.
88. Arnal, D.; Coustols, E.; and Jelliti, M.: Transition to Three-Dimensional Flow and Laminarization of the Boundary Layer on a Swept-Back Wing. *Colloque d'Aerodynamique Appliquee, 22nd (Lille, France)*, Nov. 13–15, 1985.
89. Michel, R.; Coustols E.; and Arnal, D.: *Transition Calculations in Three-Dimensional Flows*. TP 1985-7, ONERA, 1985.
90. Arnal, D.; and Juillen, J. C.: Three-Dimensional Transition Studies at ONERA/CERT. AIAA-87-1335, 1987.
91. King, Rudolph A.: Mach 3.5 Boundary-Layer Transition on a Cone at Angle of Attack. AIAA-91-1804, 1991.
92. Poll, D. I. A.: Some Observations of the Transition Process on the Windward Face of a Long Yawed Cylinder. *J. Fluid Mech.*, vol. 150, 1985, pp. 329–356.
93. Michel, R.; Arnal, D.; Coustols, E.; and Juillen, J. C.: Experimental and Theoretical Studies of Boundary Layer Transition on a Swept Infinite Wing. *Laminar-Turbulent Transition*, V. V. Kozlov, ed., Springer-Verlag, 1985, pp. 553–562.
94. Kohama, Y.; Ukaku, M.; and Ohta, F.: Boundary-Layer Transition on a Swept Cylinder. *Frontiers of Fluid Mechanics*, Shen Yuan, ed., Pergamon Press, 1988, pp. 151–156.
95. Choudhari, Meelan; and Streett, Craig L.: Boundary Layer Receptivity Phenomena in Three-Dimensional and High-Speed Boundary Layers. AIAA-90-5258, 1990.
96. Fischer, Thomas M.; and Dallmann, Uwe: *Theoretical Investigation of Secondary Instability of Three-Dimensional Boundary-Layer Flows With Application to the DFVLR-F5 Model Wing*. DFVLR-FB-87-44, 1987.
97. Fischer, T. M.; and Dallmann, U.: Primary and Secondary Stability Analysis of Three-Dimensional Boundary-Layer Flow. *Phys. Fluids A*, vol. 3, 1991, pp. 2378–2391.
98. Nitschke-Kowsky, P.; and Bippes, H.: Instability and Transition of a Three-Dimensional Boundary Layer on a Swept Flat Plate. *Phys. Fluids*, vol. 31, 1988, pp. 786–795.
99. Bippes, H.: Instability Features Appearing on Swept Wing Configurations. *Laminar-Turbulent Transition*, R. Michel and D. Arnal, eds., Springer-Verlag, 1990, pp. 419–430.

100. Mueller, B.: Experimental Study of the Travelling Waves in a Three-Dimensional Boundary Layer. *Laminar-Turbulent Transition*. R. Michel and D. Arnal, eds., Springer-Verlag, 1990, pp. 489–498.
101. Bippes, H.; and Mueller, B.: Experiments on the Laminar-Turbulent Transition on Swept Wings. *Flows With Separation*, DGLR Paper 88-05, 1988, pp. 3–16.
102. Meyer, F.; and Kleiser, L.: Numerical Simulation of the Nonlinear Evolution of Perturbation in a Three Dimensional Boundary Layer. *Flows With Separation*, DGLR Paper 88-05, 1988, pp. 39–40.
103. Meyer, F.; and Kleiser, L.: Numerical Simulation of Transition Due to Crossflow Instability. *Laminar-Turbulent Transition*, R. Michel and D. Arnal, eds., Springer-Verlag, 1990, pp. 609–619.
104. Singer, Bart A.; Meyer, F.; and Kleiser, Leonhard: Nonlinear Development of Crossflow Vortices. *Instability and Transition*, M. Y. Hussaini and R. G. Voigt, eds., Springer-Verlag, 1990, pp. 300–312.
105. Meyer, Friedrich: Numerical Simulation of Transition in Three-Dimensional Boundary Layers. ESA TT-1203, 1991.
106. Fischer, Thomas M.: *A Mathematical-Physical Model for Describing Transitional Boundary-Layer Flows. Volume 1—The Linear and Nonlinear Disturbance Differential Equations*. DLR-FB-95-06 ESA TT-1242, 1994.
107. Spalart, P. R.: Direct Numerical Study of Crossflow Instability. *Laminar-Turbulent Transition*, R. Michel and D. Arnal, eds., Springer-Verlag, 1990, pp. 621–630.
108. Reed, Helen L.; and Lin, Ray-Sing: Stability of Three-Dimensional Boundary Layers. SAE Paper 871857, 1987.
109. Lin, Ray-Sing: Stationary Crossflow Instability on an Infinite Swept Wing. Ph.D. Thesis, Arizona State Univ., 1992.
110. Malik, M. R.; and Li, F.: Three-Dimensional Boundary-Layer Stability and Transition. SAE Paper 921991, 1992.
111. Herbert, Th.: Boundary-Layer Transition—Analysis and Prediction Revisited. AIAA-91-0737, 1991.
112. Saric, W. S.; and Yeates, L. G.: Experiments on the Stability of Crossflow Vortices in Swept-Wing Flows. AIAA-85-0493, 1985.
113. Nitschke-Kowsky, Petra: *Experimental Investigations on the Stability and Transition of Three-Dimensional Boundary Layers*. ESA-TT-1026, 1986.
114. Mueller, Bernhard: Experimental Investigation of Cross-Flow Instability in the Linear and Non-Linear Stage of the Transition Region. ESA-TT-1237, 1990.
115. Bippes, H.; Mueller, B.; and Wagner, M.: Measurements and Stability Calculations of the Disturbance Growth in an Unstable Three-Dimensional Boundary Layer. *Phys. Fluids A*, vol. 3, 1991, pp. 2371–2377.
116. Kachanov, Y. S.; and Tararykin, O. I.: The Experimental Investigation of Stability and Receptivity of a Swept-Wing Flow. *Laminar-Turbulent Transition*, R. Michel and D. Arnal, eds., Springer-Verlag, 1990, pp. 499–509.
117. Saric, W. S.; Dagenhart, J. Ray; and Mousseux, Marc: Experiments in Swept-Wing Transition. *Numerical and Physical Aspects of Aerodynamic Flows IV*, Tuncer Cebeci, ed., Springer-Verlag, 1990.
118. Dagenhart, J. Ray; Stack, J. Peter; Saric, William S.; and Mousseux, Marc C.: Crossflow-Vortex Instability and Transition on a 45 Degree Swept Wing. AIAA-89-1892, 1989.
119. Dagenhart, J. R.; Saric, William S.; Hoos, Jon A.; and Mousseux, Marc: Experiments on Swept-Wing Boundary Layers. *Laminar-Turbulent Transition*, R. Michel and D. Arnal, eds., Springer-Verlag, 1990, pp. 369–380.
120. Radeztsky, Ronald H., Jr.; Reibert, Mark S.; Saric, William S.; and Takagi, Shohei: Role of Micron-Sized Roughness in Swept-Wing Transition. SAE Paper No. 921986, 1992.
121. Somers, Dan M.; and Horstman, Karl-Heinz: *Design of a Medium-Speed, Natural-Laminar-Flow Airfoil for Commuter Aircraft Application*. DFVLR IB 129-85/26, 1985.
122. Somers, Dan M.: Subsonic Natural-Laminar-Flow Airfoils. *Natural Laminar Flow and Laminar Flow Control*, R. W. Barnwell and M. Y. Hussaini, eds., Springer-Verlag, 1992, pp. 143–176.
123. Saric, William S.: The ASU Transition Research Facility. AIAA-92-3910, 1992.
124. Saric, William S.; Takagi, Shohei; and Mousseux, Marc C.: The ASU Unsteady Wind Tunnel and Fundamental Requirements for Freestream Turbulence Measurements. AIAA-88-0053, 1988.
125. Eppler, Richard; and Somers, Dan M.: *A Computer Program for the Design and Analysis of Low-Speed Airfoils*. NASA TM-80210, 1980.

126. Kaups, Kalle; and Cebeci, Tuncer: Compressible Laminar Boundary Layers With Suction on Swept and Tapered Wings. *J. Aircr.*, vol. 14, no. 7, 1977, pp. 661–667.
127. Stevens, W. A.; Goradia, S. H.; and Braden, J. A.: *Mathematical Model for Two-Dimensional Multi-Component Airfoils in Viscous Flow*. NASA CR-1843, 1971.
128. Fuciarelli, David A.; and Reed, Helen L.: Stationary Crossflow Vortices. *Phys. Fluids A*, vol. 4, no. 9, 1992, p. 1880.
129. Reda, Daniel C.: Liquid Crystals for Unsteady Surface Shear Stress Visualization. AIAA-88-3841, 1988.
130. Kline, S. J.; and McClintock, F. A.: Describing Uncertainties in Single-Sample Experiments. *Mech. Eng.*, vol. 75, no. 1, 1953, pp. 3–8.

Table 1. Crossflow Stability Analysis With SALLY Code for  $\alpha = -4^\circ$  and  $R_c = 3.81 \times 10^6$

Frequency, $f$	$N_{\max}$ for wavelength, $\lambda/c$ , of—							
	0.002	0.003	0.004	0.005	0.006	0.007	0.008	0.009
-50	4.8	10.1	11.2	10.0	8.7	7.3	6.1	5.1
0	4.9	10.7	13.1	12.6	11.6	10.4	9.3	8.3
50	5.1	10.9	14.5	14.6	13.8	12.8	11.7	10.7
100	5.2	10.6	15.4	16.0	15.5	14.6	13.5	12.4
200	5.2	9.4	15.6	17.3	17.2	16.4	15.3	13.8
300	5.2	8.2	13.8	16.2	16.6	15.8	14.6	12.9
500	4.8	6.2	7.3	7.6	7.2	6.5	5.3	4.4

Table 2. Transition Locations and Wavelengths From Naphthalene Flow Visualization

Reynolds number, $R_c$	Transition location, $(x/c)_{tr}$	Wavelength, $\lambda/c$
$1.92 \times 10^6$	0.78	0.0050
2.19	0.73	
2.37	0.58	0.0040
2.73	0.45	0.0034
3.27	0.33	0.0029
3.73	0.30	0.0024

Table 3.  $N$ -Factors at Transition Computed With SALLY Code for  $\alpha = -4^\circ$ ,  $R_c = 2.37 \times 10^6$ , and  $(x/c)_{tr} = 0.58$

Frequency, $f$	$N_{tr}$ for wavelength, $\lambda/c$ , of—						
	0.004	0.005	0.0055	0.006	0.007	0.008	0.009
0	6.2	6.8	6.8	6.7	6.2	5.6	4.5
50		8.2		8.5	8.2		6.6
100		8.3		9.1	9.1	7.8	7.4
150		7.2		8.4	8.6	8.5	7.1
200		5.3		6.3	6.9	6.8	5.5
300		2.8		2.6	2.4	1.9	1.1

Table 4.  $N$ -Factors at Transition Computed With SALLY Code for  $\alpha = -4^\circ$ ,  $R_c = 2.37 \times 10^6$ , and  $(x/c)_{tr} = 0.45$

Frequency, $f$	$N_{tr}$ for wavelength, $\lambda/c$ , of—						
	0.003	0.004	0.005	0.0055	0.006	0.007	0.008
0	4.7	6.5	6.2		5.6	5.0	4.3
50		7.3	7.6	7.4	7.2	6.6	
100		7.6	8.3	8.2	8.1	7.6	
150		7.3	8.5	8.5	8.5	7.9	
200		6.4	8.1	8.1	8.2	7.7	
300		4.7	5.2	5.3	5.5	5.3	
400		3.3	3.0	2.9	2.5	2.2	

Table 5.  $N$ -Factors at Transition Computed With SALLY Code for  $\alpha = -4^\circ$ ,  $R_c = 3.73 \times 10^6$ , and  $(x/c)_{tr} = 0.30$

Frequency, $f$	$N_{tr}$ for wavelength, $\lambda/c$ , of—						
	0.0025	0.003	0.004	0.0045	0.005	0.006	0.007
0	6.1	6.4	6.0	5.5	5.0	4.1	3.3
50		7.0	6.8	6.4	5.9		
100		7.4	7.5	7.2	6.7		
150		7.6	8.1	7.8	7.3		
200		7.7	8.4	8.2	7.8		
300		7.2	8.5	8.4	8.0		
400		6.4	7.8	7.8	7.3		
500		5.6	6.2		5.9		



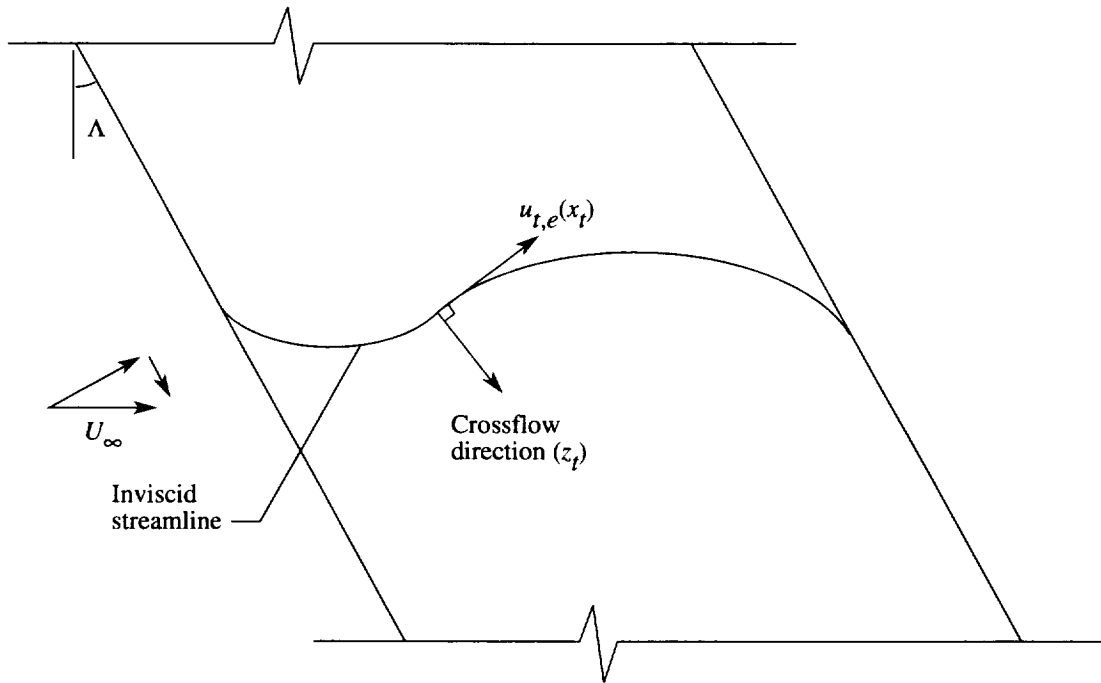


Figure 1. Curved streamlines over swept wing.

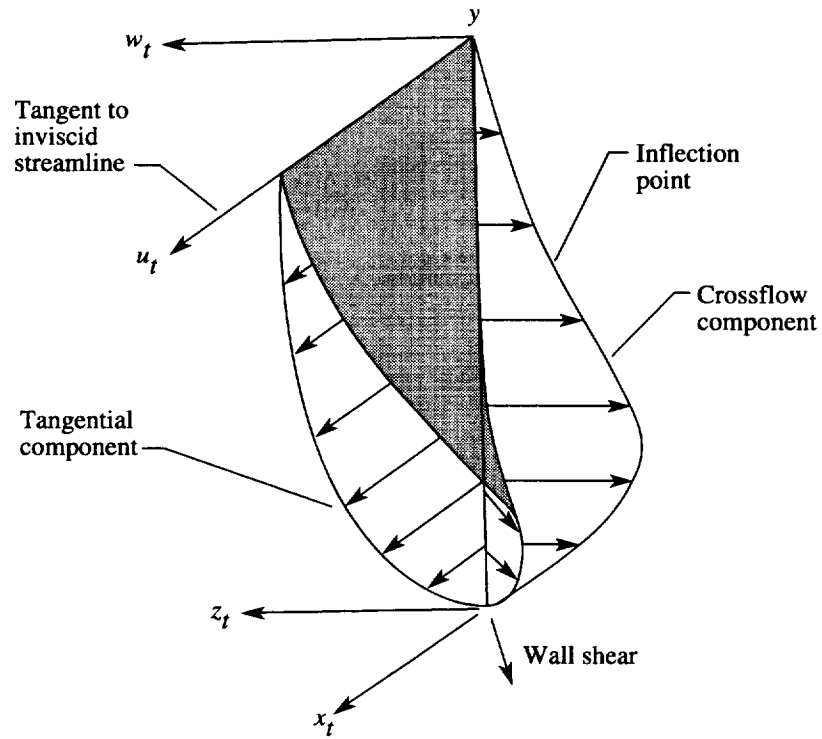


Figure 2. Boundary-layer velocity profiles on swept wing.

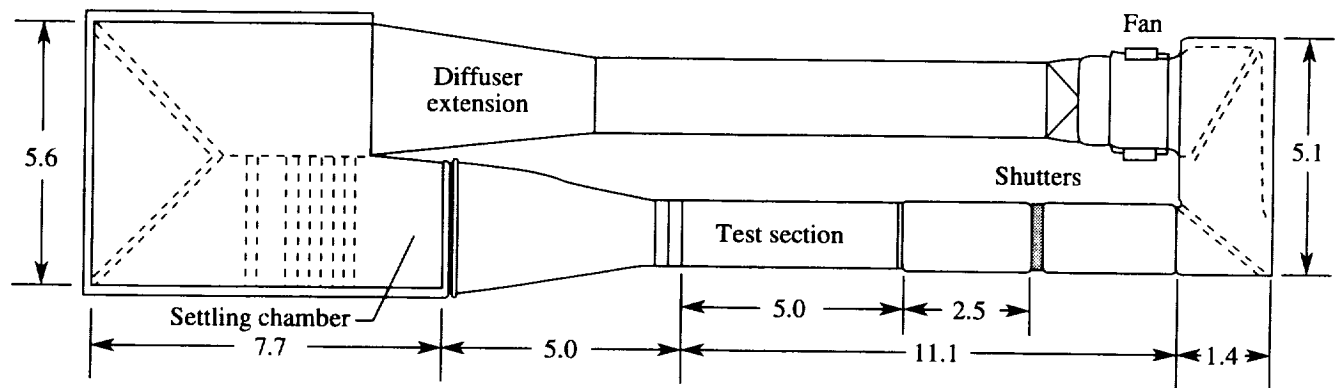


Figure 3. Plan view of Arizona State University Unsteady Wind Tunnel. Dimensions are in meters.

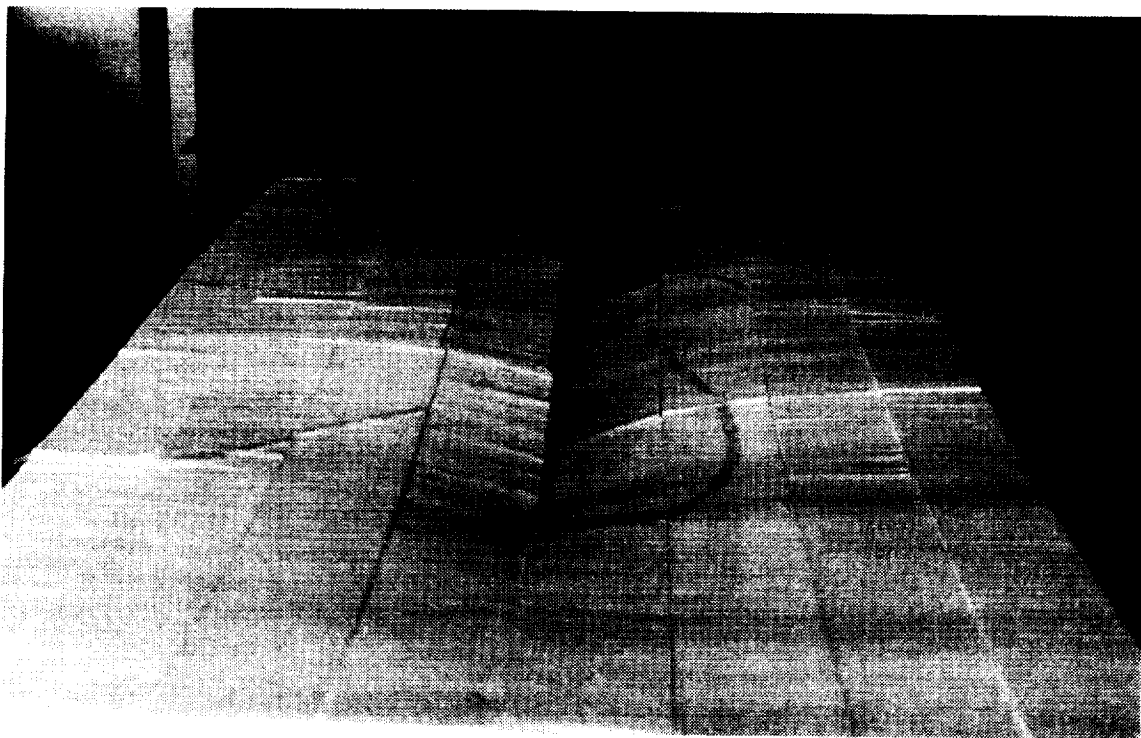


Figure 4. New UWT test section with liner under construction.

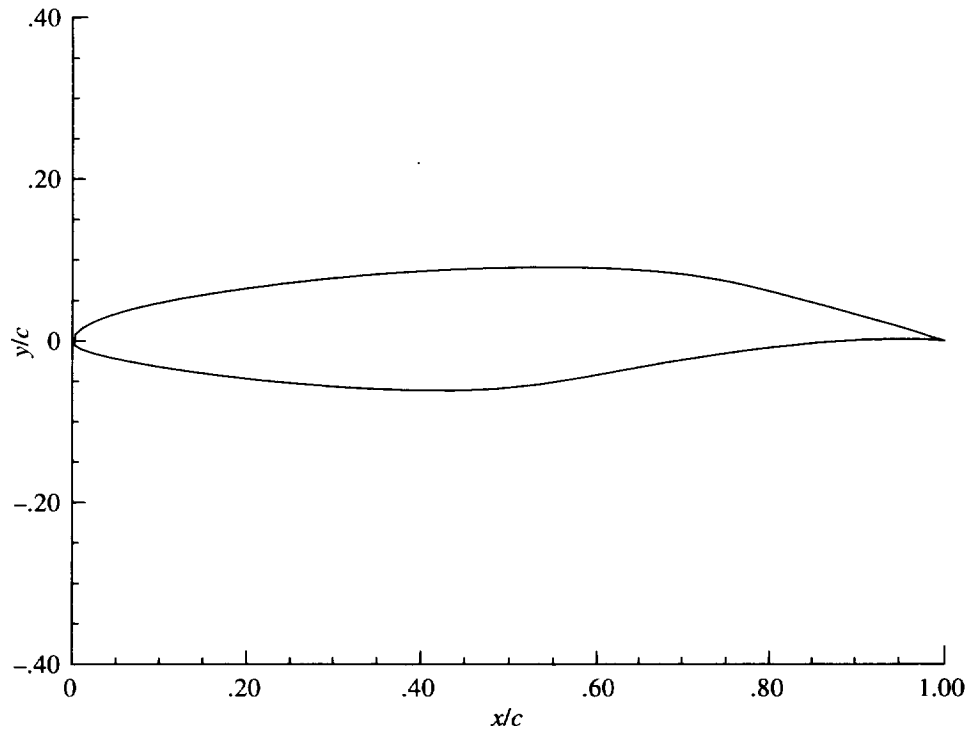


Figure 5. NASA NLF(2)-0415 airfoil.

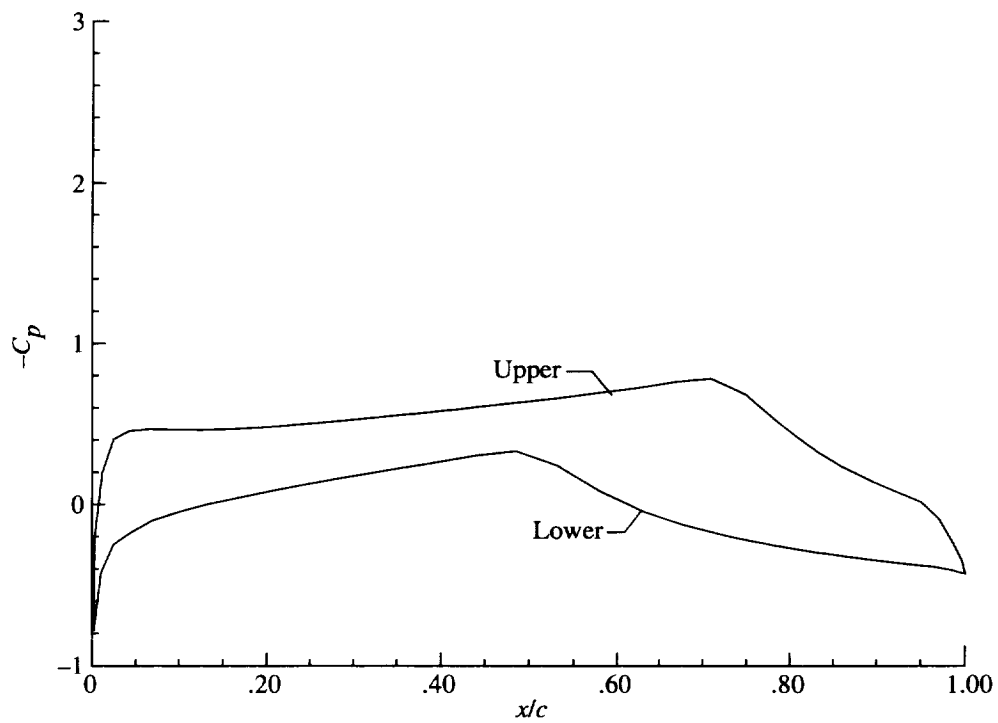


Figure 6. NASA NLF(2)-0415 design point pressure distribution at  $\alpha = 0^\circ$  and  $\delta_f = 0^\circ$  in free air.

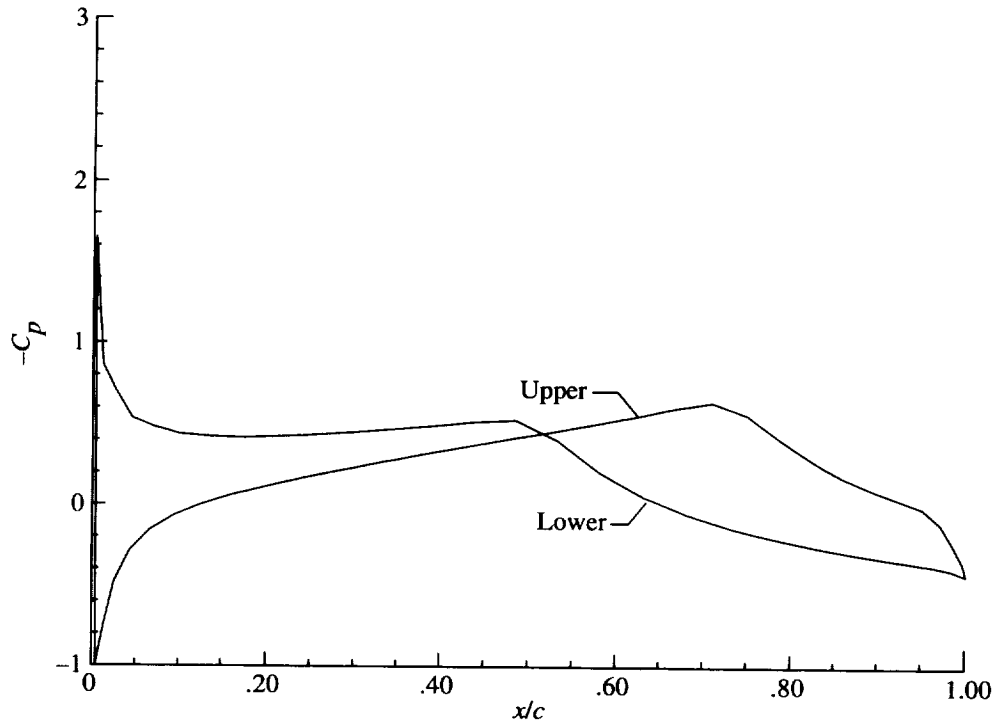


Figure 7. NASA NLF(2)-0415 pressure distribution for  $\alpha = -4^\circ$  and  $\delta_f = 0^\circ$  in free air.

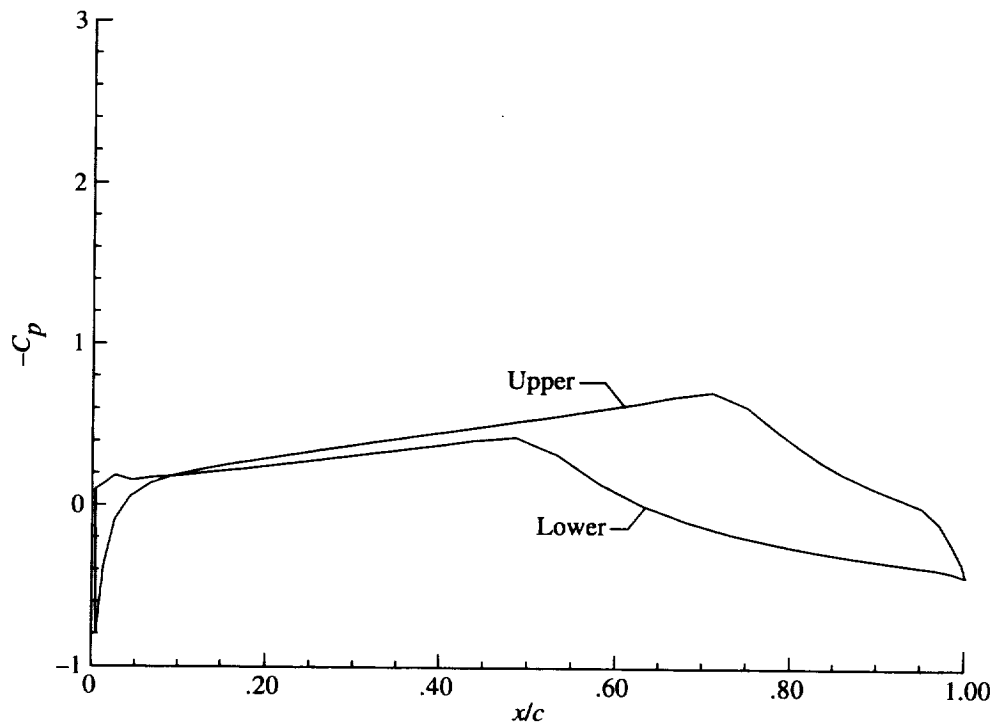


Figure 8. NASA NLF(2)-0415 pressure distribution for  $\alpha = -2^\circ$  and  $\delta_f = 0^\circ$  in free air.

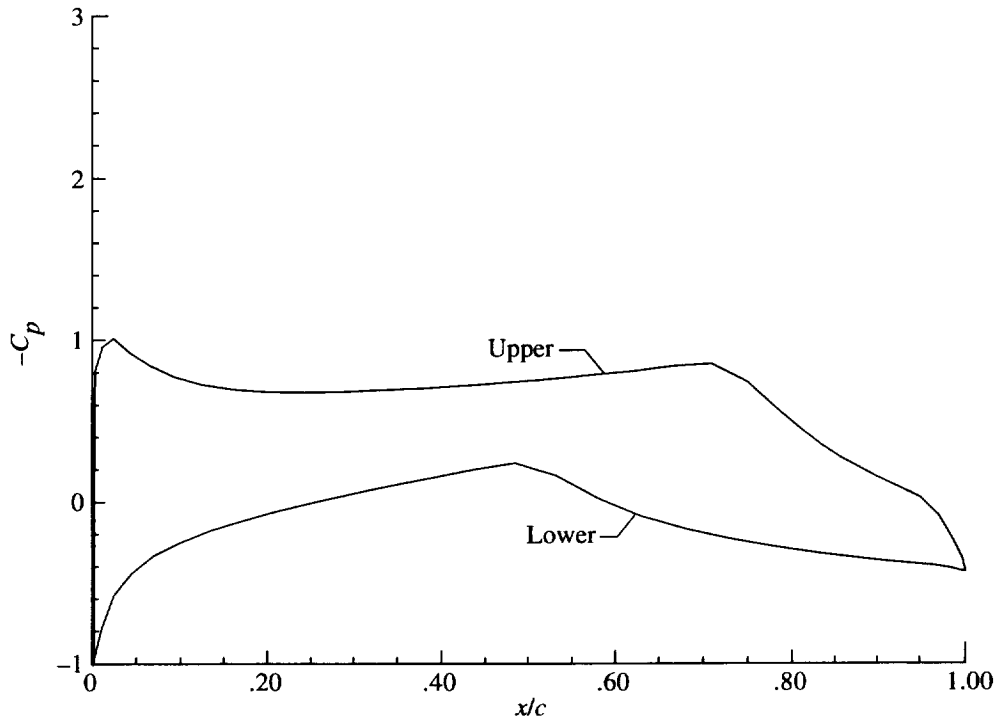


Figure 9. NASA NLF(2)-0415 pressure distribution for  $\alpha = 2^\circ$  and  $\delta_f = 0^\circ$  in free air.

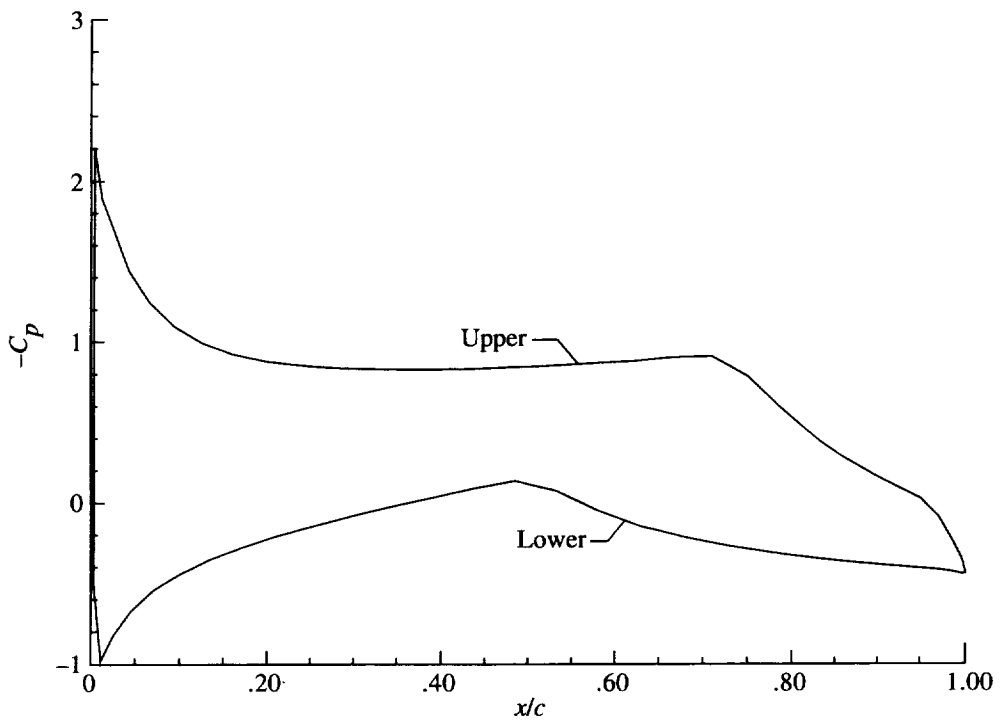


Figure 10. NASA NLF(2)-0415 pressure distribution for  $\alpha = 4^\circ$  and  $\delta_f = 0^\circ$  in free air.

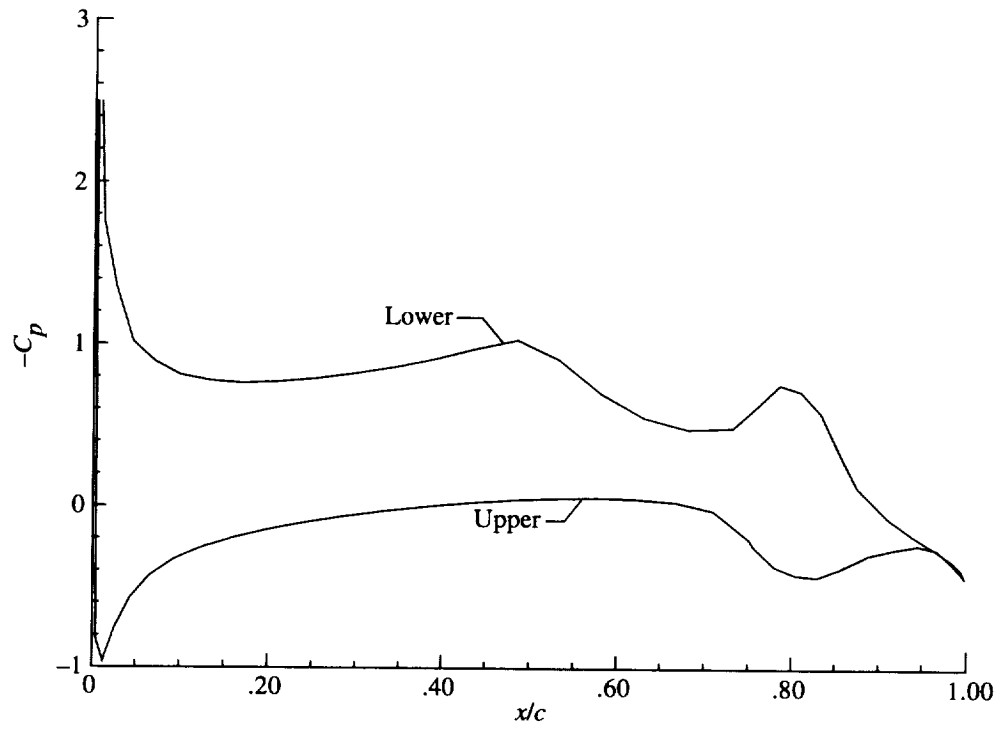


Figure 11. NASA NLF(2)-0415 pressure distribution for  $\alpha = 0^\circ$  and  $\delta_f = -20^\circ$  in free air.

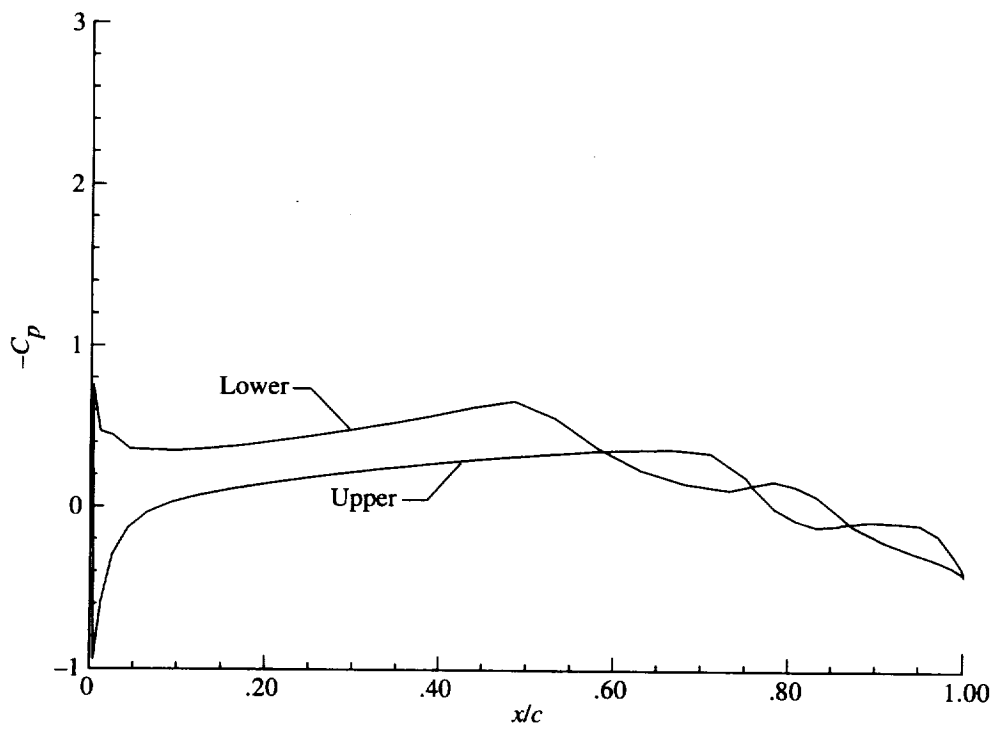


Figure 12. NASA NLF(2)-0415 pressure distribution for  $\alpha = 0^\circ$  and  $\delta_f = -10^\circ$  in free air.

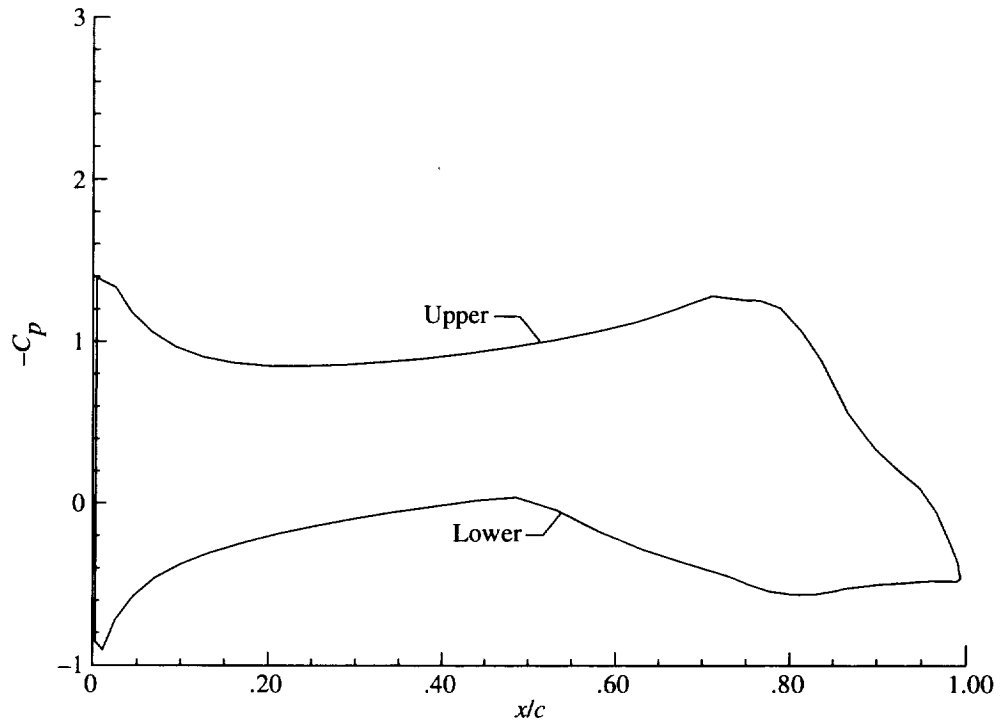


Figure 13. NASA NLF(2)-0415 pressure distribution for  $\alpha = 0^\circ$  and  $\delta_f = 10^\circ$  in free air.

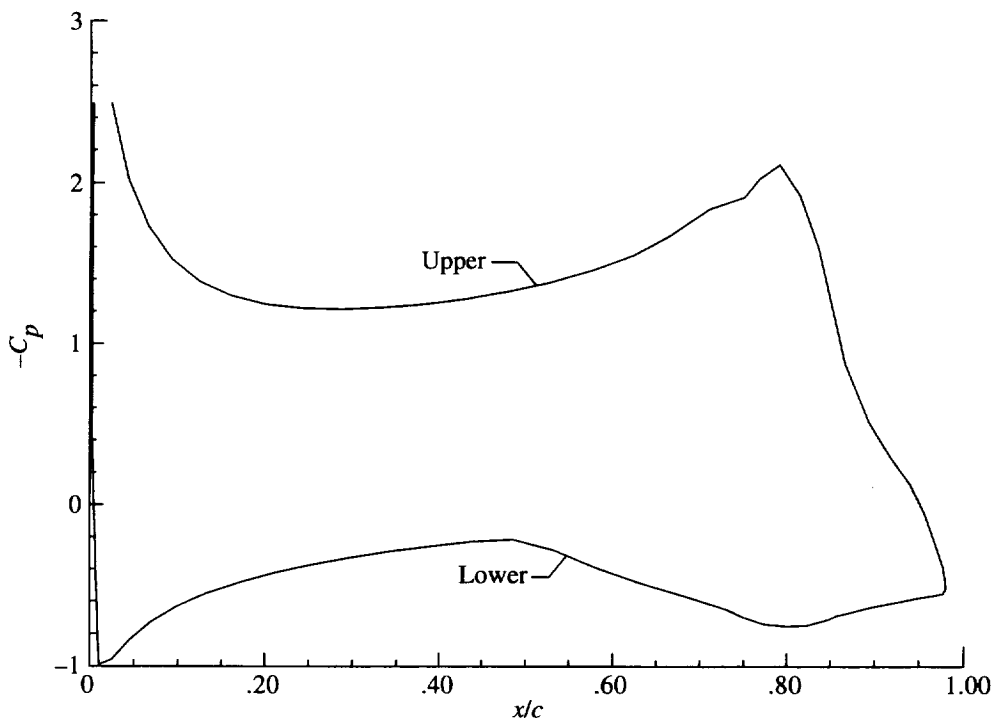


Figure 14. NASA NLF(2)-0415 pressure distribution for  $\alpha = 0^\circ$  and  $\delta_f = 20^\circ$  in free air.

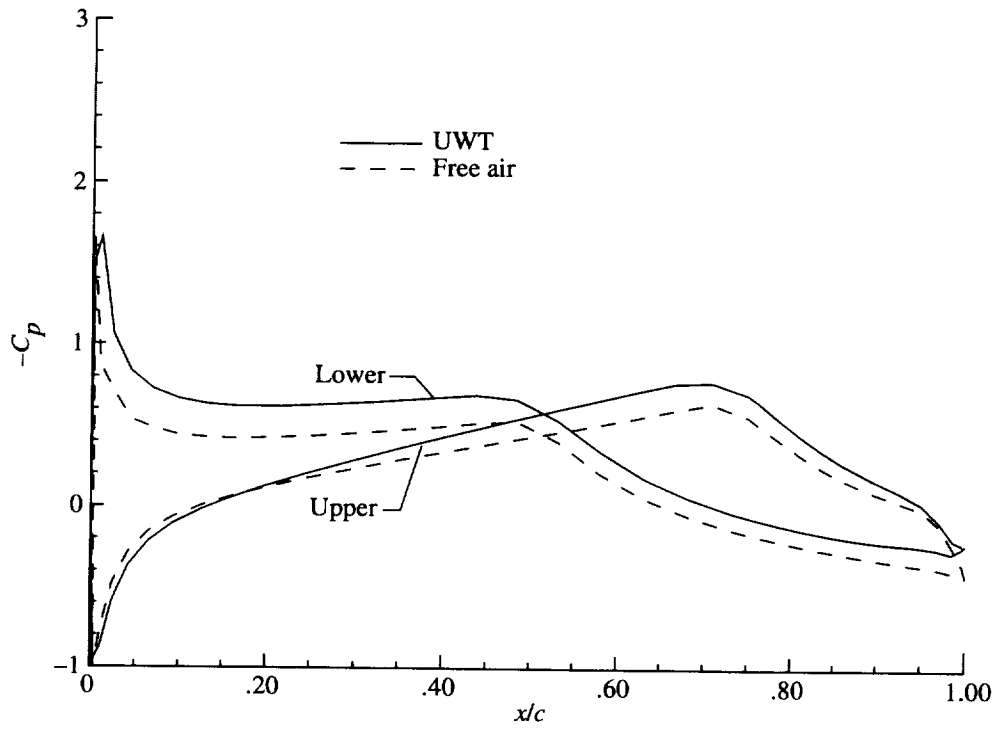


Figure 15. NASA NLF(2)-0415 pressure distribution for  $\alpha = -4^\circ$  and  $\delta_f = 0^\circ$  in UWT.

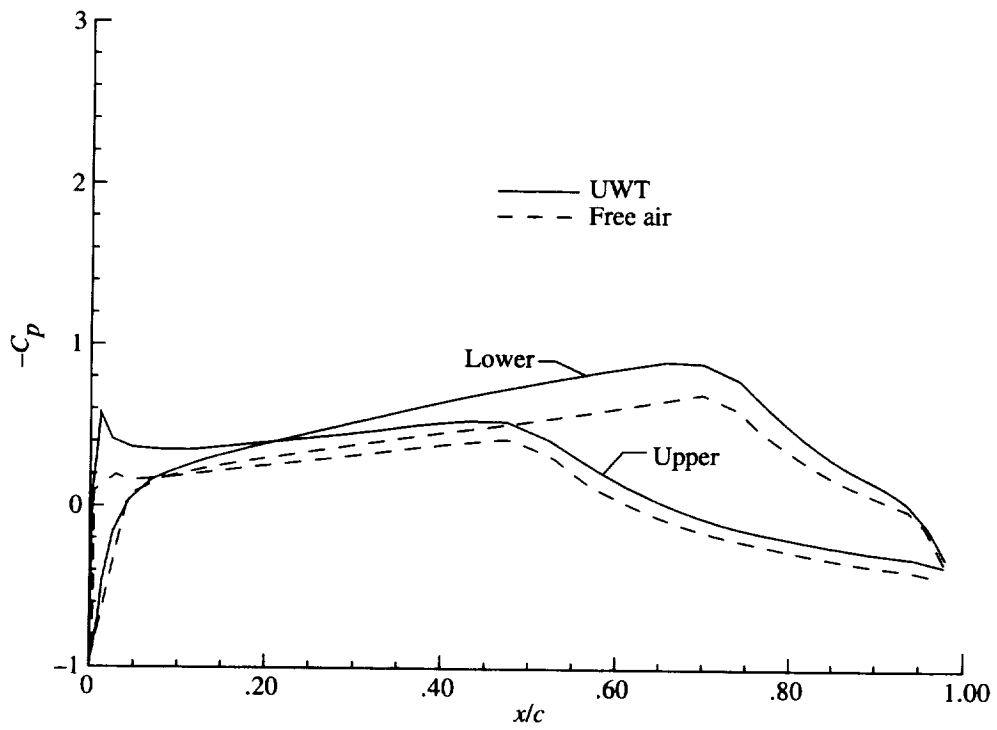


Figure 16. NASA NLF(2)-0415 pressure distribution for  $\alpha = -2^\circ$  and  $\delta_f = 0^\circ$  in UWT.



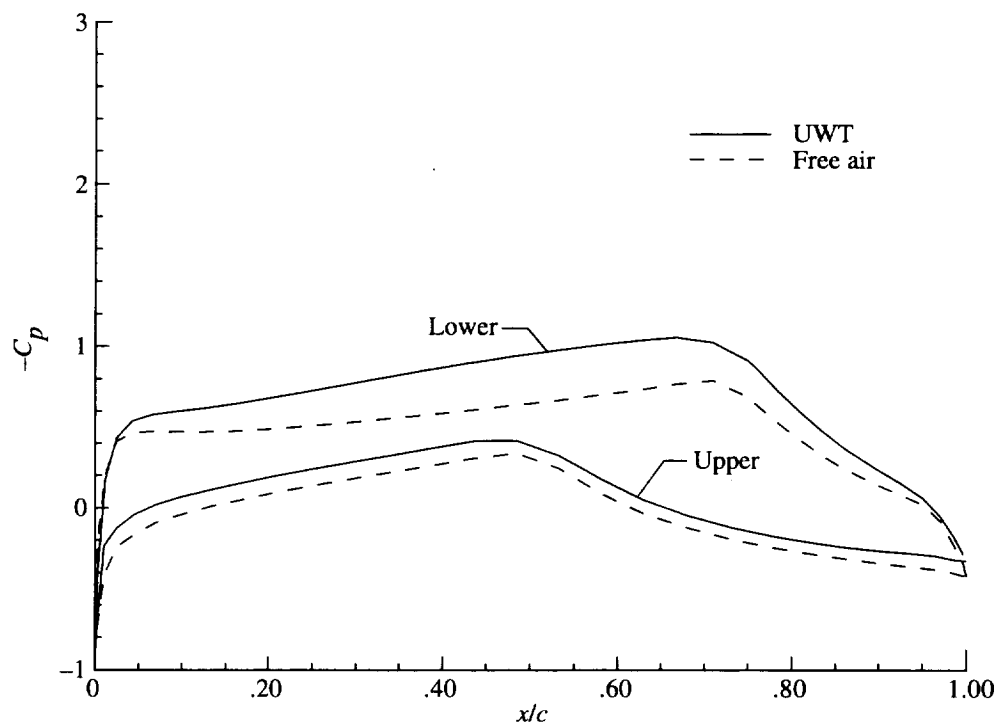


Figure 17. NASA NLF(2)-0415 pressure distribution for  $\alpha = 0^\circ$  and  $\delta_f = 0^\circ$  in UWT.

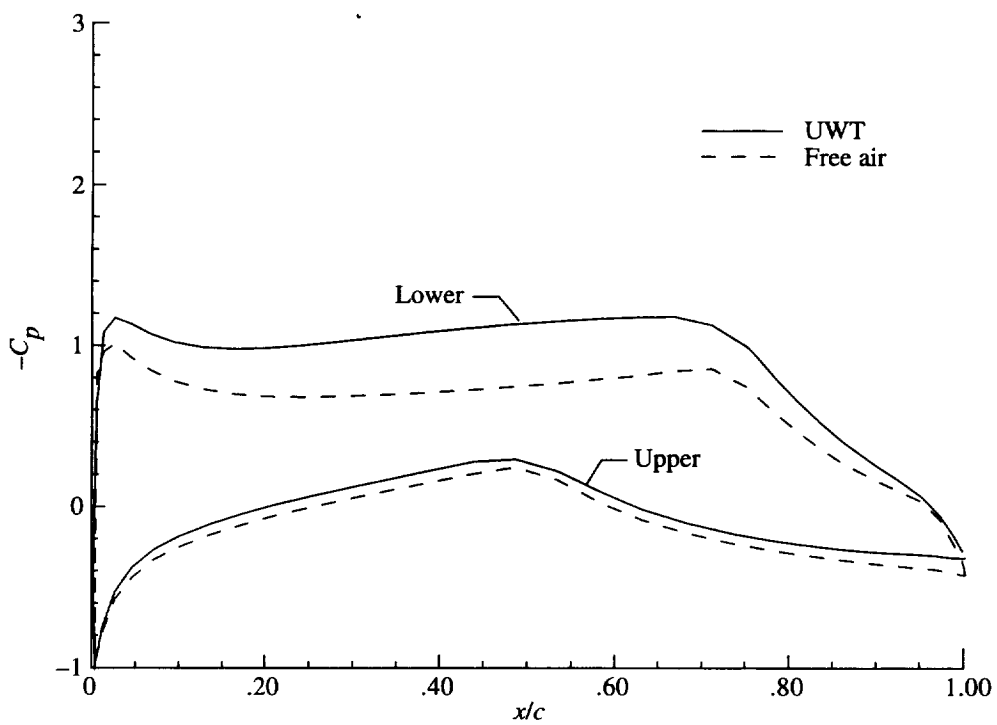


Figure 18. NASA NLF(2)-0415 pressure distribution for  $\alpha = 2^\circ$  and  $\delta_f = 0^\circ$  in UWT.

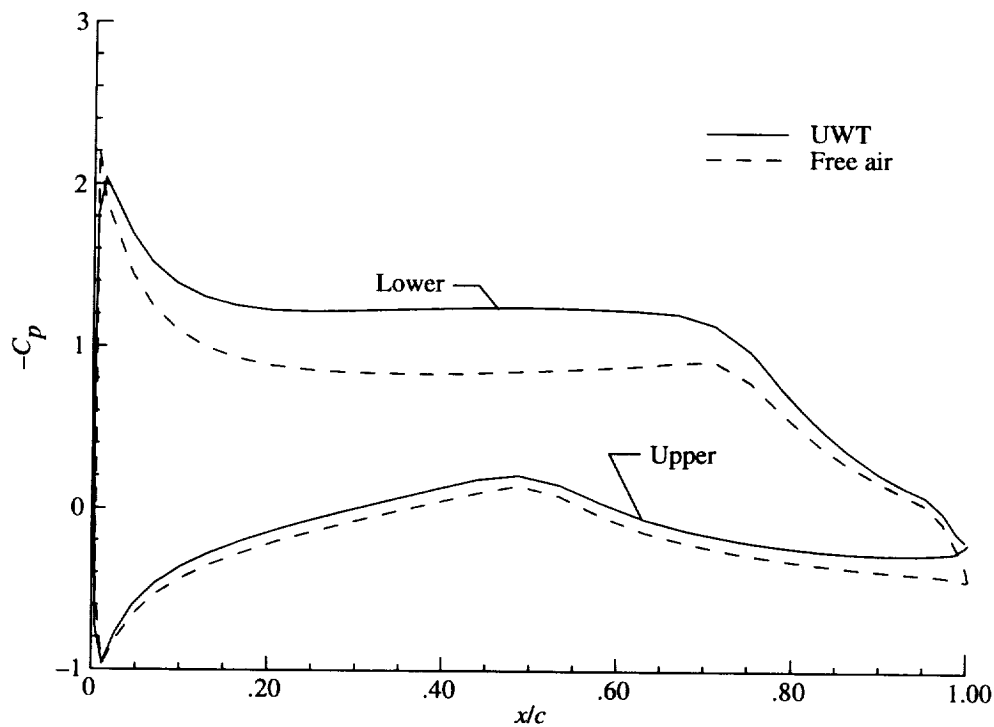


Figure 19. NASA NLF(2)-0415 pressure distribution for  $\alpha = 4^\circ$  and  $\delta_f = 0^\circ$  in UWT.

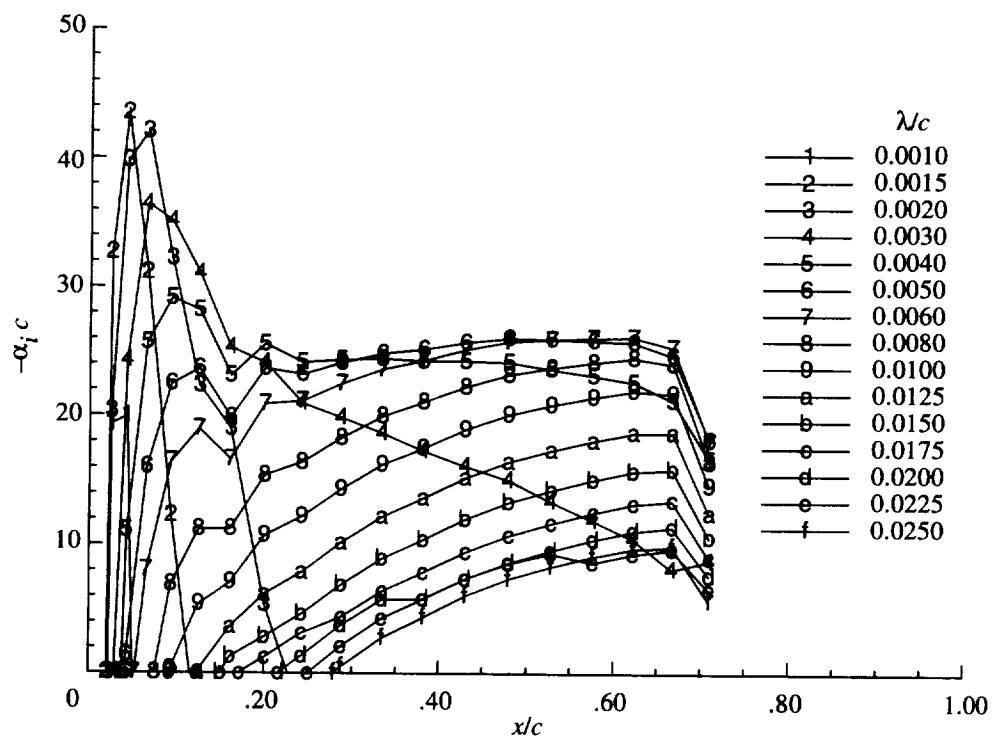


Figure 20. Local spatial growth rates for stationary crossflow vortices at  $\alpha = -4^\circ$  and  $\delta_f = 0^\circ$  in UWT at  $R_c = 3.81 \times 10^6$ .

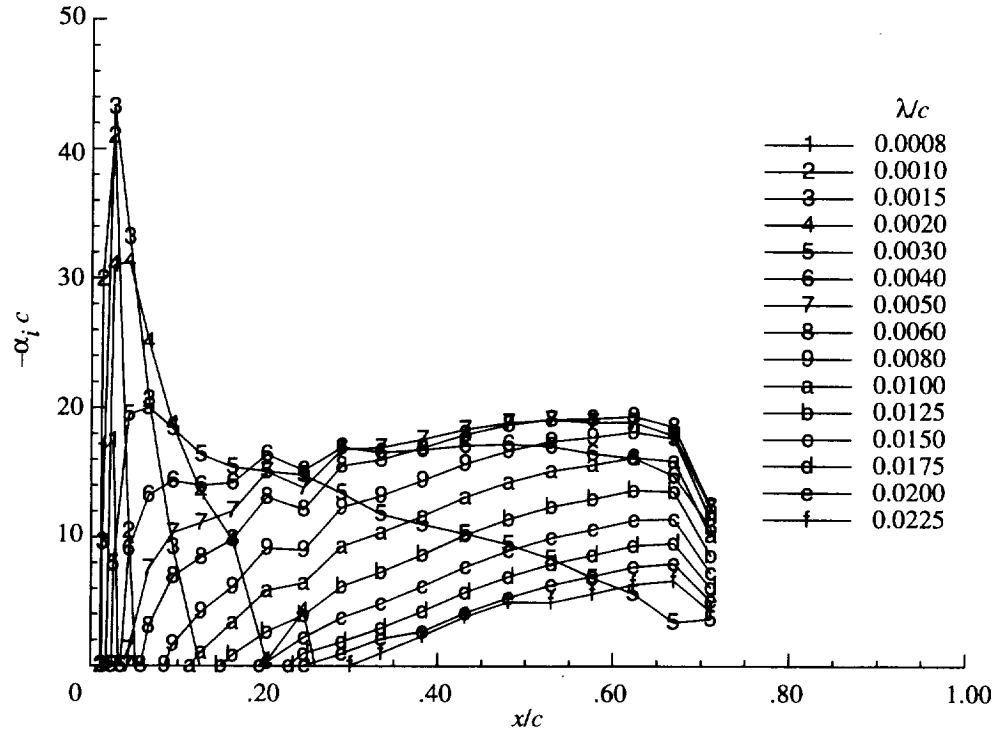


Figure 21. Local spatial growth rates for stationary crossflow vortices at  $\alpha = -2^\circ$  and  $\delta_f = 0^\circ$  in UWT at  $R_c = 3.81 \times 10^6$ .

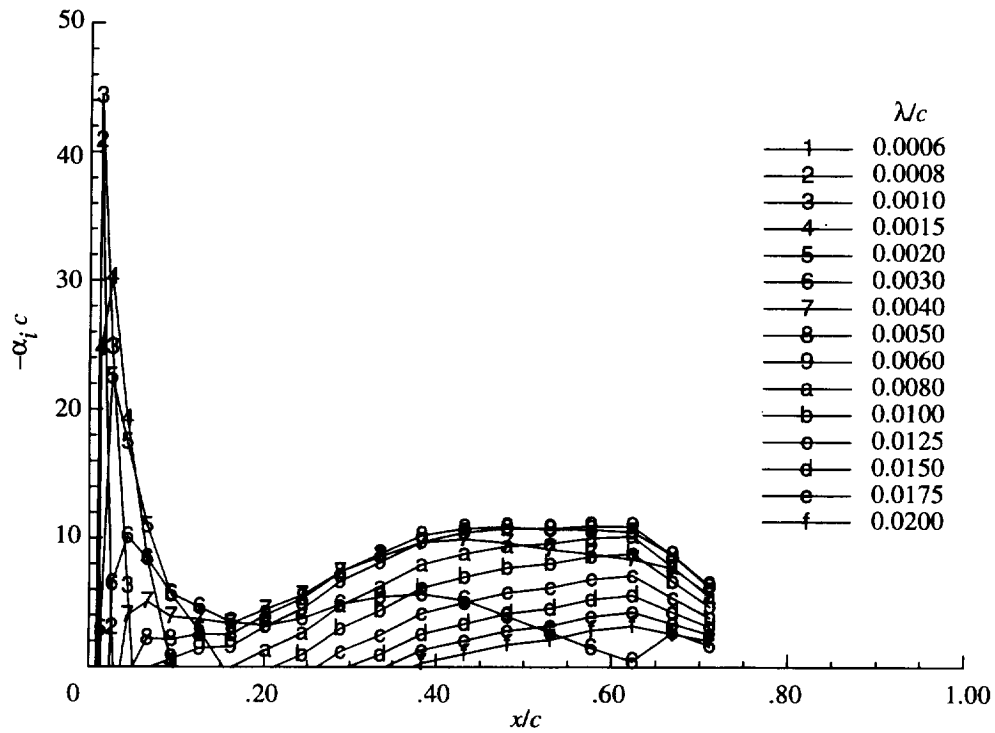


Figure 22. Local spatial growth rates for stationary crossflow vortices at  $\alpha = 0^\circ$  and  $\delta_f = 0^\circ$  in UWT at  $R_c = 3.81 \times 10^6$ .

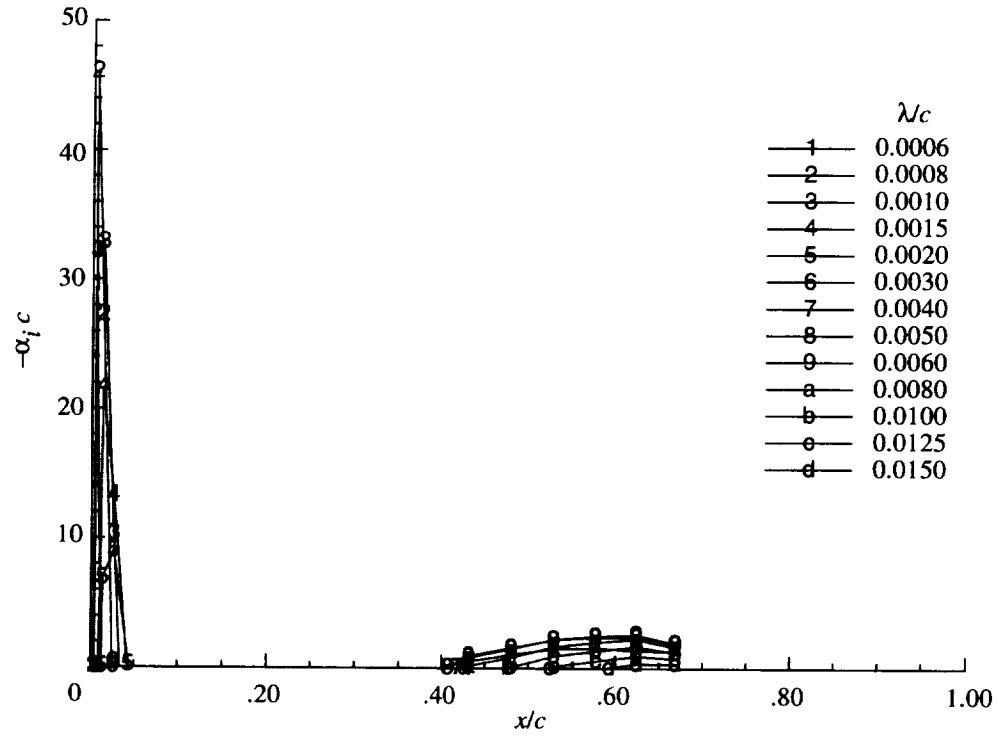


Figure 23. Local spatial growth rates for stationary crossflow vortices at  $\alpha = 2^\circ$  and  $\delta_f = 0^\circ$  in UWT at  $R_c = 3.81 \times 10^6$ .

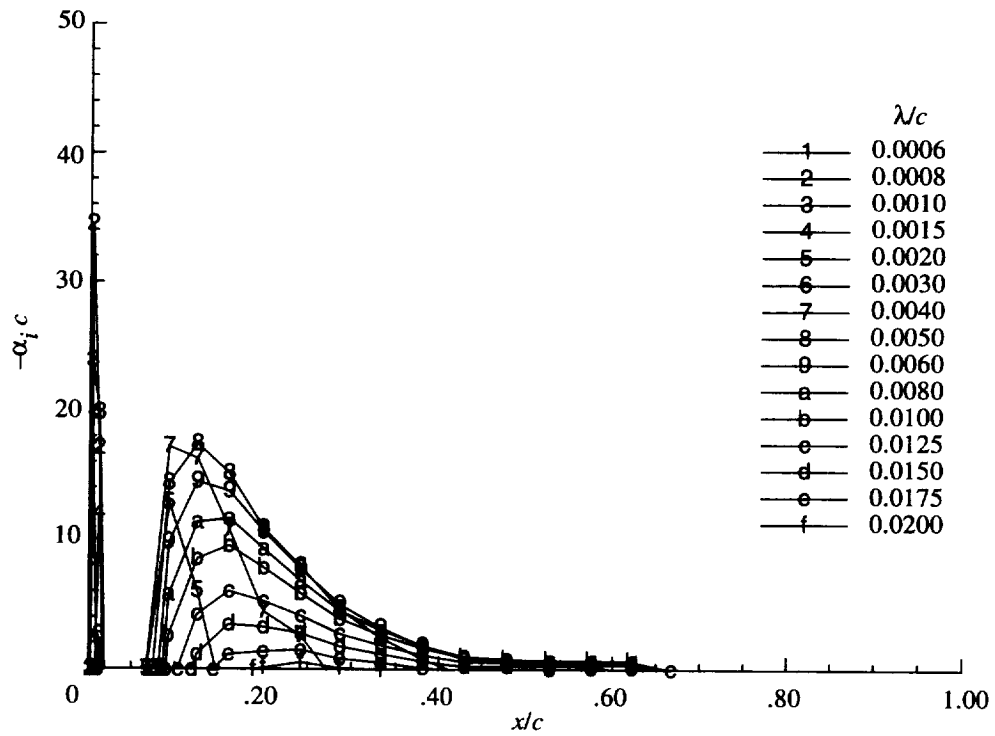


Figure 24. Local spatial growth rates for stationary crossflow vortices at  $\alpha = 4^\circ$  and  $\delta_f = 0^\circ$  in UWT at  $R_c = 3.81 \times 10^6$ .

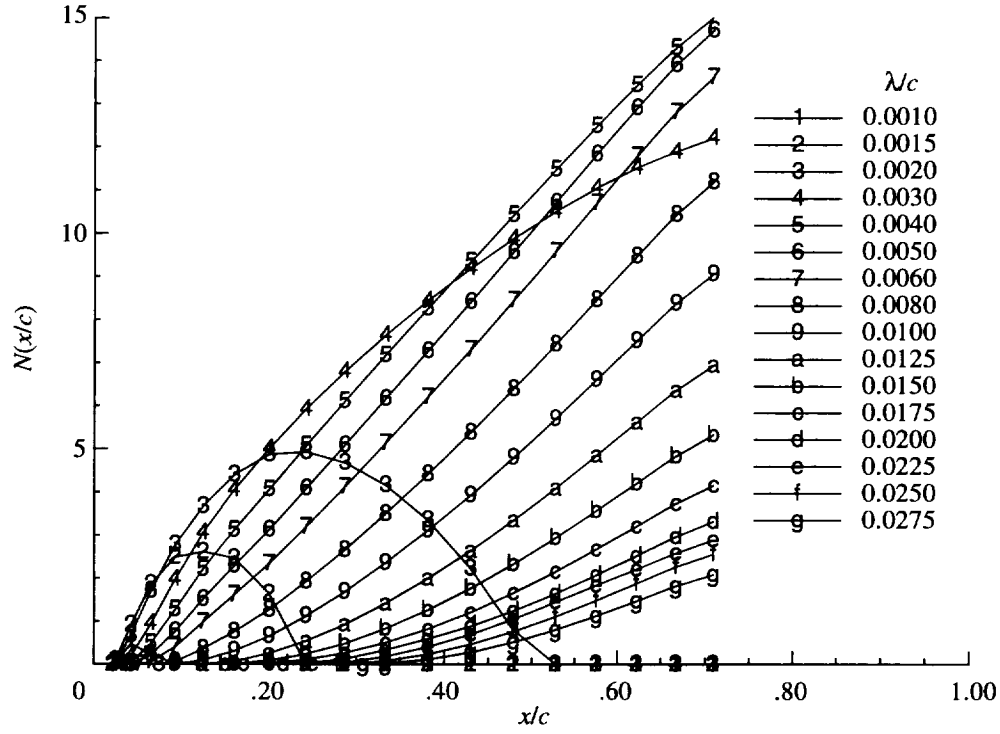


Figure 25.  $N$ -factors for stationary crossflow vortices at  $\alpha = -4^\circ$  and  $\delta_f = 0^\circ$  in UWT at  $R_c = 3.81 \times 10^6$ .

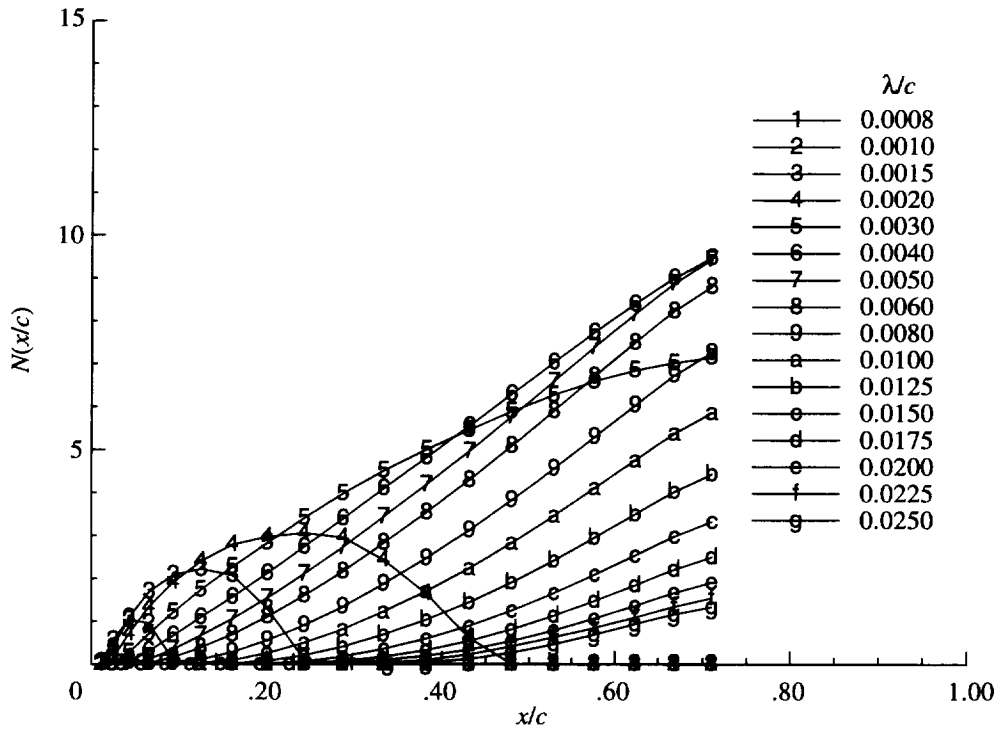


Figure 26.  $N$ -factors for stationary crossflow vortices at  $\alpha = -2^\circ$  and  $\delta_f = 0^\circ$  in UWT at  $R_c = 3.81 \times 10^6$ .

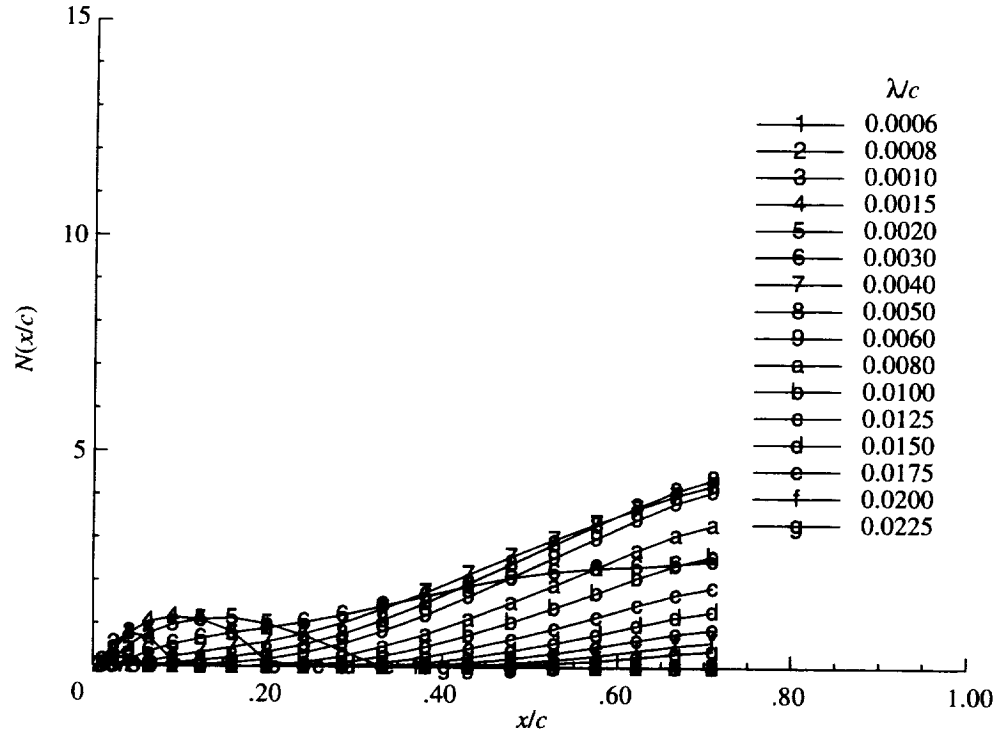


Figure 27.  $N$ -factors for stationary crossflow vortices at  $\alpha = 0^\circ$  and  $\delta_f = 0^\circ$  in UWT at  $R_c = 3.81 \times 10^6$ .

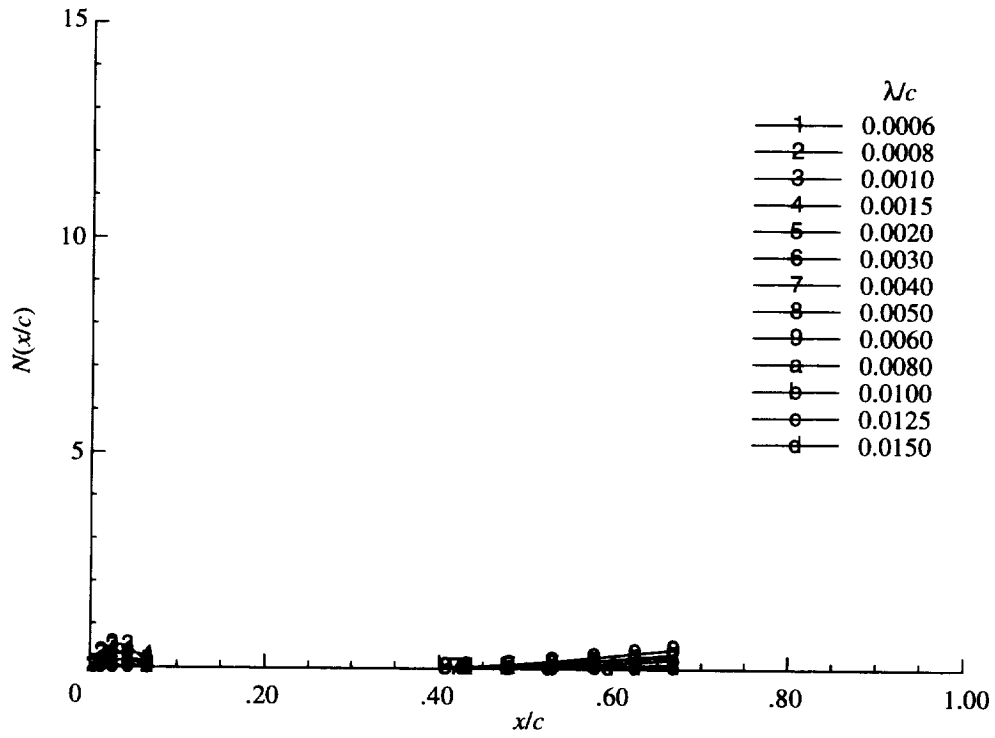


Figure 28.  $N$ -factors for stationary crossflow vortices at  $\alpha = 2^\circ$  and  $\delta_f = 0^\circ$  in UWT at  $R_c = 3.81 \times 10^6$ .

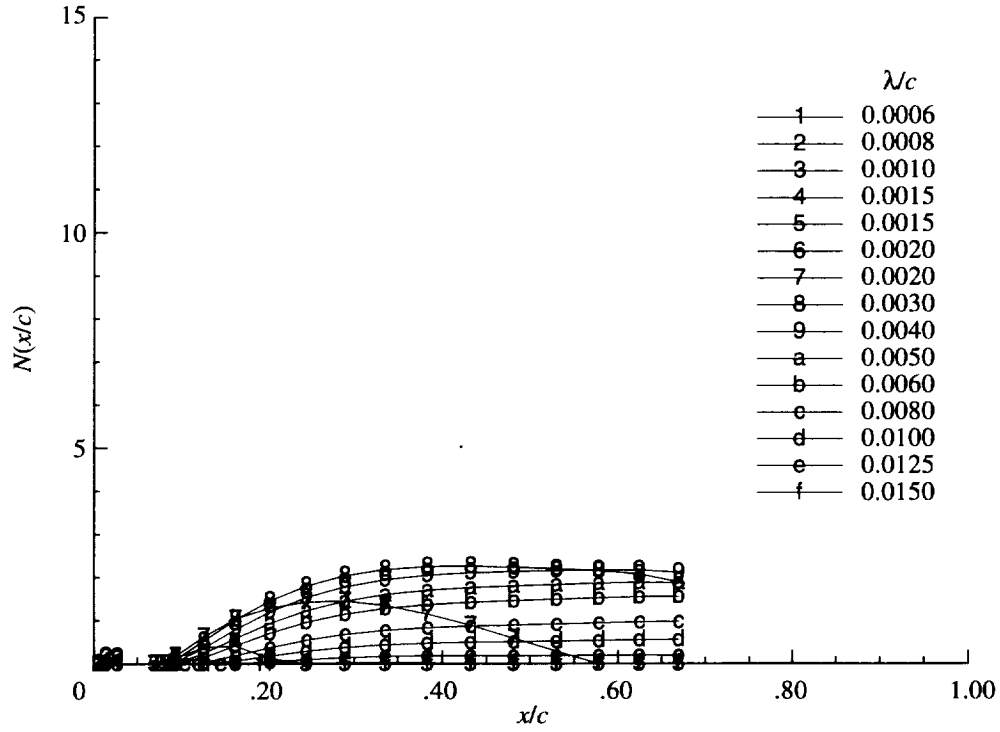


Figure 29.  $N$ -factors for stationary crossflow vortices at  $\alpha = 4^\circ$  and  $\delta_f = 0^\circ$  in UWT at  $R_c = 3.81 \times 10^6$ .

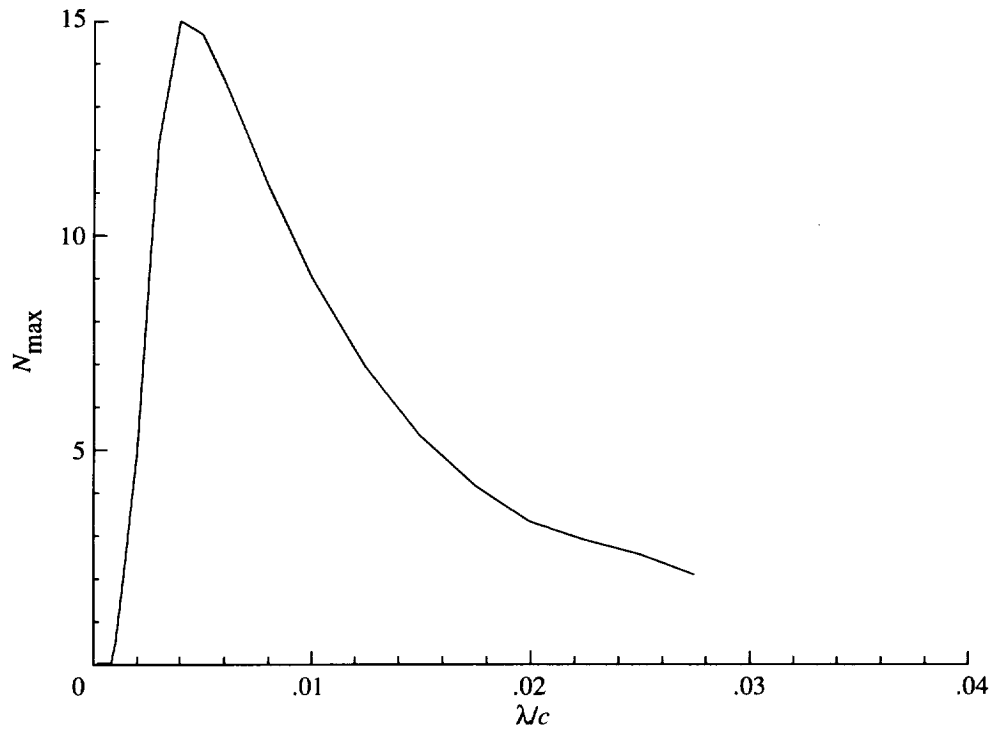


Figure 30. Maximum  $N$ -factors for stationary crossflow vortices at  $\alpha = -4^\circ$  and  $\delta_f = 0^\circ$  in UWT at  $R_c = 3.81 \times 10^6$ .

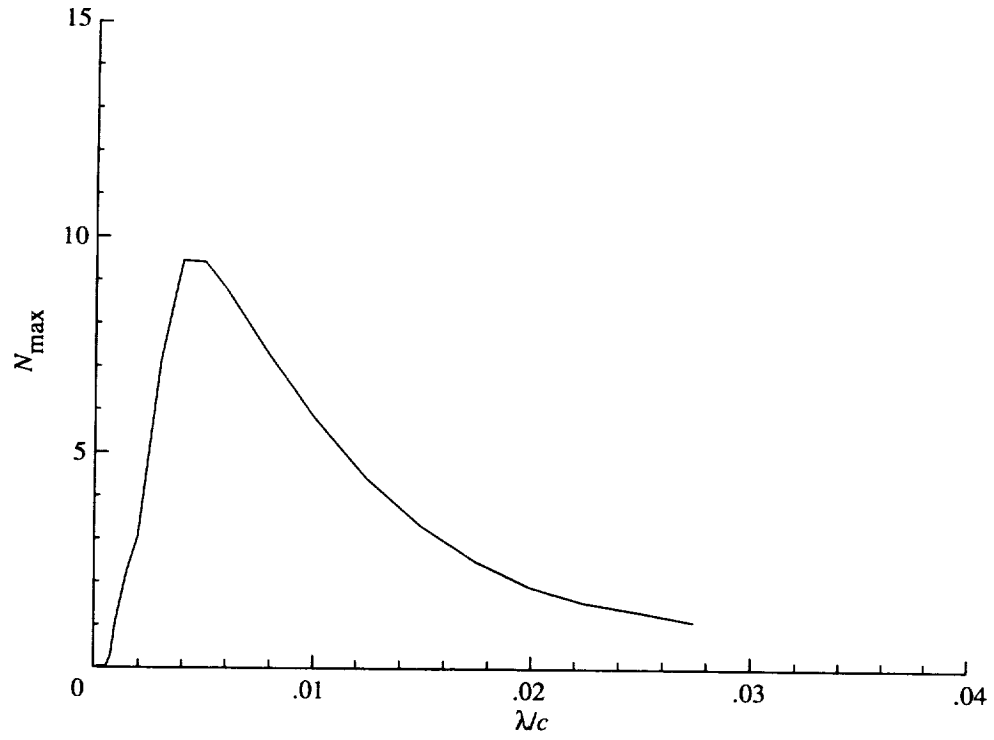


Figure 31. Maximum  $N$ -factors for stationary crossflow vortices at  $\alpha = -2^\circ$  and  $\delta_f = 0^\circ$  in UWT at  $R_c = 3.81 \times 10^6$ .

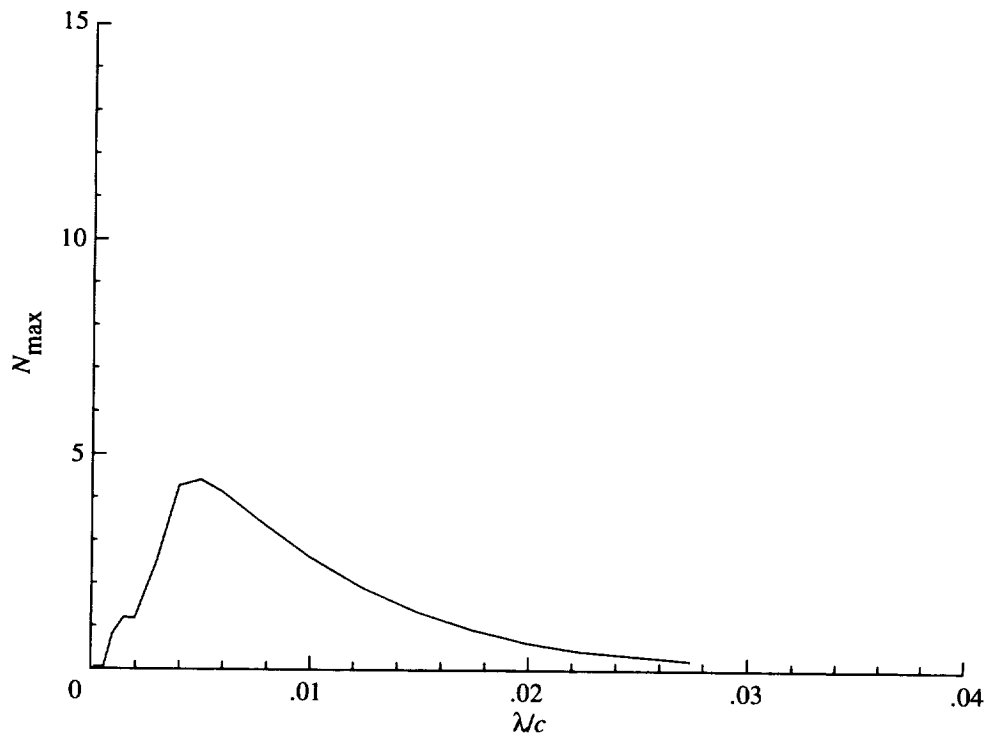


Figure 32. Maximum  $N$ -factors for stationary crossflow vortices at  $\alpha = 0^\circ$  and  $\delta_f = 0^\circ$  in UWT at  $R_c = 3.81 \times 10^6$ .



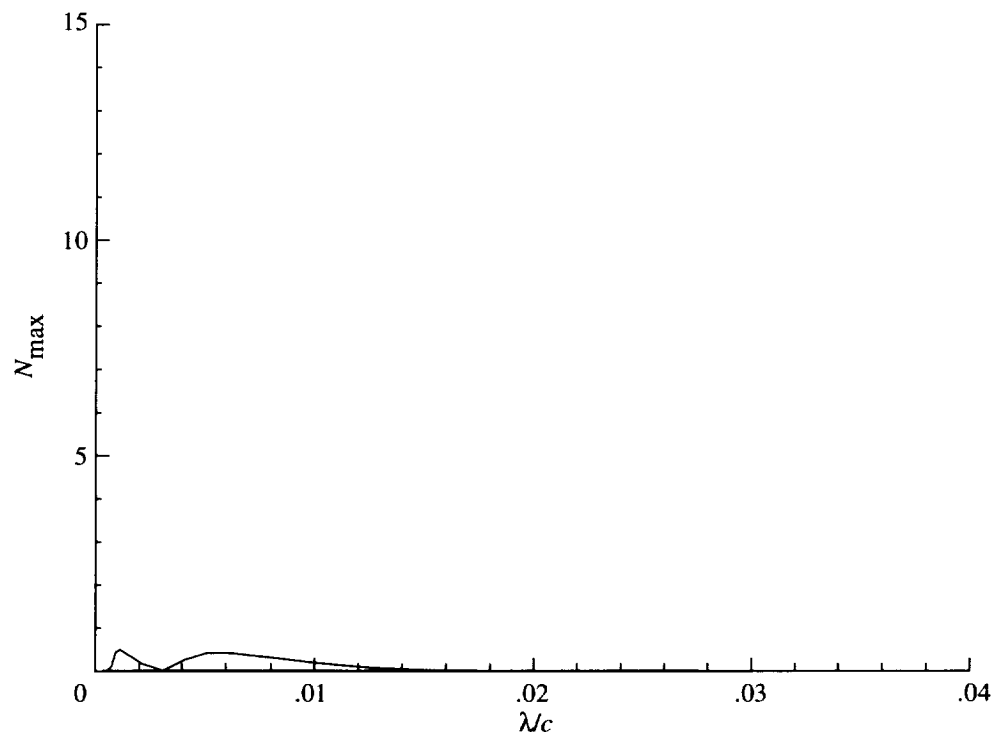


Figure 33. Maximum  $N$ -factors for stationary crossflow vortices at  $\alpha = 2^\circ$  and  $\delta_f = 0^\circ$  in UWT at  $R_c = 3.81 \times 10^6$ .

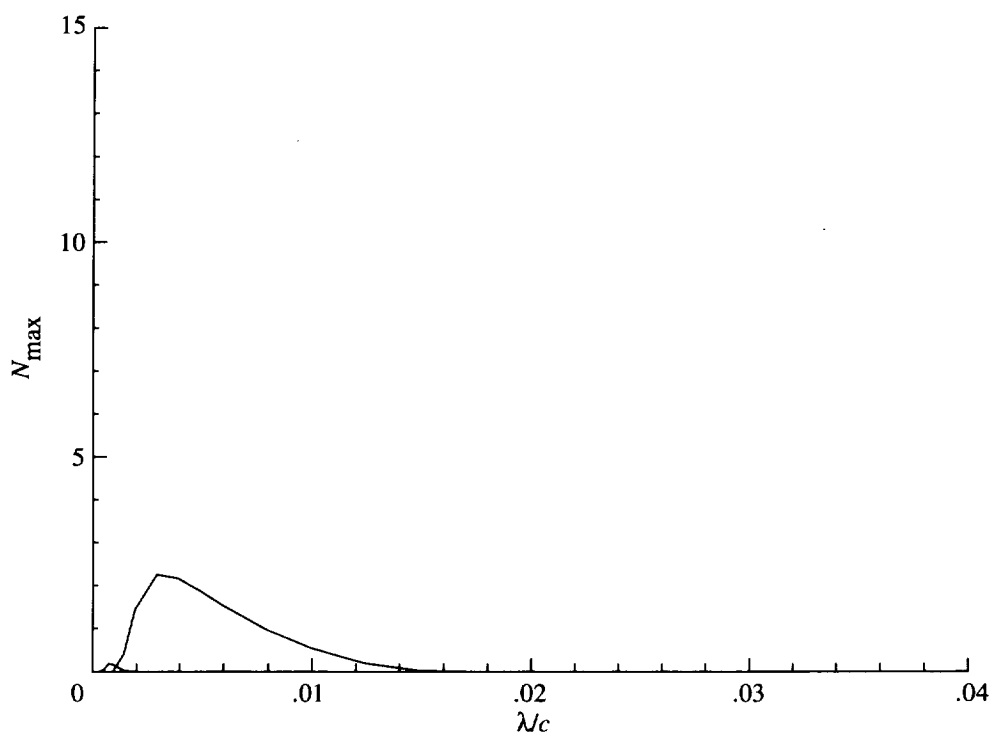


Figure 34. Maximum  $N$ -factors for stationary crossflow vortices at  $\alpha = 4^\circ$  and  $\delta_f = 0^\circ$  in UWT at  $R_c = 3.81 \times 10^6$ .

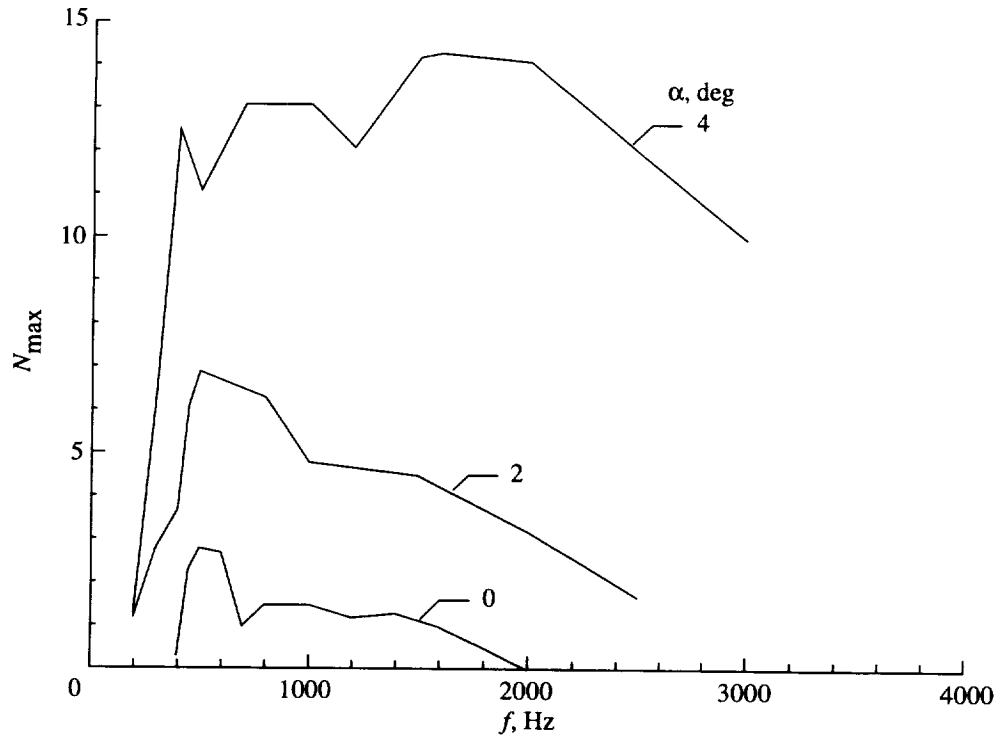


Figure 35. Maximum  $N$ -factors for Tollmien-Schlichting waves for  $\alpha = 0^\circ$ ,  $2^\circ$ , and  $4^\circ$  and  $\delta_f = 0^\circ$  in UWT at  $R_c = 3.81 \times 10^6$ .

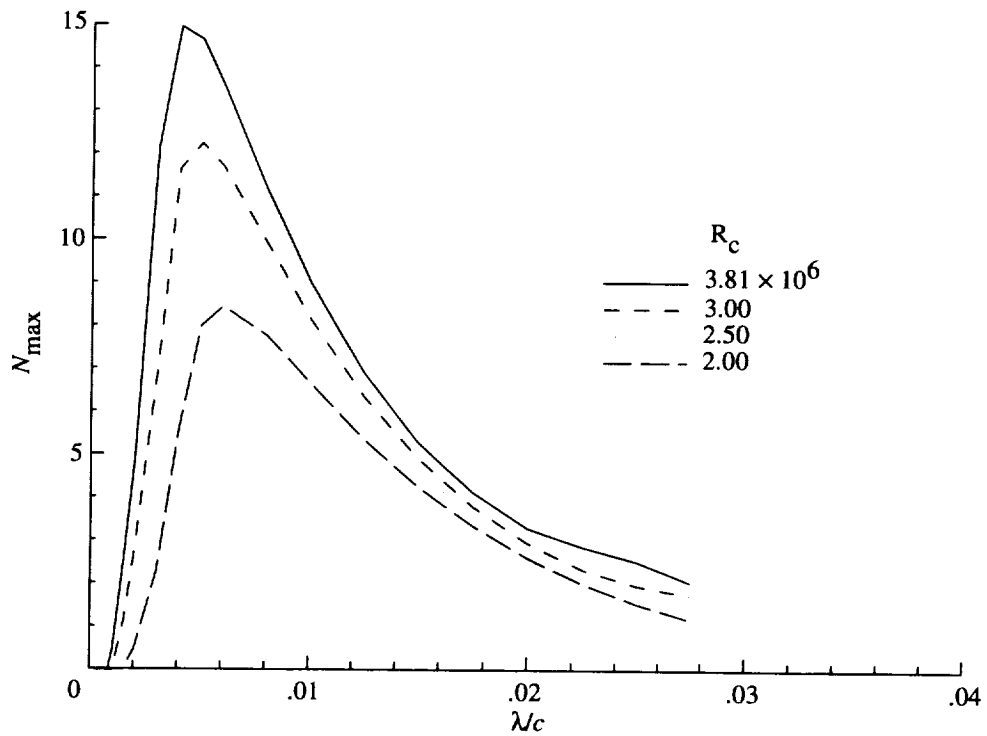


Figure 36. Maximum  $N$ -factors for stationary crossflow vortices at  $\alpha = -4^\circ$  and  $\delta_f = 0^\circ$  in UWT for a range of Reynolds number.

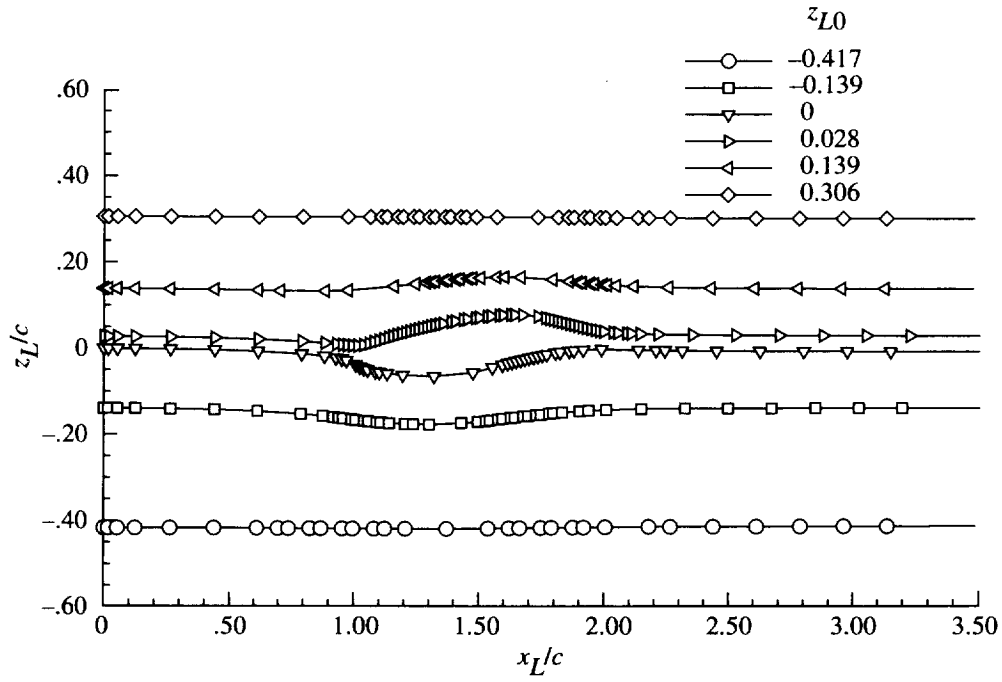


Figure 37. Streamline traces of wind tunnel end liner on  $X_L$ - $Z_L$  plane for  $\alpha = -4^\circ$ .

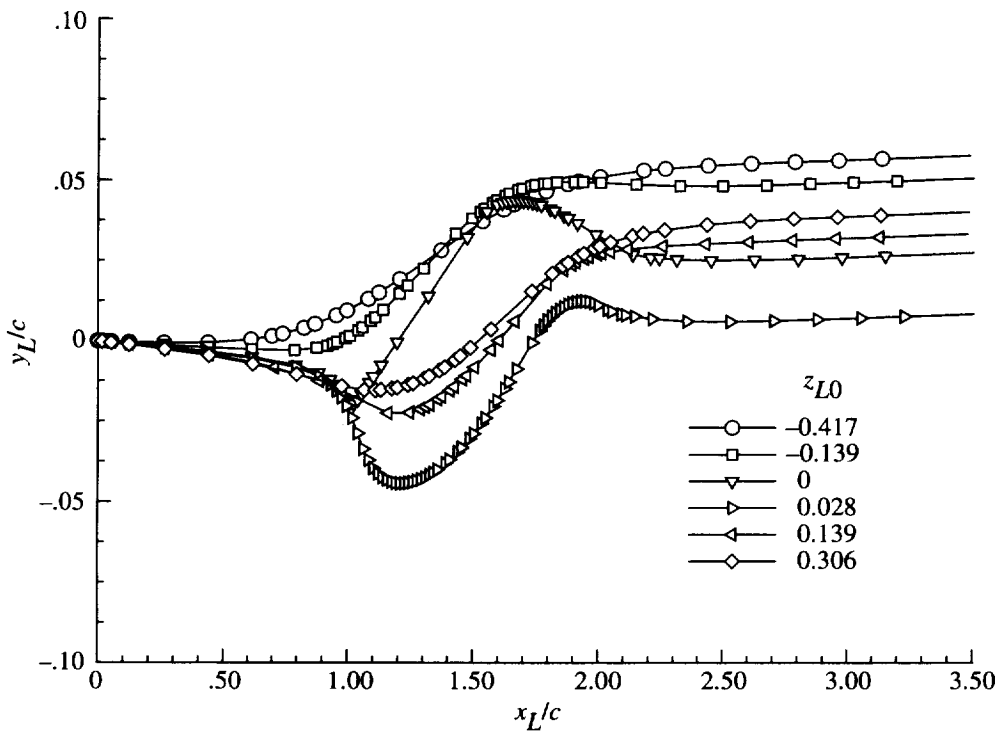


Figure 38. Lateral deflections of end-liner surface at various distances from wing chord plane for  $\alpha = -4^\circ$ .

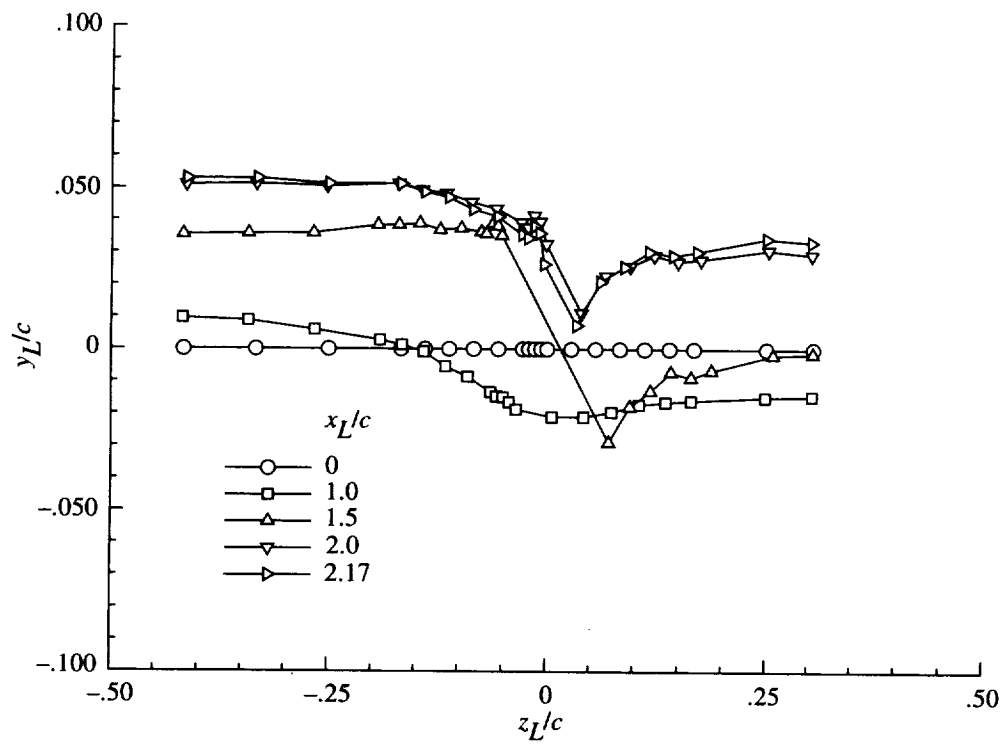


Figure 39. End-liner contours in  $Y_L$ - $Z_L$  plane at various longitudinal positions for  $\alpha = -4^\circ$ .

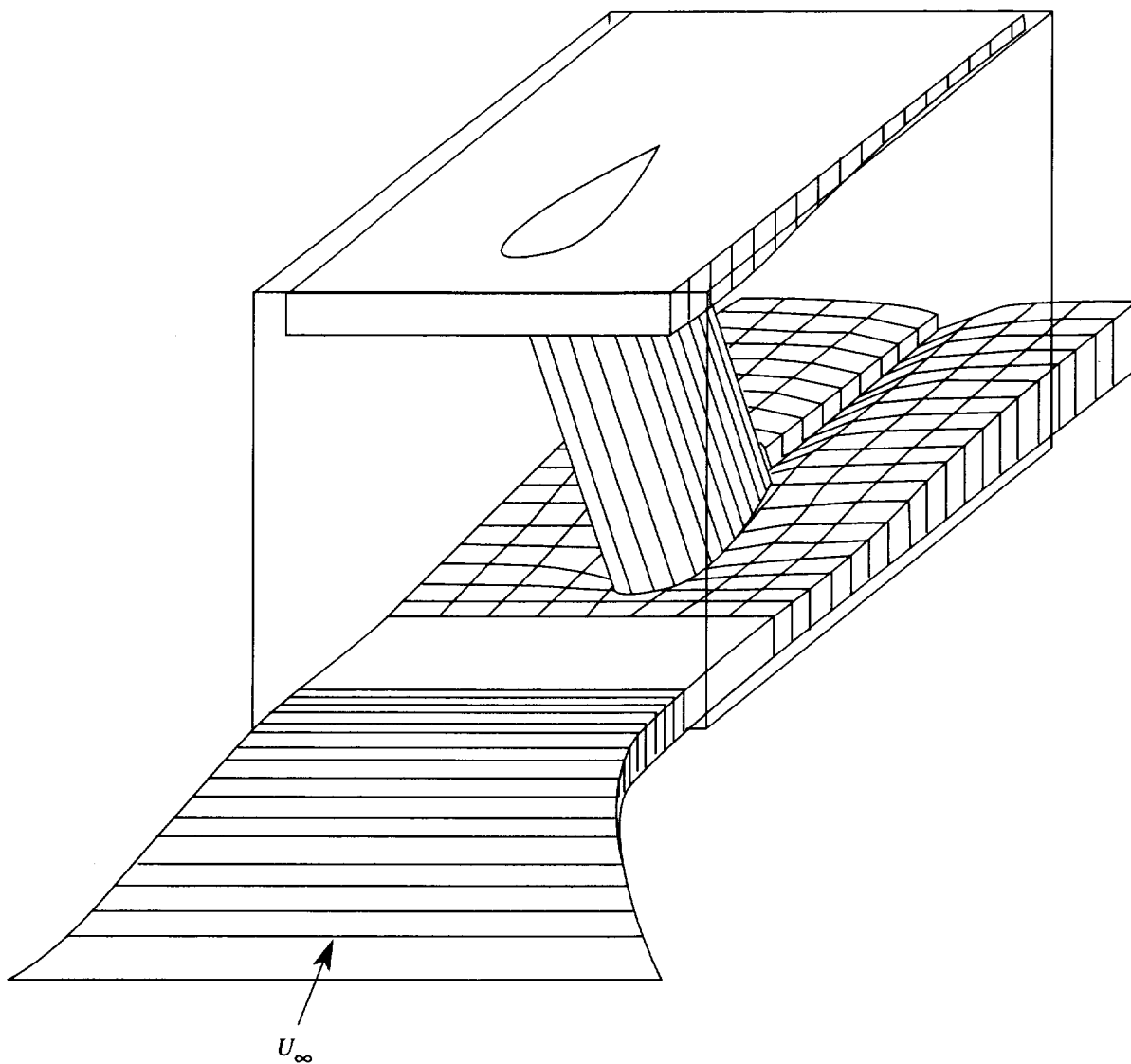


Figure 40. Wind tunnel test section with swept-wing model and end liners installed.

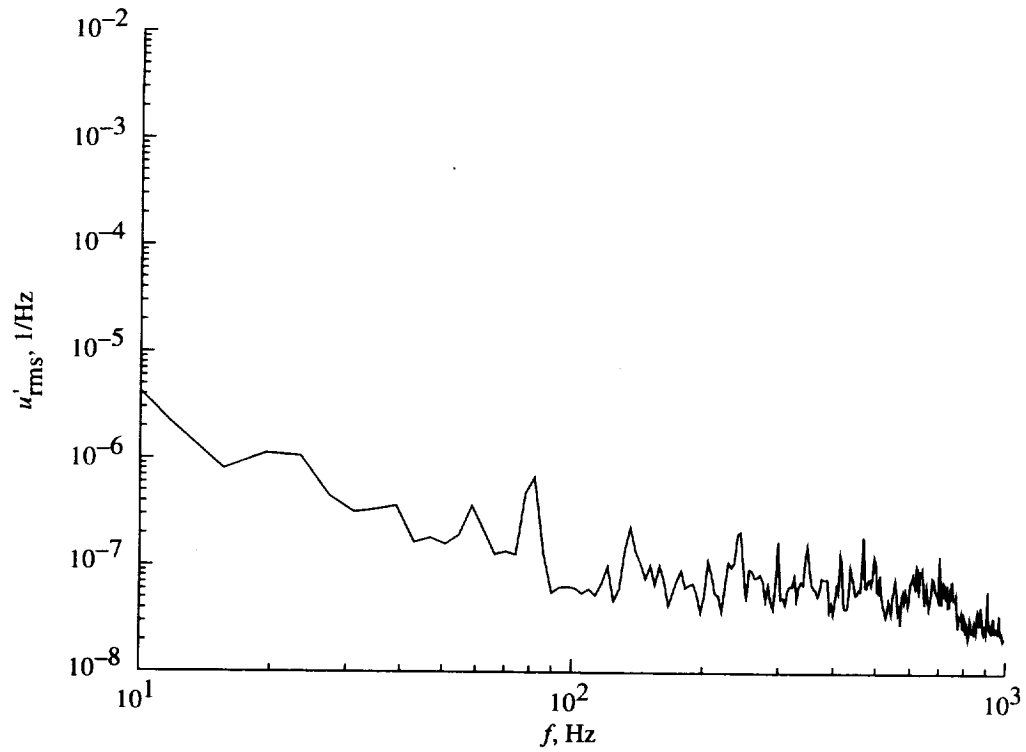


Figure 41. Free-stream velocity spectrum for  $R_c = 3.27 \times 10^6$ .

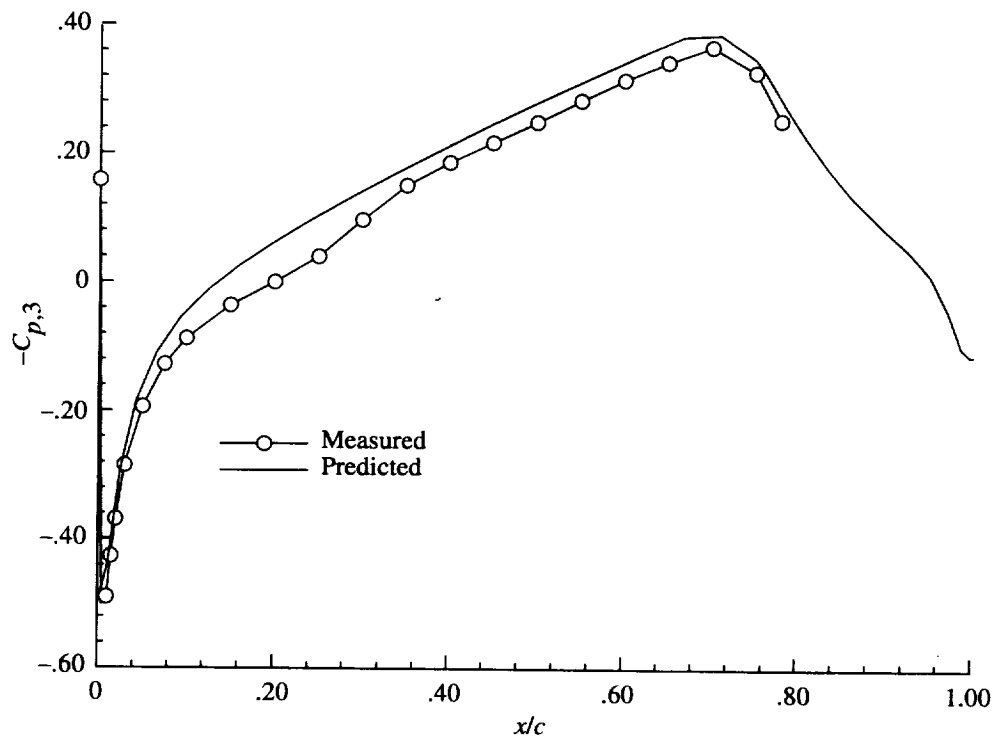


Figure 42. Measured and predicted model pressure coefficients at upper end of model for  $\alpha = -4^\circ$ .

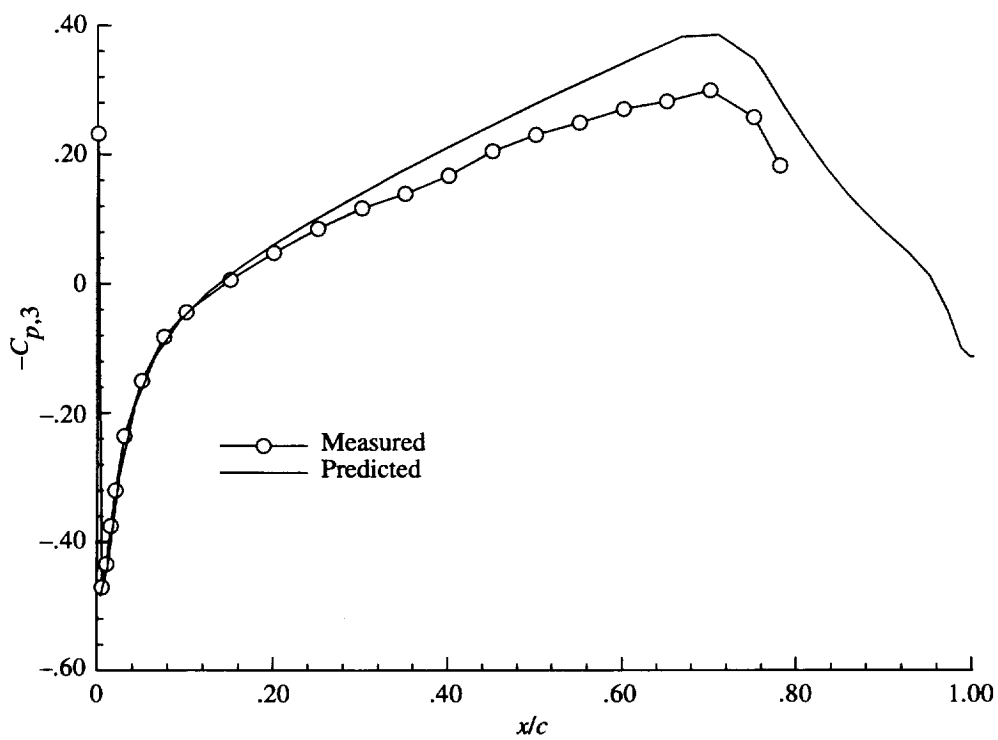


Figure 43. Measured and predicted model pressure coefficients at lower end of model for  $\alpha = -4^\circ$ .



Figure 44. Naphthalene flow visualization at  $\alpha = -4^\circ$  and  $R_c = 1.93 \times 10^6$ .



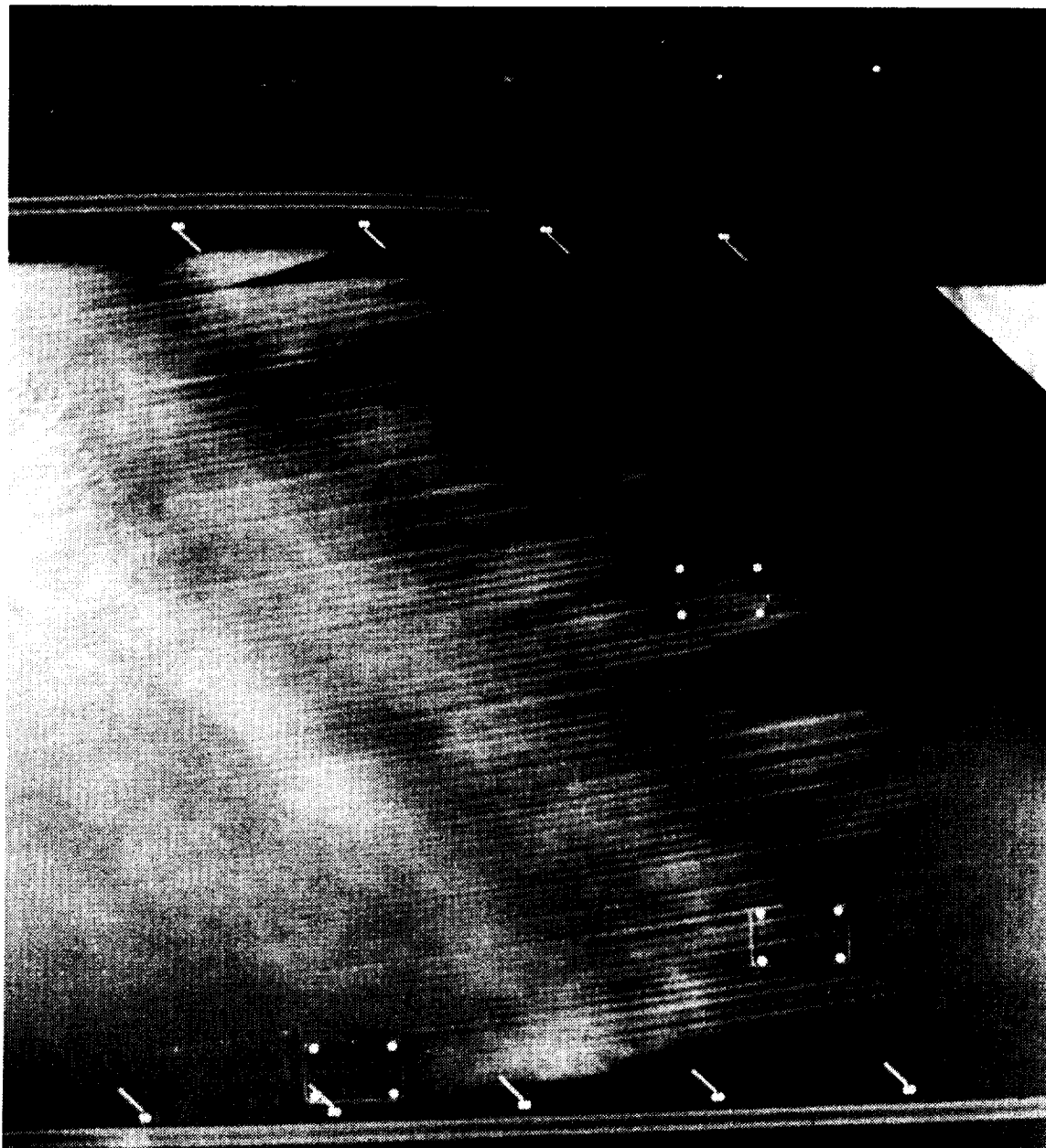


Figure 45. Naphthalene flow visualization at  $\alpha = -4^\circ$  and  $R_c = 2.19 \times 10^6$ .



Figure 46. Naphthalene flow visualization at  $\alpha = -4^\circ$  and  $R_c = 2.40 \times 10^6$ .

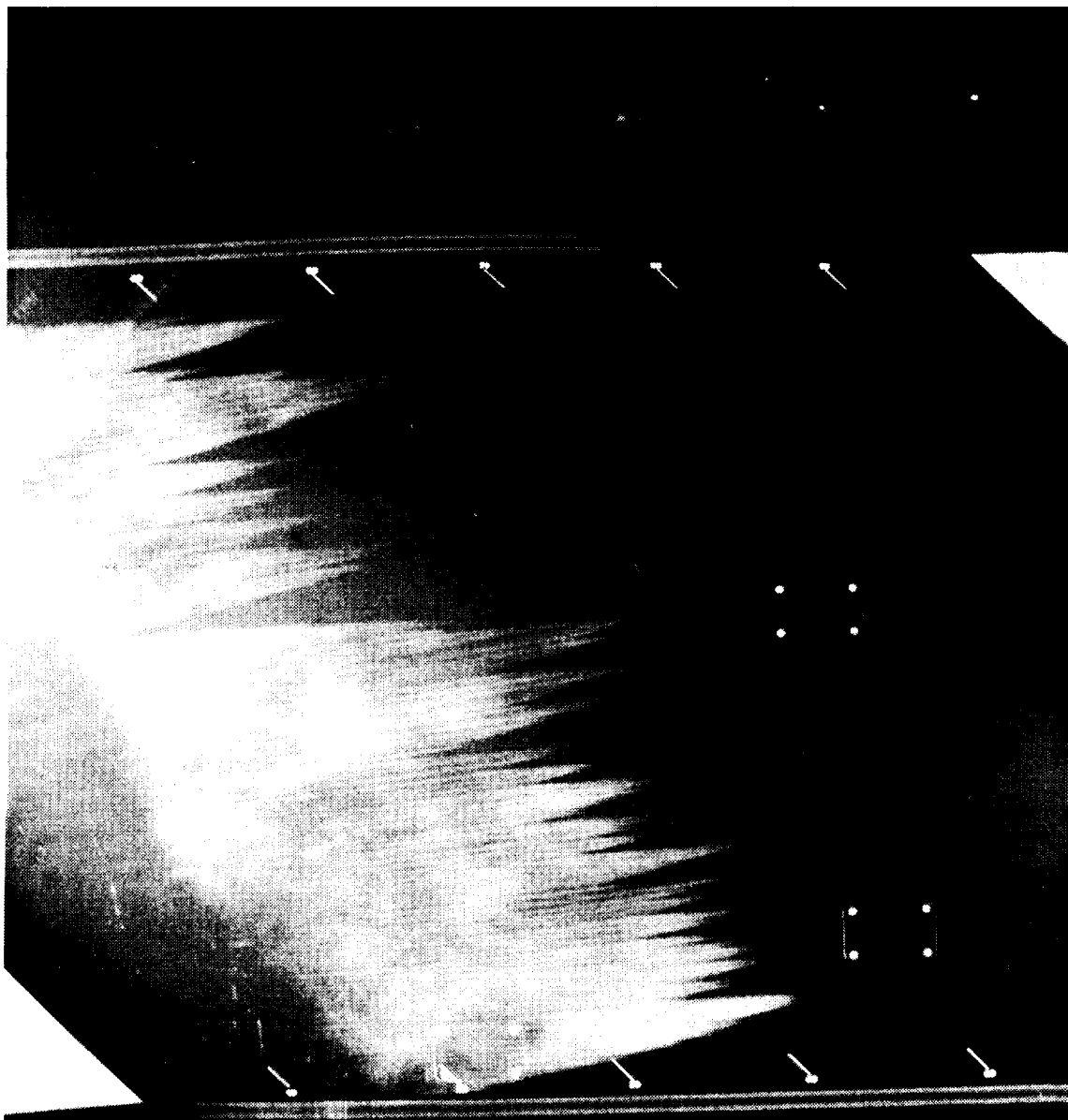


Figure 47. Naphthalene flow visualization at  $\alpha = -4^\circ$  and  $R_c = 2.73 \times 10^6$ .



Figure 48. Naphthalene flow visualization at  $\alpha = -4^\circ$  and  $R_c = 3.27 \times 10^6$ .



Figure 49. Naphthalene flow visualization with vortex tracks in turbulent regions shown.

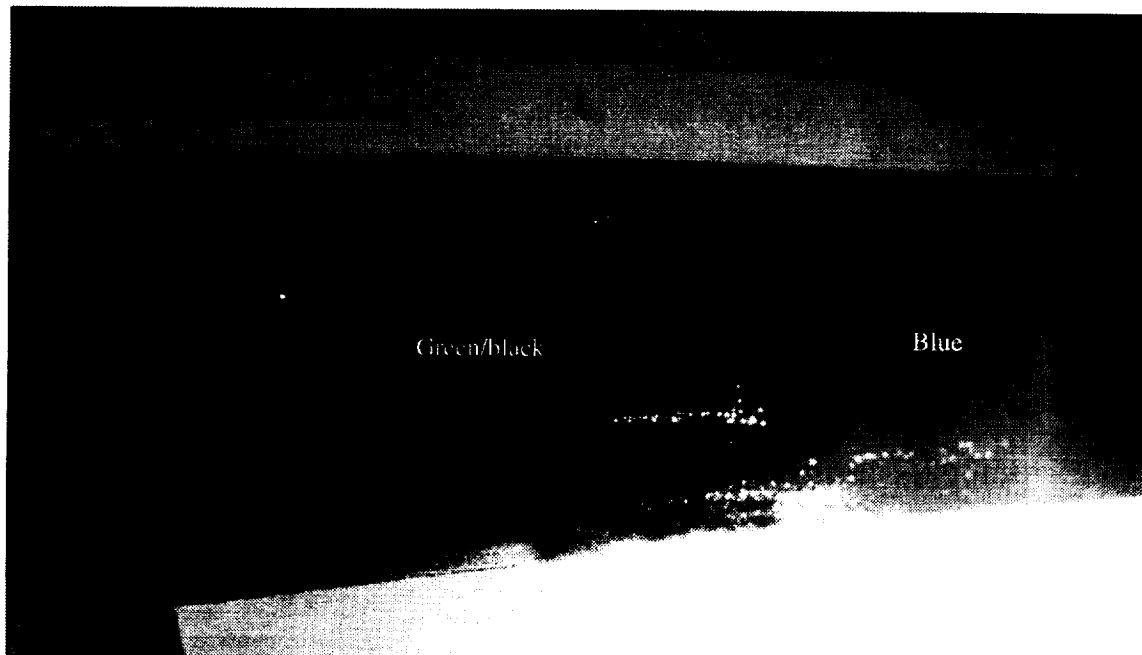


Figure 50. Liquid-crystal flow visualization.

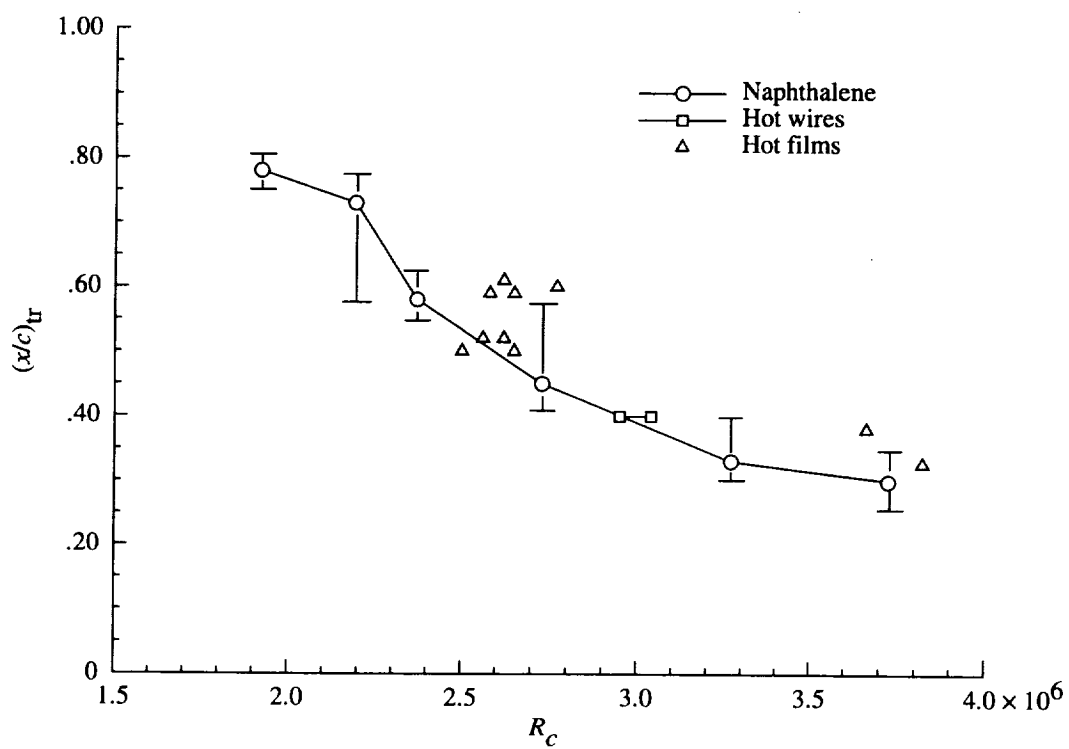


Figure 51. Transition location versus Reynolds number at  $\alpha = -4^\circ$ .

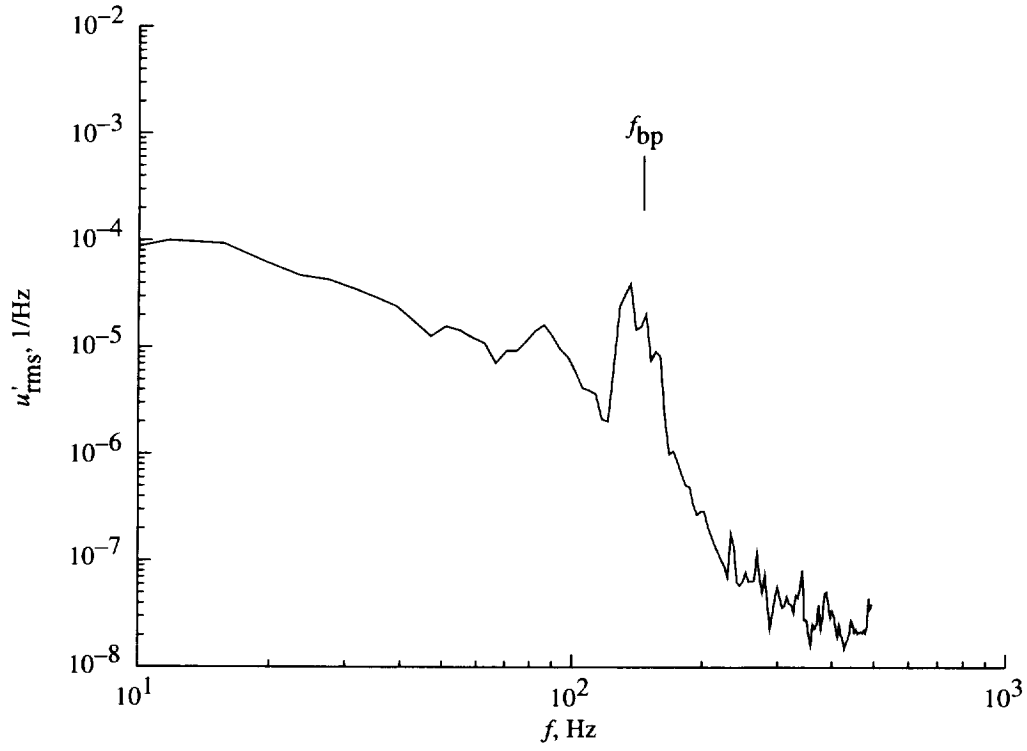


Figure 52. Boundary-layer velocity spectrum at  $\alpha = -4^\circ$  and  $R_c = 2.62 \times 10^6$  at  $x/c = 0.40$ .

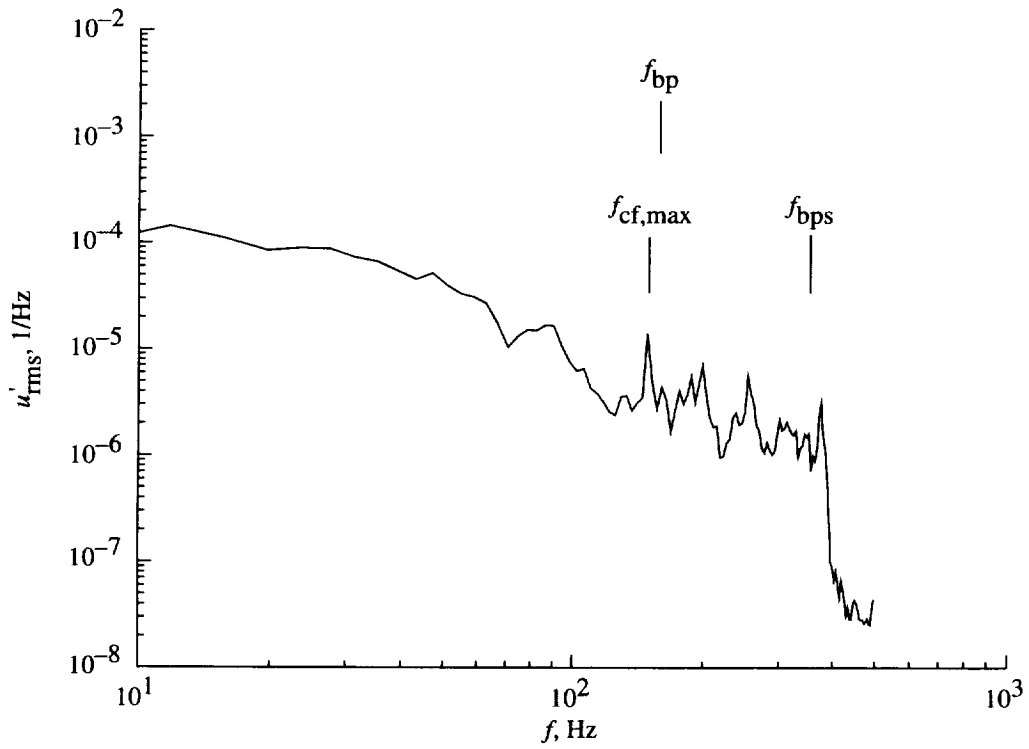


Figure 53. Boundary-layer velocity spectrum at  $\alpha = -4^\circ$  and  $R_c = 2.82 \times 10^6$  at  $x/c = 0.40$ .

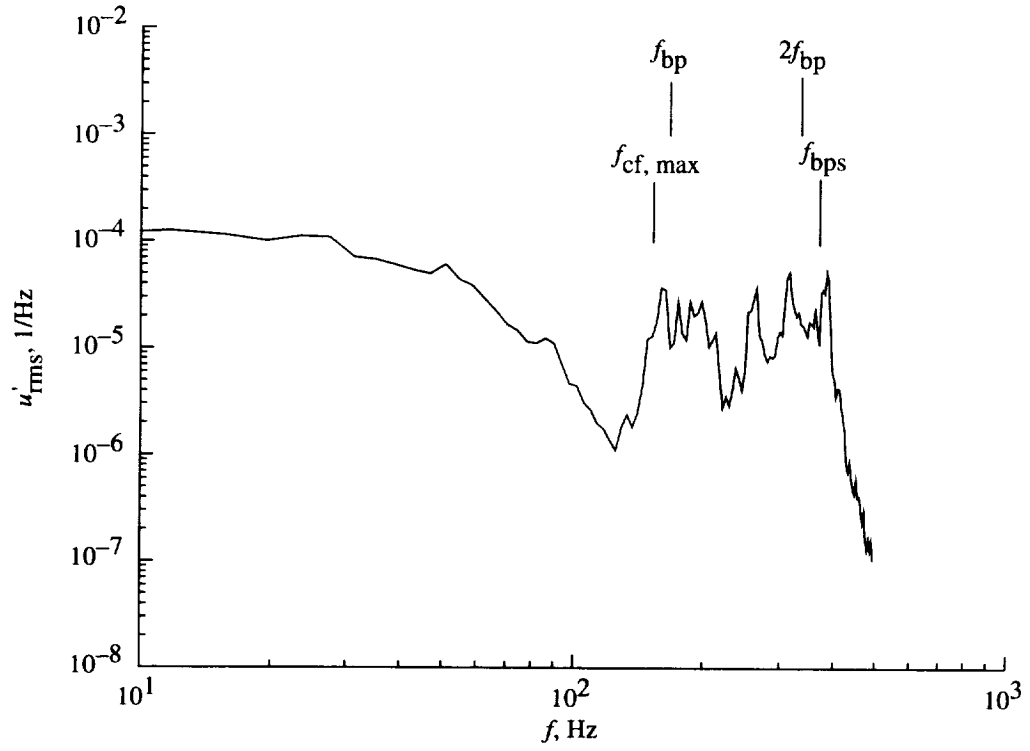


Figure 54. Boundary-layer velocity spectrum at  $\alpha = -4^\circ$  and  $R_c = 2.92 \times 10^6$  at  $x/c = 0.40$ .

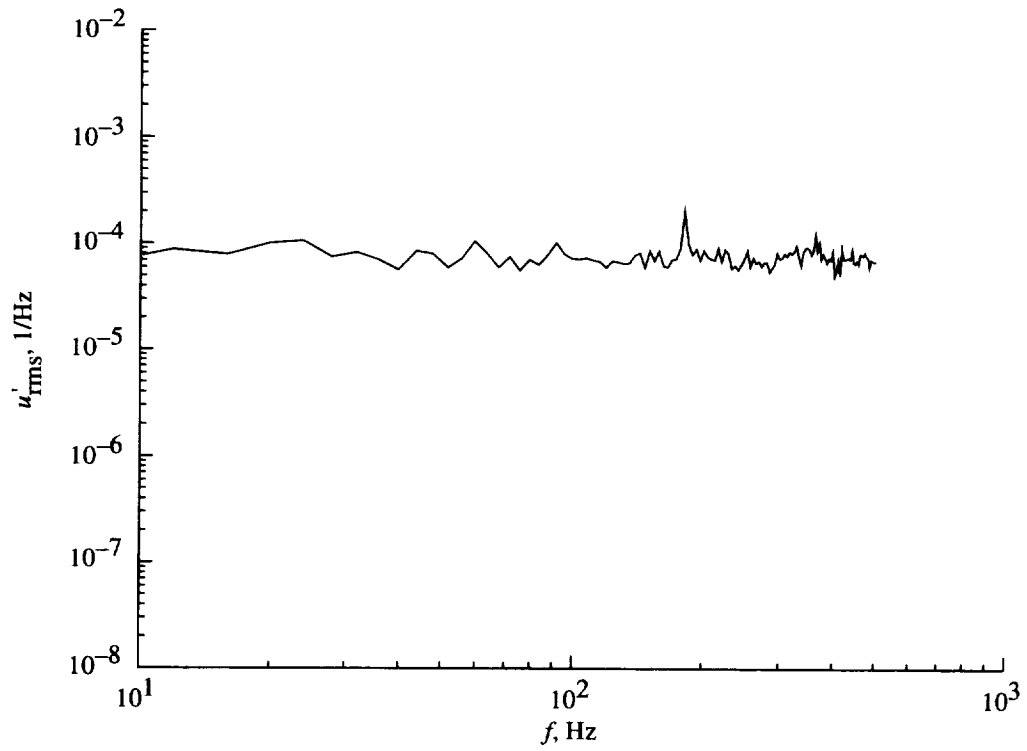


Figure 55. Boundary-layer velocity spectrum at  $\alpha = -4^\circ$  and  $R_c = 3.28 \times 10^6$  at  $x/c = 0.40$ .



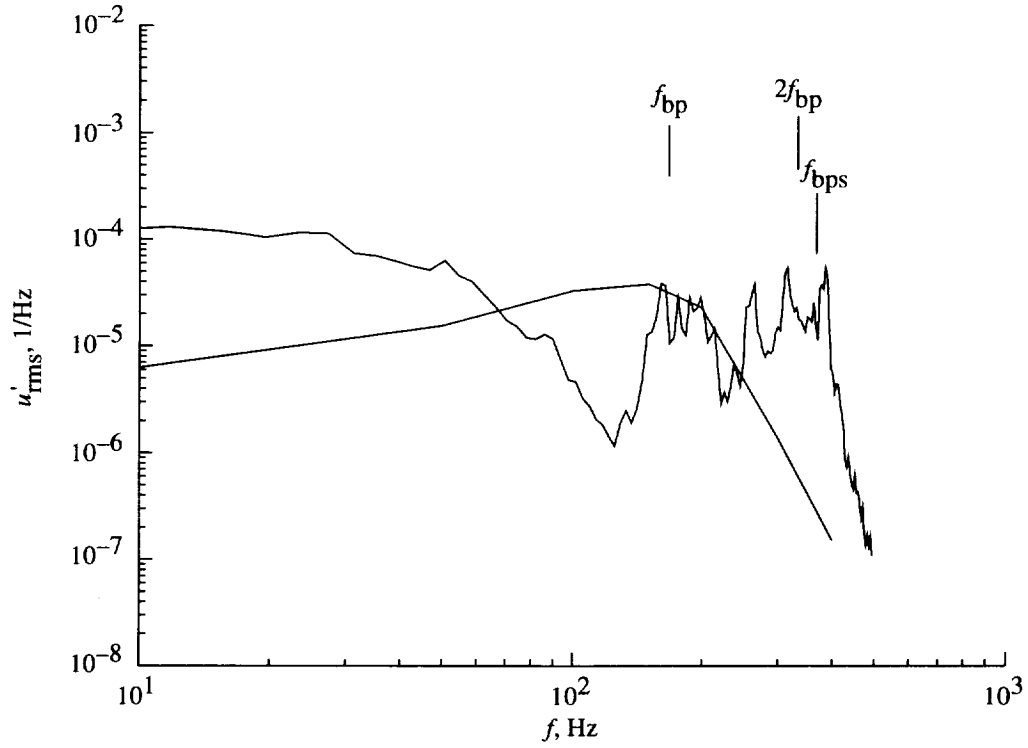


Figure 56. Measured and predicted boundary-layer velocity spectra at  $\alpha = -4^\circ$  and  $R_c = 2.92 \times 10^6$ .

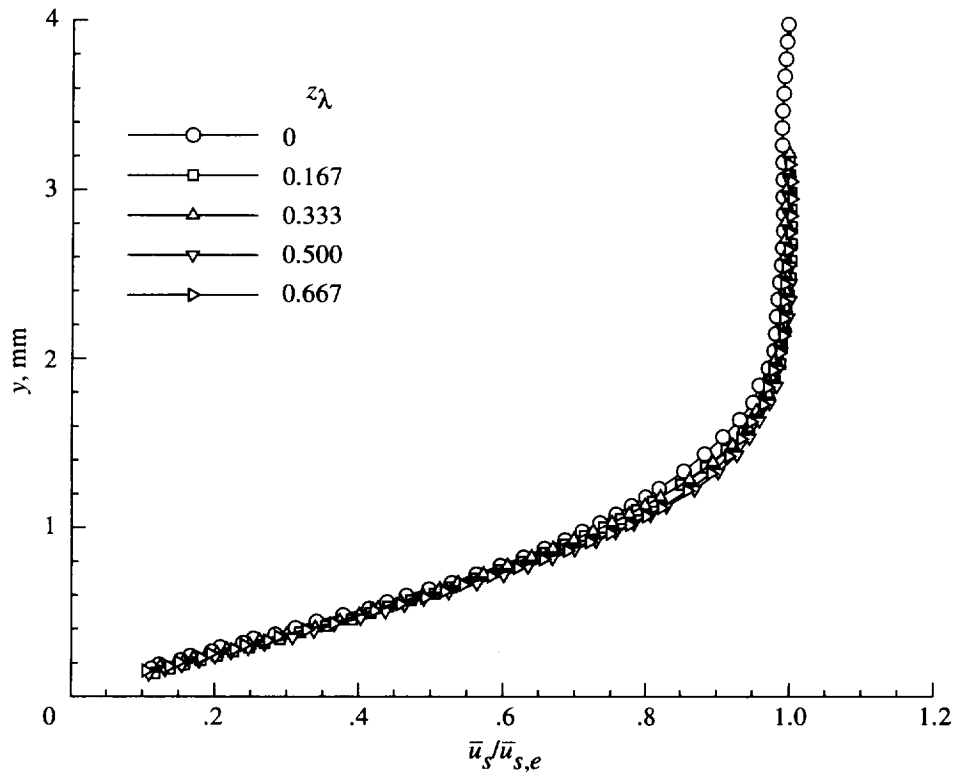


Figure 57. Streamwise velocity profiles at  $x/c = 0.20$ ,  $\alpha = -4^\circ$ , and  $R_c = 2.62 \times 10^6$ .

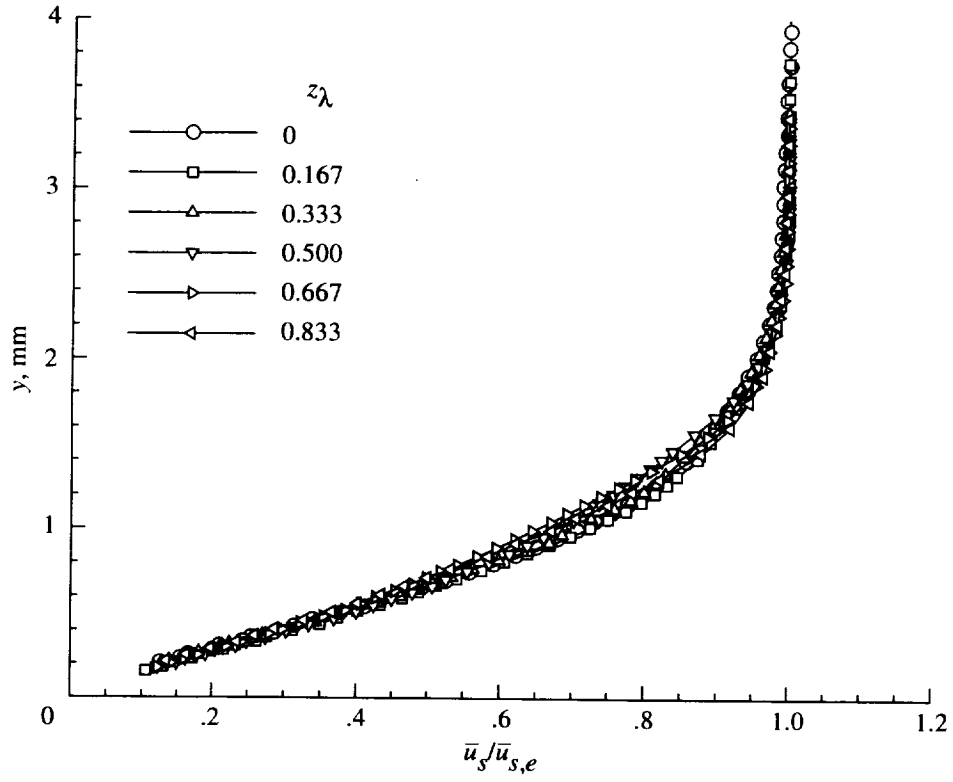


Figure 58. Streamwise velocity profiles at  $x/c = 0.25$ ,  $\alpha = -4^\circ$ , and  $R_c = 2.37 \times 10^6$ .

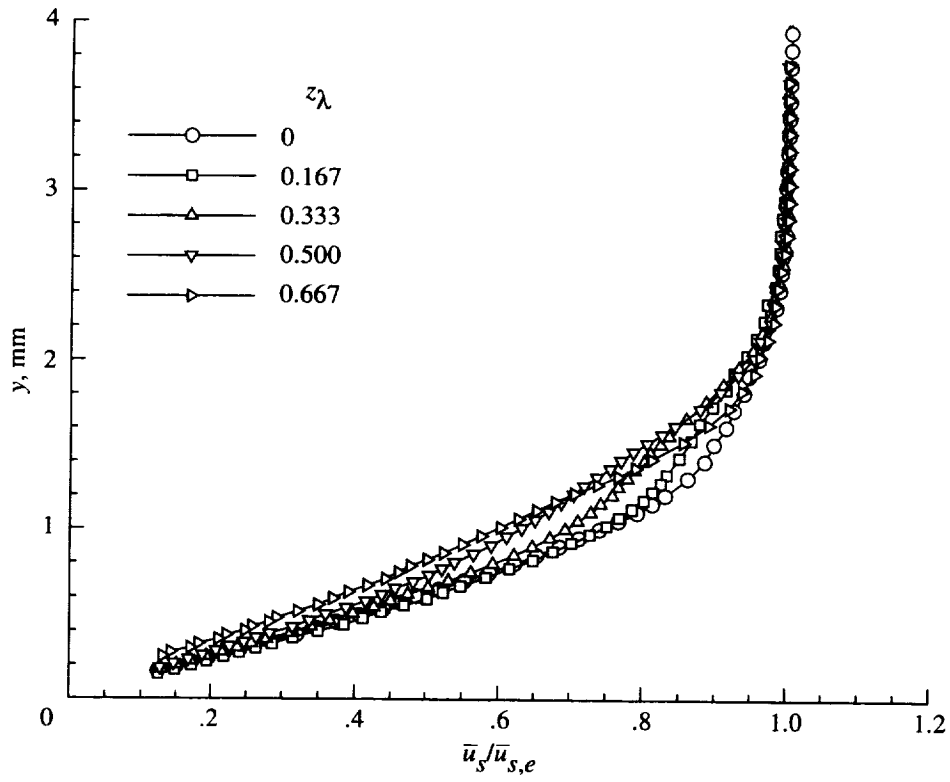


Figure 59. Streamwise velocity profiles at  $x/c = 0.30$ ,  $\alpha = -4^\circ$ , and  $R_c = 2.37 \times 10^6$ .

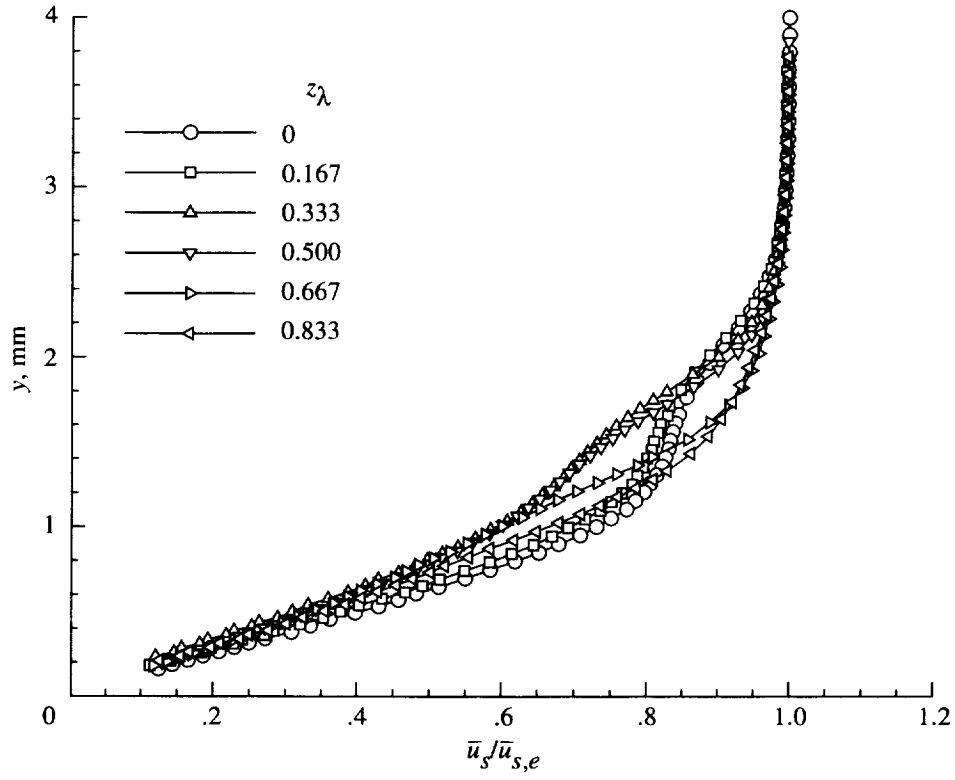


Figure 60. Streamwise velocity profiles at  $x/c = 0.35$ ,  $\alpha = -4^\circ$ , and  $R_c = 2.37 \times 10^6$ .

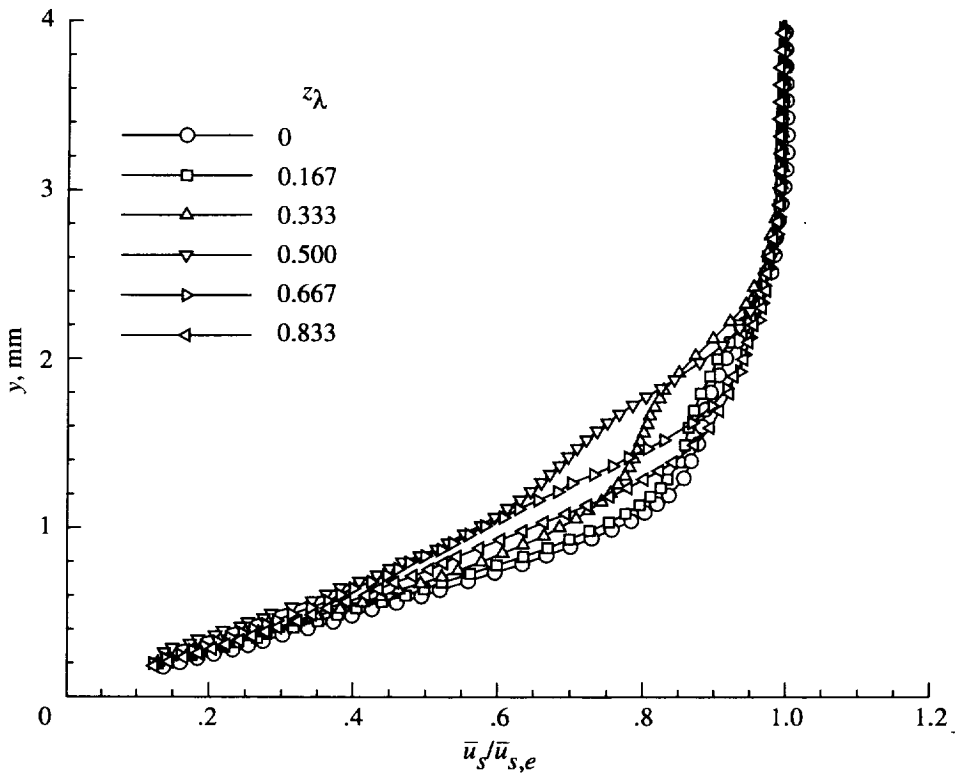


Figure 61. Streamwise velocity profiles at  $x/c = 0.40$ ,  $\alpha = -4^\circ$ , and  $R_c = 2.37 \times 10^6$ .

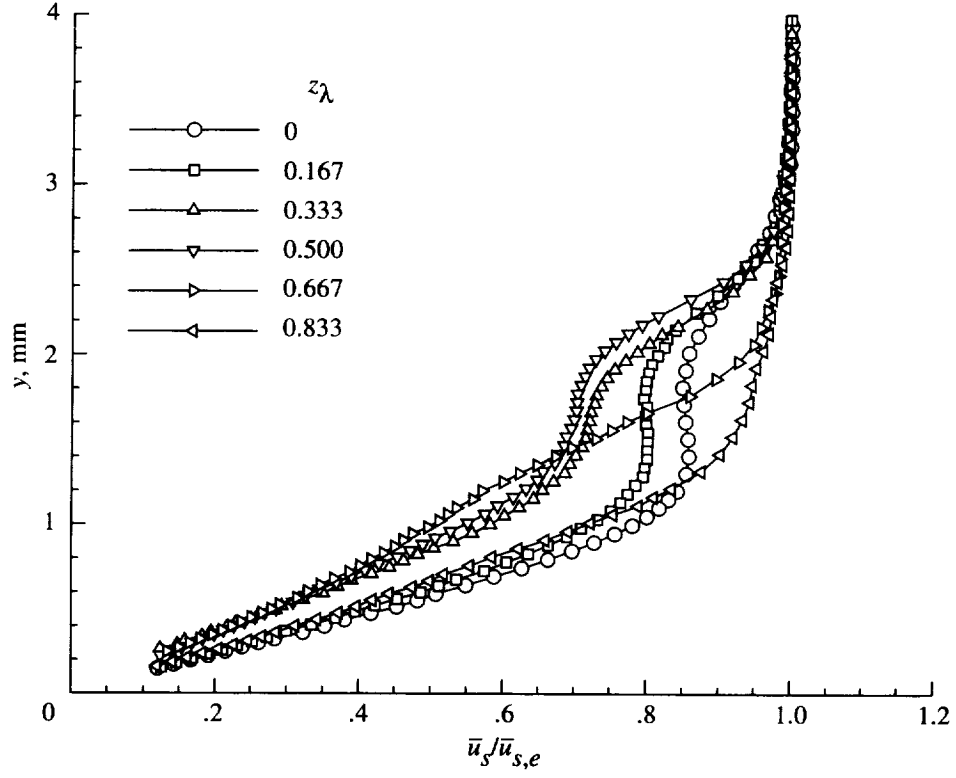


Figure 62. Streamwise velocity profiles at  $x/c = 0.45$ ,  $\alpha = -4^\circ$ , and  $R_c = 2.37 \times 10^6$ .

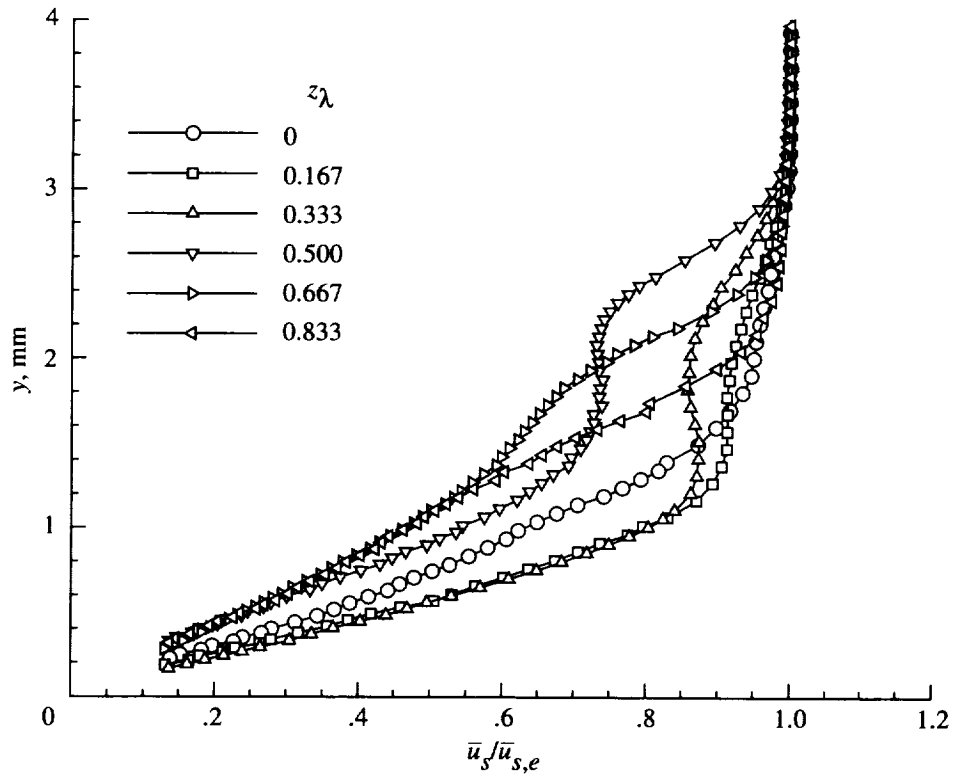


Figure 63. Streamwise velocity profiles at  $x/c = 0.50$ ,  $\alpha = -4^\circ$ , and  $R_c = 2.37 \times 10^6$ .

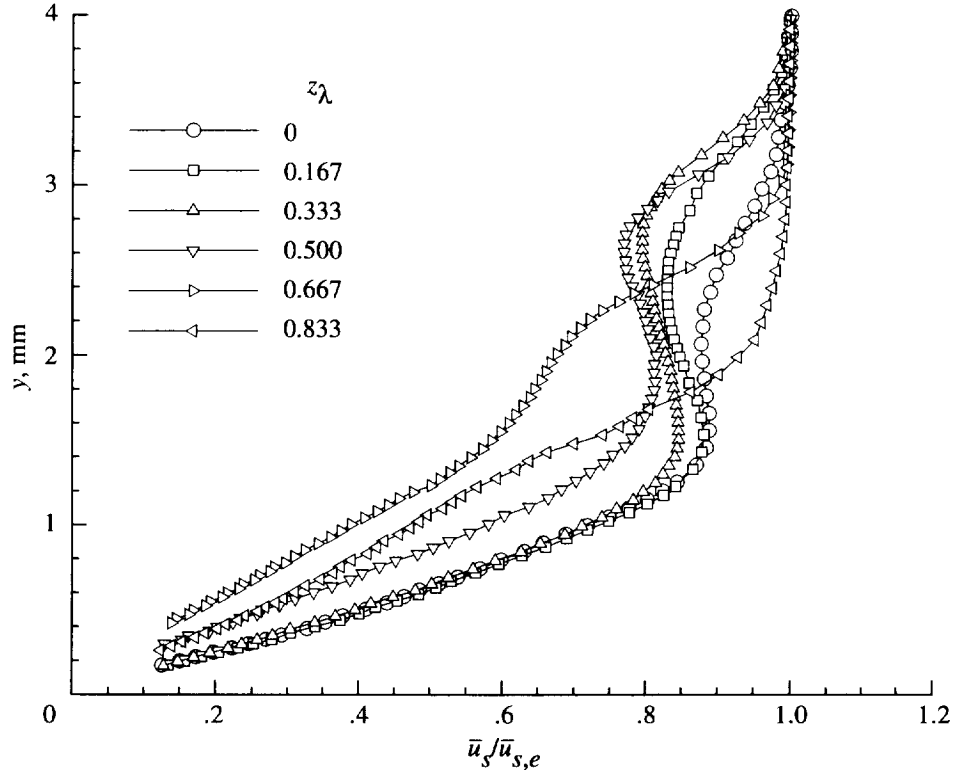


Figure 64. Streamwise velocity profiles at  $x/c = 0.55$ ,  $\alpha = -4^\circ$ , and  $R_c = 2.37 \times 10^6$ .

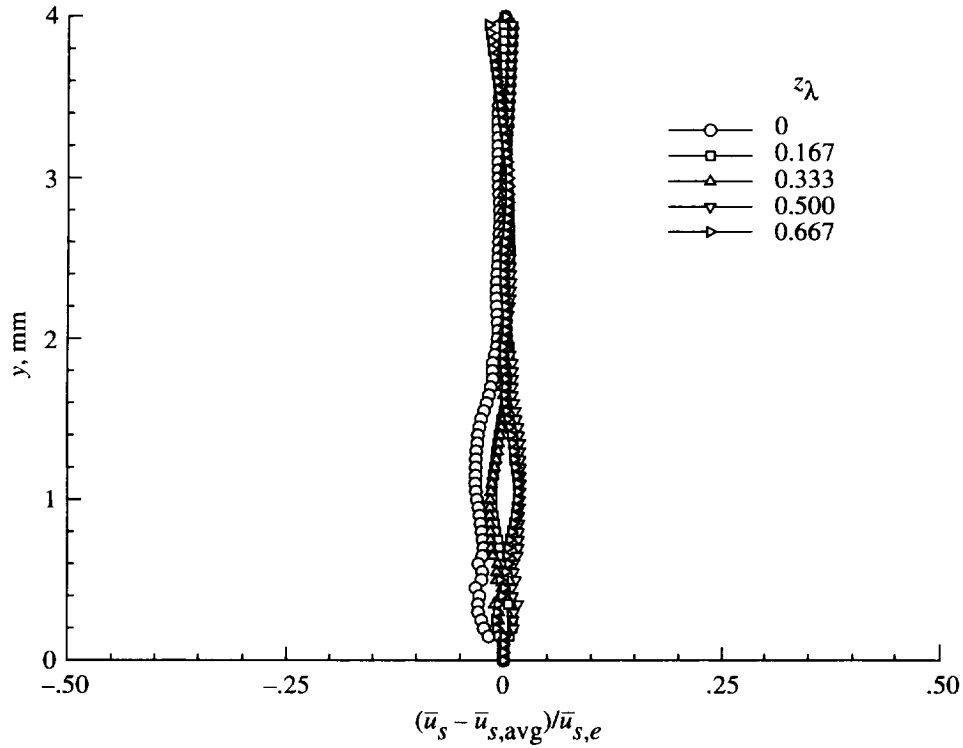


Figure 65. Stationary crossflow disturbance velocity profiles for  $f = 0$  Hz at  $x/c = 0.20$ ,  $\alpha = -4^\circ$ , and  $R_c = 2.37 \times 10^6$  obtained from  $\bar{u}_s - \bar{u}_{s,avg}$ .

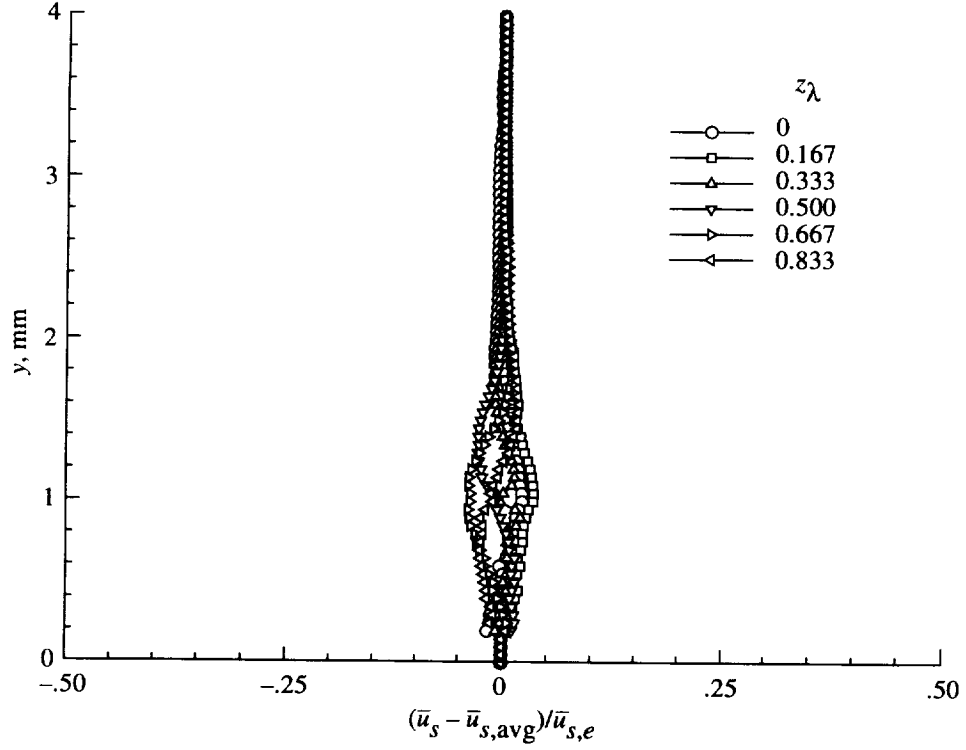


Figure 66. Stationary crossflow disturbance velocity profiles for  $f = 0$  Hz at  $x/c = 0.25$ ,  $\alpha = -4^\circ$ , and  $R_c = 2.37 \times 10^6$  obtained from  $\bar{u}_s - \bar{u}_{s,avg}$ .

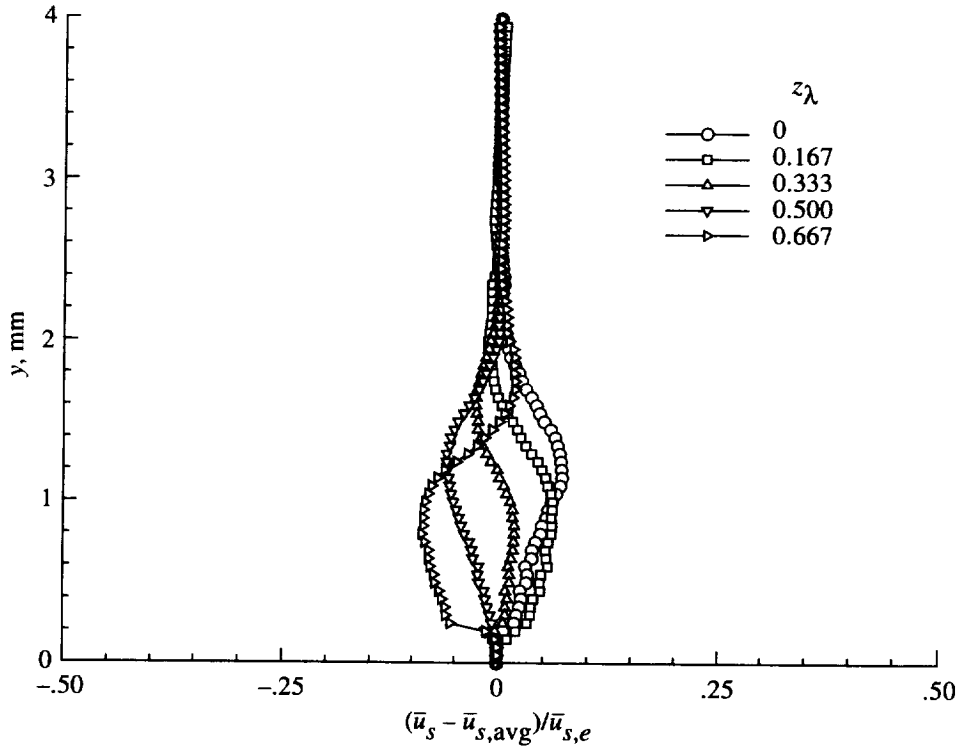


Figure 67. Stationary crossflow disturbance velocity profiles for  $f = 0$  Hz at  $x/c = 0.30$ ,  $\alpha = -4^\circ$ , and  $R_c = 2.37 \times 10^6$  obtained from  $\bar{u}_s - \bar{u}_{s,avg}$ .

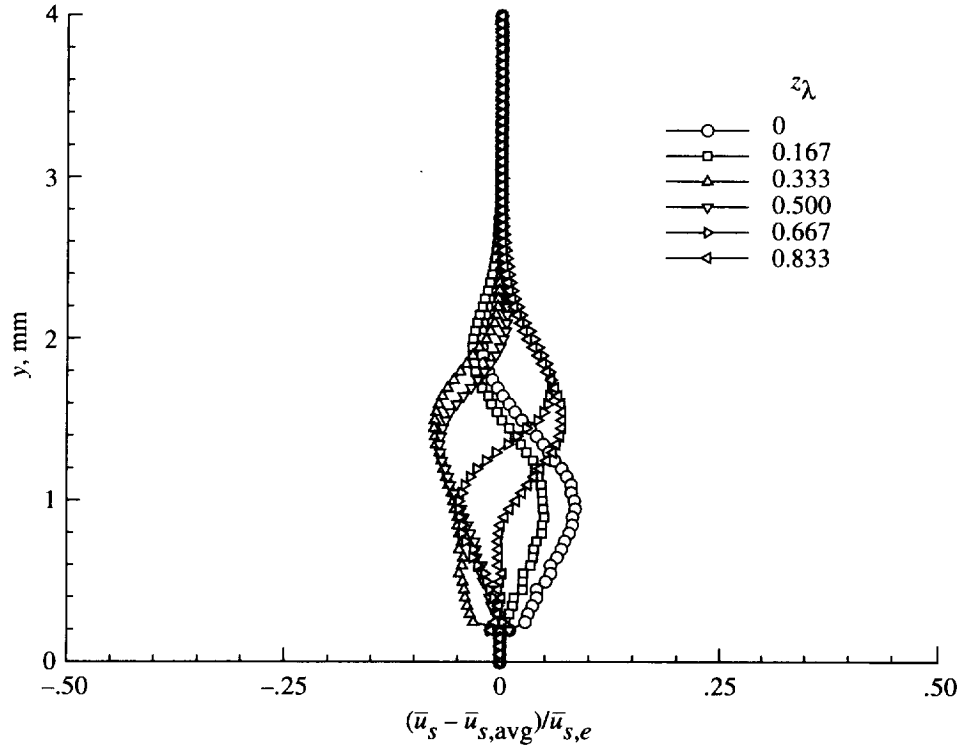


Figure 68. Stationary crossflow disturbance velocity profiles for  $f = 0$  Hz at  $x/c = 0.35$ ,  $\alpha = -4^\circ$ , and  $R_c = 2.37 \times 10^6$  obtained from  $\bar{u}_s - \bar{u}_{s,avg}$ .

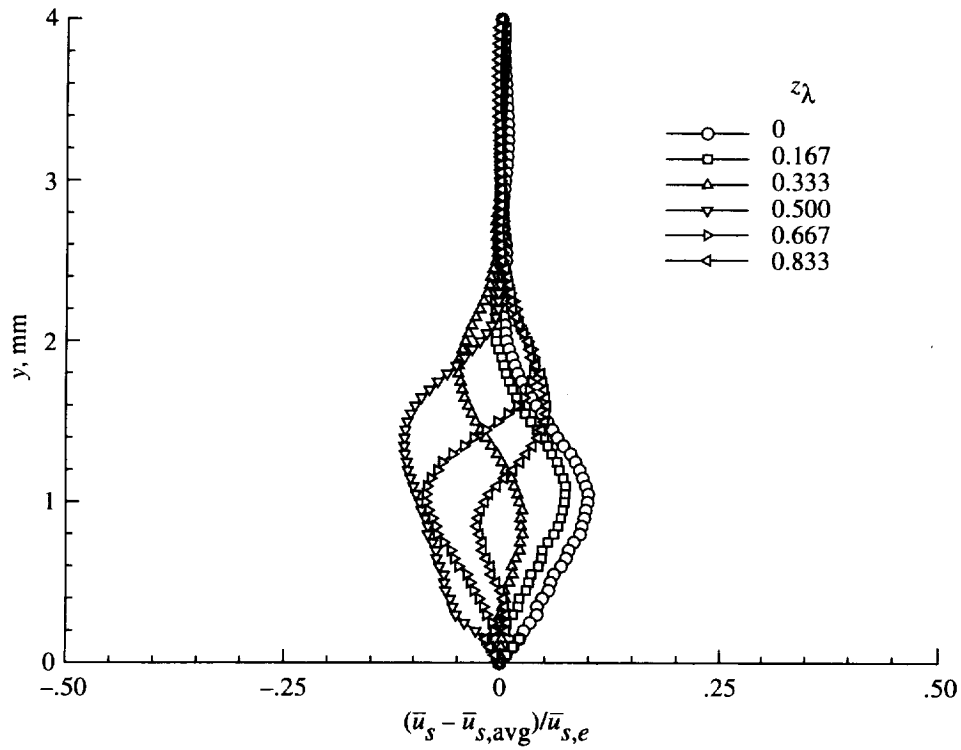


Figure 69. Stationary crossflow disturbance velocity profiles for  $f = 0$  Hz at  $x/c = 0.40$ ,  $\alpha = -4^\circ$ , and  $R_c = 2.37 \times 10^6$  obtained from  $\bar{u}_s - \bar{u}_{s,avg}$ .

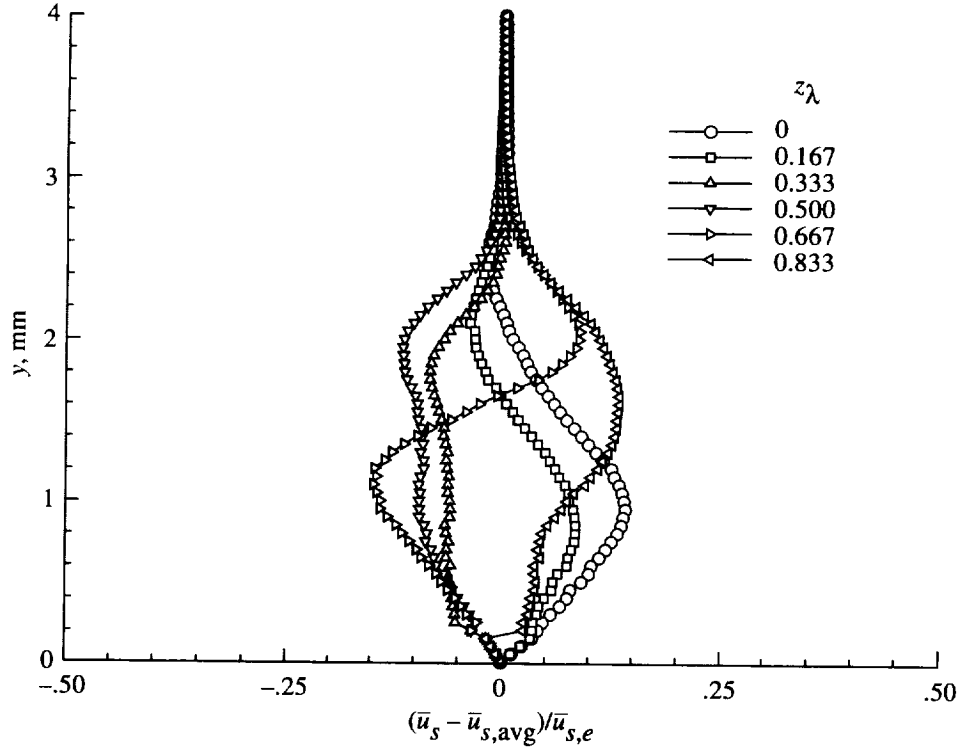


Figure 70. Stationary crossflow disturbance velocity profiles for  $f = 0$  Hz at  $x/c = 0.45$ ,  $\alpha = -4^\circ$ , and  $R_c = 2.37 \times 10^6$  obtained from  $\bar{u}_s - \bar{u}_{s,avg}$ .

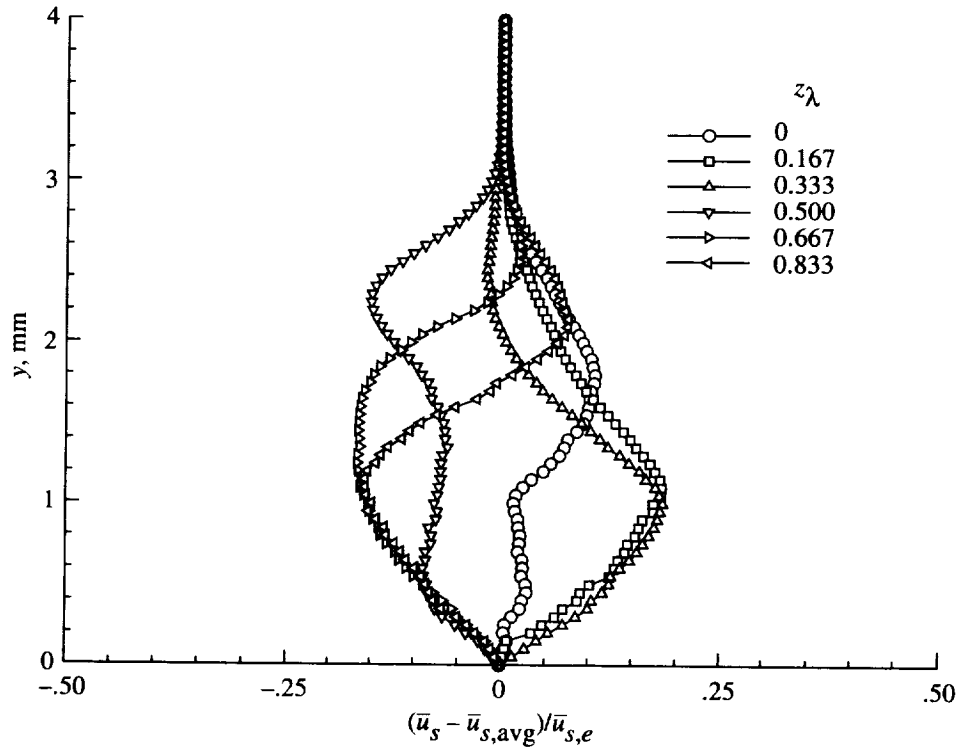


Figure 71. Stationary crossflow disturbance velocity profiles for  $f = 0$  Hz at  $x/c = 0.50$ ,  $\alpha = -4^\circ$ , and  $R_c = 2.37 \times 10^6$  obtained from  $\bar{u}_s - \bar{u}_{s,avg}$ .



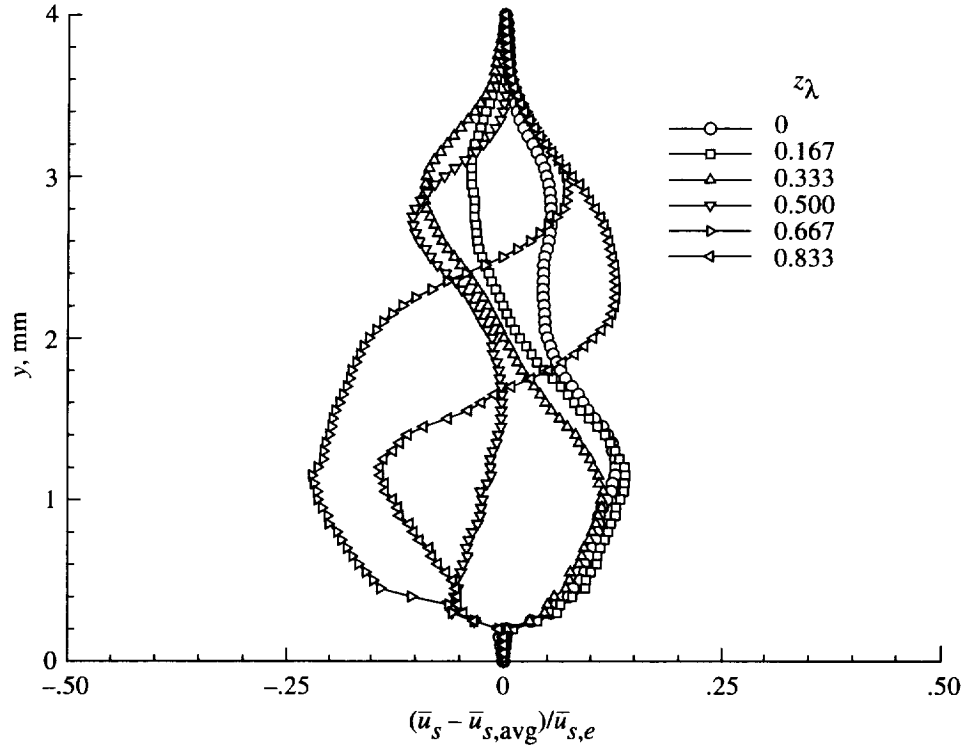


Figure 72. Stationary crossflow disturbance velocity profiles for  $f = 0$  Hz at  $x/c = 0.55$ ,  $\alpha = -4^\circ$ , and  $R_c = 2.37 \times 10^6$  obtained from  $\bar{u}_s - \bar{u}_{s,\text{avg}}$ .

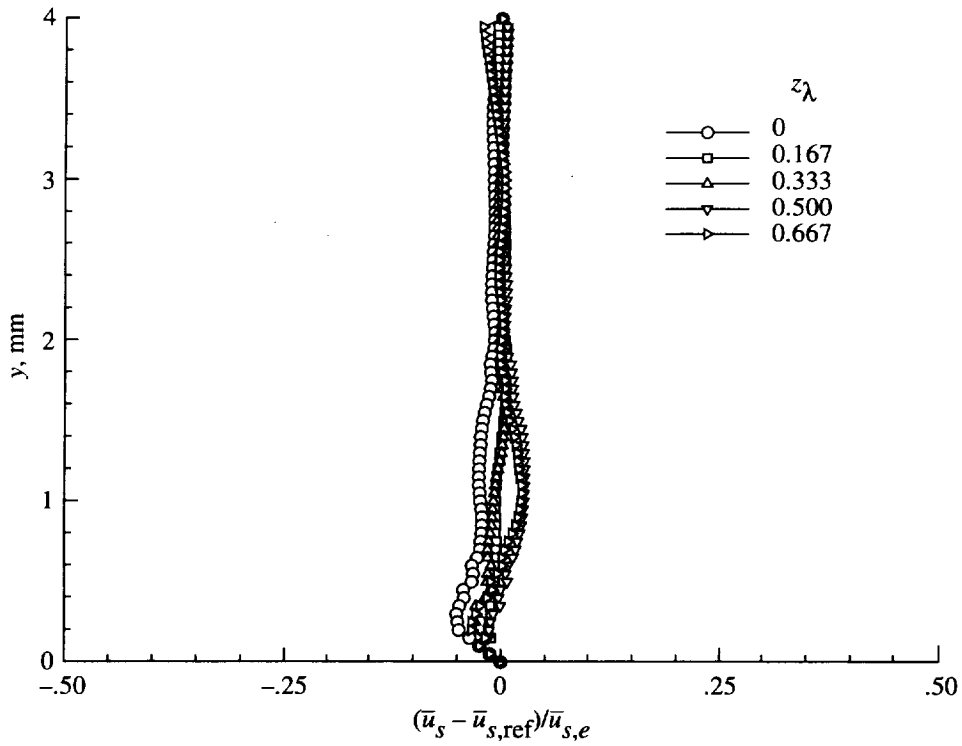


Figure 73. Stationary crossflow disturbance velocity profiles for  $f = 0$  Hz at  $x/c = 0.20$ ,  $\alpha = -4^\circ$ , and  $R_c = 2.37 \times 10^6$  obtained from  $\bar{u}_s - \bar{u}_{s,\text{ref}}$ .

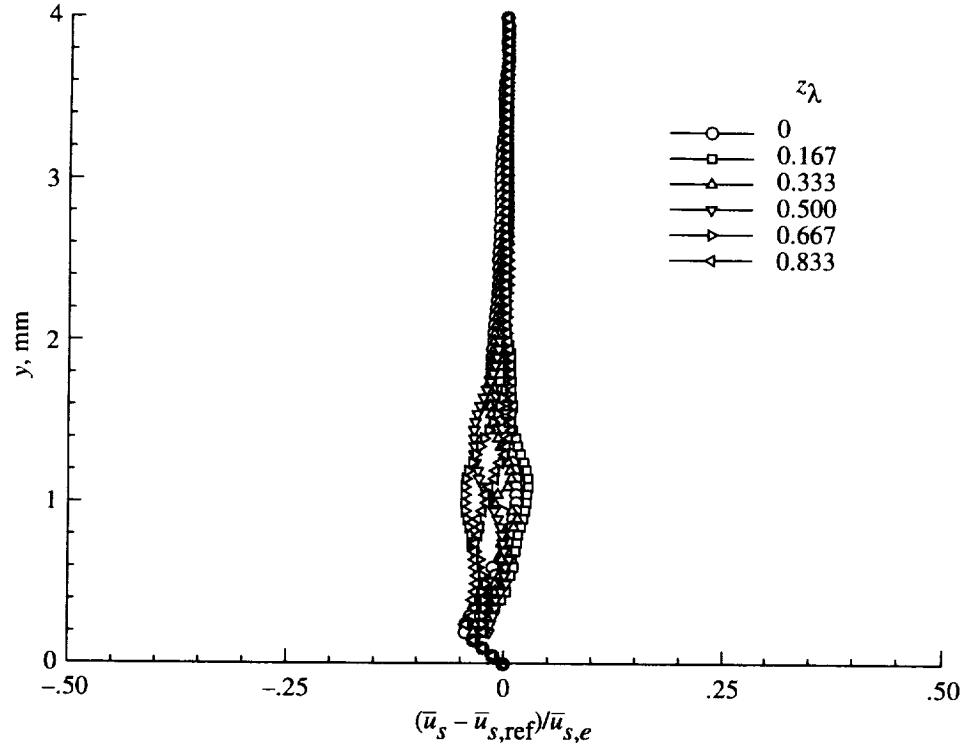


Figure 74. Stationary crossflow disturbance velocity profiles for  $f = 0 \text{ Hz}$  at  $x/c = 0.25$ ,  $\alpha = -4^\circ$ , and  $R_c = 2.37 \times 10^6$  obtained from  $\bar{u}_s - \bar{u}_{s,\text{ref}}$ .

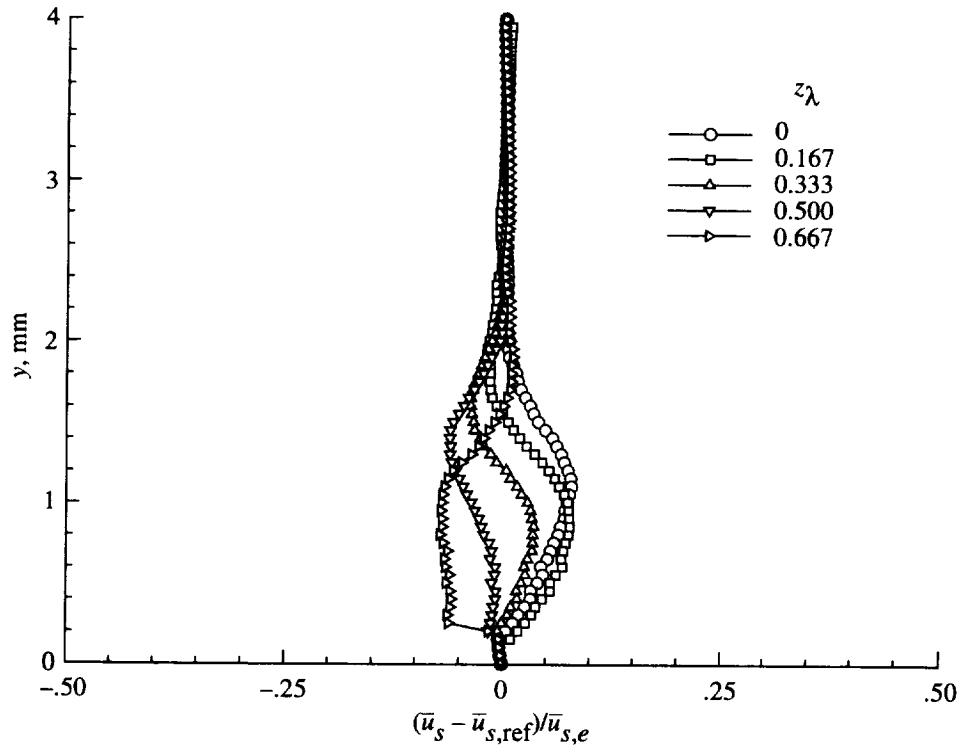


Figure 75. Stationary crossflow disturbance velocity profiles for  $f = 0 \text{ Hz}$  at  $x/c = 0.30$ ,  $\alpha = -4^\circ$ , and  $R_c = 2.37 \times 10^6$  obtained from  $\bar{u}_s - \bar{u}_{s,\text{ref}}$ .

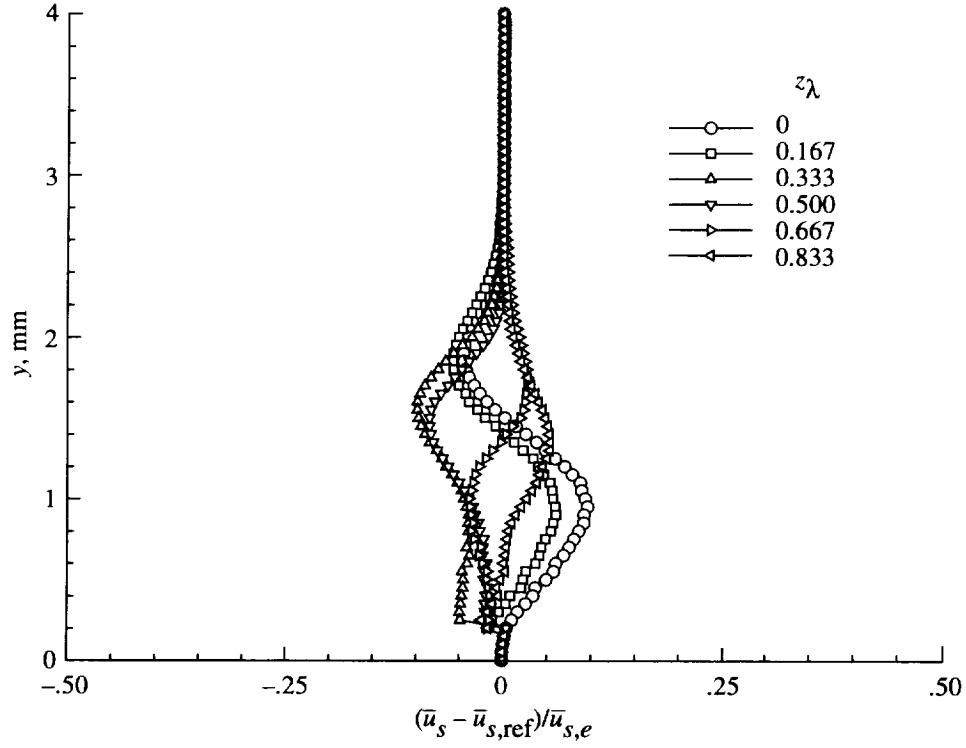


Figure 76. Stationary crossflow disturbance velocity profiles for  $f = 0 \text{ Hz}$  at  $x/c = 0.35$ ,  $\alpha = -4^\circ$ , and  $R_c = 2.37 \times 10^6$  obtained from  $\bar{u}_s - \bar{u}_{s,\text{ref}}$ .

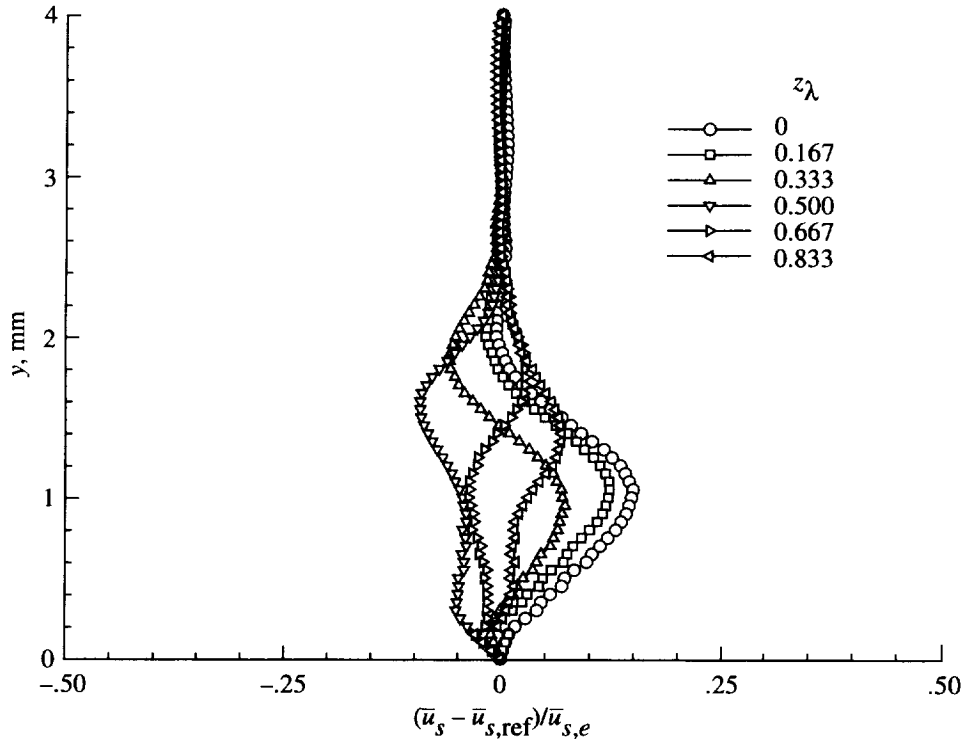


Figure 77. Stationary crossflow disturbance velocity profiles for  $f = 0 \text{ Hz}$  at  $x/c = 0.40$ ,  $\alpha = -4^\circ$ , and  $R_c = 2.37 \times 10^6$  obtained from  $\bar{u}_s - \bar{u}_{s,\text{ref}}$ .

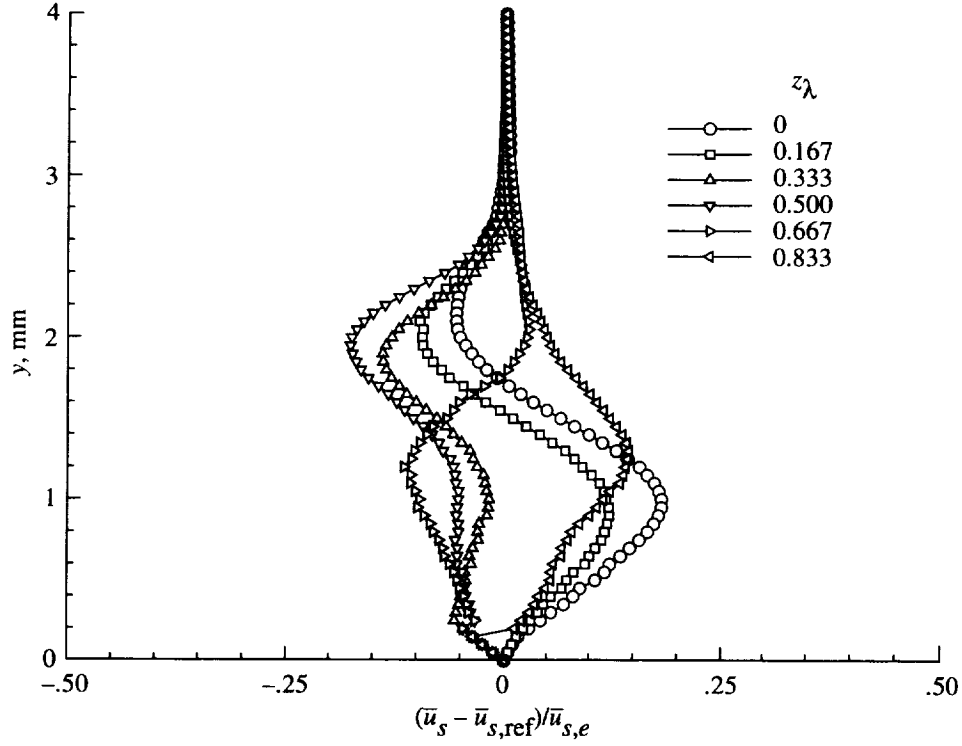


Figure 78. Stationary crossflow disturbance velocity profiles for  $f = 0$  Hz at  $x/c = 0.45$ ,  $\alpha = -4^\circ$ , and  $R_c = 2.37 \times 10^6$  obtained from  $\bar{u}_s - \bar{u}_{s,\text{ref}}$ .

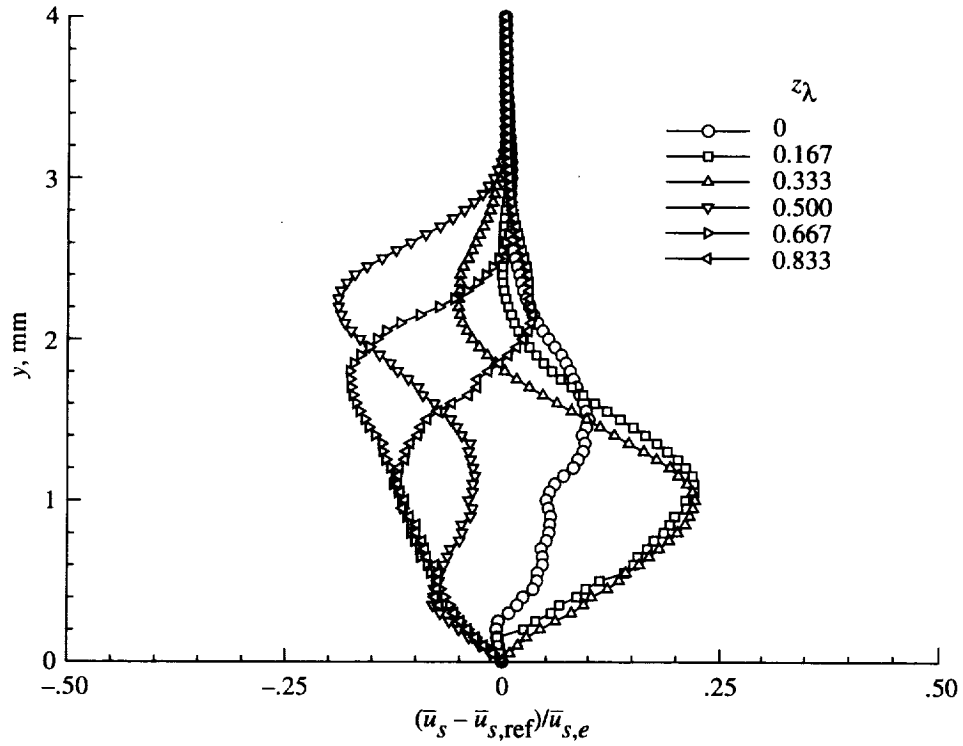


Figure 79. Stationary crossflow disturbance velocity profiles for  $f = 0$  Hz at  $x/c = 0.50$ ,  $\alpha = -4^\circ$ , and  $R_c = 2.37 \times 10^6$  obtained from  $\bar{u}_s - \bar{u}_{s,\text{ref}}$ .

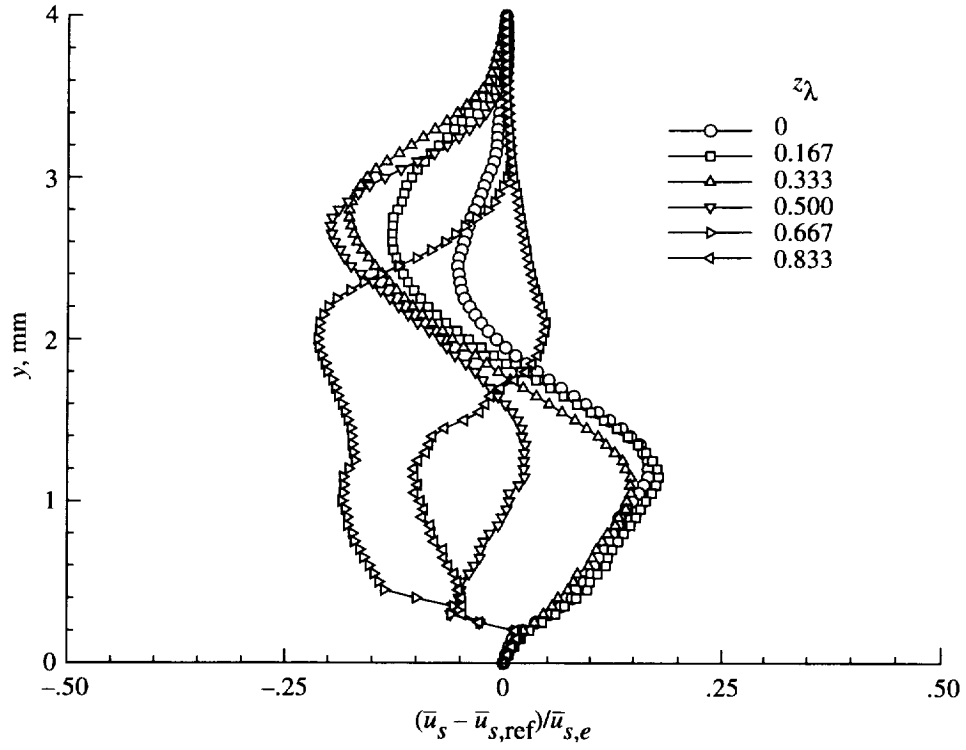


Figure 80. Stationary crossflow disturbance velocity profiles for  $f = 0$  Hz at  $x/c = 0.55$ ,  $\alpha = -4^\circ$ , and  $R_c = 2.37 \times 10^6$  obtained from  $\bar{u}_s - \bar{u}_{s,\text{ref}}$ .

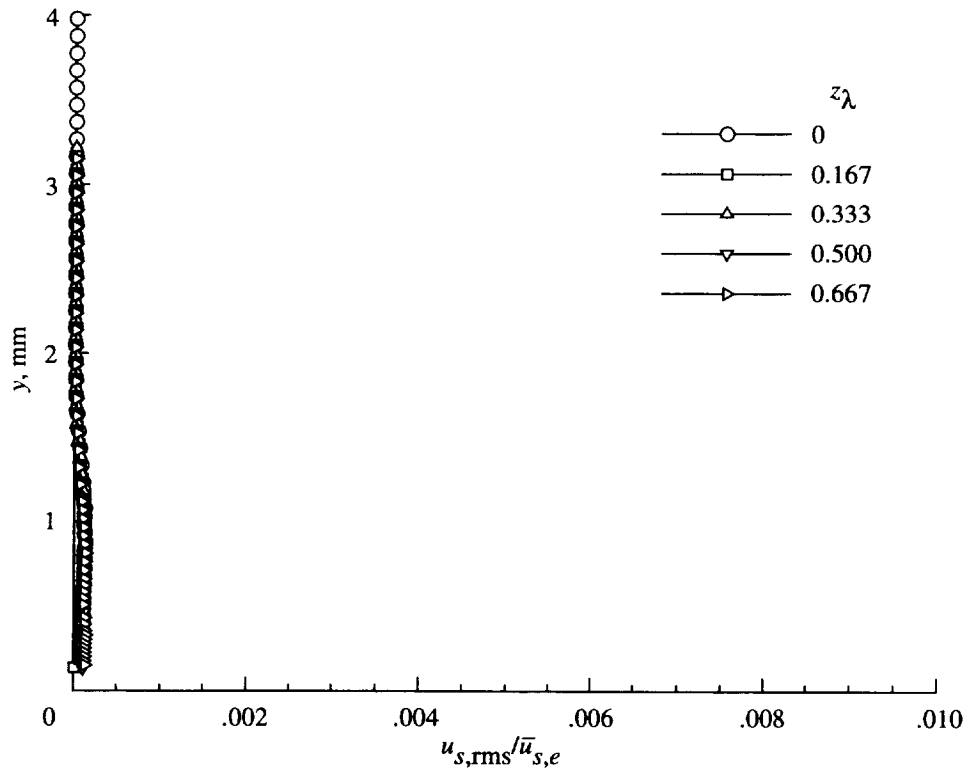


Figure 81. Travelling wave disturbance velocity profiles for  $f = 100$  Hz at  $x/c = 0.20$ ,  $\alpha = -4^\circ$ , and  $R_c = 2.37 \times 10^6$ .

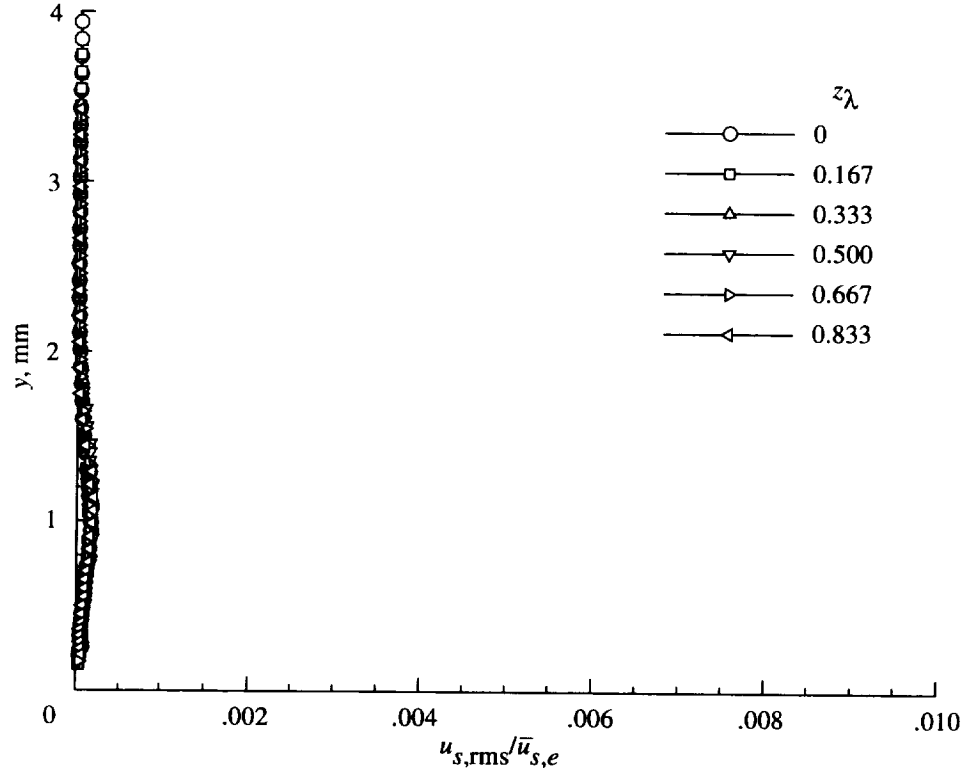


Figure 82. Travelling wave disturbance velocity profiles for  $f = 100$  Hz at  $x/c = 0.25$ ,  $\alpha = -4^\circ$ , and  $R_c = 2.37 \times 10^6$ .

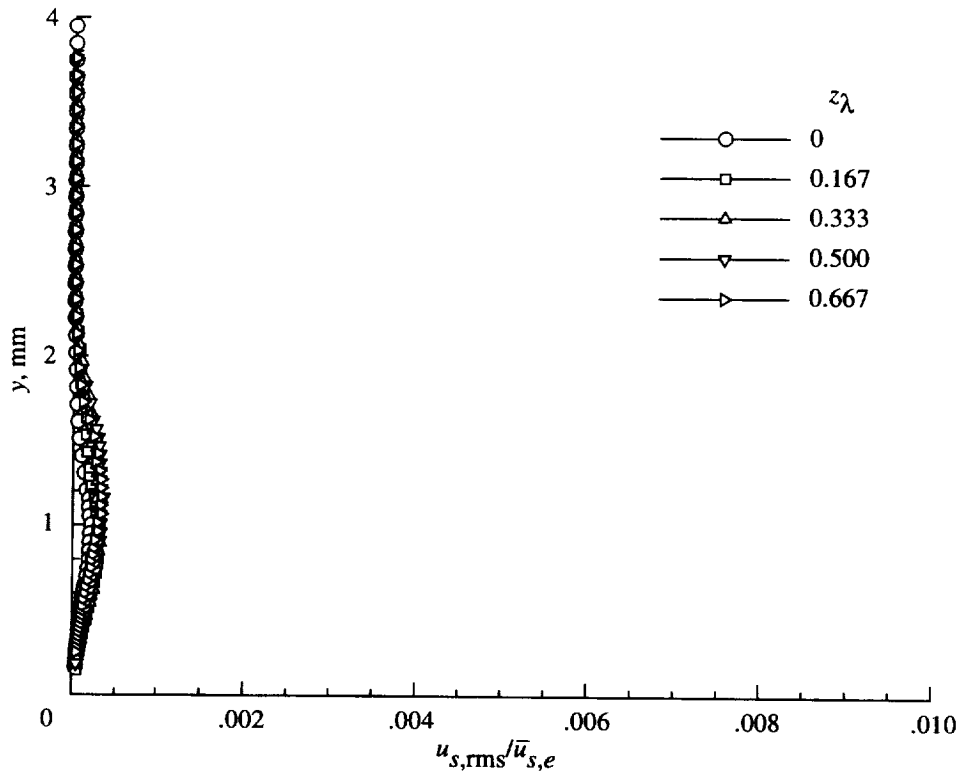


Figure 83. Travelling wave disturbance velocity profiles for  $f = 100$  Hz at  $x/c = 0.30$ ,  $\alpha = -4^\circ$ , and  $R_c = 2.37 \times 10^6$ .

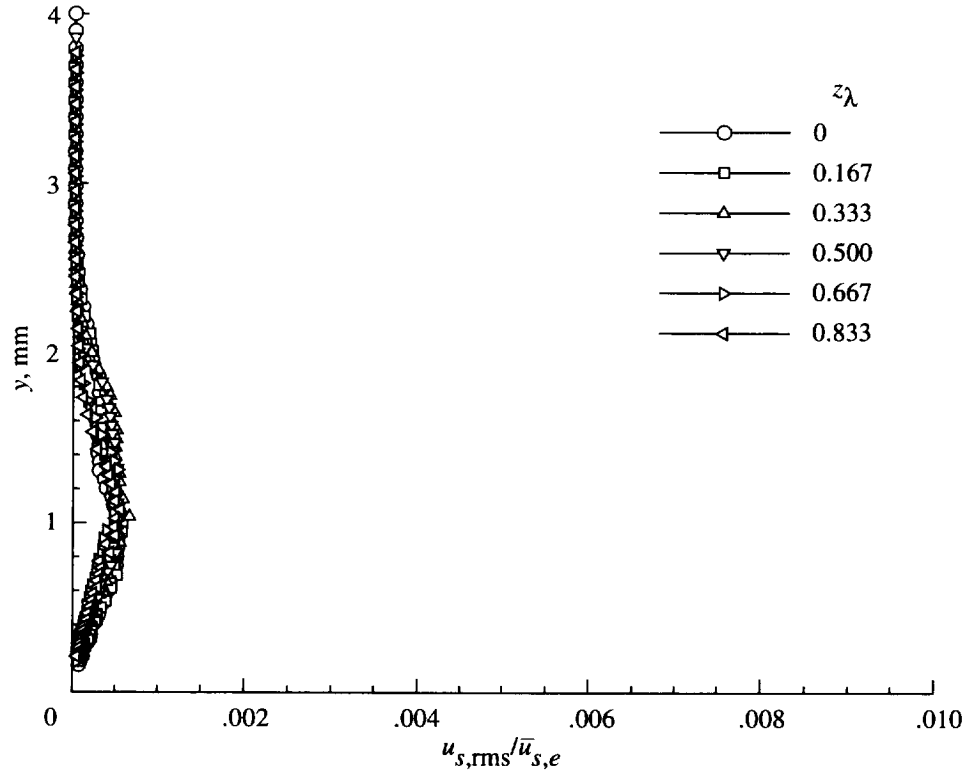


Figure 84. Travelling wave disturbance velocity profiles for  $f = 100$  Hz at  $x/c = 0.35$ ,  $\alpha = -4^\circ$ , and  $R_c = 2.37 \times 10^6$ .

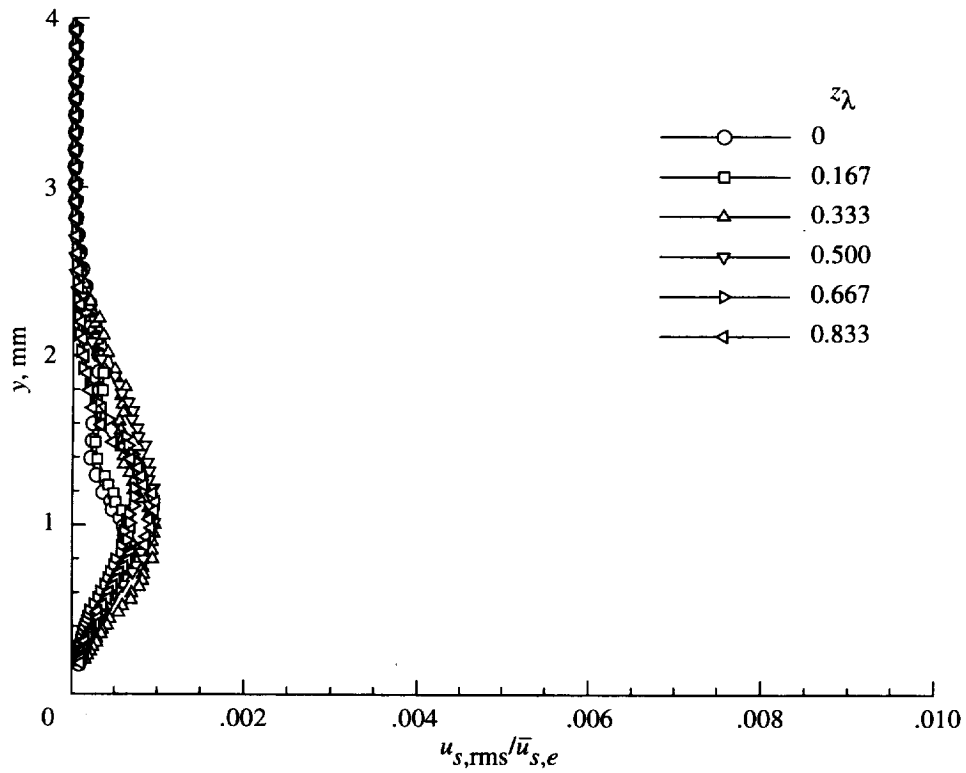


Figure 85. Travelling wave disturbance velocity profiles for  $f = 100$  Hz at  $x/c = 0.40$ ,  $\alpha = -4^\circ$ , and  $R_c = 2.37 \times 10^6$ .

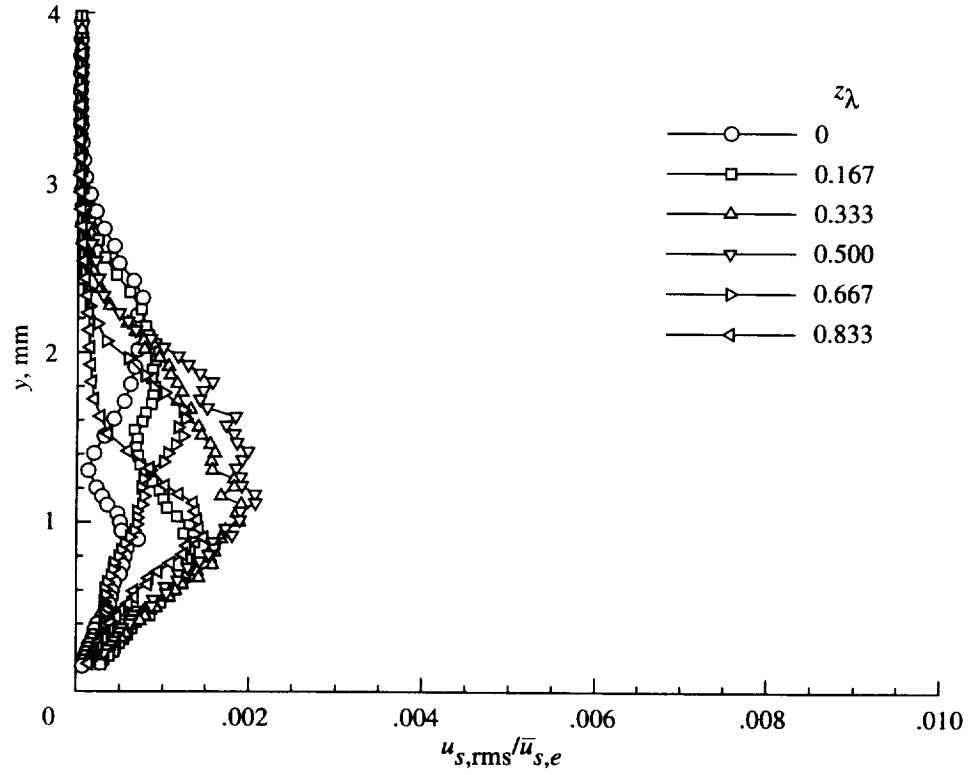


Figure 86. Travelling wave disturbance velocity profiles for  $f = 100$  Hz at  $x/c = 0.45$ ,  $\alpha = -4^\circ$ , and  $R_c = 2.37 \times 10^6$ .

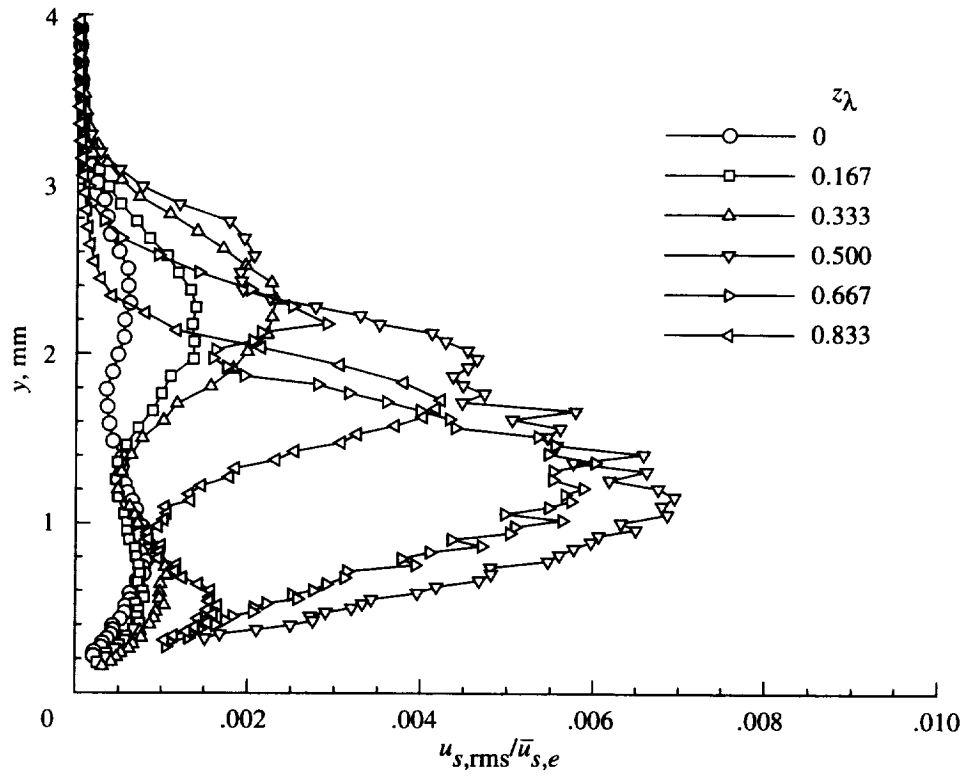


Figure 87. Travelling wave disturbance velocity profiles for  $f = 100$  Hz at  $x/c = 0.50$ ,  $\alpha = -4^\circ$ , and  $R_c = 2.37 \times 10^6$ .



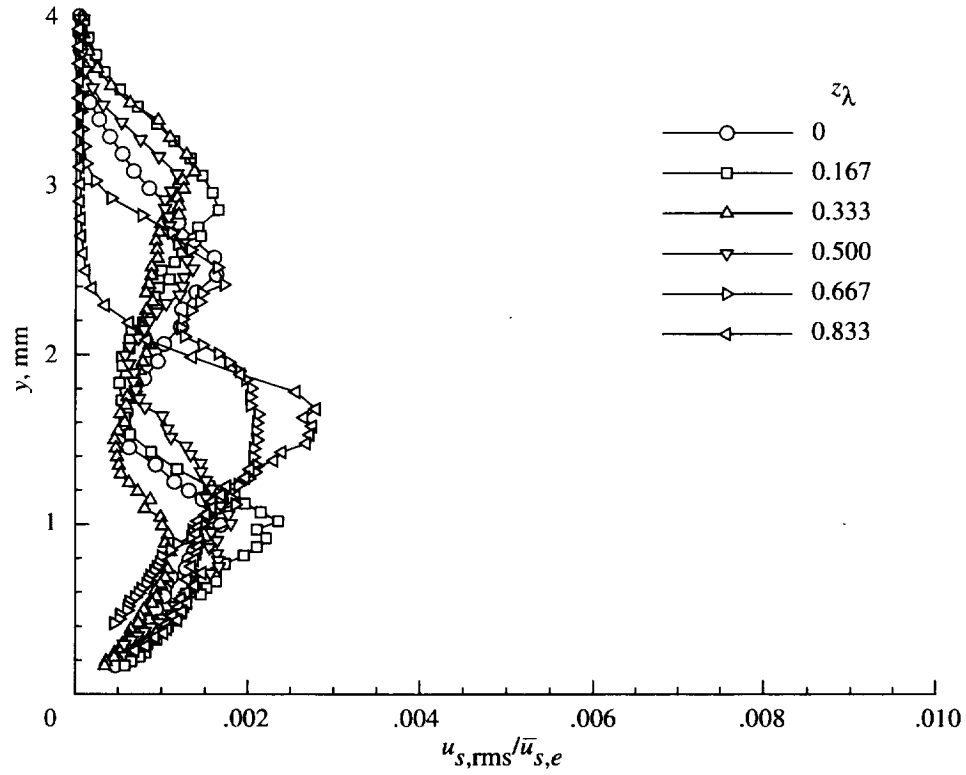


Figure 88. Travelling wave disturbance velocity profiles for  $f = 100$  Hz at  $x/c = 0.55$ ,  $\alpha = -4^\circ$ , and  $R_c = 2.37 \times 10^6$ .

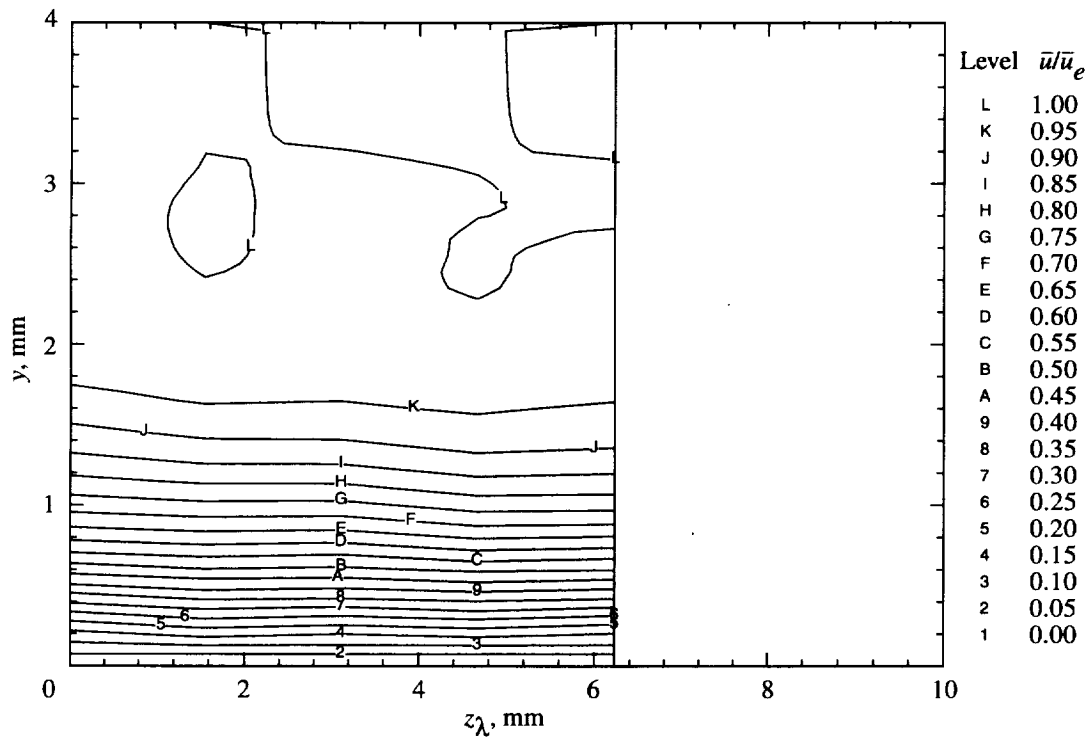


Figure 89. Mean streamwise velocity contours at  $x/c = 0.20$ ,  $\alpha = -4^\circ$ , and  $R_c = 2.37 \times 10^6$ .

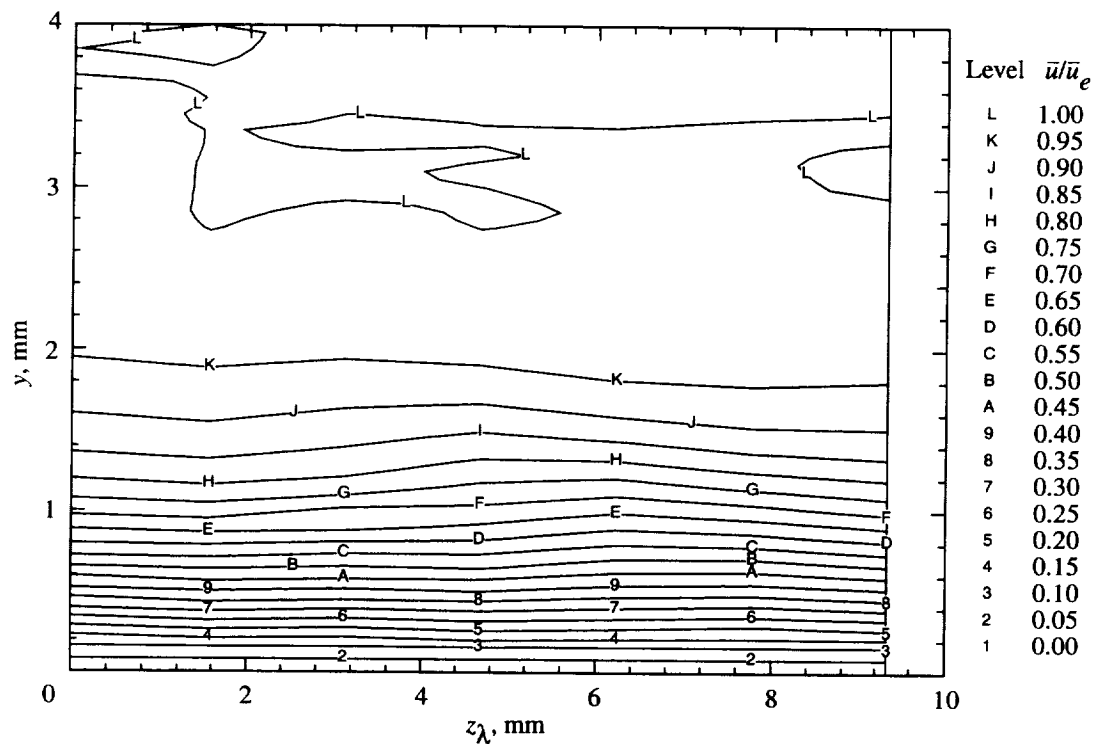


Figure 90. Mean streamwise velocity contours at  $x/c = 0.25$ ,  $\alpha = -4^\circ$ , and  $R_c = 2.37 \times 10^6$ .

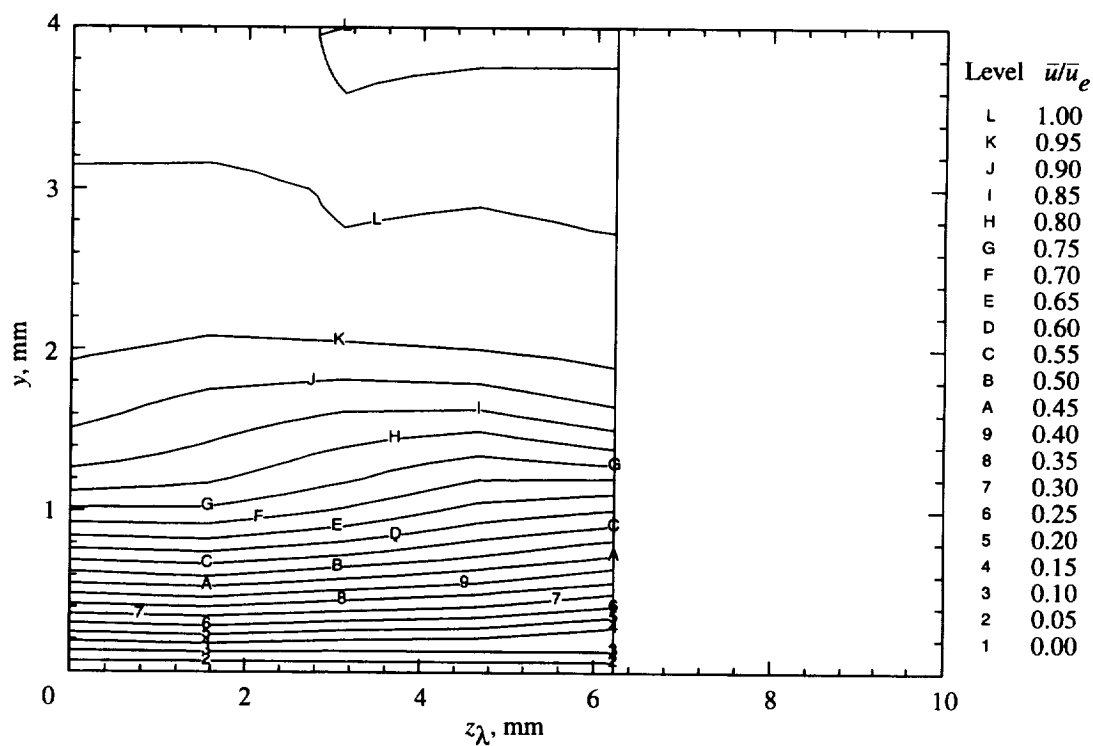


Figure 91. Mean streamwise velocity contours at  $x/c = 0.30$ ,  $\alpha = -4^\circ$ , and  $R_c = 2.37 \times 10^6$ .

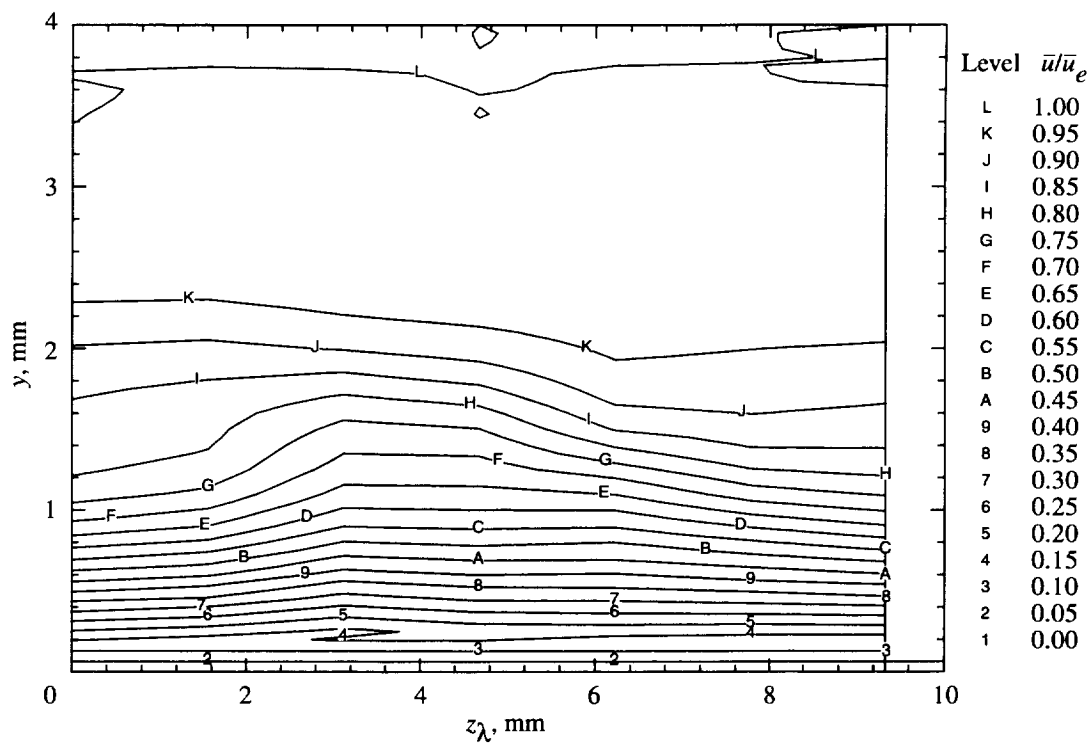


Figure 92. Mean streamwise velocity contours at  $x/c = 0.35$ ,  $\alpha = -4^\circ$ , and  $R_c = 2.37 \times 10^6$ .

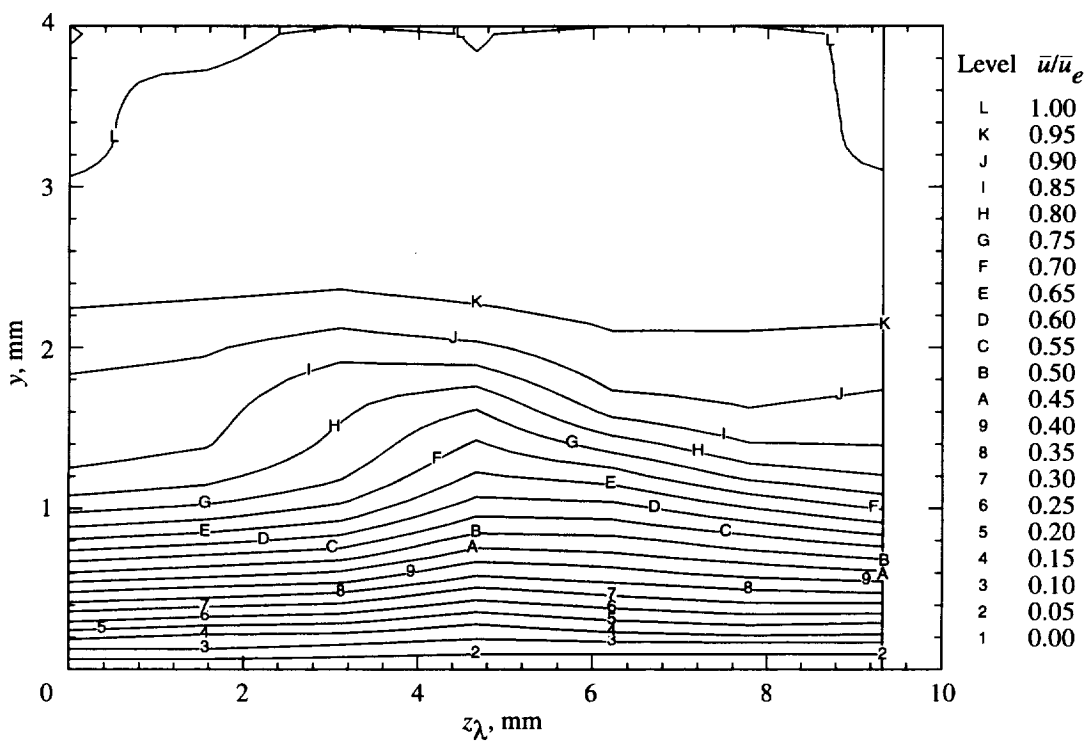


Figure 93. Mean streamwise velocity contours at  $x/c = 0.40$ ,  $\alpha = -4^\circ$ , and  $R_c = 2.37 \times 10^6$ .

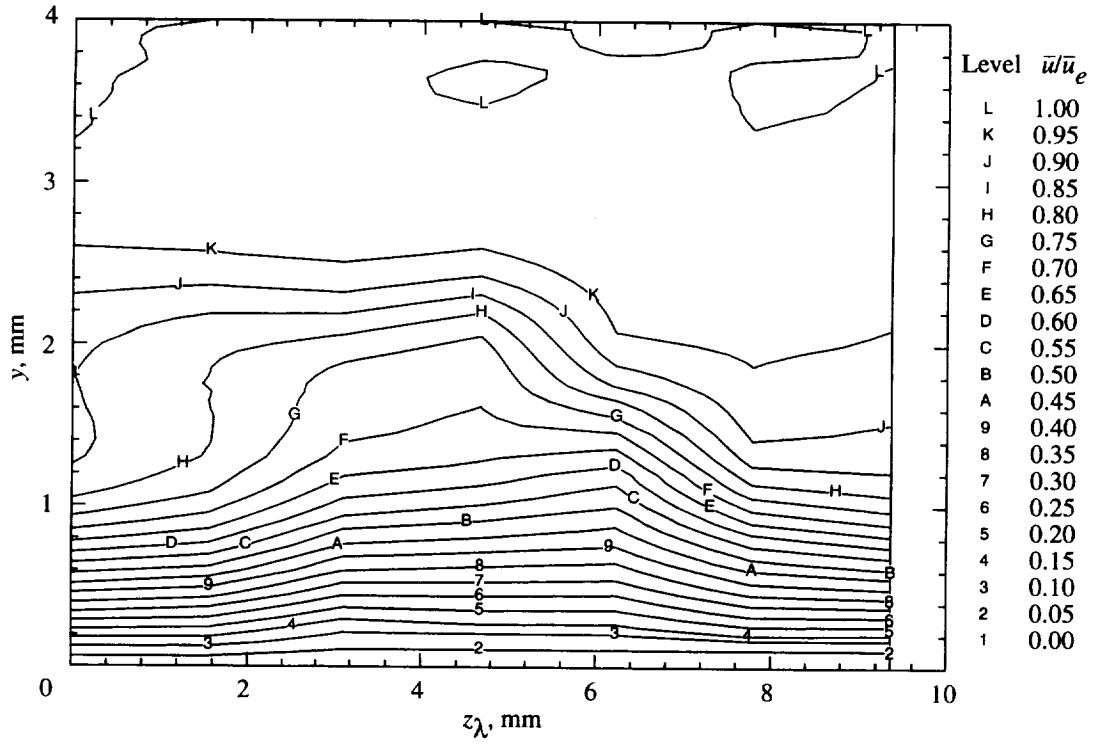


Figure 94. Mean streamwise velocity contours at  $x/c = 0.45$ ,  $\alpha = -4^\circ$ , and  $R_c = 2.37 \times 10^6$ .

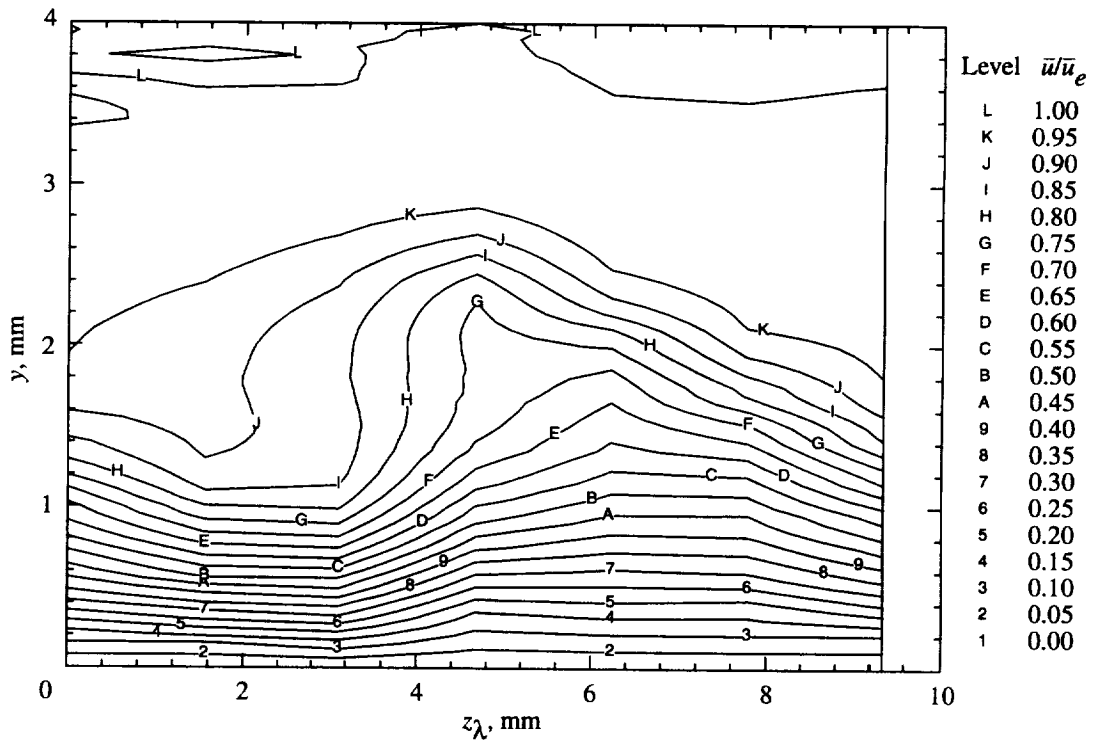


Figure 95. Mean streamwise velocity contours at  $x/c = 0.50$ ,  $\alpha = -4^\circ$ , and  $R_c = 2.37 \times 10^6$ .

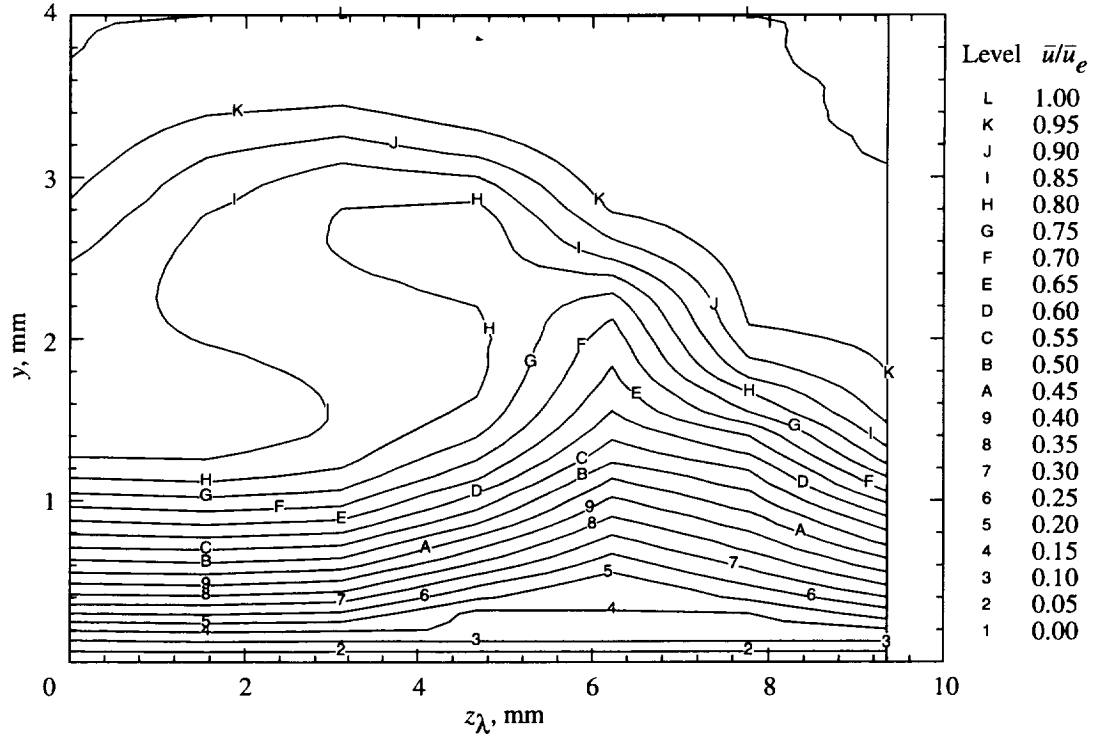


Figure 96. Mean streamwise velocity contours at  $x/c = 0.55$ ,  $\alpha = -4^\circ$ , and  $R_c = 2.37 \times 10^6$ .

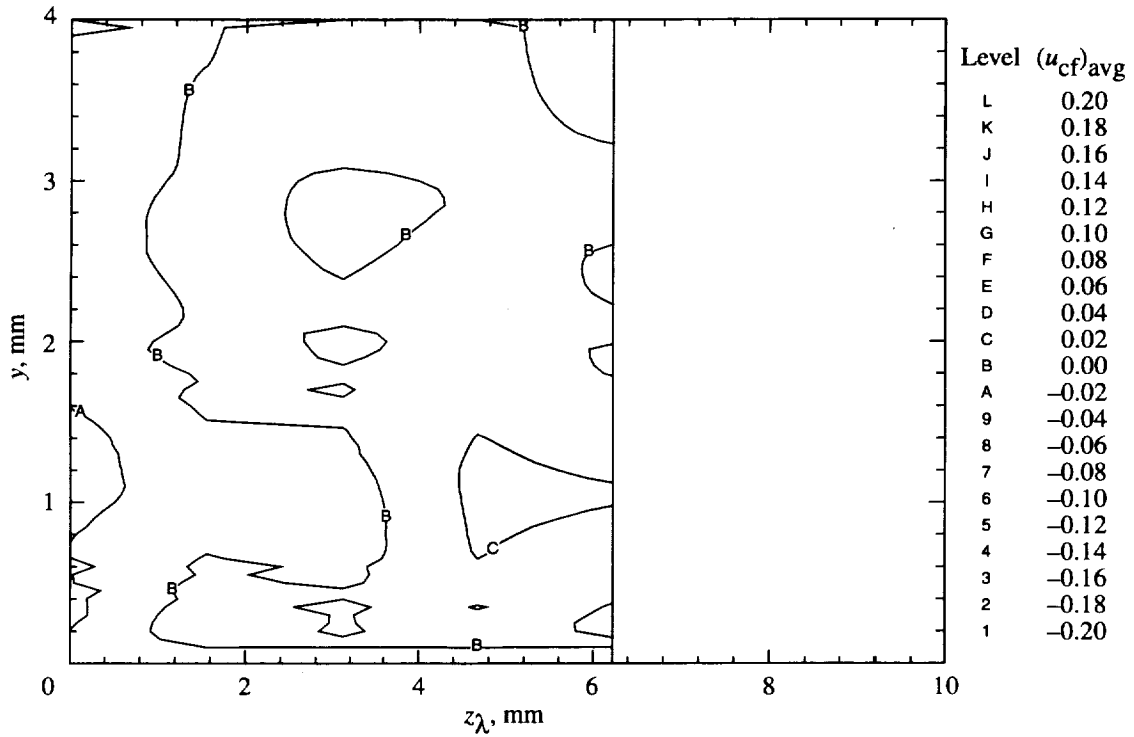


Figure 97. Stationary crossflow vortex velocity contours obtained from  $\bar{u}_s - \bar{u}_{s,avg}$  at  $x/c = 0.20$ ,  $\alpha = -4^\circ$ , and  $R_c = 2.37 \times 10^6$ .

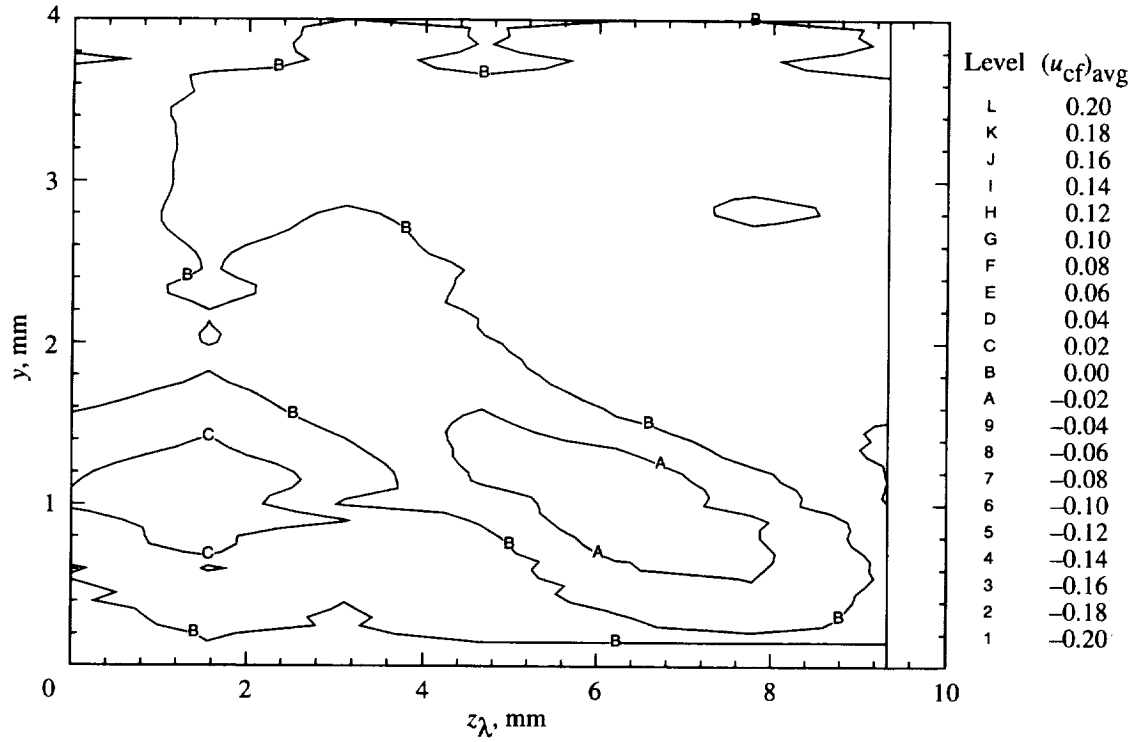


Figure 98. Stationary crossflow vortex velocity contours obtained from  $\bar{u}_s - \bar{u}_{s,avg}$  at  $x/c = 0.25$ ,  $\alpha = -4^\circ$ , and  $R_c = 2.37 \times 10^6$ .

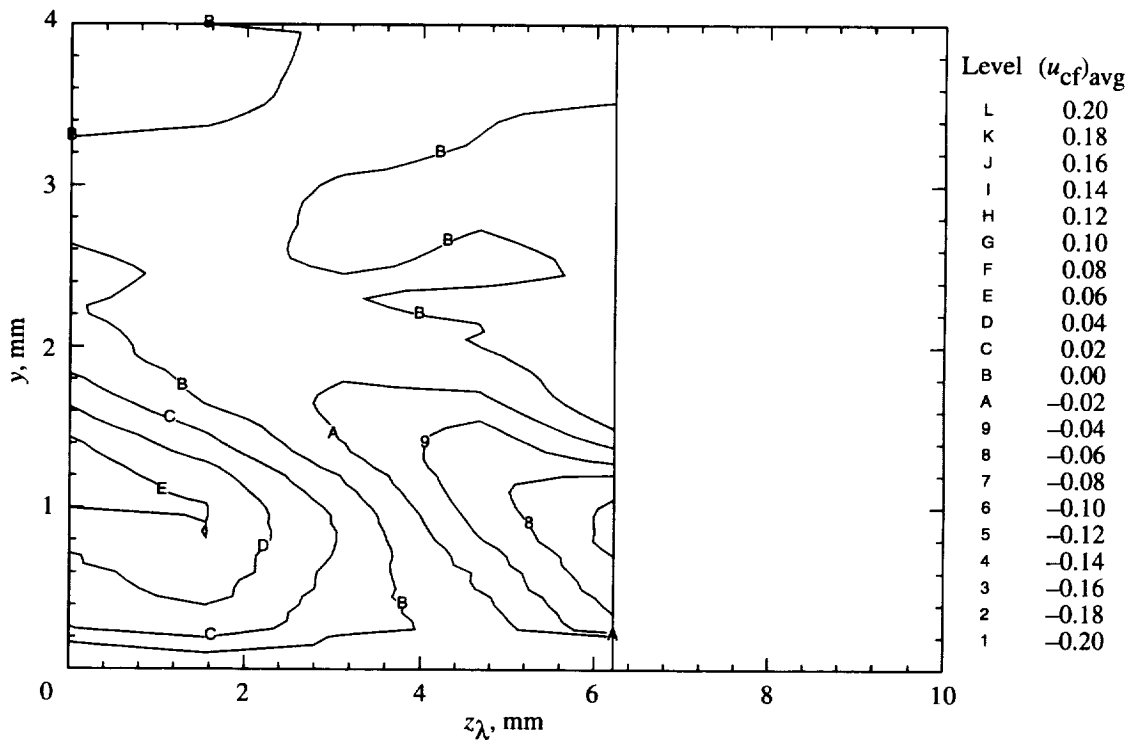


Figure 99. Stationary crossflow vortex velocity contours obtained from  $\bar{u}_s - \bar{u}_{s,avg}$  at  $x/c = 0.30$ ,  $\alpha = -4^\circ$ , and  $R_c = 2.37 \times 10^6$ .

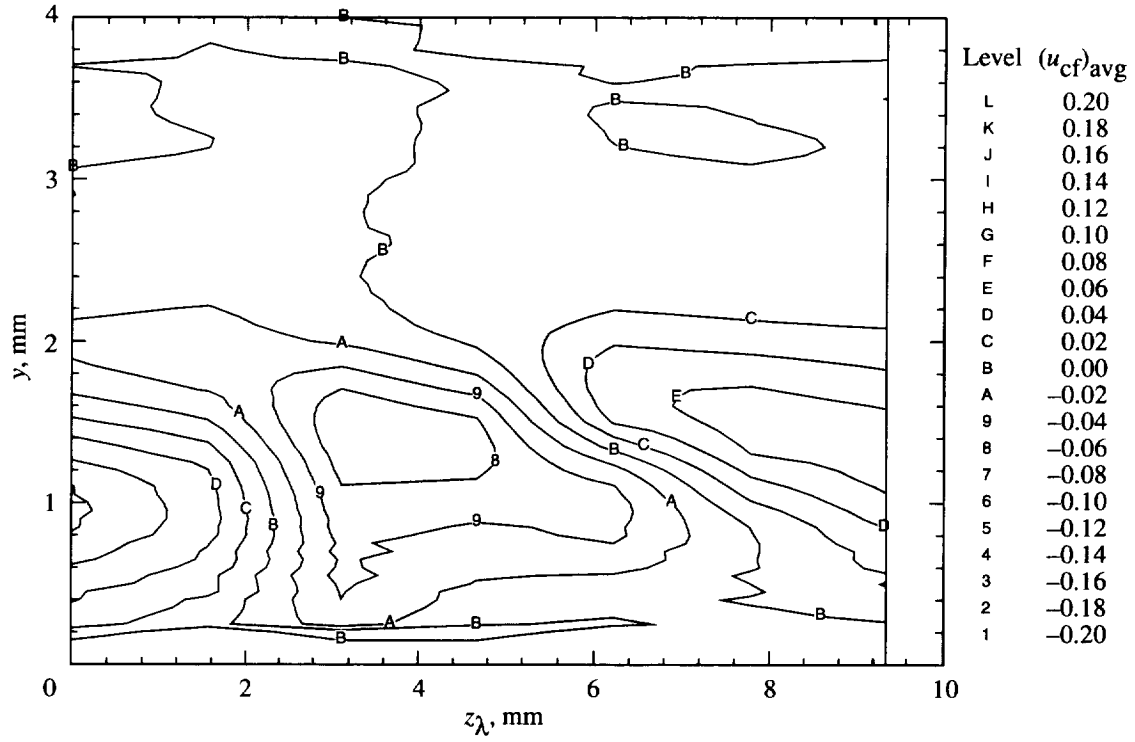


Figure 100. Stationary crossflow vortex velocity contours obtained from  $\bar{u}_s - \bar{u}_{s,avg}$  at  $x/c = 0.35$ ,  $\alpha = -4^\circ$ , and  $R_c = 2.37 \times 10^6$ .

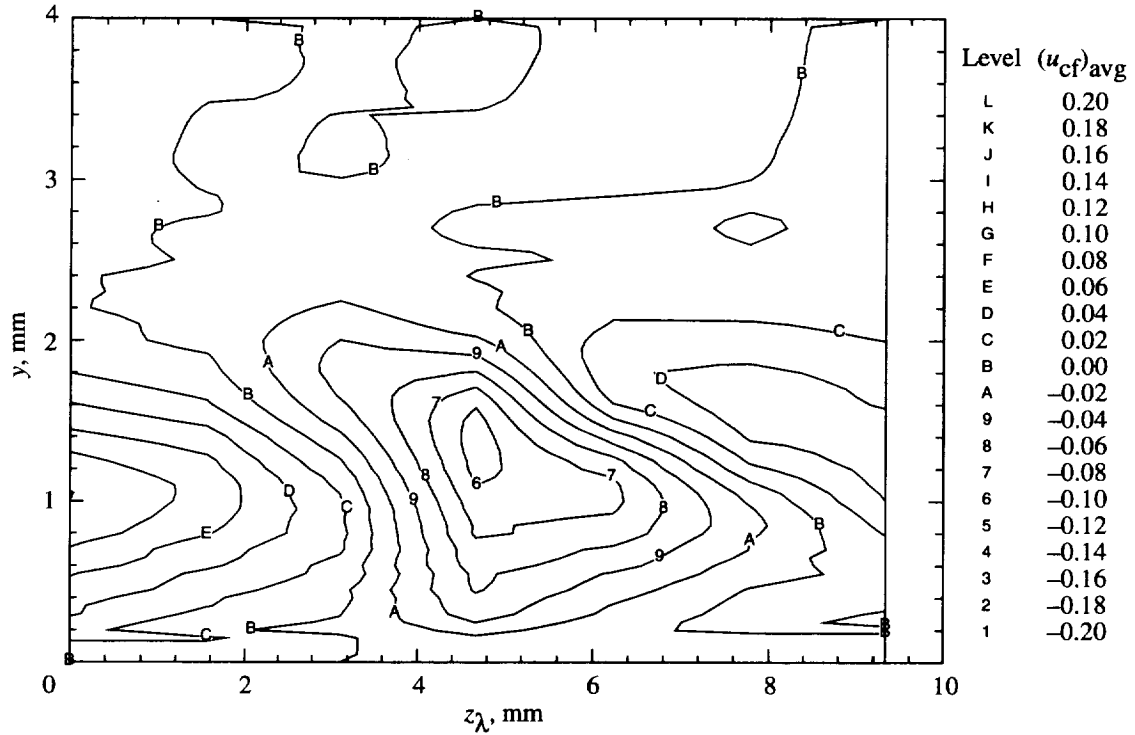


Figure 101. Stationary crossflow vortex velocity contours obtained from  $\bar{u}_s - \bar{u}_{s,avg}$  at  $x/c = 0.40$ ,  $\alpha = -4^\circ$ , and  $R_c = 2.37 \times 10^6$ .

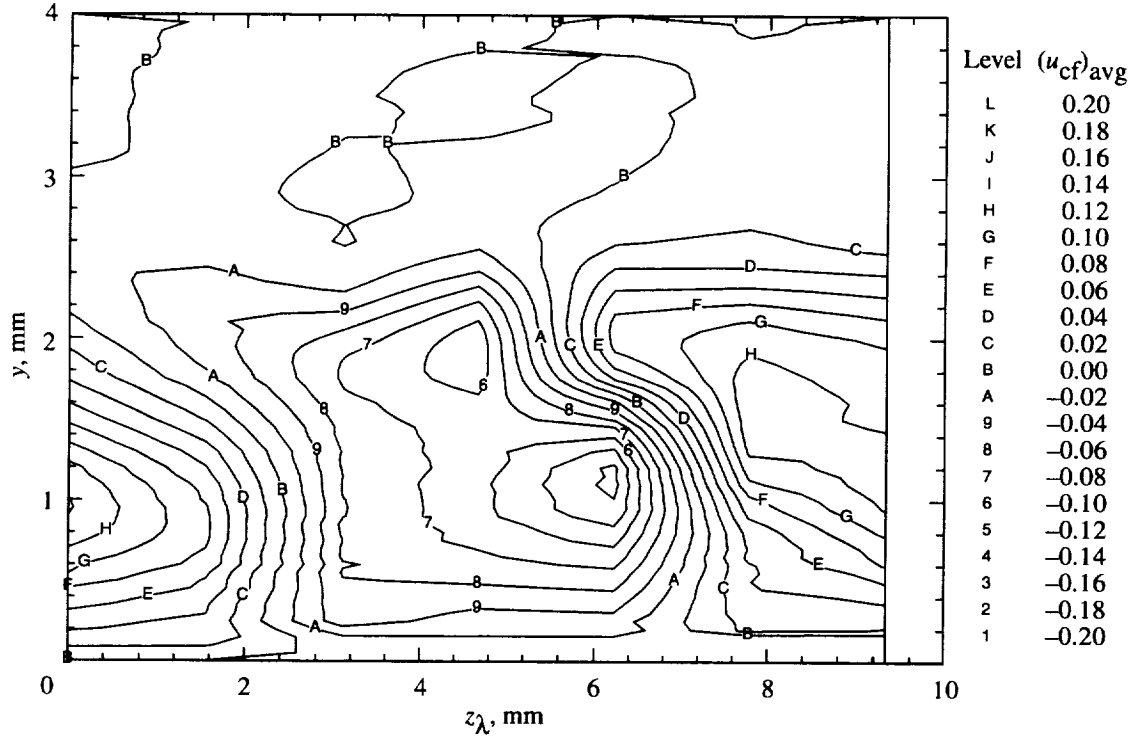


Figure 102. Stationary crossflow vortex velocity contours obtained from  $\bar{u}_s - \bar{u}_{s,avg}$  at  $x/c = 0.45$ ,  $\alpha = -4^\circ$ , and  $R_c = 2.37 \times 10^6$ .

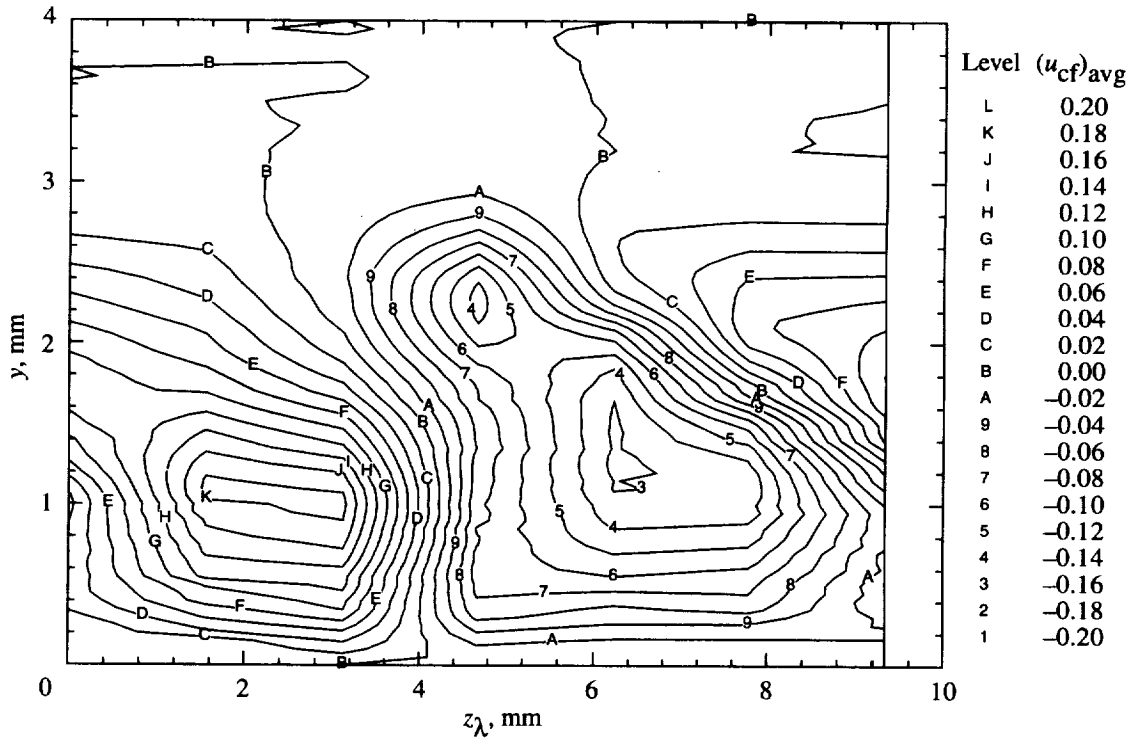


Figure 103. Stationary crossflow vortex velocity contours obtained from  $\bar{u}_s - \bar{u}_{s,avg}$  at  $x/c = 0.50$ ,  $\alpha = -4^\circ$ , and  $R_c = 2.37 \times 10^6$ .



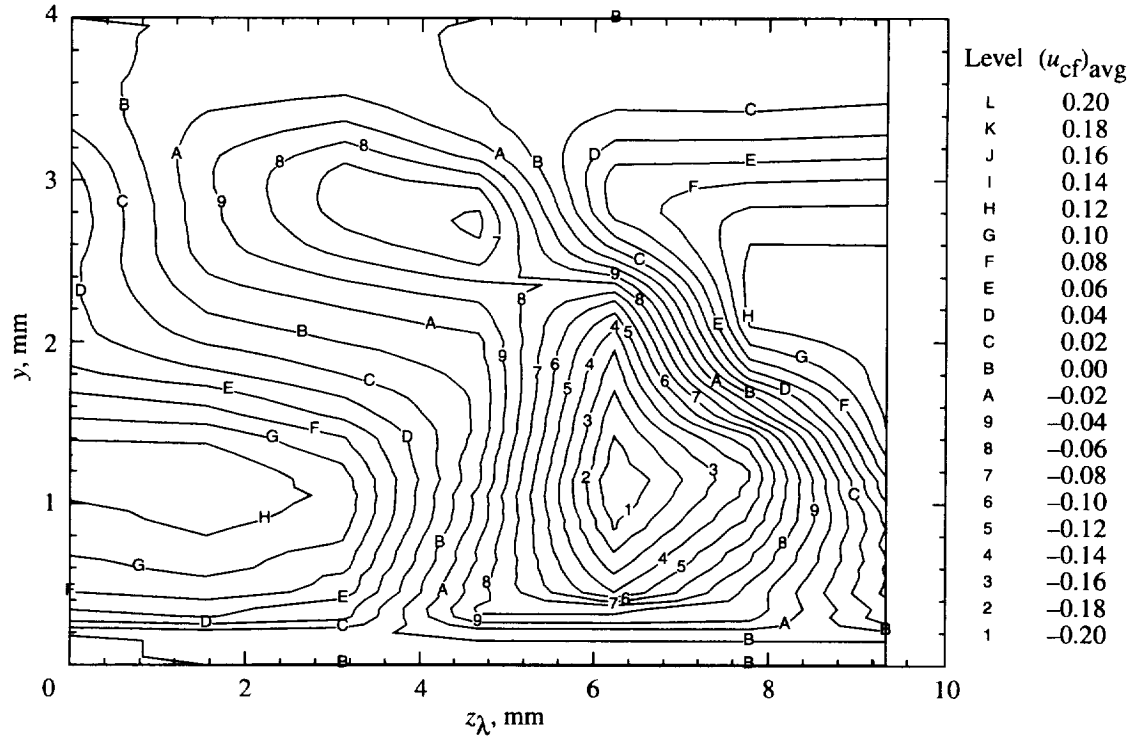


Figure 104. Stationary crossflow vortex velocity contours obtained from  $\bar{u}_s - \bar{u}_{s,avg}$  at  $x/c = 0.55$ ,  $\alpha = -4^\circ$ , and  $R_c = 2.37 \times 10^6$ .

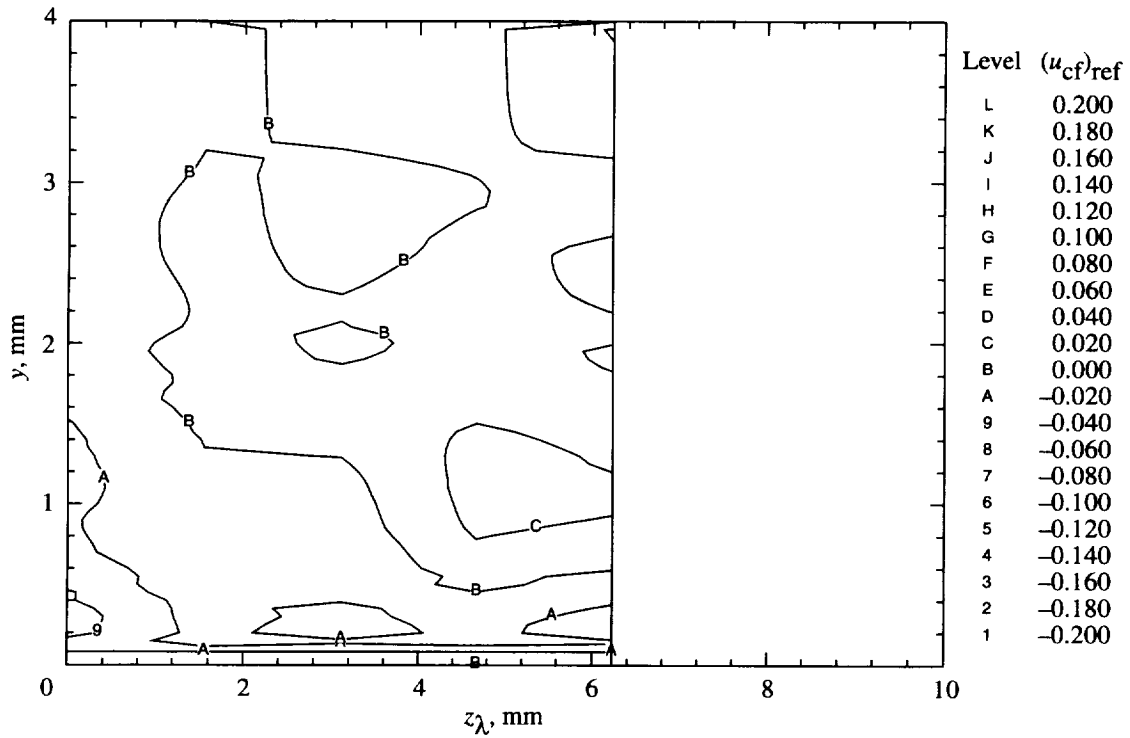


Figure 105. Stationary crossflow vortex velocity contours obtained from  $\bar{u}_s - \bar{u}_{s,ref}$  at  $x/c = 0.20$ ,  $\alpha = -4^\circ$ , and  $R_c = 2.37 \times 10^6$ .

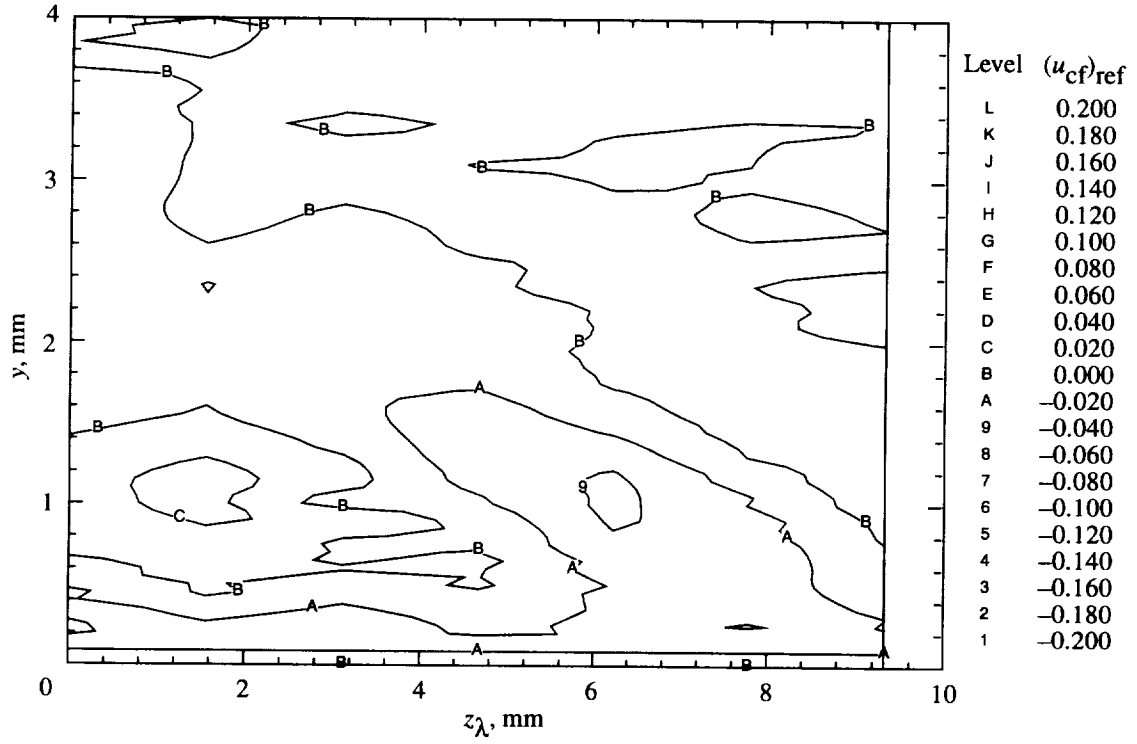


Figure 106. Stationary crossflow vortex velocity contours obtained from  $\bar{u}_s - \bar{u}_{s,ref}$  at  $x/c = 0.25$ ,  $\alpha = -4^\circ$ , and  $R_c = 2.37 \times 10^6$ .

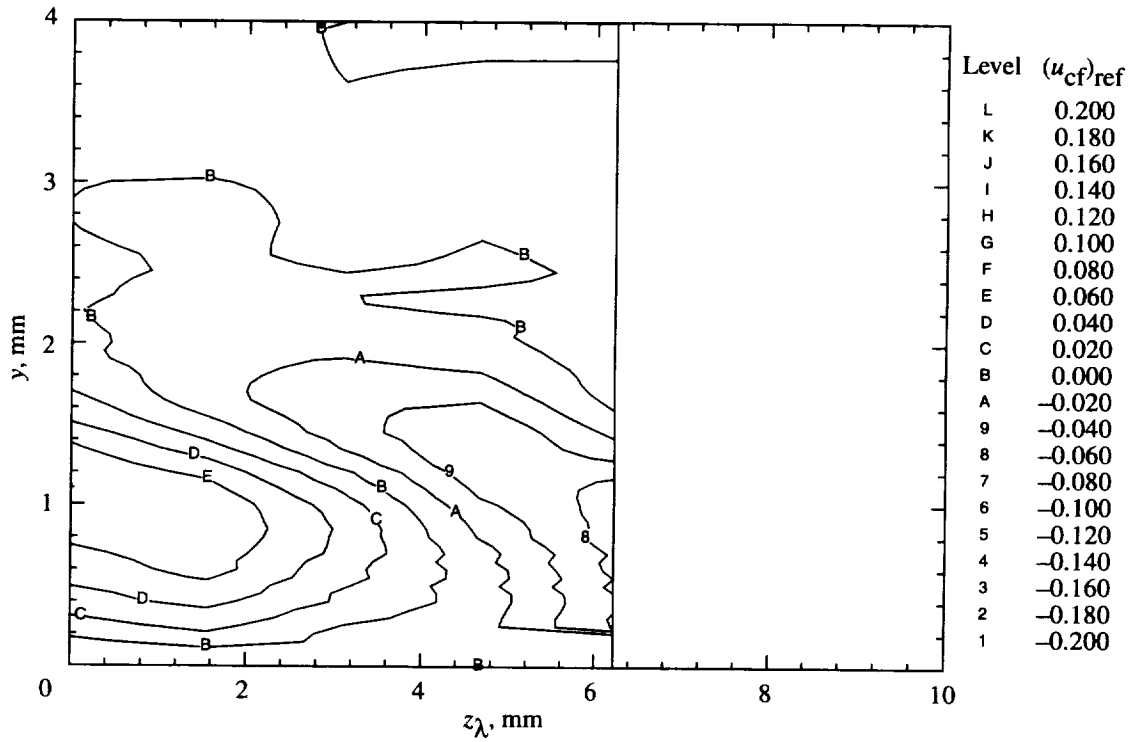


Figure 107. Stationary crossflow vortex velocity contours obtained from  $\bar{u}_s - \bar{u}_{s,ref}$  at  $x/c = 0.30$ ,  $\alpha = -4^\circ$ , and  $R_c = 2.37 \times 10^6$ .

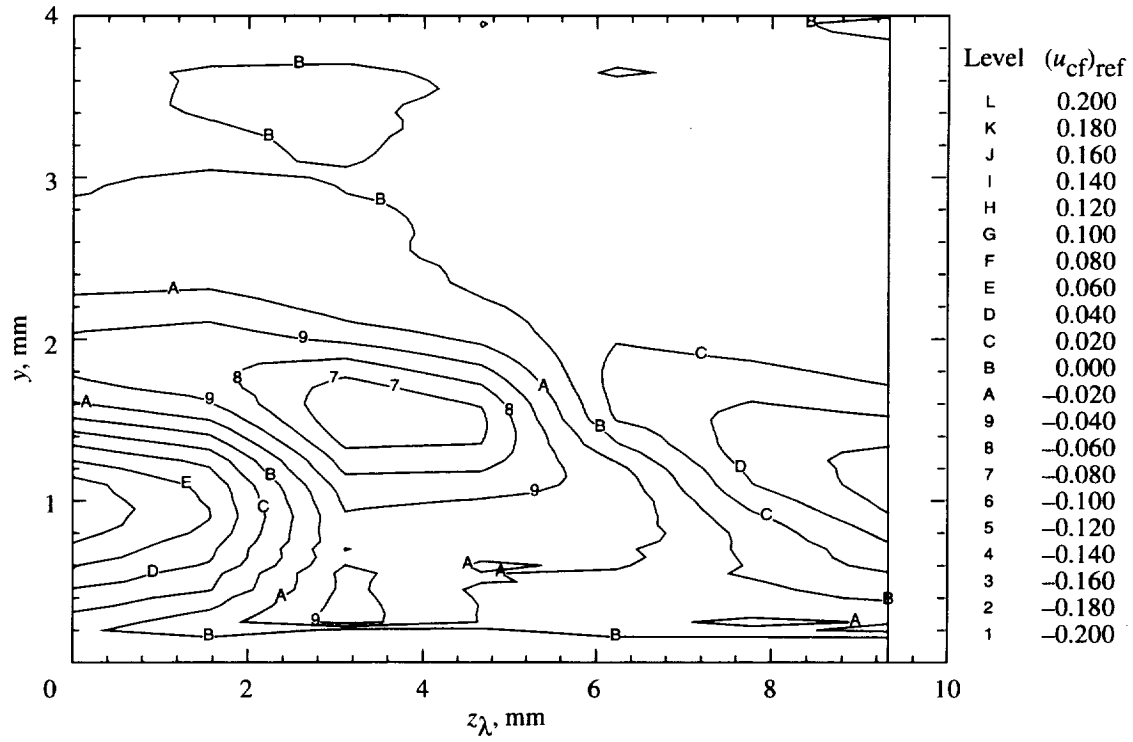


Figure 108. Stationary crossflow vortex velocity contours obtained from  $\bar{u}_s - \bar{u}_{s,ref}$  at  $x/c = 0.35$ ,  $\alpha = -4^\circ$ , and  $R_c = 2.37 \times 10^6$ .

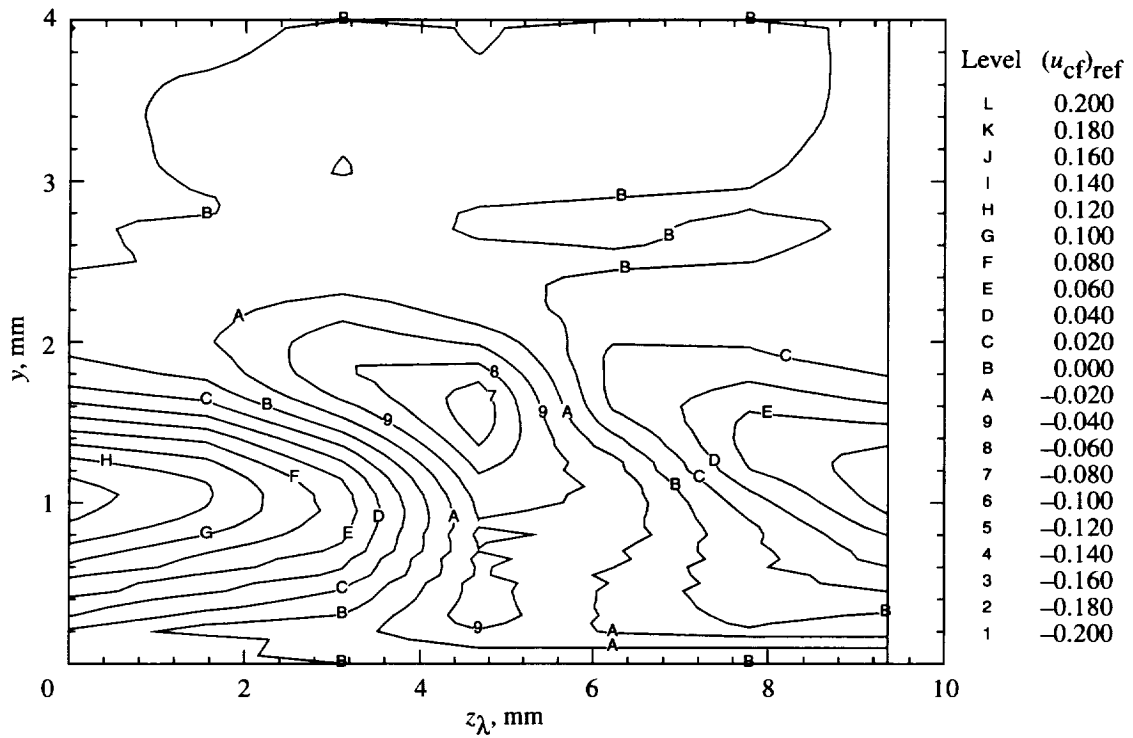


Figure 109. Stationary crossflow vortex velocity contours obtained from  $\bar{u}_s - \bar{u}_{s,ref}$  at  $x/c = 0.40$ ,  $\alpha = -4^\circ$ , and  $R_c = 2.37 \times 10^6$ .

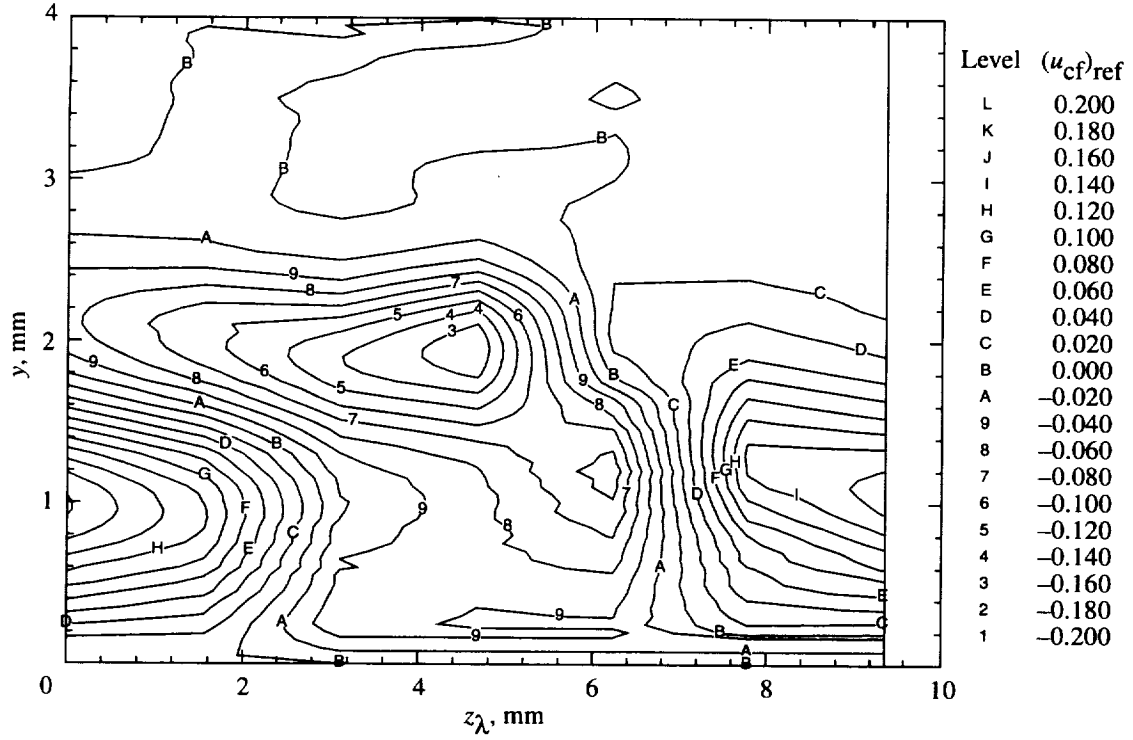


Figure 110. Stationary crossflow vortex velocity contours obtained from  $\bar{u}_s - \bar{u}_{s,ref}$  at  $x/c = 0.45$ ,  $\alpha = -4^\circ$ , and  $R_c = 2.37 \times 10^6$ .

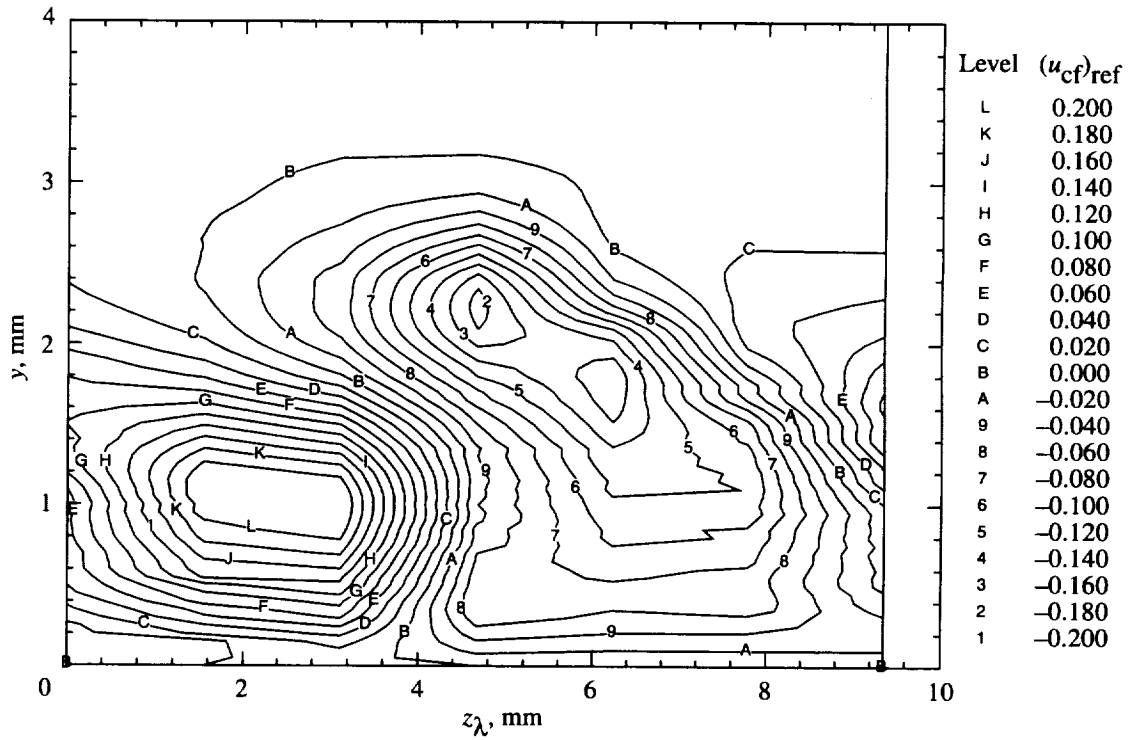


Figure 111. Stationary crossflow vortex velocity contours obtained from  $\bar{u}_s - \bar{u}_{s,ref}$  at  $x/c = 0.50$ ,  $\alpha = -4^\circ$ , and  $R_c = 2.37 \times 10^6$ .

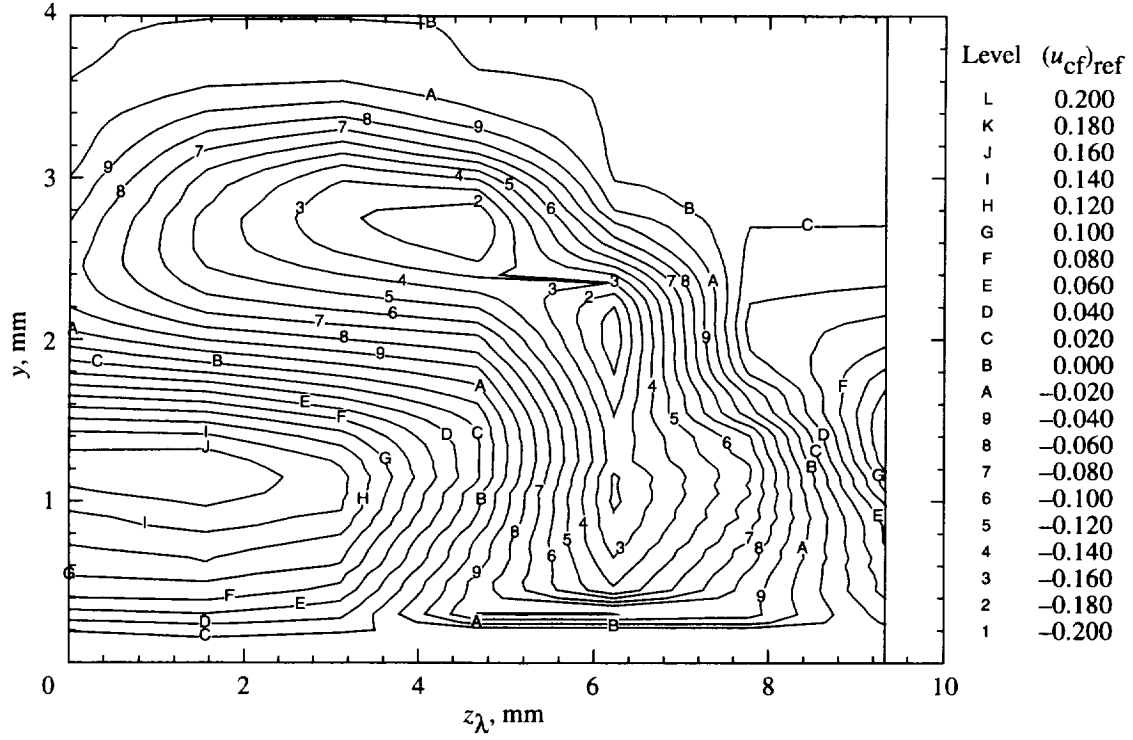


Figure 112. Stationary crossflow vortex velocity contours obtained from  $\bar{u}_s - \bar{u}_{s,ref}$  at  $x/c = 0.55$ ,  $\alpha = -4^\circ$ , and  $R_c = 2.37 \times 10^6$ .

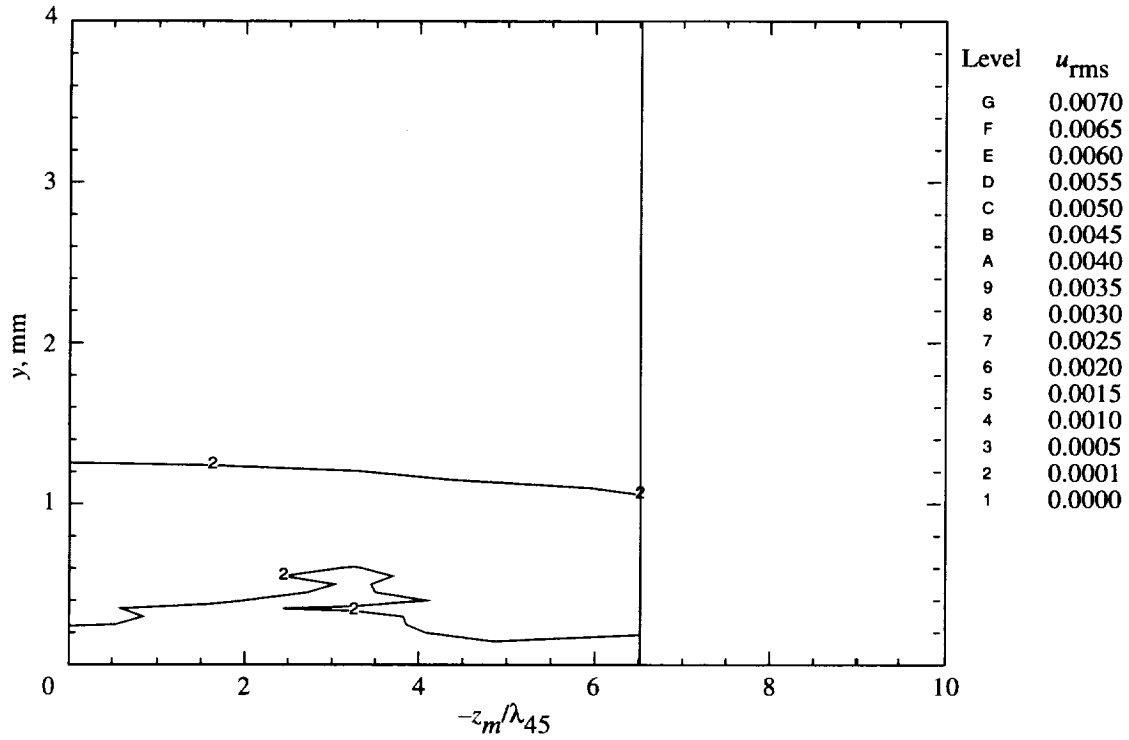


Figure 113. Travelling wave rms velocity contours for  $f = 100$  Hz at  $x/c = 0.20$ ,  $\alpha = -4^\circ$ , and  $R_c = 2.37 \times 10^6$ .

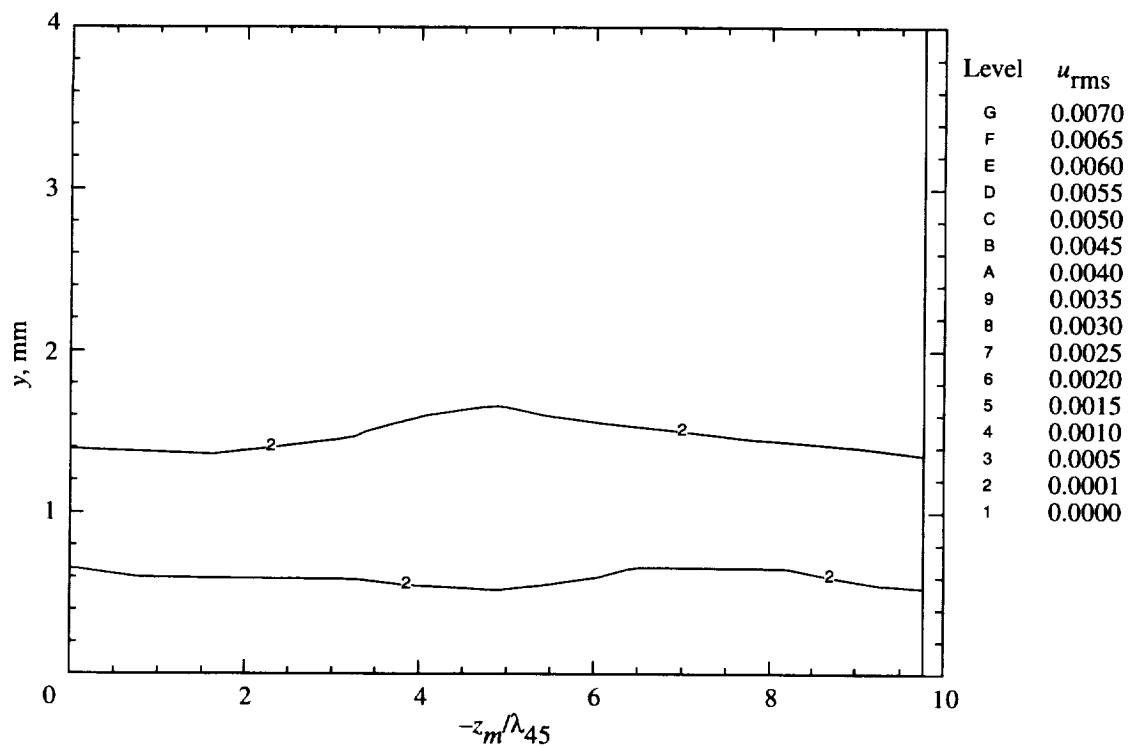


Figure 114. Travelling wave rms velocity contours for  $f = 100$  Hz at  $x/c = 0.25$ ,  $\alpha = -4^\circ$ , and  $R_c = 2.37 \times 10^6$ .

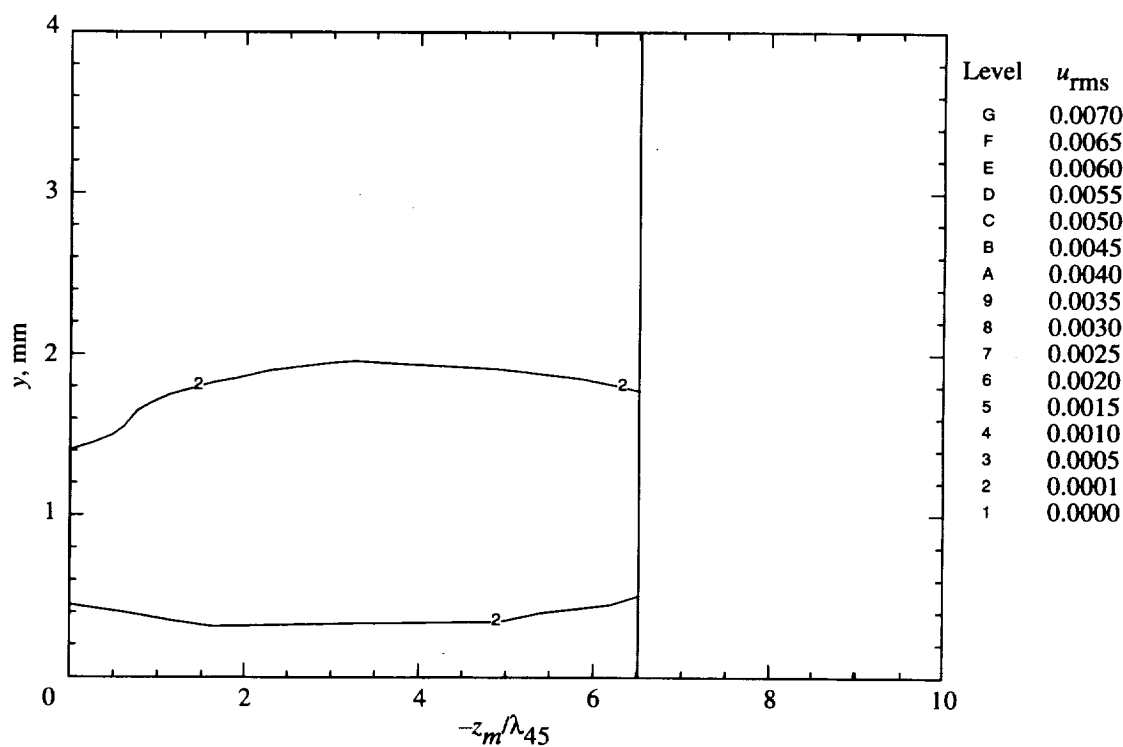


Figure 115. Travelling wave rms velocity contours for  $f = 100$  Hz at  $x/c = 0.30$ ,  $\alpha = -4^\circ$ , and  $R_c = 2.37 \times 10^6$ .

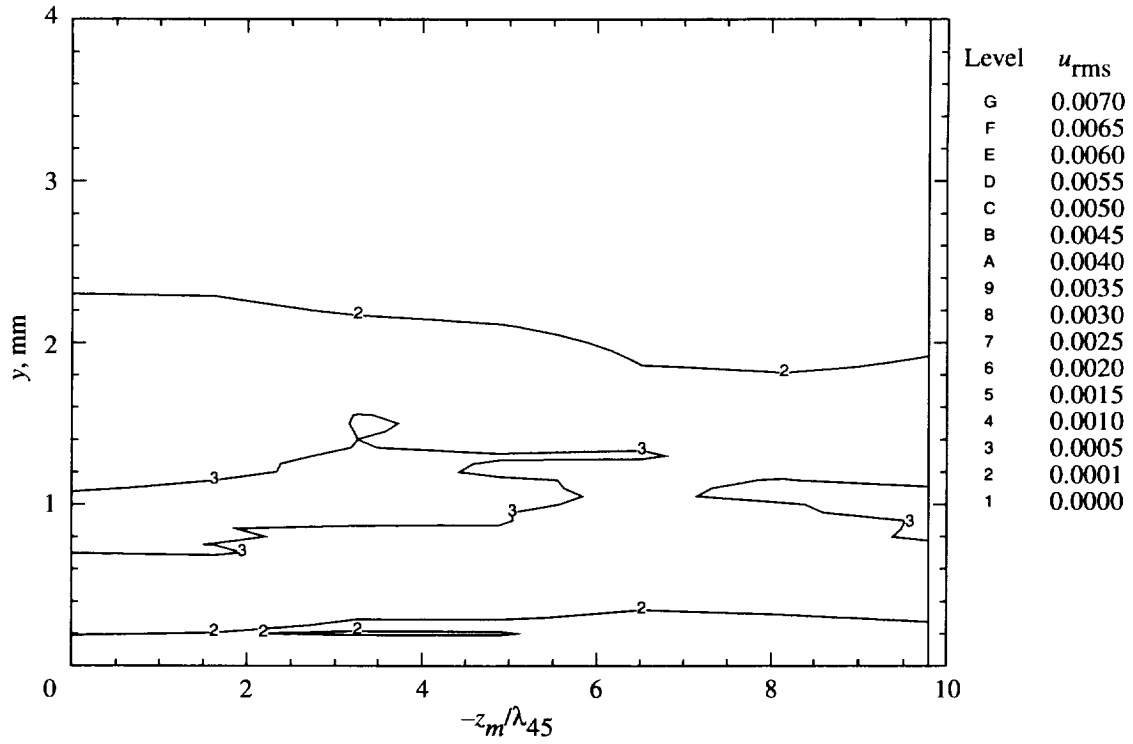


Figure 116. Travelling wave rms velocity contours for  $f = 100$  Hz at  $x/c = 0.35$ ,  $\alpha = -4^\circ$ , and  $R_c = 2.37 \times 10^6$ .

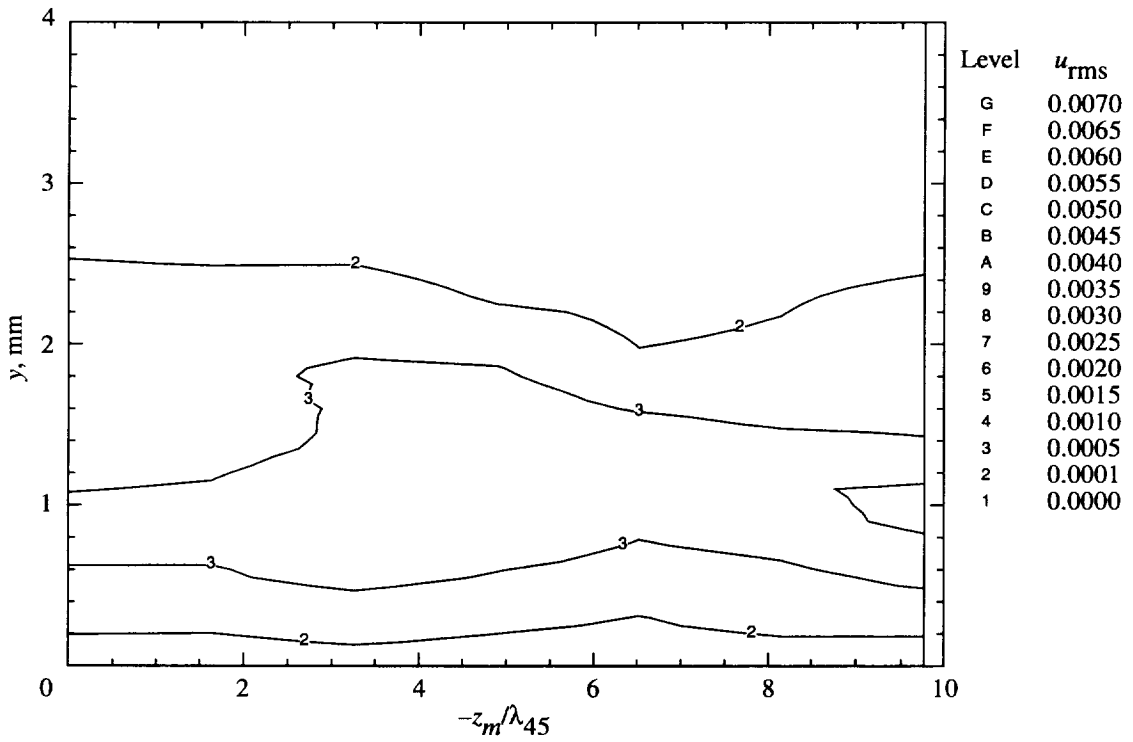


Figure 117. Travelling wave rms velocity contours for  $f = 100$  Hz at  $x/c = 0.40$ ,  $\alpha = -4^\circ$ , and  $R_c = 2.37 \times 10^6$ .

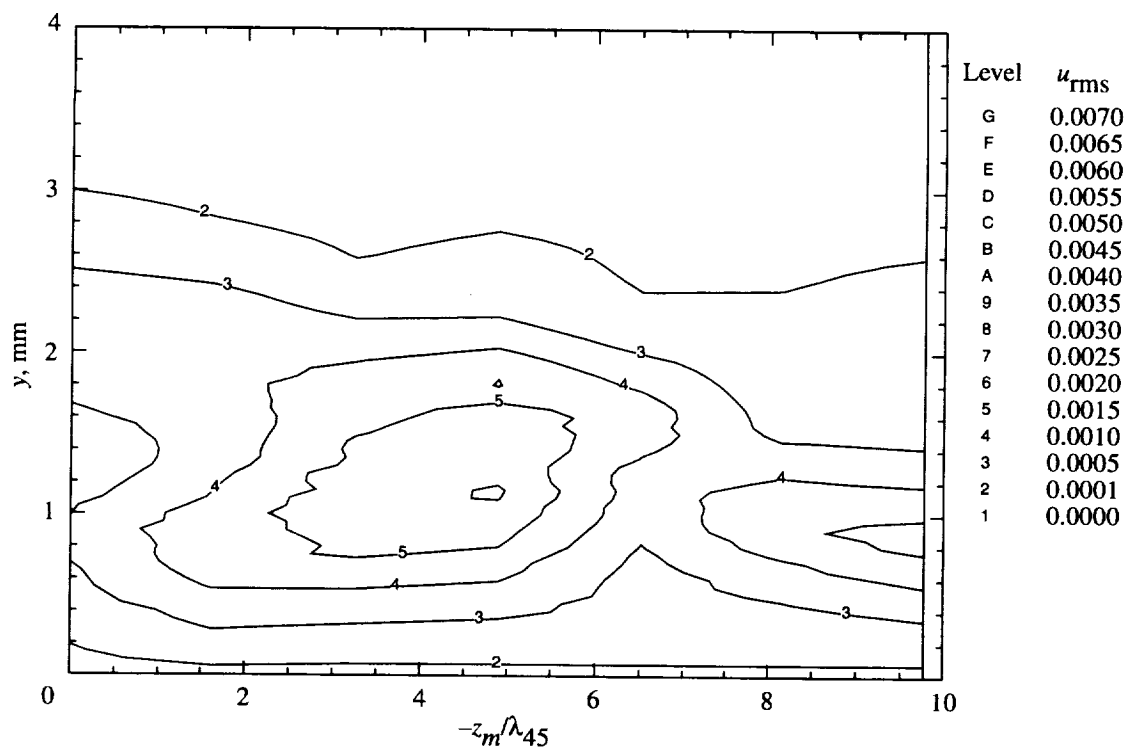


Figure 118. Travelling wave rms velocity contours for  $f = 100$  Hz at  $x/c = 0.45$ ,  $\alpha = -4^\circ$ , and  $R_c = 2.37 \times 10^6$ .

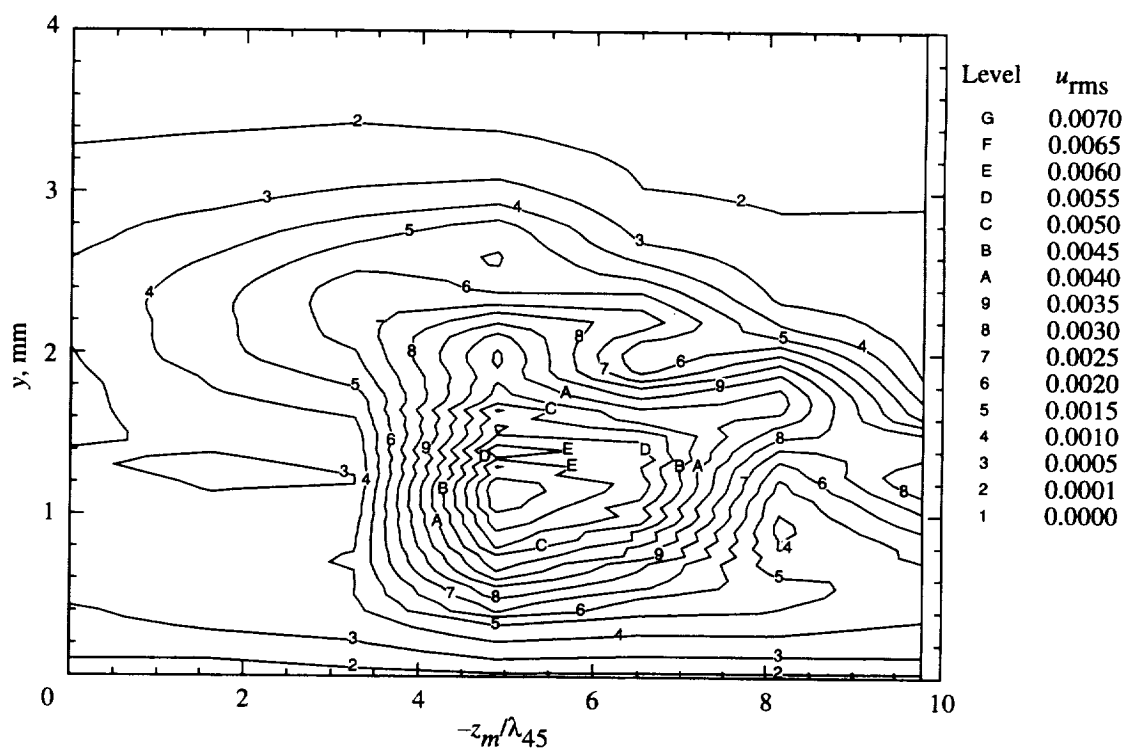


Figure 119. Travelling wave rms velocity contours for  $f = 100$  Hz at  $x/c = 0.50$ ,  $\alpha = -4^\circ$ , and  $R_c = 2.37 \times 10^6$ .



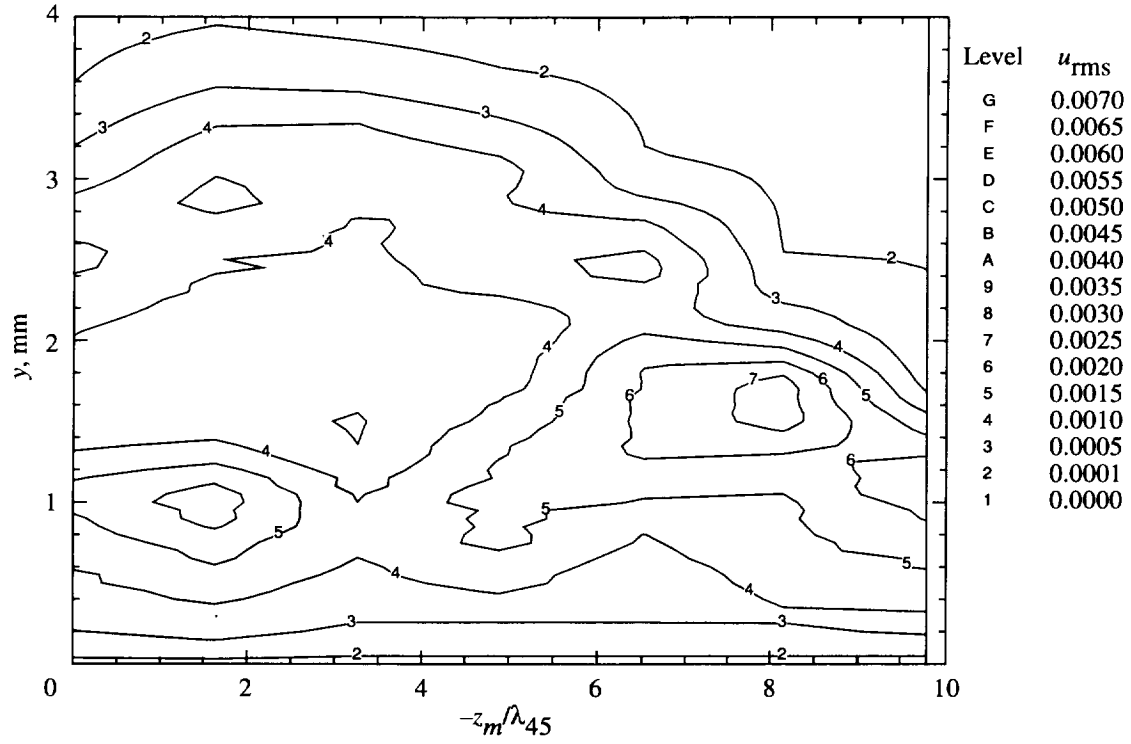


Figure 120. Travelling wave rms velocity contours for  $f = 100$  Hz at  $x/c = 0.55$ ,  $\alpha = -4^\circ$ , and  $R_c = 2.37 \times 10^6$ .

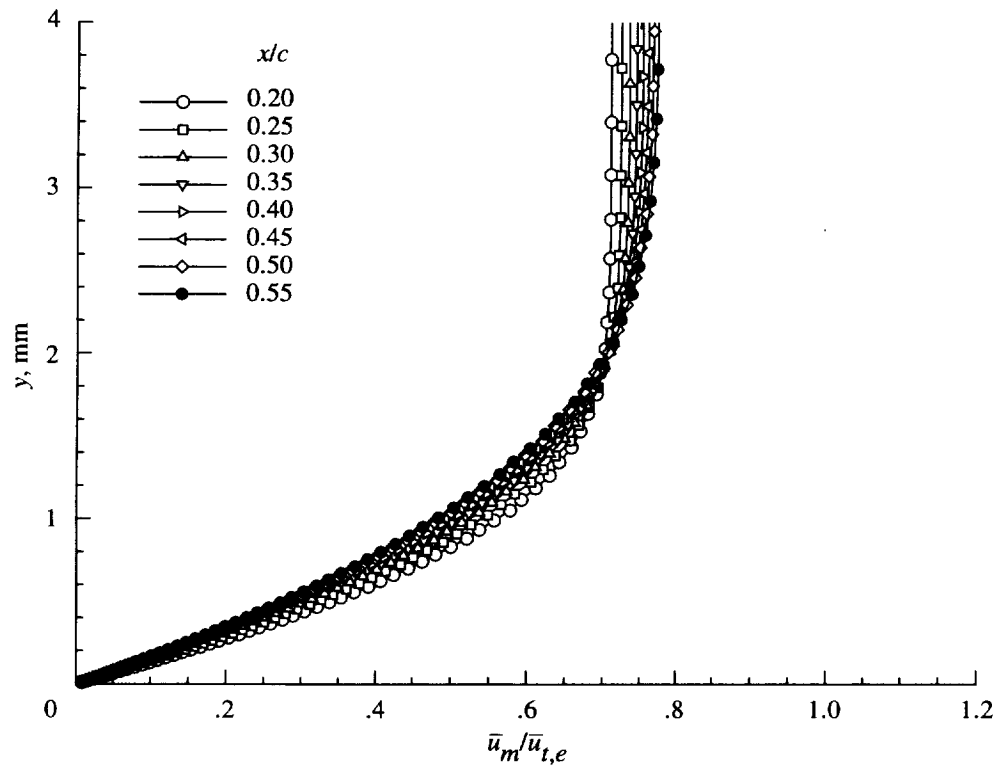


Figure 121. Theoretical mean chordwise velocity profiles for  $\alpha_{ref} = -5^\circ$  and  $R_c = 2.37 \times 10^6$ . Theory from reference 126.

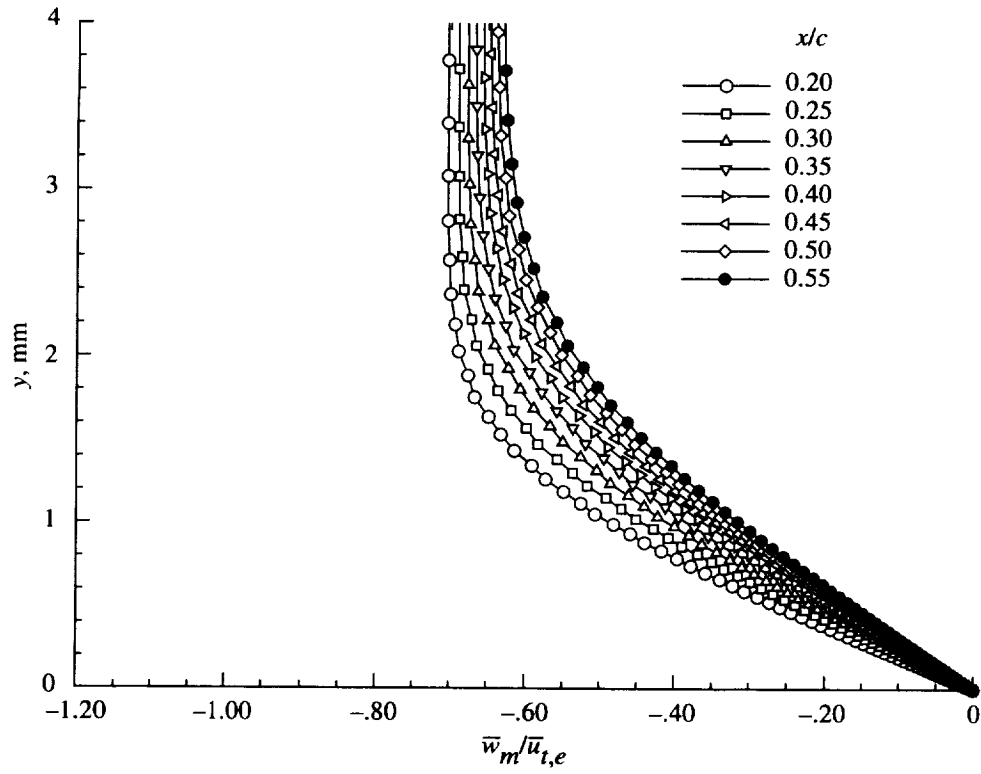


Figure 122. Theoretical mean spanwise velocity profiles for  $\alpha_{\text{ref}} = -5^\circ$  and  $R_c = 2.37 \times 10^6$ . Theory from reference 126.

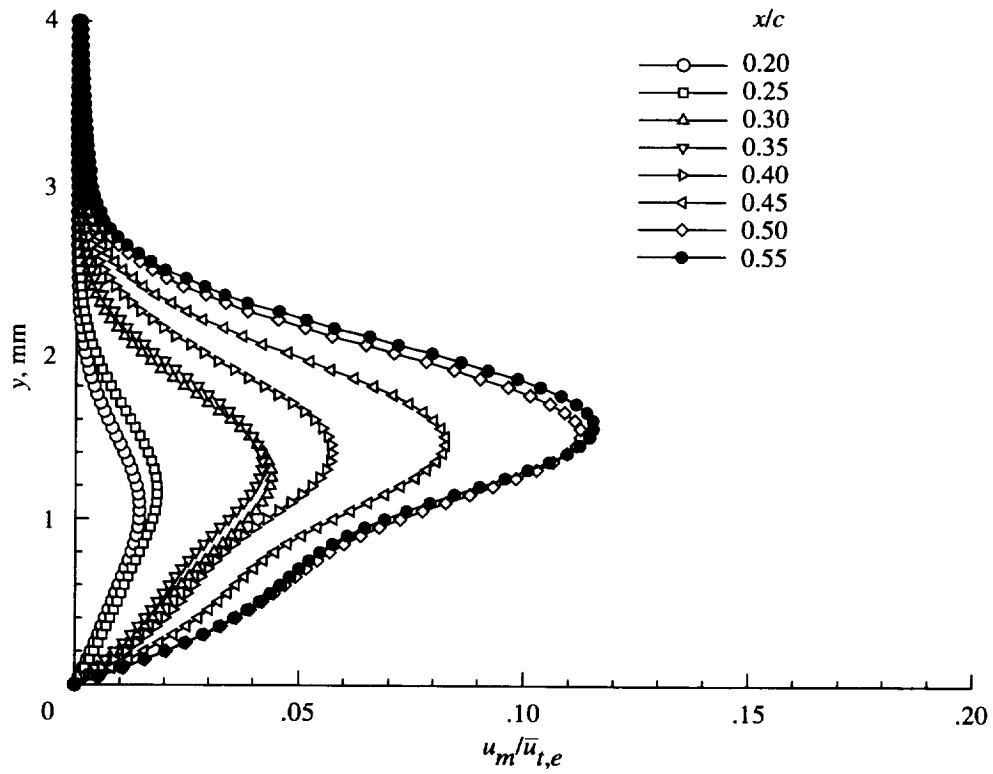


Figure 123. Theoretical stationary crossflow disturbance velocity profiles (chordwise component) for  $\alpha_{\text{ref}} = -5^\circ$  and  $R_c = 2.37 \times 10^6$ . Theory from reference 128.

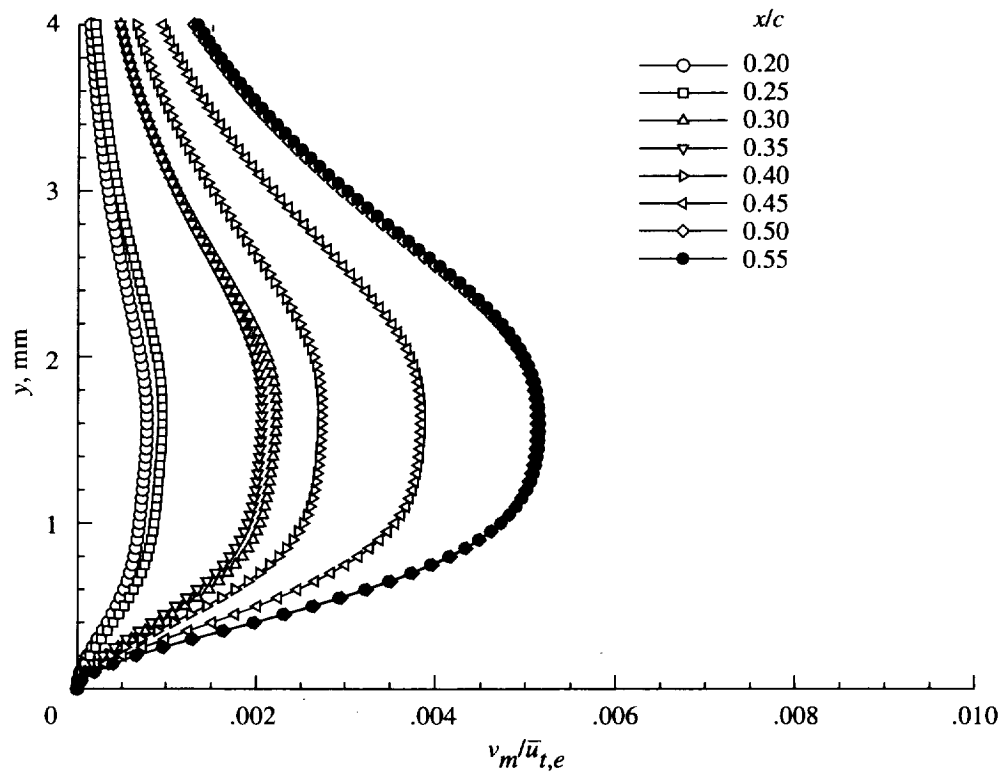


Figure 124. Theoretical stationary crossflow disturbance velocity profiles (surface normal component) for  $\alpha_{\text{ref}} = -5^\circ$  and  $R_c = 2.37 \times 10^6$ . Theory from reference 128.

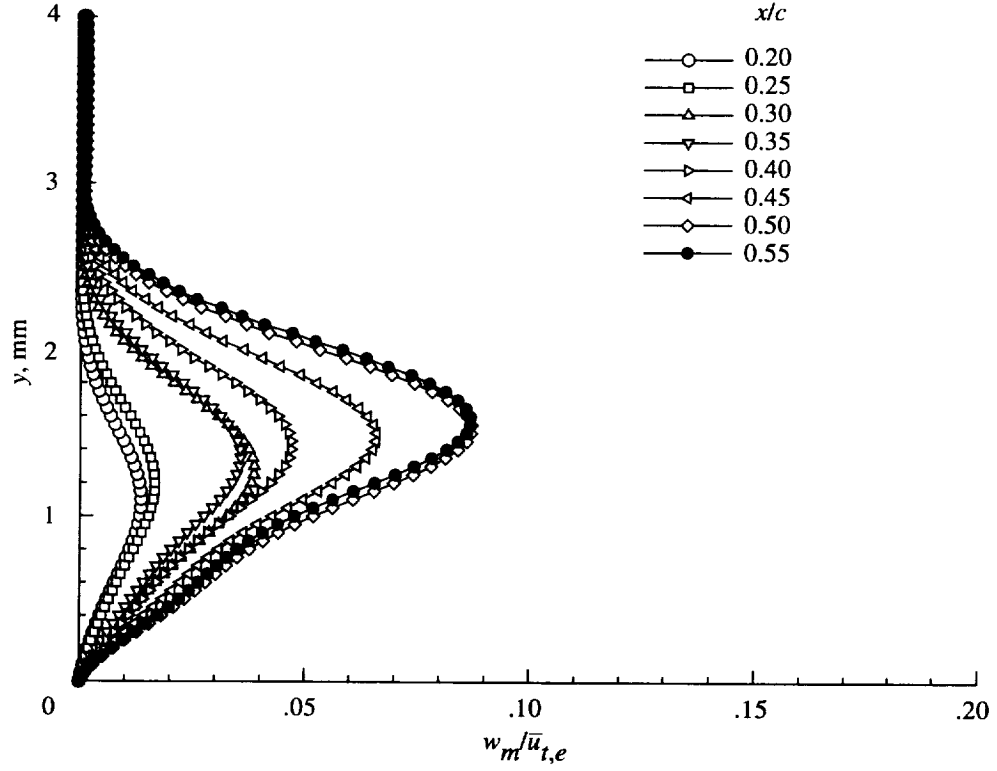


Figure 125. Theoretical stationary crossflow disturbance velocity profiles (spanwise component) for  $\alpha_{\text{ref}} = -5^\circ$  and  $R_c = 2.37 \times 10^6$ . Theory from reference 128.

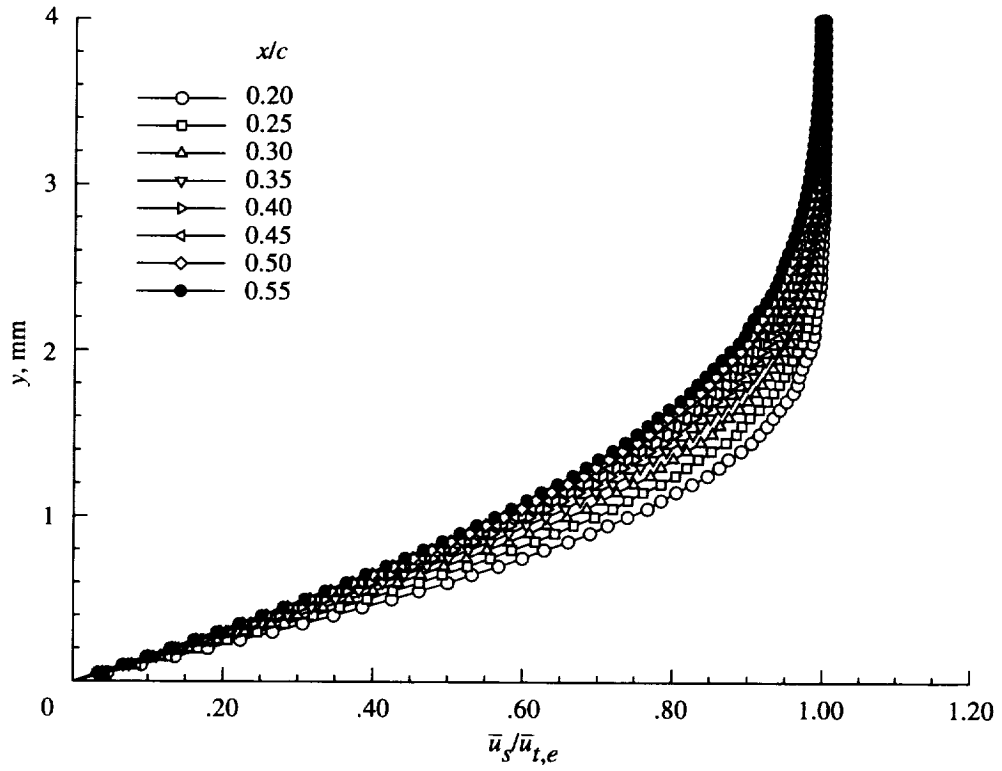


Figure 126. Theoretical mean streamwise velocity profiles for  $\alpha_{\text{ref}} = -5^\circ$  and  $R_c = 2.37 \times 10^6$ . Theory from reference 126.

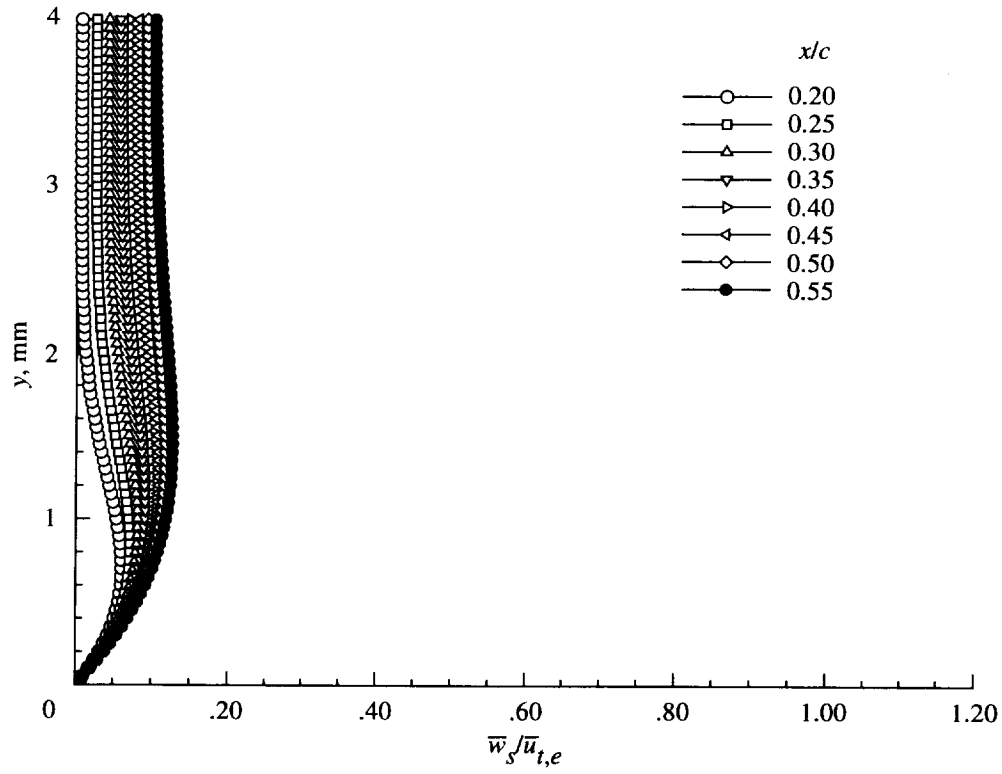


Figure 127. Theoretical mean cross-stream velocity profiles for  $\alpha_{\text{ref}} = -5^\circ$  and  $R_c = 2.37 \times 10^6$ . Theory from reference 126.

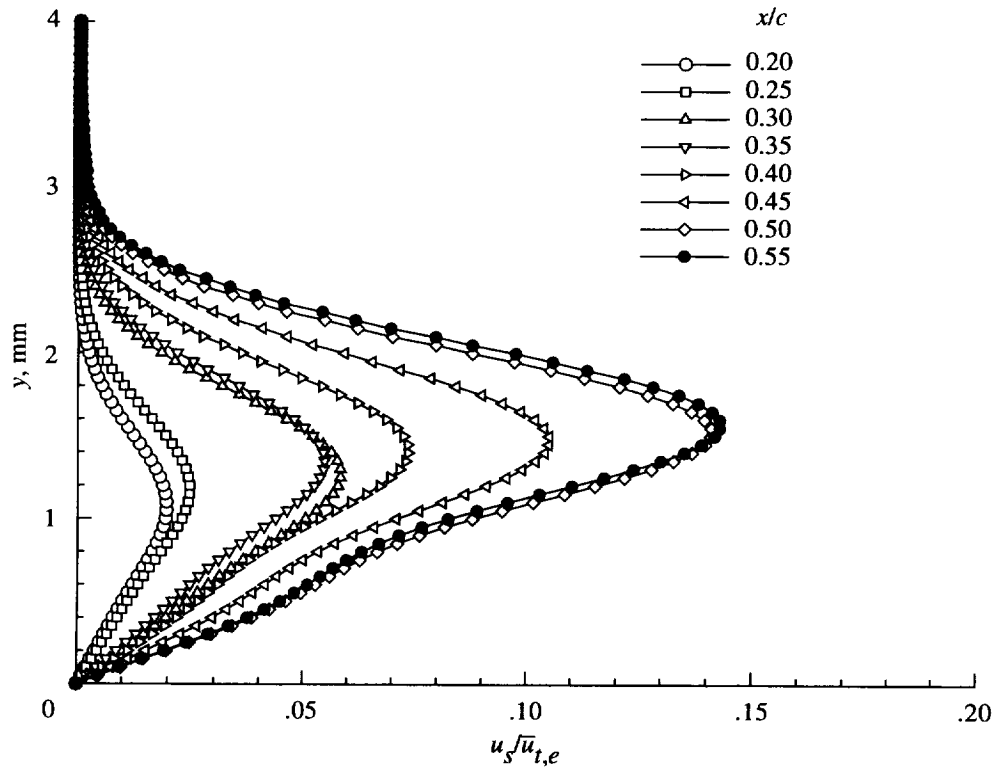


Figure 128. Theoretical stationary crossflow disturbance velocity profiles (streamwise component) for  $\alpha_{\text{ref}} = -5^\circ$  and  $R_c = 2.37 \times 10^6$ . Theory from reference 128.

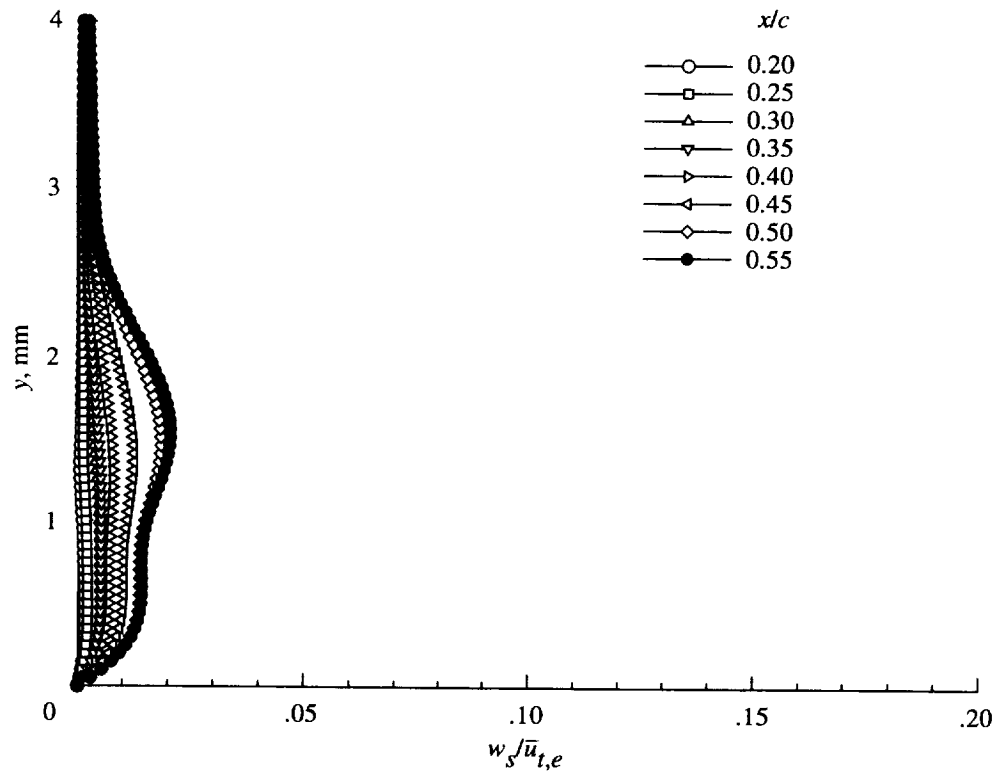


Figure 129. Theoretical stationary crossflow disturbance velocity profiles (cross-stream component) for  $\alpha_{\text{ref}} = -5^\circ$  and  $R_c = 2.37 \times 10^6$ . Theory from reference 128.

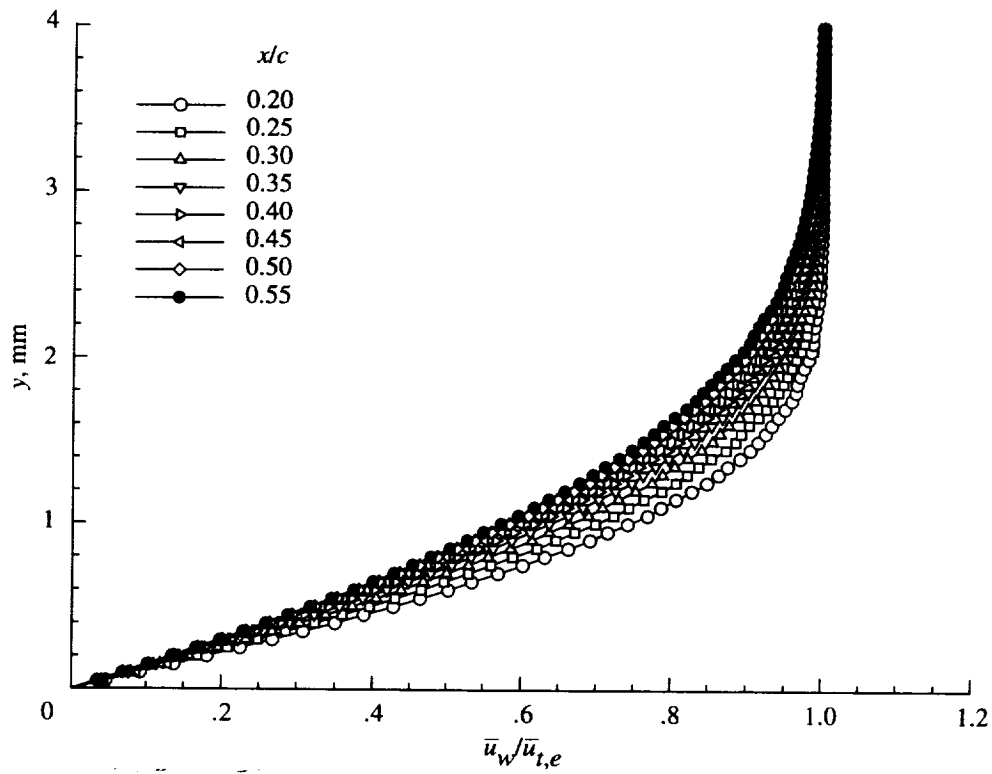


Figure 130. Theoretical mean velocity profiles along vortex axis for  $\alpha_{\text{ref}} = -5^\circ$  and  $R_c = 2.37 \times 10^6$ . Theory from reference 126.

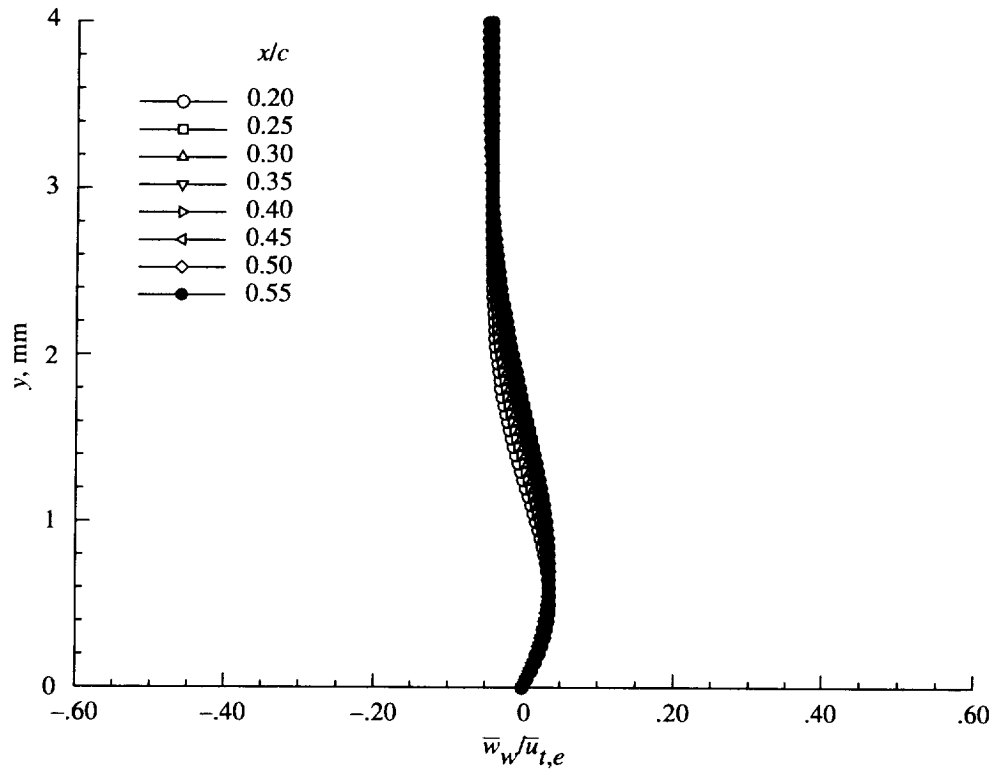


Figure 131. Theoretical mean velocity profiles perpendicular to vortex axis for  $\alpha_{\text{ref}} = -5^\circ$  and  $R_c = 2.37 \times 10^6$ . Theory from reference 126.

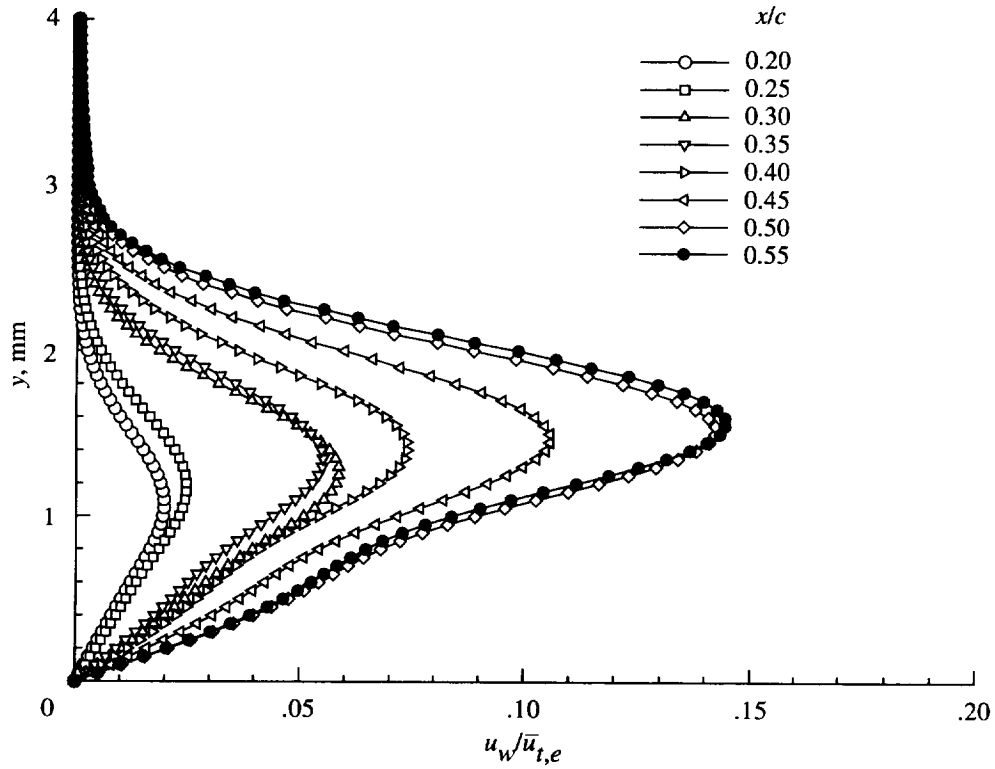


Figure 132. Theoretical stationary crossflow disturbance velocity profiles along vortex axis for  $\alpha_{\text{ref}} = -5^\circ$  and  $R_c = 2.37 \times 10^6$ . Theory from reference 128.

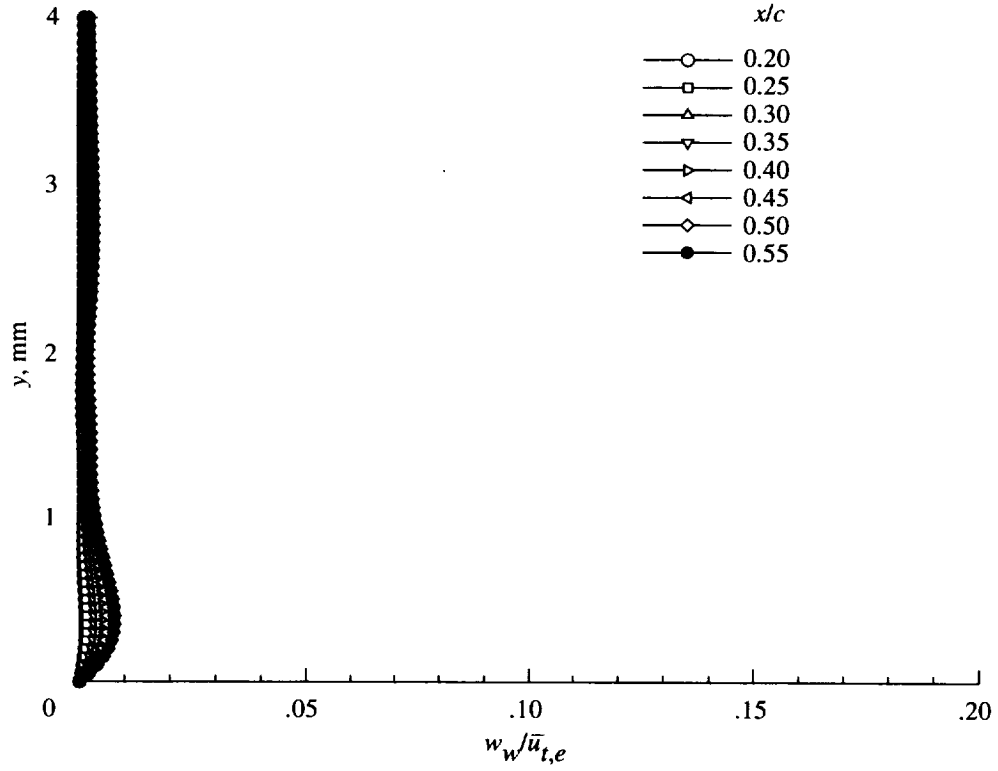


Figure 133. Theoretical stationary crossflow disturbance velocity profiles perpendicular to vortex axis for  $\alpha_{\text{ref}} = -5^\circ$  and  $R_c = 2.37 \times 10^6$ . Theory from reference 128.

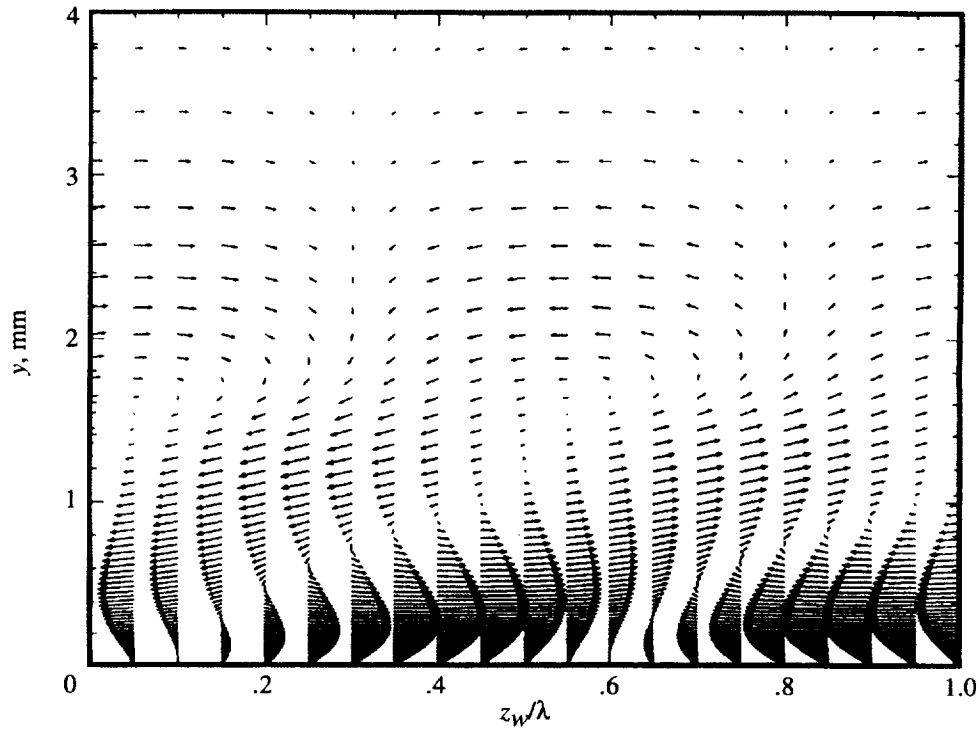


Figure 134. Theoretical stationary crossflow disturbance velocity vectors across single vortex wavelength for  $\alpha_{\text{ref}} = -5^\circ$  and  $R_c = 2.37 \times 10^6$ .



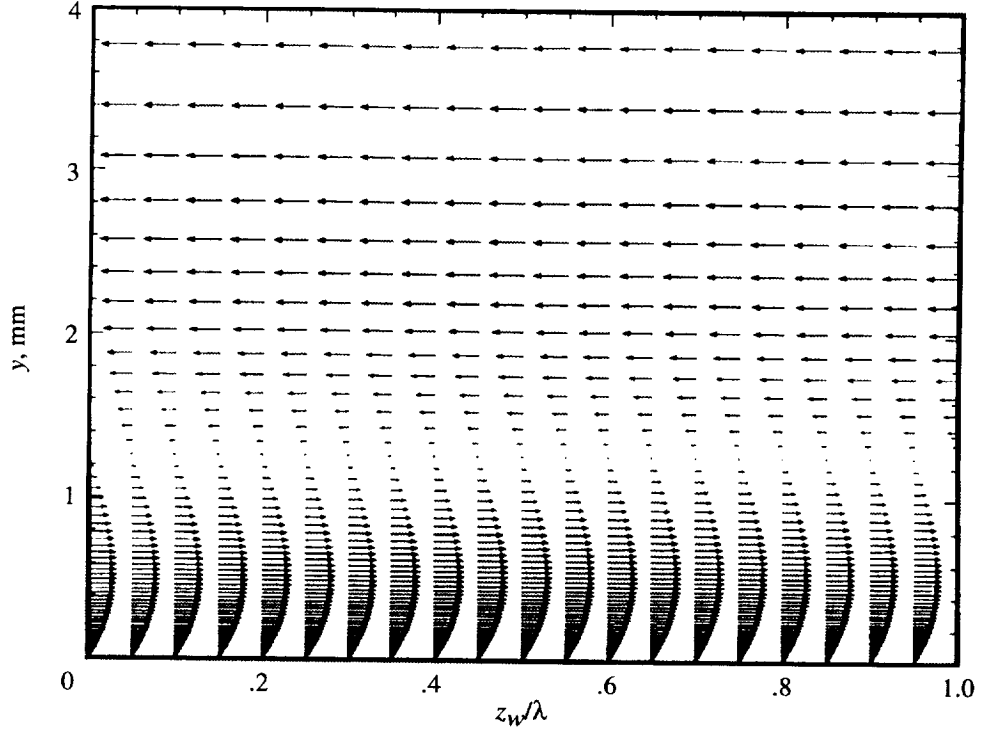


Figure 135. Theoretical total velocity vectors (disturbance plus mean flow) across single vortex wavelength for  $\alpha_{\text{ref}} = -5^\circ$  and  $R_c = 2.37 \times 10^6$ .

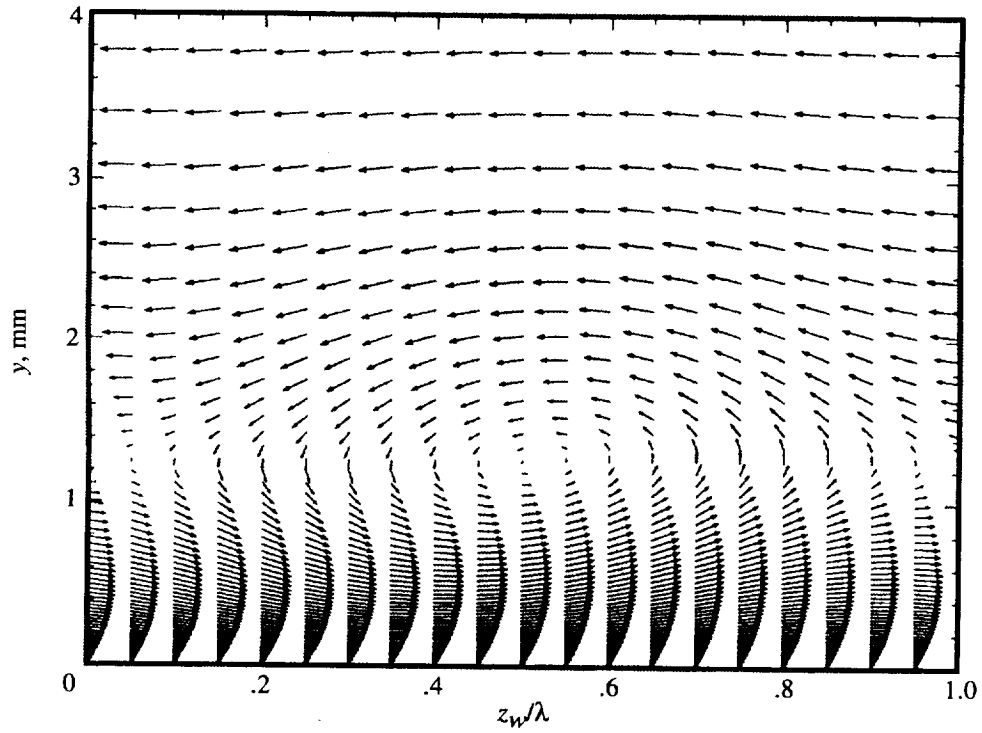


Figure 136. Theoretical total velocity vectors (disturbance plus mean flow) across single vortex wavelength with normal velocity components scaled 100 for  $\alpha_{\text{ref}} = -5^\circ$  and  $R_c = 2.37 \times 10^6$ .

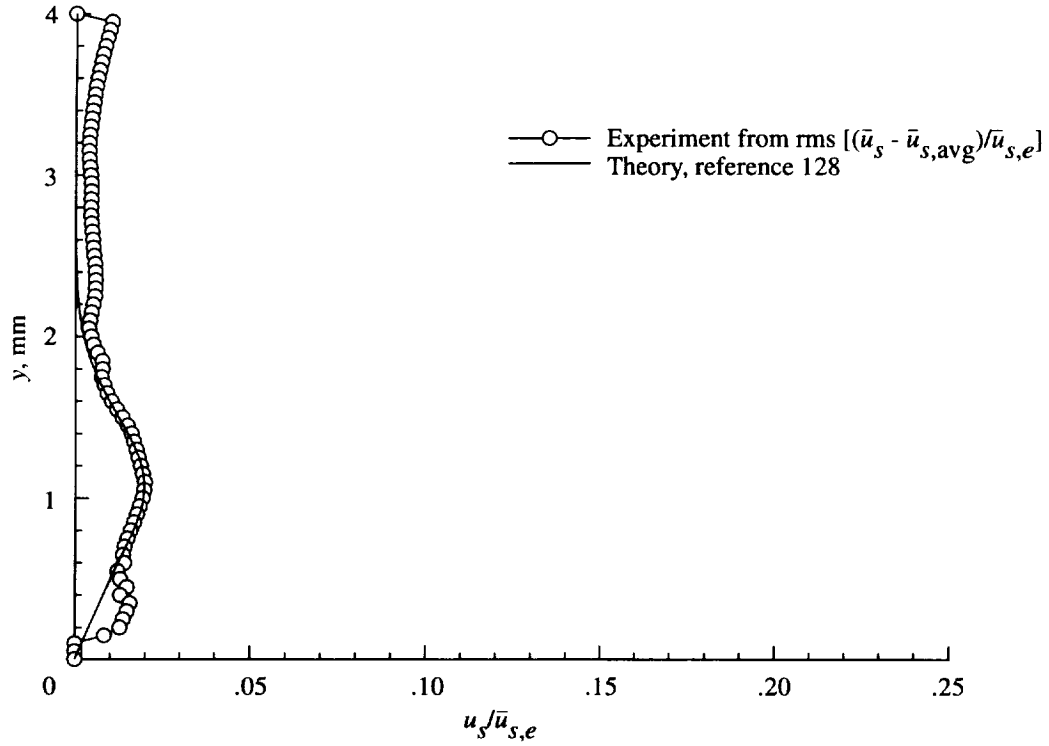


Figure 137. Experimental streamwise disturbance velocity profile determined from  $\bar{u}_s - \bar{u}_{s,avg}$  and theoretical eigenfunction for  $x/c = 0.20$ ,  $\alpha = -4^\circ$ , and  $R_c = 2.37 \times 10^6$ .

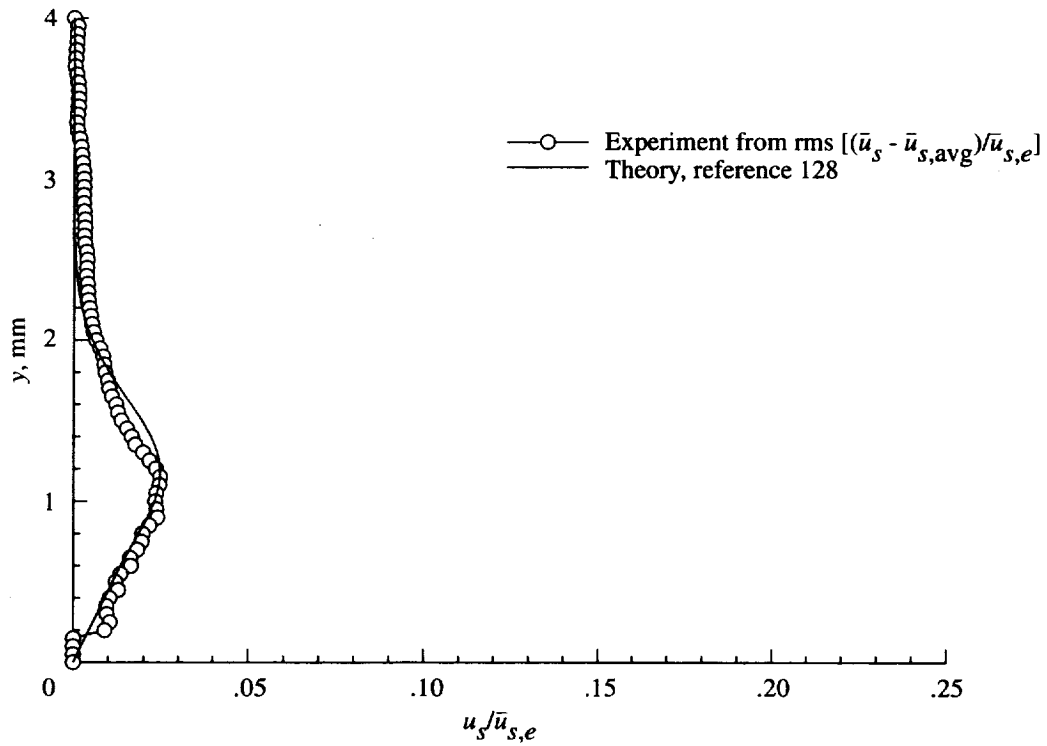


Figure 138. Experimental streamwise disturbance velocity profile determined from  $\bar{u}_s - \bar{u}_{s,avg}$  and theoretical eigenfunction for  $x/c = 0.25$ ,  $\alpha = -4^\circ$ , and  $R_c = 2.37 \times 10^6$ .

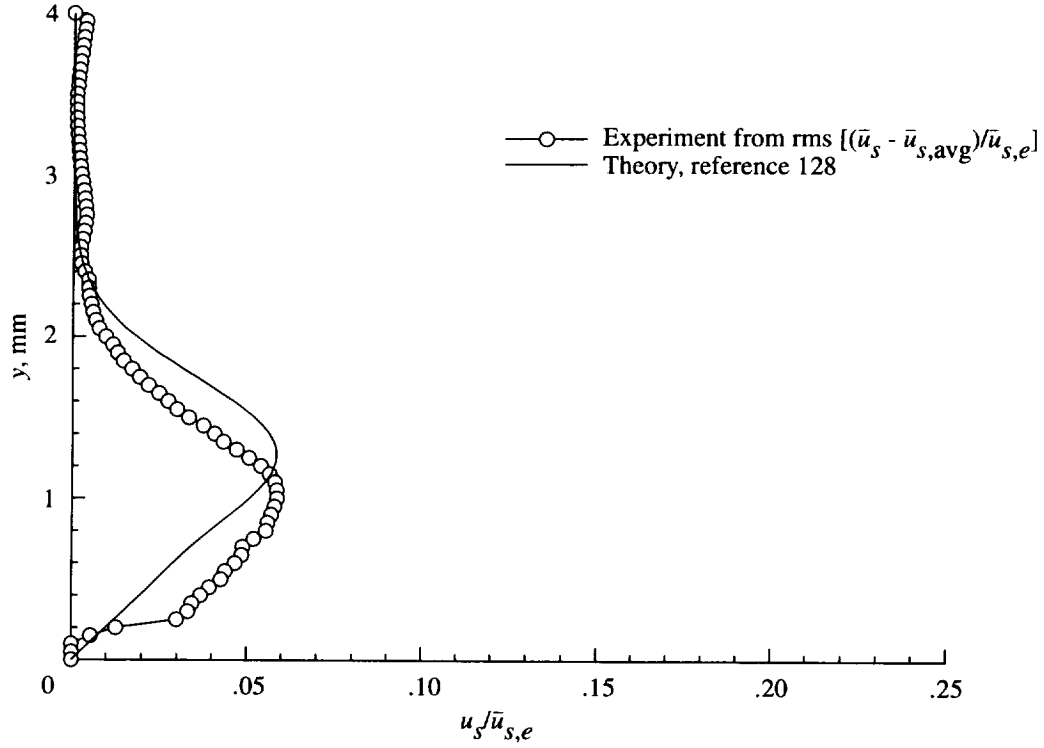


Figure 139. Experimental streamwise disturbance velocity profile determined from  $\bar{u}_s - \bar{u}_{s,\text{avg}}$  and theoretical eigenfunction for  $x/c = 0.30$ ,  $\alpha = -4^\circ$ , and  $R_c = 2.37 \times 10^6$ .

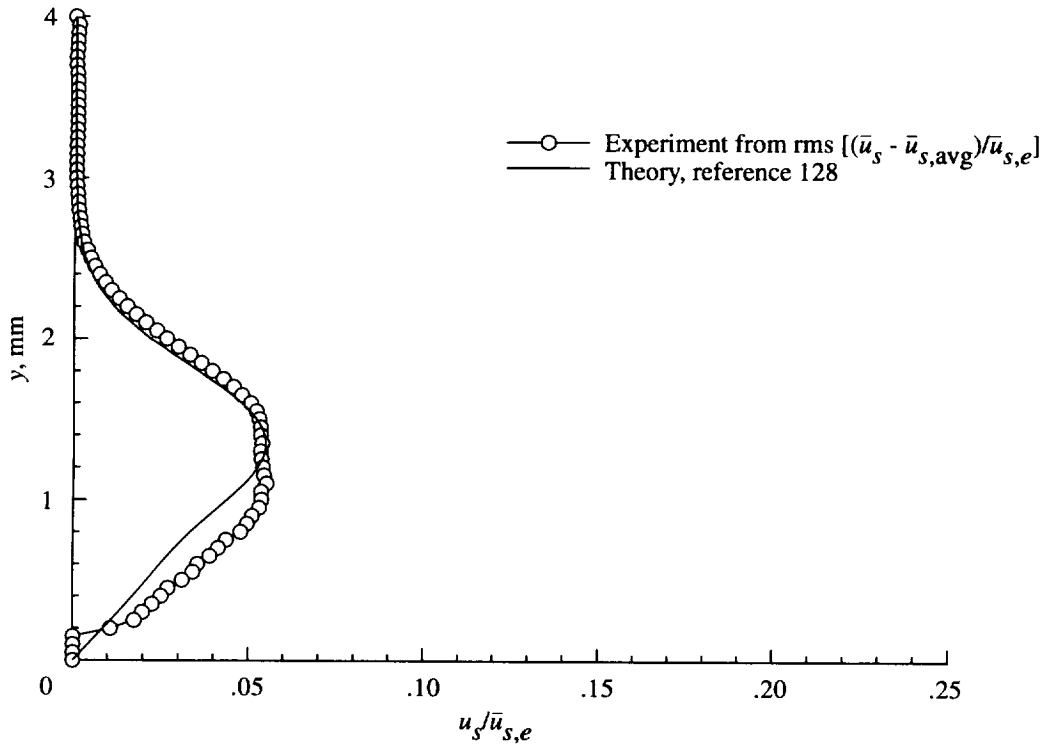


Figure 140. Experimental streamwise disturbance velocity profile determined from  $\bar{u}_s - \bar{u}_{s,\text{avg}}$  and theoretical eigenfunction for  $x/c = 0.30$ ,  $\alpha = -4^\circ$ , and  $R_c = 2.37 \times 10^6$ .

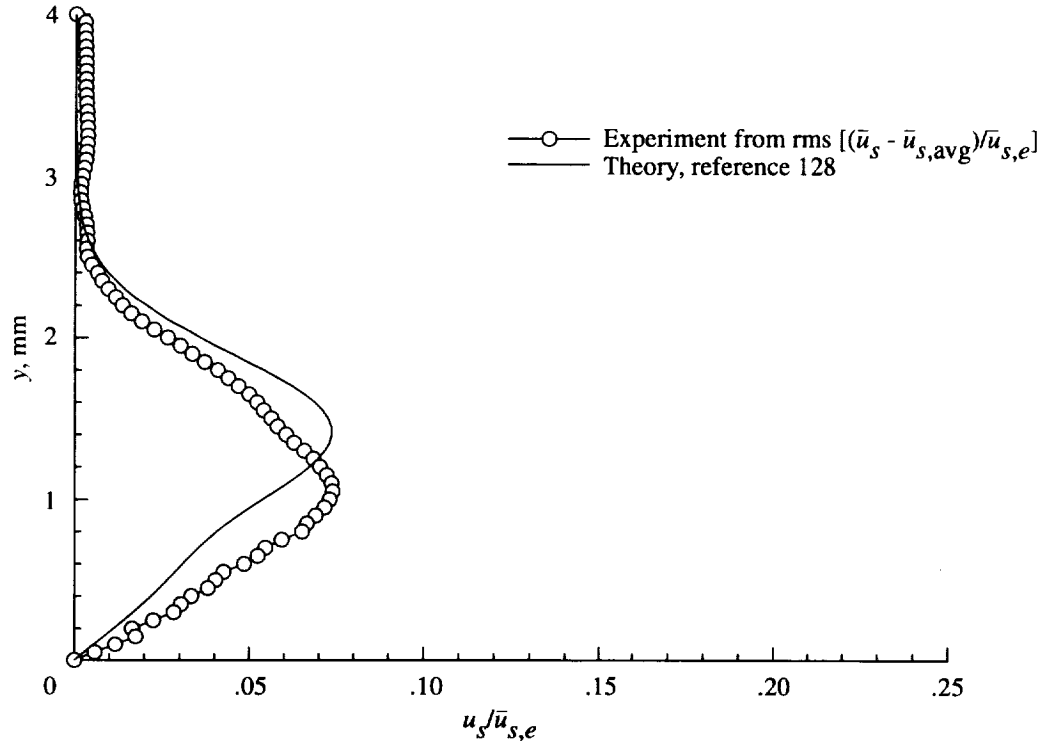


Figure 141. Experimental streamwise disturbance velocity profile determined from  $\bar{u}_s - \bar{u}_{s,avg}$  and theoretical eigenfunction for  $x/c = 0.40$ ,  $\alpha = -4^\circ$ , and  $R_c = 2.37 \times 10^6$ .

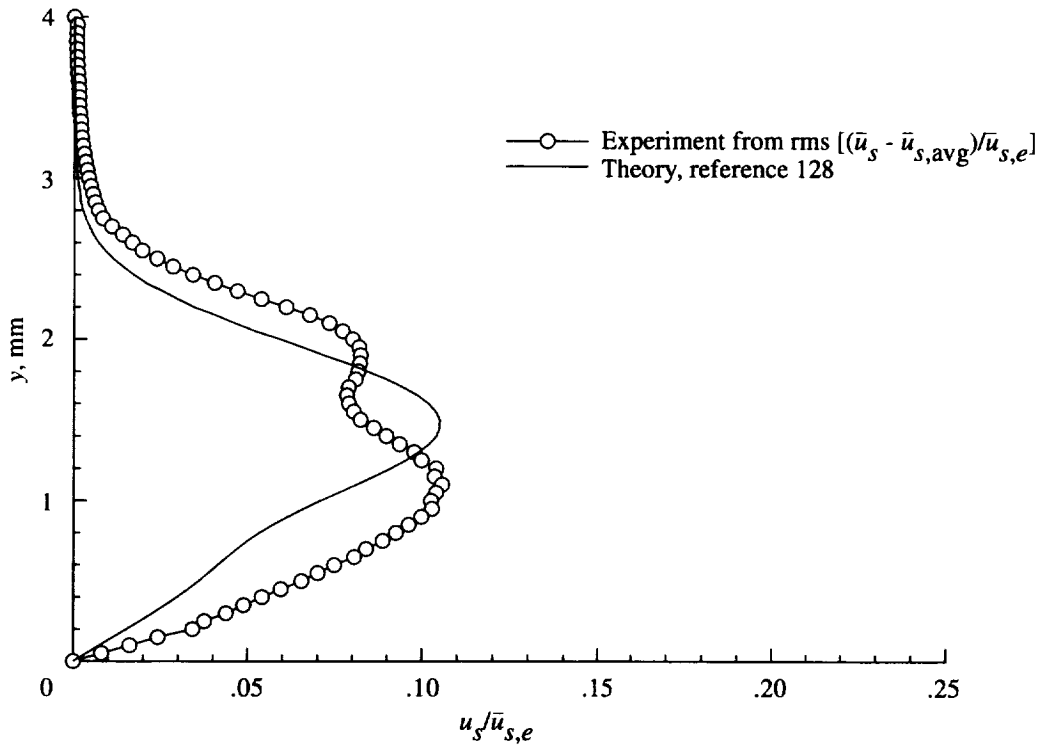


Figure 142. Experimental streamwise disturbance velocity profile determined from  $\bar{u}_s - \bar{u}_{s,avg}$  and theoretical eigenfunction for  $x/c = 0.45$ ,  $\alpha = -4^\circ$ , and  $R_c = 2.37 \times 10^6$ .

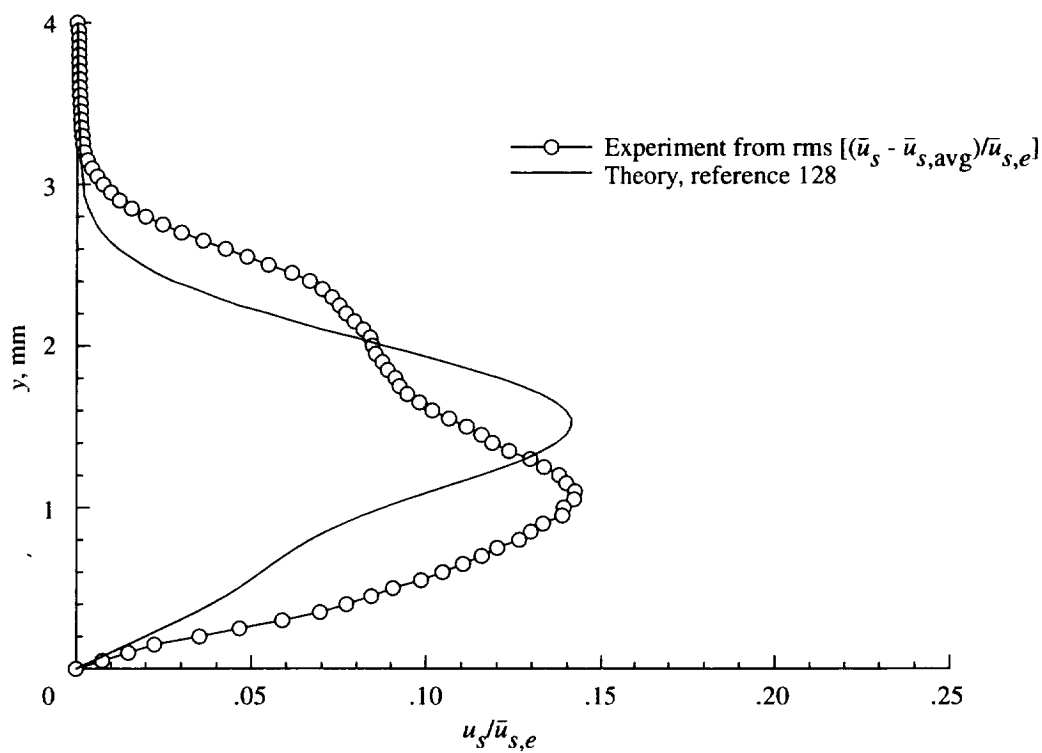


Figure 143. Experimental streamwise disturbance velocity profile determined from  $\bar{u}_s - \bar{u}_{s,avg}$  and theoretical eigenfunction for  $x/c = 0.50$ ,  $\alpha = -4^\circ$ , and  $R_c = 2.37 \times 10^6$ .

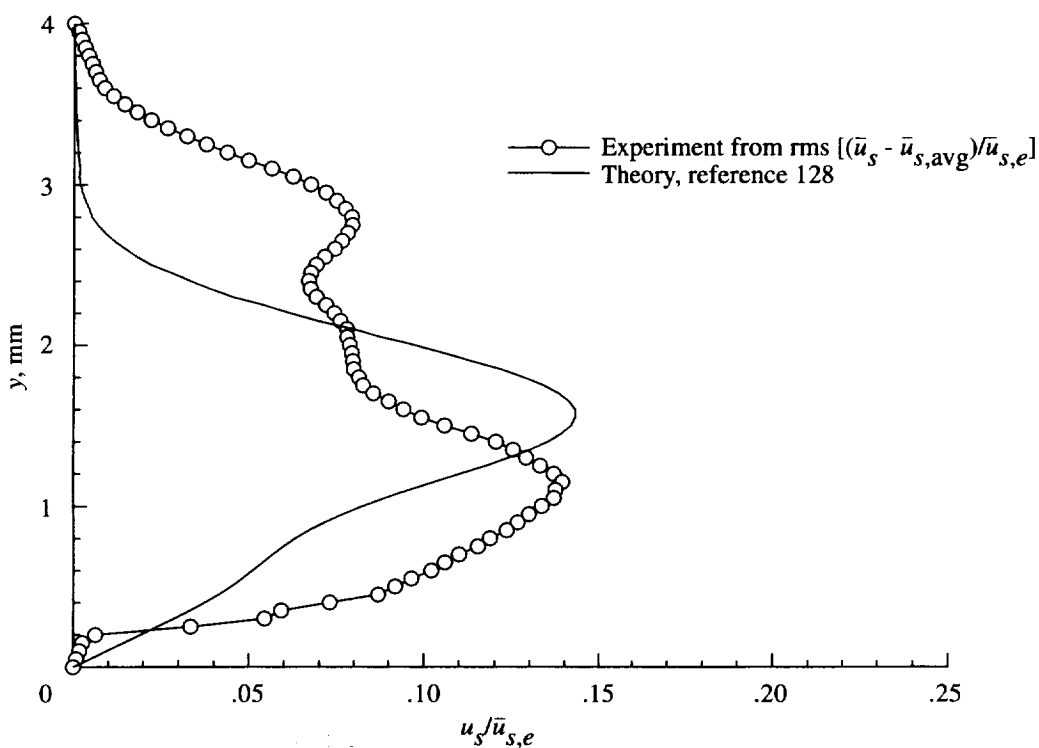


Figure 144. Experimental streamwise disturbance velocity profile determined from  $\bar{u}_s - \bar{u}_{s,avg}$  and theoretical eigenfunction for  $x/c = 0.55$ ,  $\alpha = -4^\circ$ , and  $R_c = 2.37 \times 10^6$ .

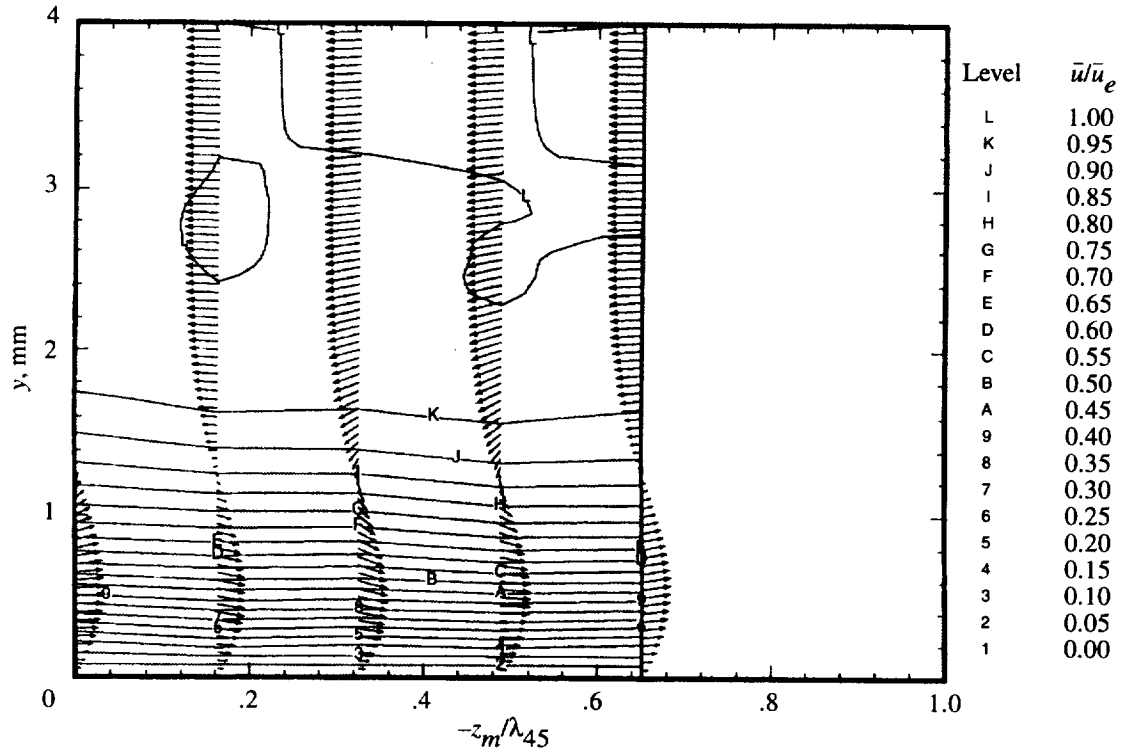


Figure 145. Experimental mean streamwise velocity contours and theoretical vortex velocity vector field for  $x/c = 0.20$ ,  $\alpha = -4^\circ$ , and  $R_c = 2.37 \times 10^6$ .

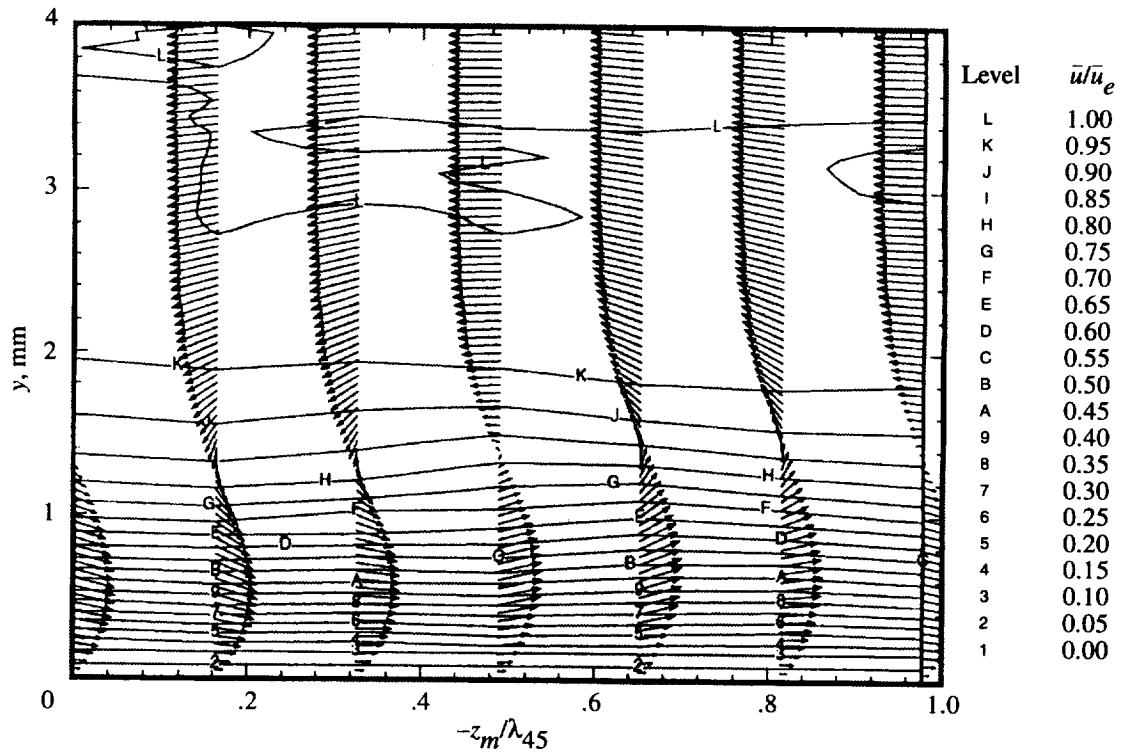


Figure 146. Experimental mean streamwise velocity contours and theoretical vortex velocity vector field for  $x/c = 0.25$ ,  $\alpha = -4^\circ$ , and  $R_c = 2.37 \times 10^6$ .

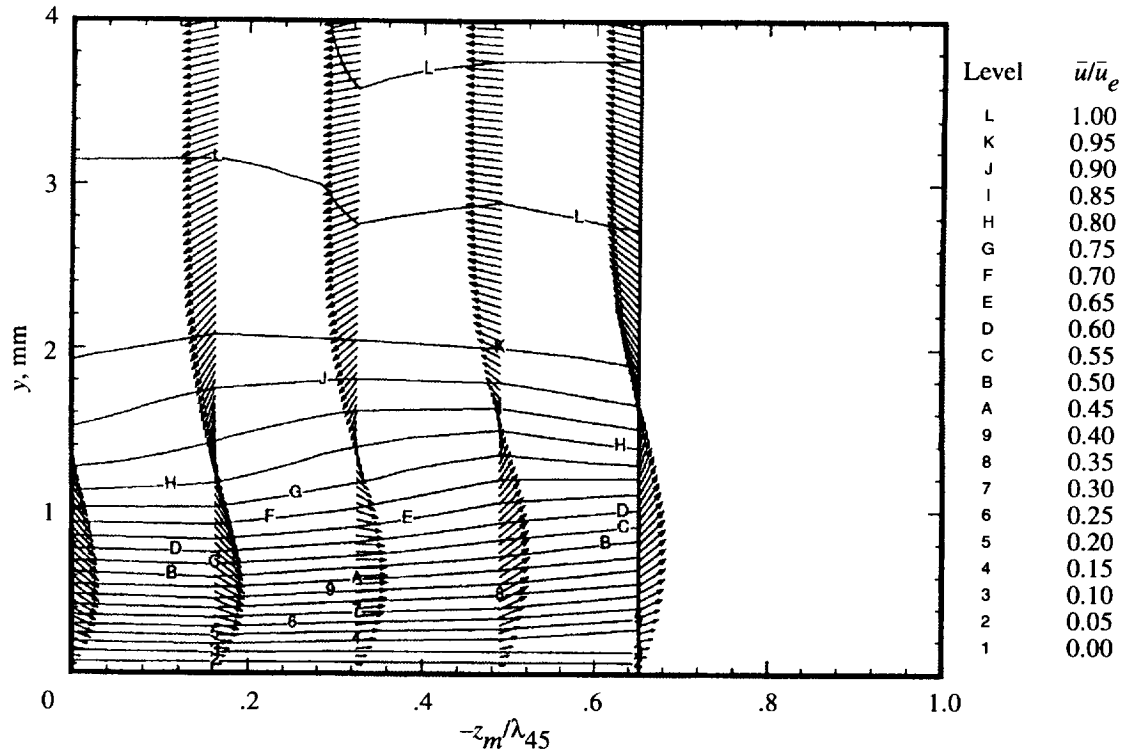


Figure 147. Experimental mean streamwise velocity contours and theoretical vortex velocity vector field for  $x/c = 0.30$ ,  $\alpha = -4^\circ$ , and  $R_c = 2.37 \times 10^6$ .

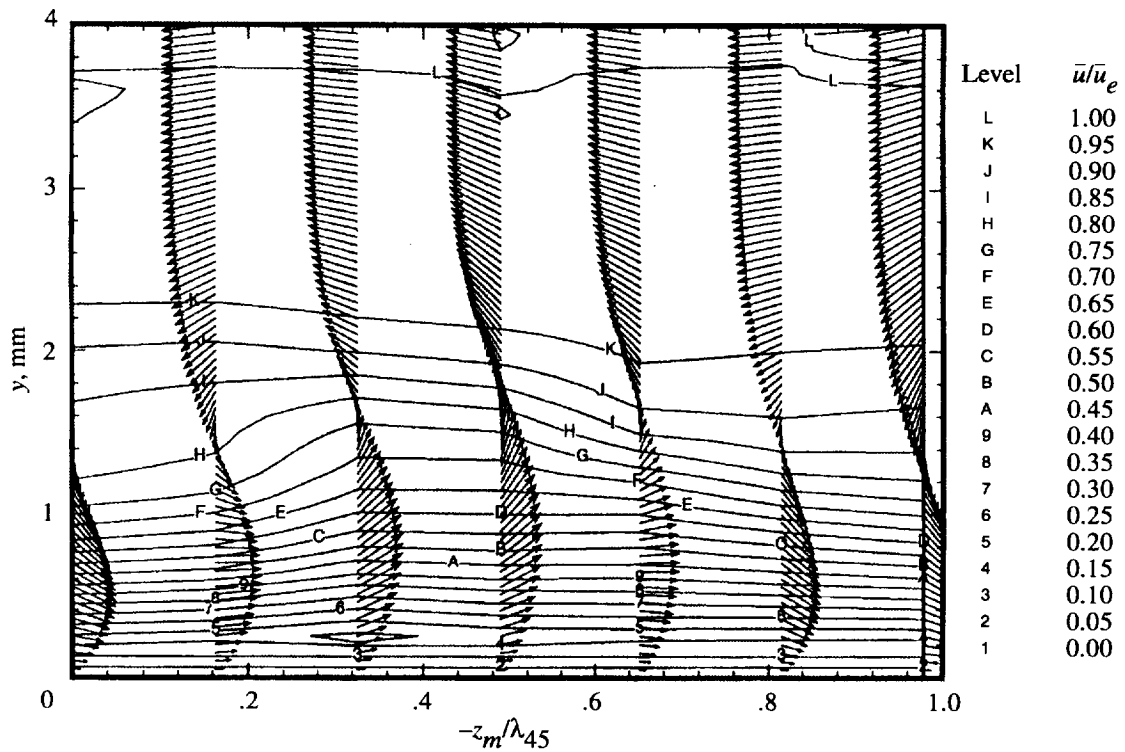


Figure 148. Experimental mean streamwise velocity contours and theoretical vortex velocity vector field for  $x/c = 0.35$ ,  $\alpha = -4^\circ$ , and  $R_c = 2.37 \times 10^6$ .

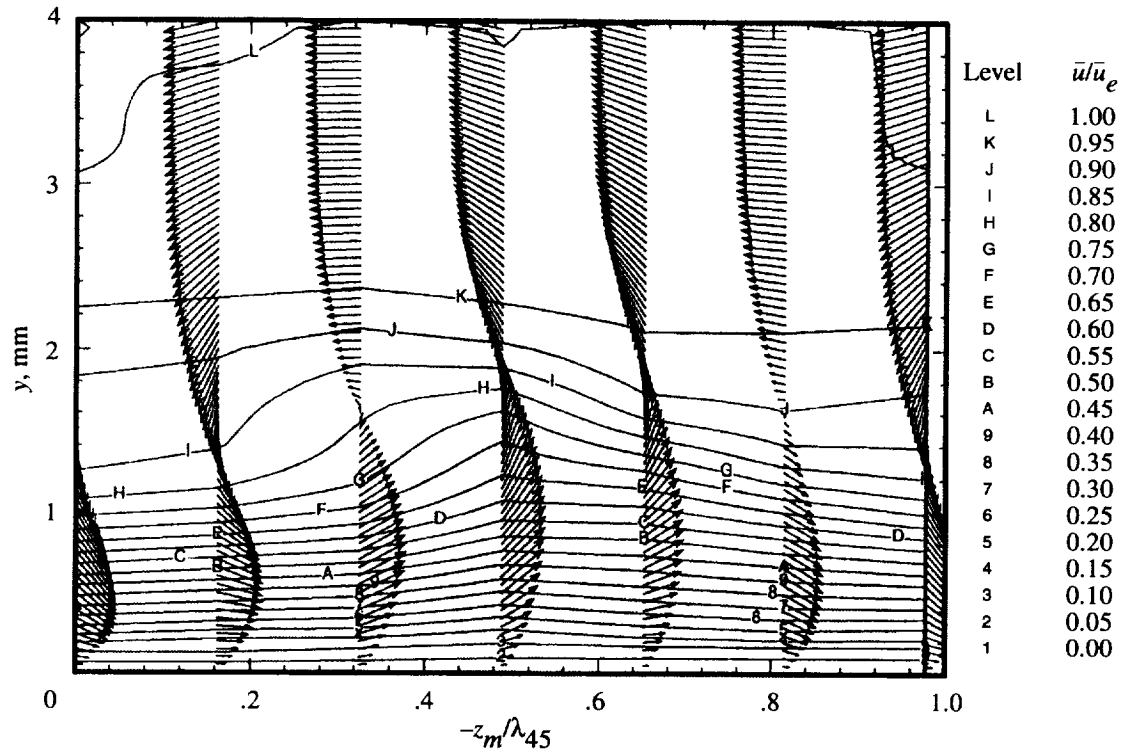


Figure 149. Experimental mean streamwise velocity contours and theoretical vortex velocity vector field for  $x/c = 0.40$ ,  $\alpha = -4^\circ$ , and  $R_c = 2.37 \times 10^6$ .

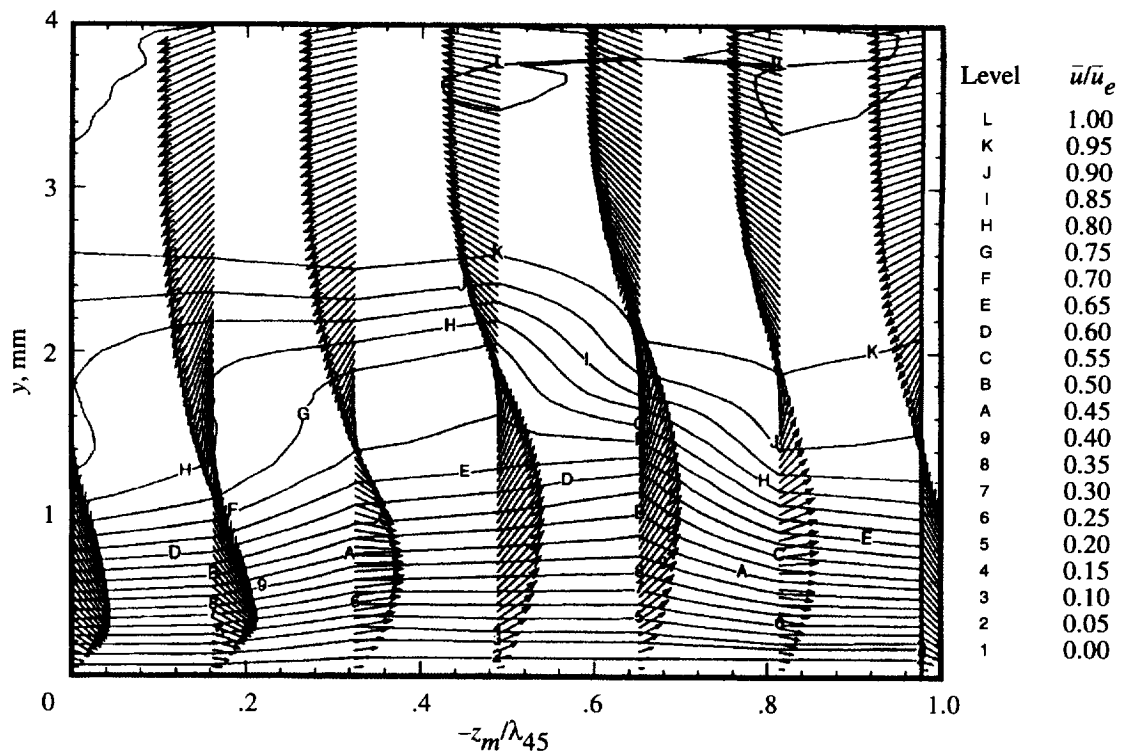


Figure 150. Experimental mean streamwise velocity contours and theoretical vortex velocity vector field for  $x/c = 0.45$ ,  $\alpha = -4^\circ$ , and  $R_c = 2.37 \times 10^6$ .



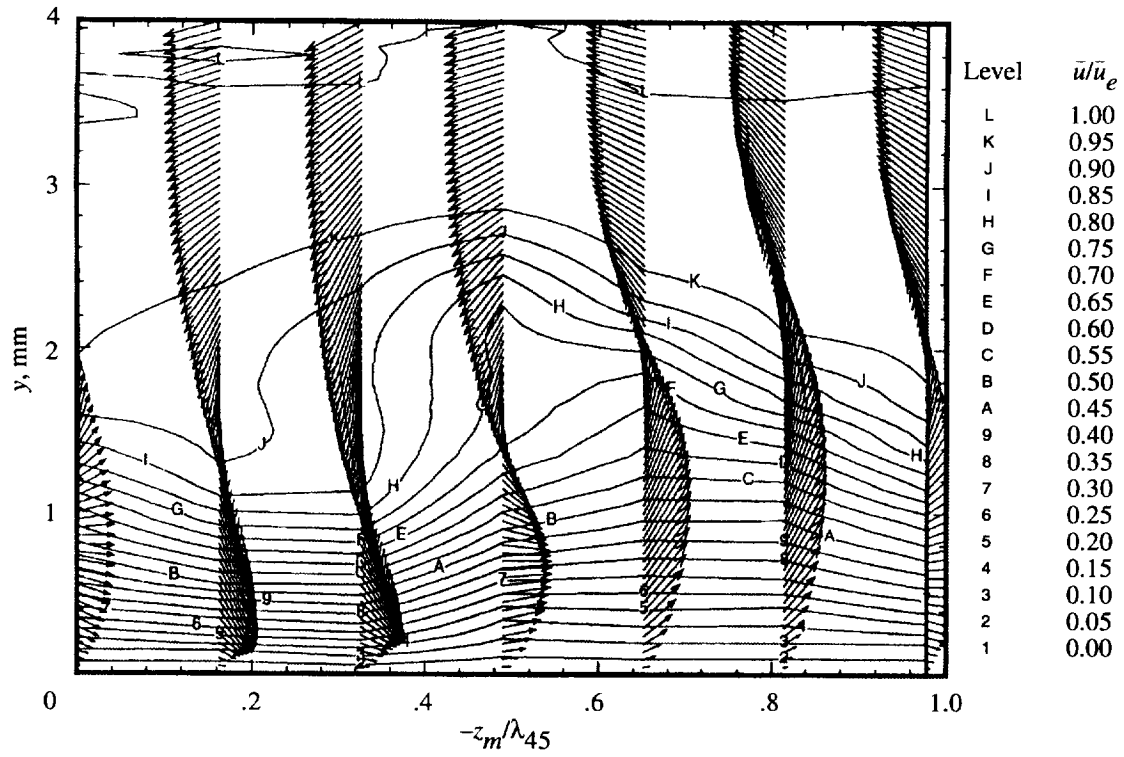


Figure 151. Experimental mean streamwise velocity contours and theoretical vortex velocity vector field for  $x/c = 0.50$ ,  $\alpha = -4^\circ$ , and  $R_c = 2.37 \times 10^6$ .

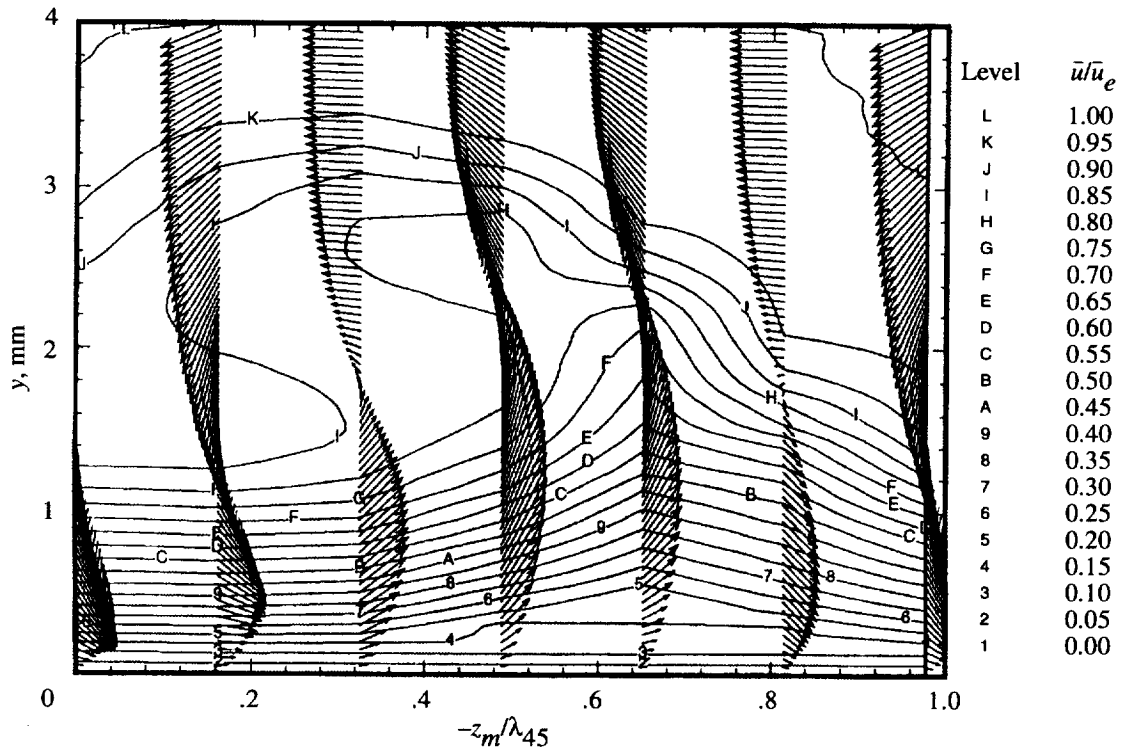


Figure 152. Experimental mean streamwise velocity contours and theoretical vortex velocity vector field for  $x/c = 0.55$ ,  $\alpha = -4^\circ$ , and  $R_c = 2.37 \times 10^6$ .

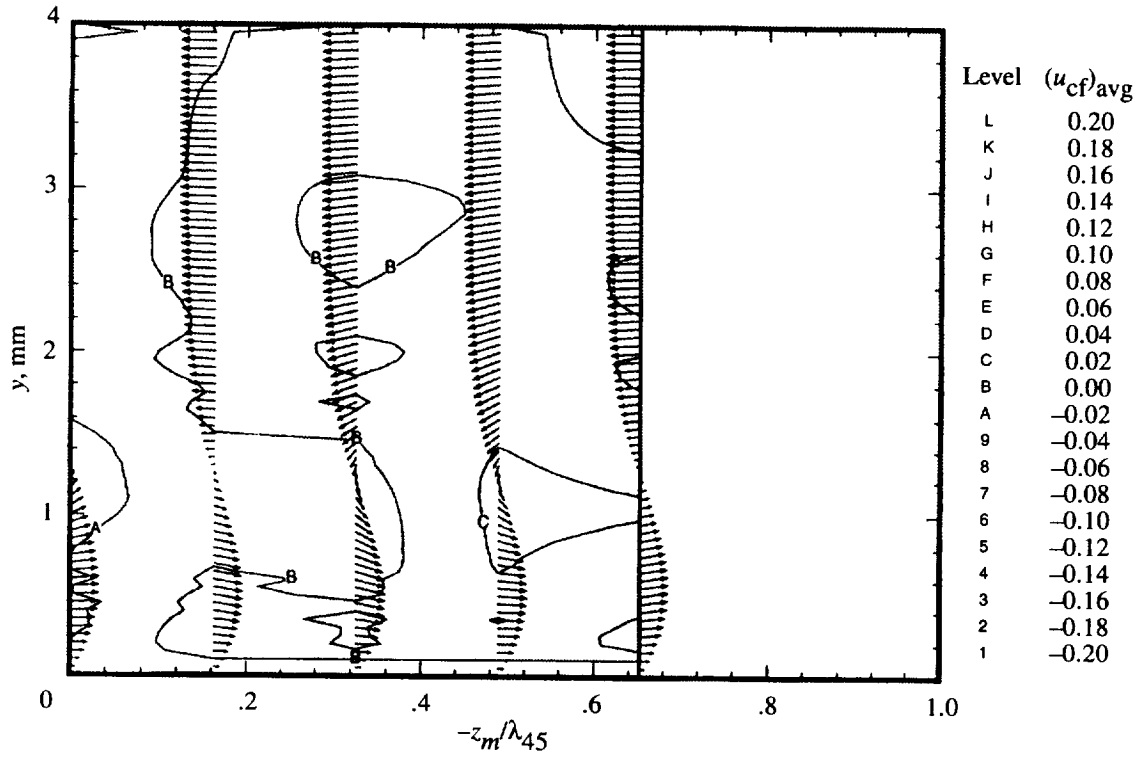


Figure 153. Experimental stationary crossflow disturbance velocity contours and theoretical vortex velocity vector field for  $x/c = 0.20$ ,  $\alpha = -4^\circ$ , and  $R_c = 2.37 \times 10^6$ .

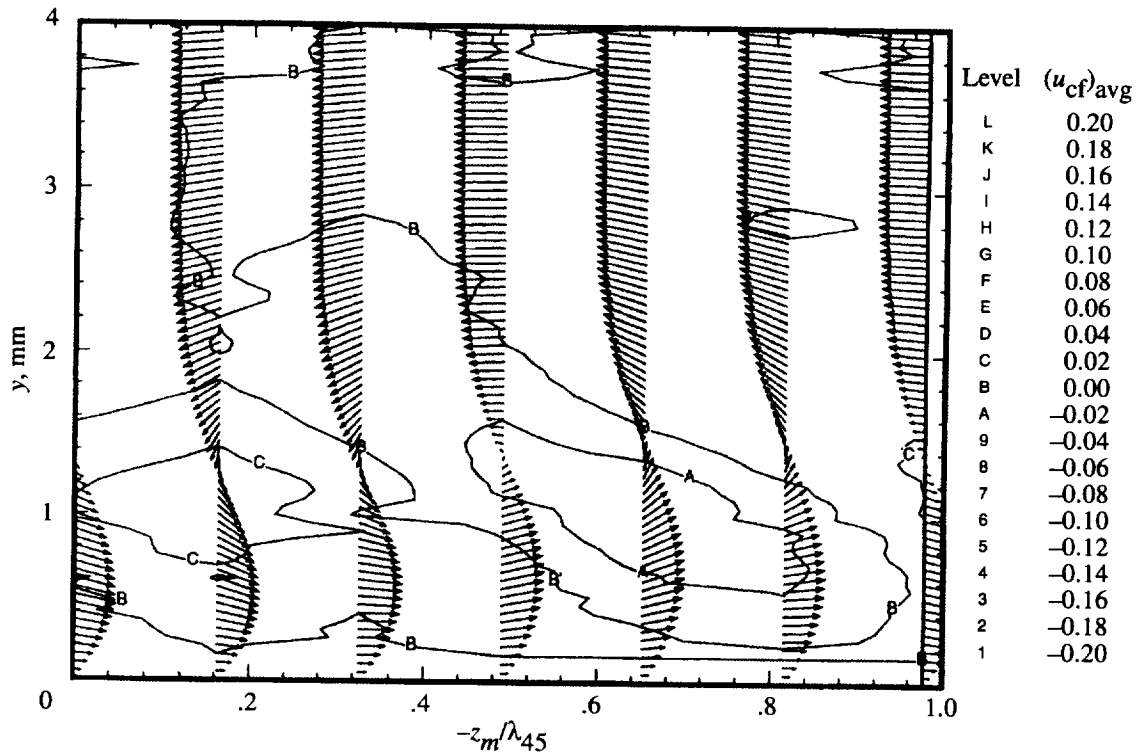


Figure 154. Experimental stationary crossflow disturbance velocity contours and theoretical vortex velocity vector field for  $x/c = 0.25$ ,  $\alpha = -4^\circ$ , and  $R_c = 2.37 \times 10^6$ .

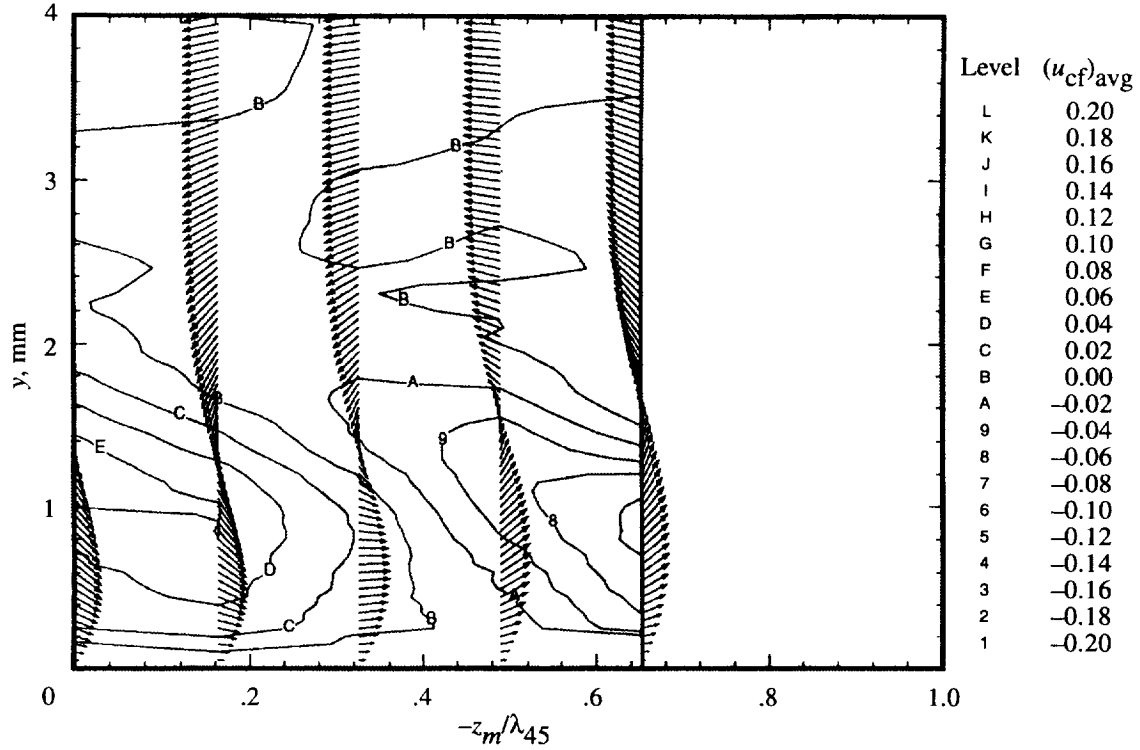


Figure 155. Experimental stationary crossflow disturbance velocity contours and theoretical vortex velocity vector field for  $x/c = 0.30$ ,  $\alpha = -4^\circ$ , and  $R_c = 2.37 \times 10^6$ .

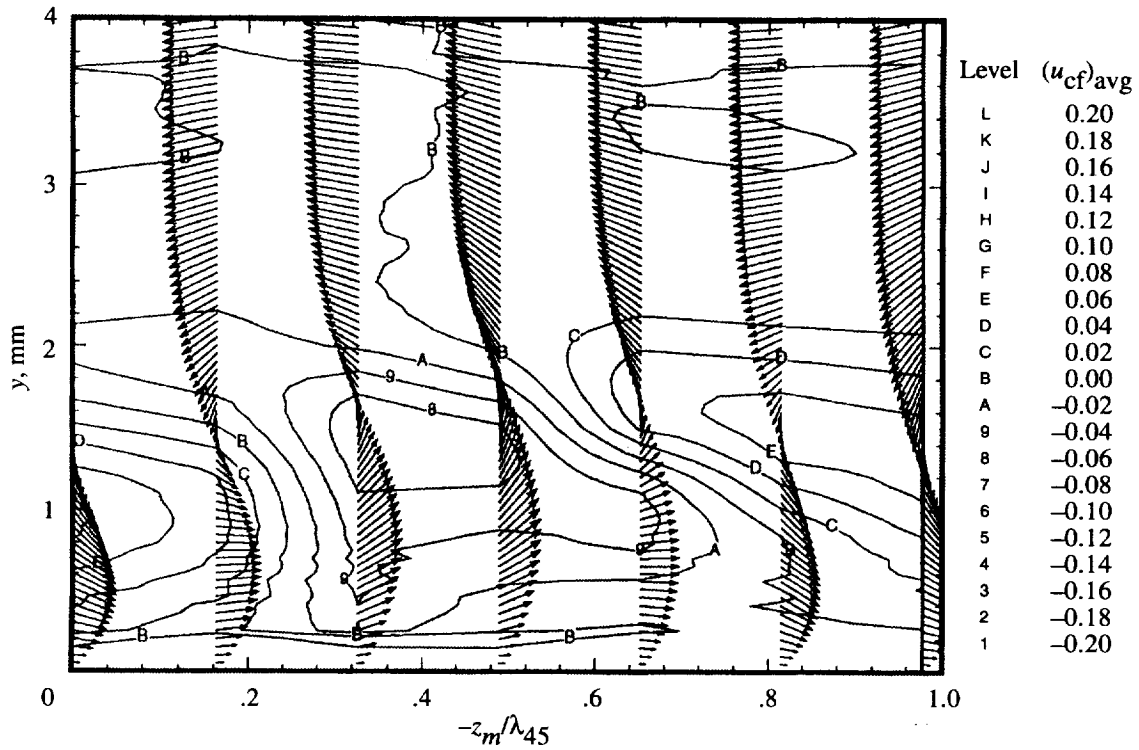


Figure 156. Experimental stationary crossflow disturbance velocity contours and theoretical vortex velocity vector field for  $x/c = 0.35$ ,  $\alpha = -4^\circ$ , and  $R_c = 2.37 \times 10^6$ .

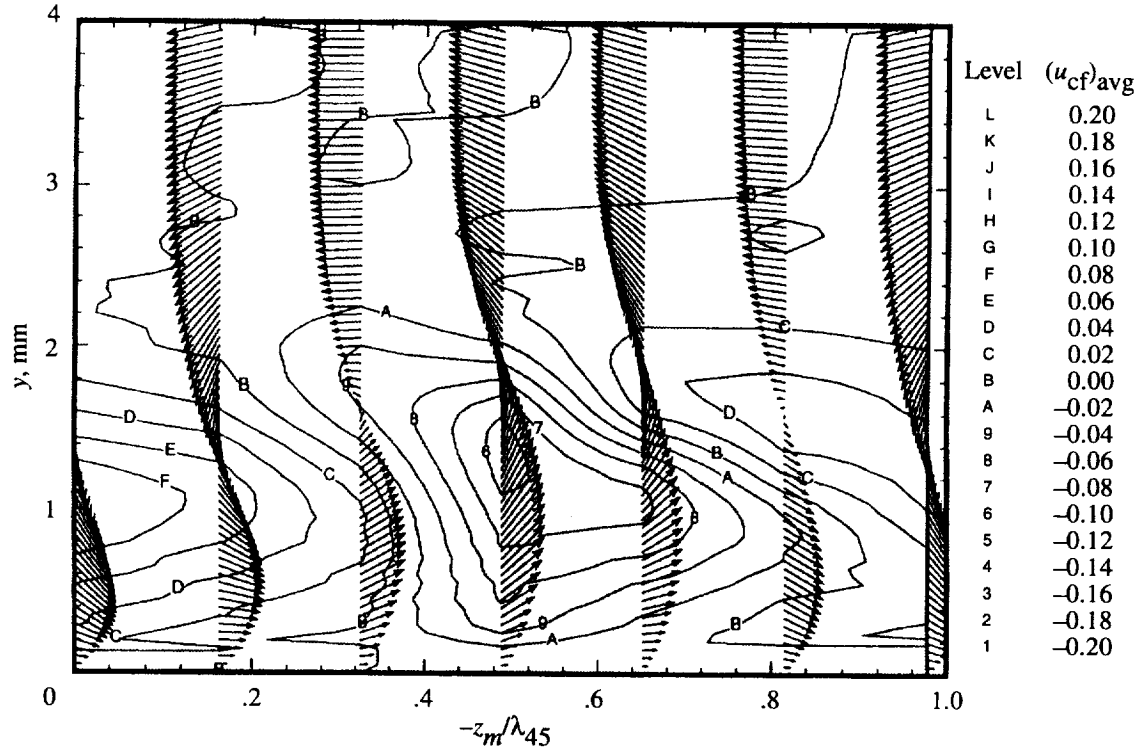


Figure 157. Experimental stationary crossflow disturbance velocity contours and theoretical vortex velocity vector field for  $x/c = 0.40$ ,  $\alpha = -4^\circ$ , and  $R_c = 2.37 \times 10^6$ .

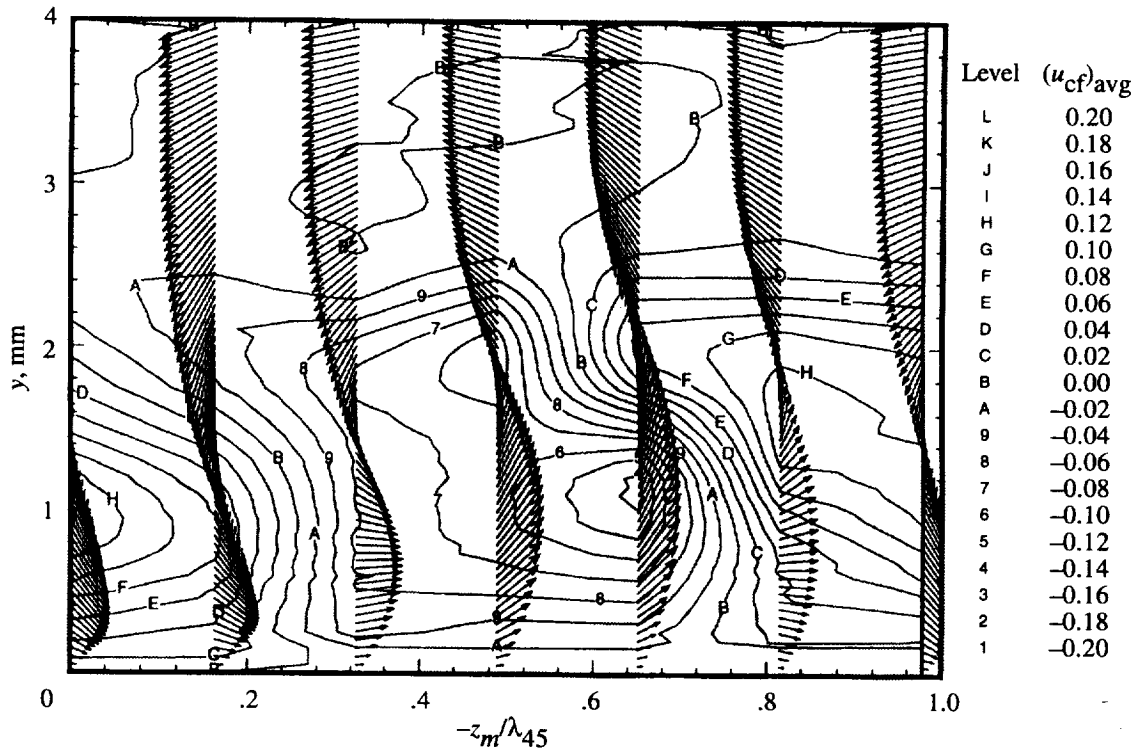


Figure 158. Experimental stationary crossflow disturbance velocity contours and theoretical vortex velocity vector field for  $x/c = 0.45$ ,  $\alpha = -4^\circ$ , and  $R_c = 2.37 \times 10^6$ .

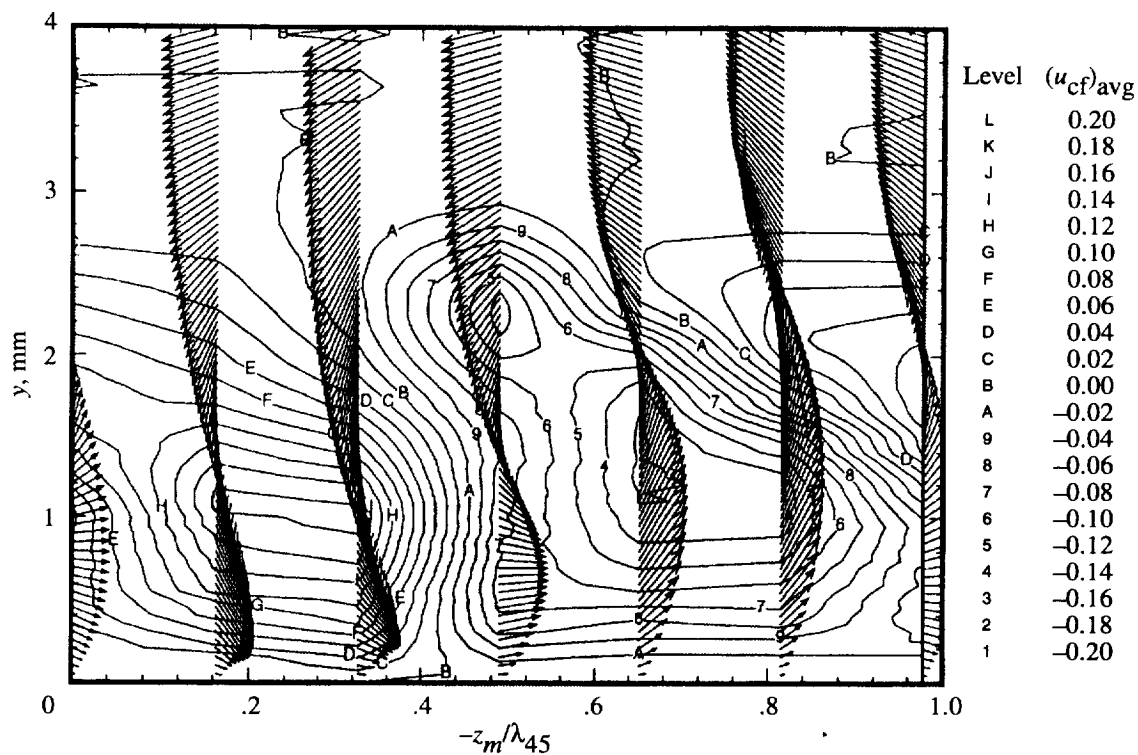


Figure 159. Experimental stationary crossflow disturbance velocity contours and theoretical vortex velocity vector field for  $x/c = 0.50$ ,  $\alpha = -4^\circ$ , and  $R_c = 2.37 \times 10^6$ .

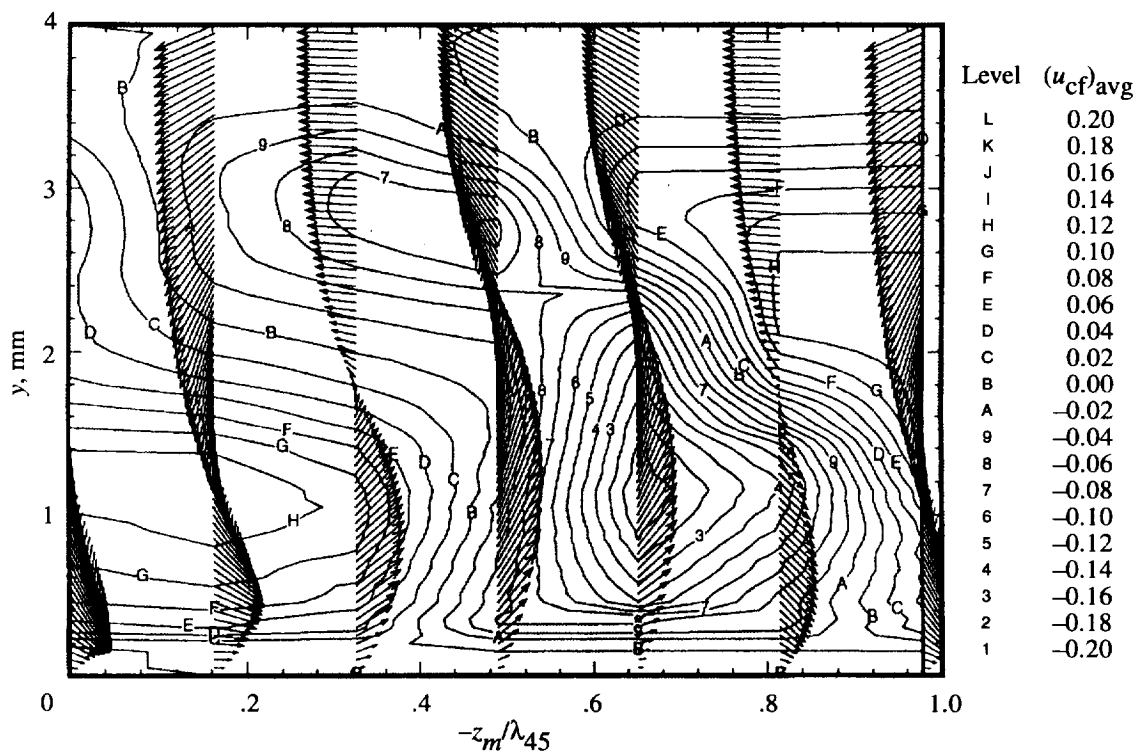


Figure 160. Experimental stationary crossflow disturbance velocity contours and theoretical vortex velocity vector field for  $x/c = 0.55$ ,  $\alpha = -4^\circ$ , and  $R_c = 2.37 \times 10^6$ .

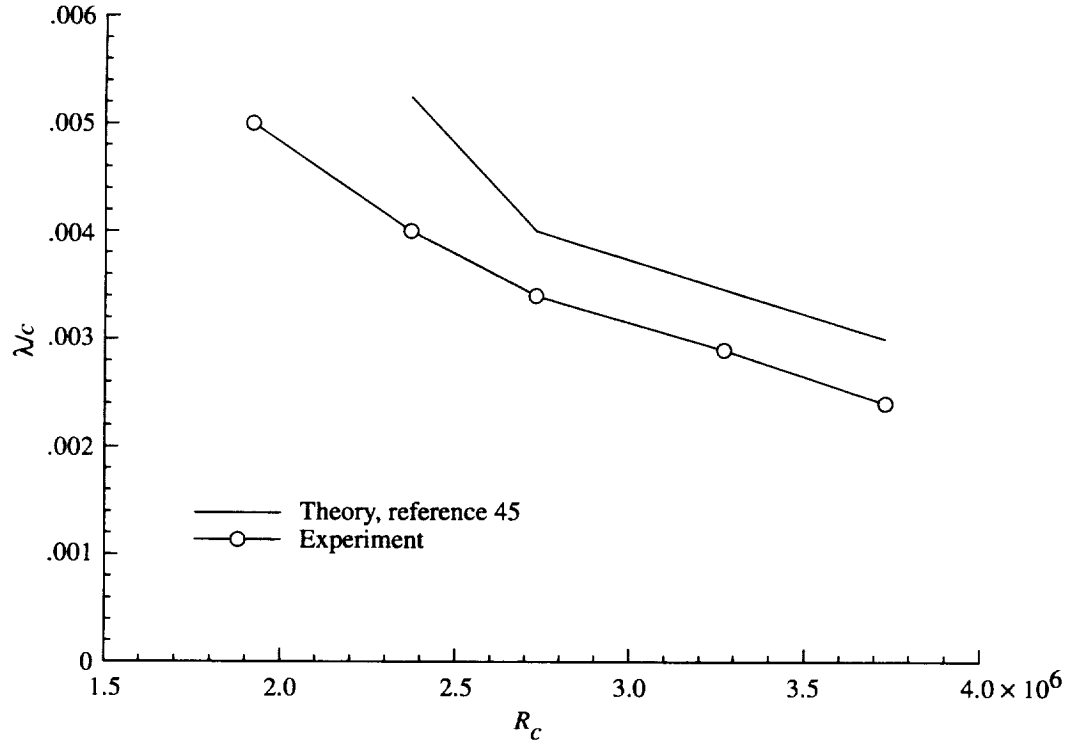


Figure 161. Theoretical and experimental stationary crossflow vortex wavelengths for  $\alpha = -4^\circ$  and  $R_c = 2.37 \times 10^6$ .

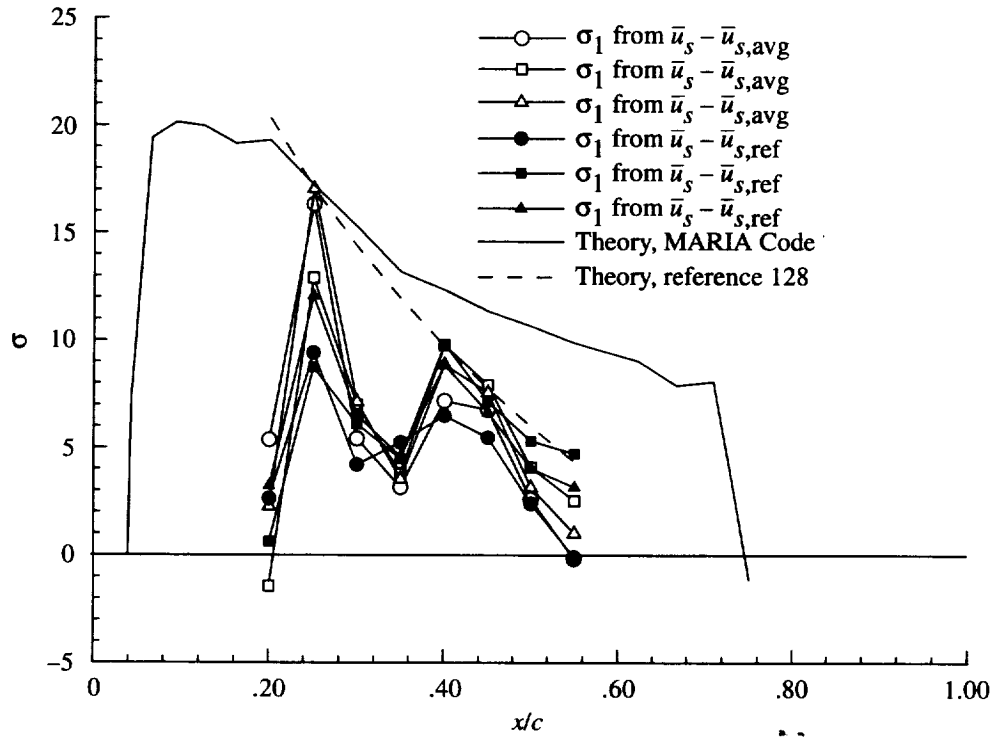


Figure 162. Theoretical and experimental stationary crossflow vortex growth rates for  $\alpha = -4^\circ$  and  $R_c = 2.37 \times 10^6$ .

REPORT DOCUMENTATION PAGE			Form Approved OMB No. 07704-0188	
Public reporting burden for this collection of information is estimated to average 1 hour per response, including the time for reviewing instructions, searching existing data sources, gathering and maintaining the data needed, and completing and reviewing the collection of information. Send comments regarding this burden estimate or any other aspect of this collection of information, including suggestions for reducing this burden, to Washington Headquarters Services, Directorate for Information Operations and Reports, 1215 Jefferson Davis Highway, Suite 1204, Arlington, VA 22202-4302, and to the Office of Management and Budget, Paperwork Reduction Project (0704-0188), Washington, DC 20503.				
1. AGENCY USE ONLY (Leave blank)	2. REPORT DATE July 1999	3. REPORT TYPE AND DATES COVERED Technical Publication		
4. TITLE AND SUBTITLE Crossflow Stability and Transition Experiments in Swept-Wing Flow		5. FUNDING NUMBERS WU 522-31-11-03		
6. AUTHOR(S) J. Ray Dagenhart and William S. Saric				
7. PERFORMING ORGANIZATION NAME(S) AND ADDRESS(ES) NASA Langley Research Center Hampton, VA 23681-2199		8. PERFORMING ORGANIZATION REPORT NUMBER L-17658		
9. SPONSORING/MONITORING AGENCY NAME(S) AND ADDRESS(ES) National Aeronautics and Space Administration Washington, DC 20546-0001		10. SPONSORING/MONITORING AGENCY REPORT NUMBER NASA/TP-1999-209344		
11. SUPPLEMENTARY NOTES Dagenhart: Langley Research Center, Hampton, VA; Saric: Arizona State University, Tempe, AZ.				
12a. DISTRIBUTION/AVAILABILITY STATEMENT Unclassified-Unlimited Subject Category 34 Availability: NASA CASI (301) 621-0390		12b. DISTRIBUTION CODE		
13. ABSTRACT (Maximum 200 words) An experimental examination of crossflow instability and transition on a 45° swept wing was conducted in the Arizona State University Unsteady Wind Tunnel. The stationary-vortex pattern and transition location are visualized by using both sublimating chemical and liquid-crystal coatings. Extensive hot-wire measurements were obtained at several measurement stations across a single vortex track. The mean and travelling wave disturbances were measured simultaneously. Stationary crossflow disturbance profiles were determined by subtracting either a reference or a span-averaged velocity profile from the mean velocity data. Mean, stationary crossflow, and travelling wave velocity data were presented as local boundary layer profiles and contour plots across a single stationary crossflow vortex track. Disturbance mode profiles and growth rates were determined. The experimental data are compared with predictions from linear stability theory.				
14. SUBJECT TERMS Swept-wing transition; Experiments; Crossflow instability; Natural laminar flow			15. NUMBER OF PAGES 150	
			16. PRICE CODE A07	
17. SECURITY CLASSIFICATION OF REPORT Unclassified	18. SECURITY CLASSIFICATION OF THIS PAGE Unclassified	19. SECURITY CLASSIFICATION OF ABSTRACT Unclassified	20. LIMITATION OF ABSTRACT UL	

1000